

Radar Observations of Artificial Ionospheric Modification Effects

Thesis submitted for the degree of
Doctor of Philosophy
at the University of Leicester

by

Hannah Vickers

Radio and Space Plasma Physics Group
Department of Physics and Astronomy
University of Leicester

December 2010

Radar Observations of Artificial Ionospheric Modification Effects

Hannah Vickers

Abstract

Artificial ionospheric modification experiments by means of high power, high frequency radio waves using the EISCAT (European Incoherent SCATter) heater at Tromsø, northern Norway have been carried out for nearly three decades. These experiments are associated with large-scale increases in the electron temperature and density and generation of small-scale plasma irregularities, which are diagnosed by the EISCAT UHF and CUTLASS (Cooperative UK Twin Located Auroral Sounding System) HF radars.

Experimental results from the EISCAT UHF radar, obtained from heating campaigns at Tromsø between 1996 and 1999, are used to study the effects of heater-induced instabilities on the analyses of EISCAT spectra. Plasma turbulence induced by high power heater waves produces unphysical estimates of ionospheric plasma parameters during the initial phase of heating, and a method is developed to correct for these problems. It is shown that these estimates are nevertheless, reliable over longer timescales of heating

In the second study, relaxation characteristics of small-scale density perturbations measured using the CUTLASS Finland radar are modelled theoretically and shown to be largely consistent with large-scale temperatures measured using the EISCAT UHF radar. Certain cases are identified where alternative models of irregularity decay are required to describe the temporal behaviour in radar backscatter. These models consider influences such as electron temperature reductions, wave-wave coupling and background flow.

The final study concentrates on a heating experiment in October 2000, where unusually broadened spectral widths of artificial HF backscatter measured with the CUTLASS Finland and Iceland radars was observed. The results were incompatible with previous explanations of similar observations. The Burg maximum entropy analysis was implemented to formulate a tentative explanation for the observations, involving simultaneous detection of artificial and natural irregularity echoes by the Iceland radar. This required the heater amplification of non co-located natural irregularities, already above the noise threshold of the radar.

Acknowledgements

This is without doubt one of the most important pages of my thesis so I am going to make sure I have been quite thorough in my list of people whom I would like to thank.

Firstly, to Professor Stan Cowley for welcoming and allowing me to undertake my postgraduate studies in the Radio and Space Plasma Physics Group here at Leicester; Professor Terry Robinson, for all his in-depth supervision of my PhD – and patience when I've not understood things! Also, to Dr. Ian McCrea at the Rutherford-Appleton Laboratory, and Dr. Ranvir Dhillon for their help with EISCAT problems and work, and Professor Mark Lester, Professor Tim Yeoman and Dr. Steve Milan for all things CUTLASS-related.

I also want to thank my past and present office companions – Gabby, Carlos, Ingrid, Atousa and James for putting up with my changeable moods (depending on how work-productive my days are) and general lack of conversation..... and to Steph, Suzie and Sarah for providing occasional light entertainment and sweet delights next door when I have turned up, and in particular to Steph for agreeing to do the Great North Run this year with me despite all her huge commitments. Also, I should probably also thank the Science and Technology Facilities Council (i.e. the STFC) for the studentship and their generous contribution of funding towards my overseas field trips and workshops over the last three years!

Lastly I want to make sure I thank my former housemates, Lucy, Dee, Michelle and Alise, for just living with me and the good times we had together, and all of my family – Dad, who would have been really proud to see this thesis, and Mum, Serena, Christina and Daniel for their continuous support, encouragement and amusement.

Contents

1. Introduction	Page
1.1. Earth's Atmosphere	1
1.2. Ionospheric Layers	2
1.3. Ionospheric Temperatures	4
1.4. Magnetosphere	4
1.5. Ionospheric Modification Experiments	7
1.6. Aims of the Study	8
2. Theory of Artificial Ionospheric Modification	
2.1. Particle motion in a plasma	10
2.2. Refractive Index and the Appleton-Hartree Equation	12
2.3. Upper Hybrid Waves	14
2.4. Review of Early Heating Experiments at Platteville	15
2.5. Theory of Artificial Modification: F region heating	19
2.5.1. Parametric Decay Instability	19
2.5.2. Thermal Parametric Instability	21
2.6. Theory of Small-Scale Field-Aligned Irregularity Growth	22
2.7. Large-Scale Electron Temperature and Density Response	25
2.8. Review of Experimental Work	28
2.9. Theory and Observations of Irregularity Relaxation	35

3. Instrumentation	Page
3.1. Artificial Ionospheric Heating Facility	40
3.1.1. Facility Overview	40
3.1.2. Transmitters	40
3.1.3. Antenna Arrays	41
3.1.4. Beam Modulation	43
3.2. Incoherent Scatter Radar Measurements	45
3.3. Incoherent Scatter Technique: Background	45
3.4. Radar Equation	47
3.5. Ion-Acoustic Waves	47
3.6. Langmuir Waves	49
3.7. The EISCAT Radars	49
3.8. Bragg Scattering	51
3.9. Incoherent Scatter Spectrum Shape	52
3.10. Incoherent Scatter Spectrum Analysis: GUIDAP	53
3.11. CUTLASS Radars	56
3.12. CUTLASS Pulse Schemes	61
3.13. Tromsø Dynasonde	63
3.14. Concluding Remarks	63

4. Evaluation of the Electron Temperatures Recovered by Incoherent Scatter Analysis during Artificial Ionospheric Modification Experiments	Page
4.1. Introduction	65
4.2. Motivation for the Study	66
4.3. Epstein Function Analysis	69
4.3.1. Epstein Model Function	69
4.3.2. Results of the Temperature Profile Fitting	71
4.4. Theoretical Model of Large Scale Heating	77
4.5. Results: Simple Theoretical Model	78
4.5.1. Example 1: 1308-1312UT, 21 st October 1999	78
4.5.2. Example 2: 1410-1412UT, 7 th October 1997	80
4.5.3. Example 3: 1532-1536UT, 19 th October 1999	81
4.6. Ion-Acoustic Spectra: Removal of PGM	84
4.7. Results: Ion-Acoustic Spectrum Corrections	86
4.7.1. Example 1: 1358-1400UT, 7 th October 1997	86
4.7.2. Example 2: 1255-1256UT, 7 th October 1997	89
4.8. Application to a Wider Study of Artificial Heating Spectra	92
4.8.1. Overshoot Spectra	92
4.8.2. Application to a wider study of Averaged Spectra	97
4.9. Summary	106

5. Characterisation of Field-Aligned Irregularity Relaxation and Evidence for the Existence of Isolated Striations	Page
5.1. Introduction	109
5.2. Simple Model of FAI Decay	110
5.3. Alternative Models of FAI Relaxation	122
5.3.1. Time-Dependent Temperature Decay Model	122
5.3.2. Wave-Wave Model of FAI Decay	124
5.4. Alternative Decay Model Fit Results	125
5.5. Drift Velocity Dependence	137
5.6. Flow Effects on the Decay of CUTLASS Backscatter	142
5.7. Summary and Concluding Remarks	147
6. Observation of Artificial HF Backscatter in the presence of Strong Flows and Natural Irregularities	
6.1. Introduction	149
6.2. Background	149
6.3. Heating Experiment Details	151
6.4. CUTLASS Observations	153
6.5. Results of the Burg Spectrum Analysis	165
6.6. Discussion	175
6.6.1. Comparison with Previous Work	175
6.6.2. Other Possible Factors	178
6.7. Summary	185

7. Summary of Major Results	Page
7.1. Introduction	187
7.2. Principal Scientific Findings	188
7.3. Outstanding Questions and Further Work	190
Appendices	
Appendix 1. Ionospheric Sounding and the Tromsø Dynasonde	193
Appendix 2. Epstein Function Fitting Procedure	196
Appendix 3. Incoherent Scatter Spectrum Correction	199
Appendix 4. Rates of Decay from Transport and Chemical Processes	200
Appendix 5. Burg Spectrum Analysis	207
Bibliography	209

Chapter 1

Introduction

1.1 Earth's Atmosphere

The Earth's lower atmosphere, below about 20km consists of molecular oxygen and nitrogen, and small amounts of carbon dioxide and water vapour. The chemical composition and distribution of species in the atmosphere changes with altitude, and this in turn affects the pressure and density, which decrease with height. At high altitudes at 100km and above, where the density is very low, solar radiation in the form of ultraviolet (UV) and X-rays arriving from the Sun, is energetic enough to cause chemical dissociation and ionization of neutral molecules. These ionized particles may remain charged for a sufficiently long period of time due to the low atmospheric pressure and therefore rate of collisions which serve in chemical recombination. Their presence gives rise to a state of matter otherwise known as plasma, which is composed of both charged ('electrons' and 'ions') and electrically neutral particles, and thus termed the ionosphere. Overall, the concentration of ions and electrons must balance across the ionosphere to maintain charge neutrality of the layer, and this is typically only 1% of the neutral particle concentration.

The ionospheric plasma is an electrically conductive medium due to its composition of charged particles, and can therefore also interact with electrostatic and magnetic perturbations, and electromagnetic waves. It was in the early part of the 20th century that the ionosphere was first discovered due to its profound effect on the propagation of radio waves through the medium. The successful transmission of radio waves across the Atlantic by Marconi in 1901 led the scientists Heaviside and Kennelly (1902) to believe

that there must be a reflective, conducting layer present in the atmosphere and this was later proven in experiments of Appleton and Barnett in England, 1924.

1.2 Ionospheric Layers

The ionosphere does not possess a uniform distribution of particles but can instead be identified to possess three distinct layers, known as the 'D', 'E' and 'F' layers. The existence of these layers was initially proven through frequency-sweep ionosonde experiments by Breit and Tuve. Amongst a large number of factors, the height profile of electron concentration across these regions can change with time of day, season, solar activity and also geographic latitude, due to the impact of varying strengths of solar illumination on the number of charged particles created by the photoionization process. In the lowest layer, namely the 'D' region, chemical processes and collisions dominate the creation and destruction of ionization, whereas in the highest layers, transport processes play a much more important role in the distribution of ionization. A typical profile of the electron density with altitude during day and night time conditions, and at solar minimum and maximum is shown in Figure 1.1. The first of these layers to be discovered was in fact the 'E' layer, due to its ability to reflect electromagnetic fields (Brekke, 1997), and is formed mainly by the process of photoionization and composed mainly of molecular ions. This region occupies the altitude region between 90 and 140km. Solar radiation is also responsible for the creation of two distinct regions within the 'F' layer, namely the 'F1' and 'F2' layers, which peak in electron density at approximately 170km and 300km respectively during the daytime. At altitudes below 180km, the dominant constituents of the F region plasma are molecular oxygen (O_2^+) and nitrous oxide (NO^+). Whilst both the E and F1 layers both disappear during the night time, the 'F2' layer remains. It is the F region that is of greatest interest in the topics of this study.

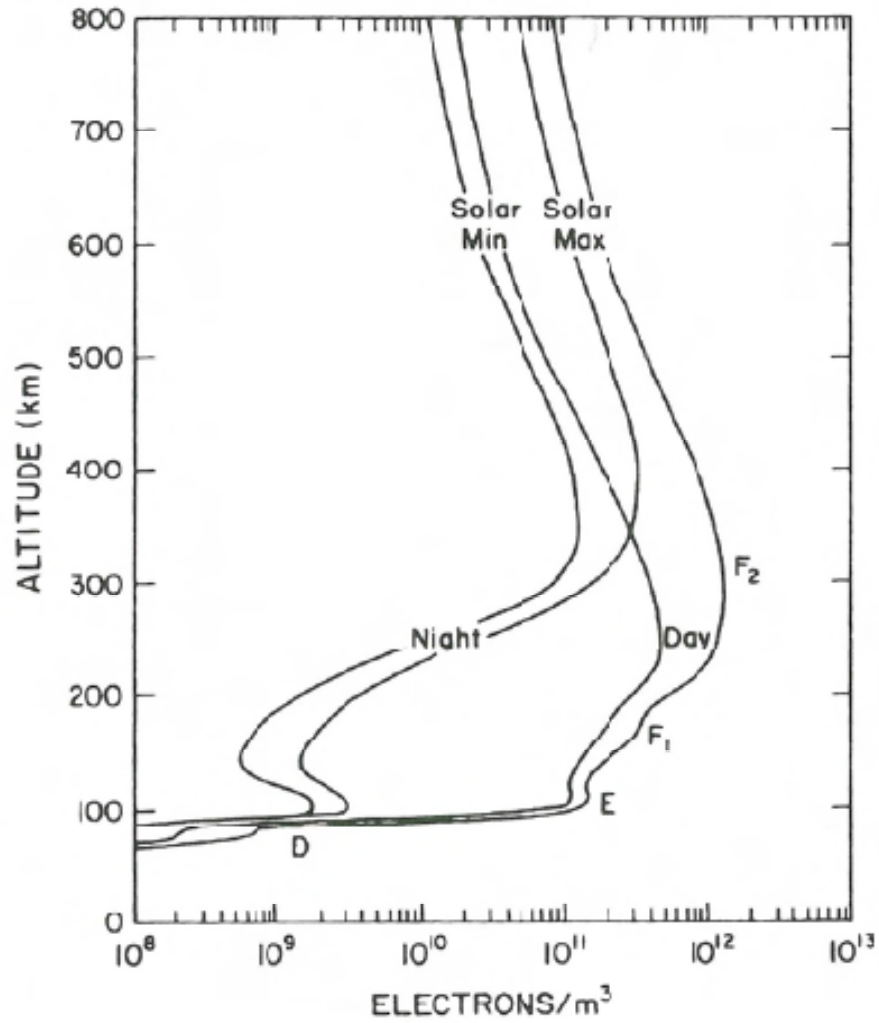


Figure 1.1 A typical height profile of the electron density during solar minimum and maximum, and during daytime and night-time conditions (from Dahlgren, 2008 after Richmond, 1987)

1.3 Ionospheric Temperatures

Within the lowest regions of the ionosphere, electrons and ions typically possess equal temperatures and move at a characteristic thermal speed which is dictated by both this temperature and the mass of the charged particle. With an increasing altitude however, the difference between the temperatures increases, and at the F region peak, typical electron and ion temperatures are 2000K and 1400K respectively (Stubbe and Hagfors, 1997). Any external driving force, such as that supplied by an electric field, will also serve to accelerate the charged particles and consequently act as a source of energy that heats the plasma. As a result of the large difference in mass between the ions and electrons, it is principally the electron temperature that is enhanced significantly when the plasma is heated.

1.4 Magnetosphere

The Earth possesses a strong magnetic field of internal origin, which plays a significant role in controlling and characterising plasma dynamics in the ionosphere. The topology of this 'geomagnetic' field is one of a dipole field, at distances near in to the surface. This field is tilted at 11 degrees to the axis about which the Earth spins. The relative importance of the geomagnetic field, on charged particle motion within the plasma, increases with altitude as ionization increases up to the F region peak, since the collision frequency of ionized and neutral particles decreases. High energy particles are constantly ejected by the Sun, and this stream of particles is commonly known as the 'solar wind'. Carried within this stream is the 'interplanetary' magnetic field, which is effectively 'frozen' into the flow of particles. The solar wind stream typically approaches the Earth at speeds at hundreds of kilometres per second, and is largely controlled by the degree of activity occurring at the Sun's surface. Since no plasma can penetrate the Earth's field in the transverse direction, a boundary is formed between the

solar wind and the outermost limits of the geomagnetic field, and it is here that a rapid deceleration of the supersonic solar wind particles takes place, leading to the formation of a shock front, often termed the 'bow shock'. Behind this lies the magnetopause, where the pressure due to the kinetic energy of the solar wind plasma is balanced by the magnetic pressure of the geomagnetic field. Behind here lies the magnetosphere, which represents the uppermost limits of the ionosphere. It also acts as a shell which protects the Earth's surface from penetration by the high energy particles of the solar wind. As a result of the pressure imposed by the stream of high-speed particles at the magnetopause, the dipole shape of the geomagnetic field is altered in such a way that a cavity with a compressed sunward side and elongated night side (the 'magnetotail') is created due to the anisotropy in solar wind pressure at each end. Figure 1.2 illustrates this magnetospheric cavity, the different plasma populations confined within it and the associated current systems. Although the magnetosphere as a whole will not play a central part in the much smaller-scale phenomena that are studied here, Figure 1.2 provides a background for the near-Earth upper atmosphere processes that govern the plasma response to external forces.

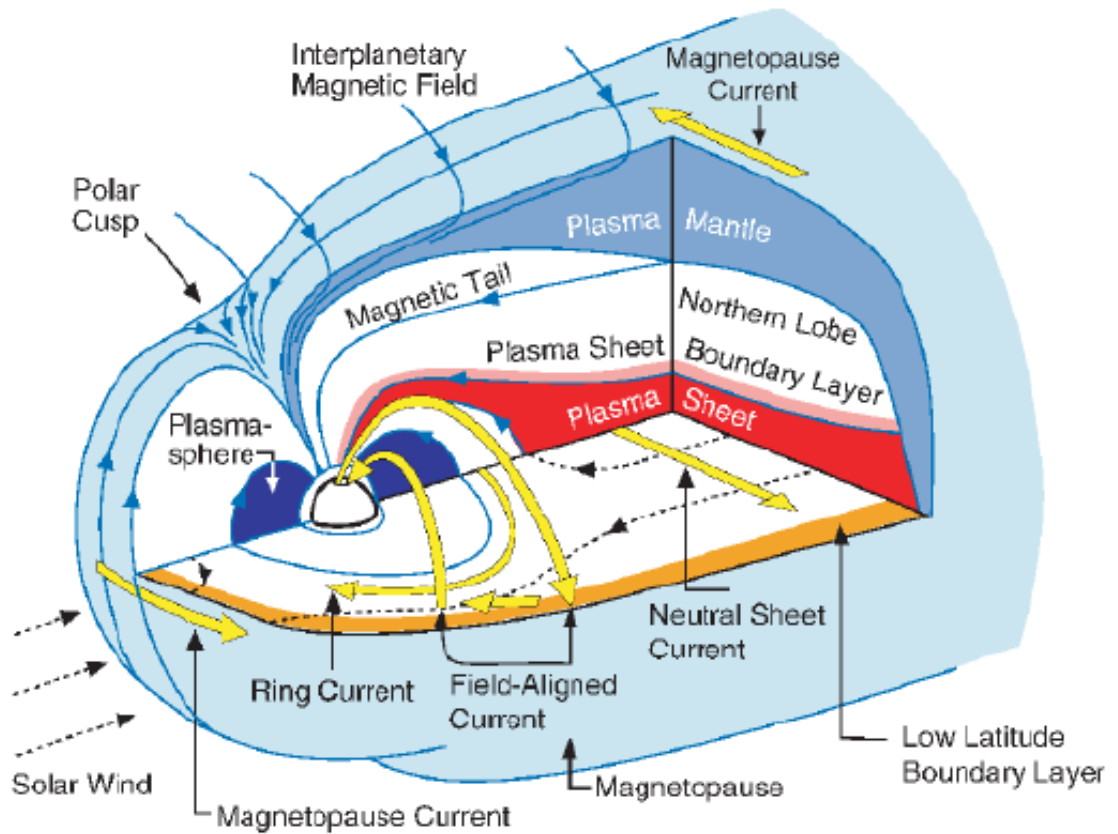


Figure 1.2 The magnetospheric cavity with its associated current systems and plasma boundaries (from Paschmann et al., 2003 after Kivelson and Russell, 1995)

1.5 Ionospheric Modification Experiments

Artificial modification of the ionosphere is the intentional act of changing the properties of the ionosphere by means of radio waves. It did not originally evolve as a deliberate attempt to modify the ionosphere, but its consequences were first observed and reported by Tellegen in 1933 at Eindhoven in Holland, when the Luxembourg radio broadcast severely interrupted the reception of the Beromunster programme signal. This interruption was caused by a cross-modulation effect, which was explained by Tellegen to be due to the modification of the radio wave path through the ionosphere as a result of the high power waves transmitted from the Luxembourg station. Since then, a growth in interest of the potential modification effects of high power radio waves on the ionosphere have led to the development of several purpose-built high power facilities operating in the high frequency (HF) band. These have been established worldwide, the first of which was situated at Platteville, Colorado with experiments commencing in 1970 and later followed by developments at Arecibo (Puerto Rico), Sura (Russia), Fairbanks and Gakona (Alaska) and at Tromsø (Norway). The severity and characteristics of artificial modification effects observed by each of the facilities vary widely due to the angle made between the transmitted HF wave and the direction of the geomagnetic field above the heating facility. This can be understood in terms of the geographic latitude at which the facilities are located. At lower latitudes the angle of the geomagnetic field approaches horizontality with respect to the Earth's surface whilst at the highest latitudes it is near-vertical. It will be seen in Chapter 2 that the geomagnetic field is a crucial factor in determining the plasma response to heating processes. In order to understand some of the physical phenomena and effects that can be achieved through artificial ionospheric modification experiments, the proceeding chapter will attempt to address basic plasma dynamics, waves and instabilities due to external

perturbations, and the nature of radio wave propagation through the ionospheric medium.

1.6 Aims of the study

The ionosphere is very much a natural plasma laboratory whose variability can greatly impact a wide range of environmental and technological systems. Extensive knowledge of solar-terrestrial interactions occurring at the edge of the magnetosphere can be gained through waves associated with these perturbations which are communicated to the ionosphere via the geomagnetic field. Waves disturb the plasma and allow instabilities to develop. These instabilities give rise to turbulence and density irregularities in the plasma which can in turn affect significantly the performance and reliability of satellite systems, navigation applications, radio communications and electrical power supplies. For this reason, forecasting of the likely effects of solar-terrestrial activity on the structure and properties of the ionosphere remains an ongoing, highly important topic.

The irregularities that exist naturally through magnetosphere-ionosphere dynamics can often be reproduced artificially by means of ionospheric modification facilities. Hence, they provide a novel method of simulating various ‘space weather’ effects on the ionosphere under controlled conditions which may be removed almost instantaneously, depending on the characteristic lifetime of the phenomena. Artificial heating experiments are therefore very useful for studying and predicting the behaviour of plasma irregularities, with the knowledge gained being of interest to those in the communications industries. Throughout the past few decades, remote sensing and probing of the ionosphere at both low, mid- and high-latitudes has played a central role in obtaining information on the state of the plasma. However the technique by which

plasma properties are determined by such diagnostic facilities can often suffer problems of its own when the plasma is turbulent, whether naturally or artificially induced. These instrumental issues form a major part of the motivation of Chapter 4.

The focus of this work is based on the irregularities that can be generated by artificial heating experiments. More precisely, a study of the large-scale electron temperatures measured during artificial heating is made in Chapter 4, since they bear a great influence on the expected behaviour and characteristics of these irregularities. This is followed on by Chapter 5 with work investigating the relaxation of the irregularities which sometimes requires a more complex description than what simple theoretical models can provide. The final topic of the study, Chapter 6, is concerned with the interrelationship of natural and artificially-induced phenomena, and the often unusual observations that can be made using ground-based diagnostic facilities. Before the study is introduced however, it is crucial to understand first the way in which plasma behaves, and the nature of radio wave propagation through such a medium. An overview of the physical concepts and processes, fundamental to this work will be presented in Chapter 2. A brief review of the types of artificial modification experiments that have been carried out in the past few decades will also be given in Chapter 2, and in Chapter 3 a broad description of the diagnostic instruments and facilities used to obtain the data presented in this thesis will be outlined. This section will not only provide a factual background of the instruments but also attempt to address the basic theoretical ideas on which the operations of the instruments are based. This is followed by the three main research topics of the thesis that have been described above and in Chapter 7 the work will be concluded with a summary of the key results and findings of this thesis, together with an identification of the science questions that remain outstanding.

Chapter 2

Theory of Artificial Ionospheric Modification

In order to understand how high power radio waves modify the ionospheric plasma, through which geomagnetic field lines are threaded, it is necessary to understand the dynamics of plasma particles and the forces they are subjected to. The following section introduces concepts associated with particle motion under typical ionospheric conditions.

2.1 Particle motion in a plasma

Charged particles in a magnetic field \mathbf{B} , experience a force known as the ‘Lorentz’ force, which supplies the centripetal acceleration to engage the particles in a circular orbit of radius r around the magnetic field. The Lorentz force, \mathbf{F} on a particle with charge e , mass m and travelling with tangential velocity \mathbf{v} is given by,

$$\mathbf{F} = e\mathbf{v} \times \mathbf{B} = \frac{mv^2}{r} \hat{\mathbf{r}} \quad (2.1)$$

The radius and frequency ω_B of gyration around the magnetic field are thus:

$$r = \frac{mv}{eB} \quad (2.2)$$

$$\omega_B = \frac{eB}{m} \quad (2.3)$$

For an electron under the influence of a magnetic field at altitudes in the F region where the geomagnetic field strength is typically of the order of 10^{-5}T , the electron gyrofrequency is approximately 8.48×10^6 radians s^{-1} .

Similarly, when electrons in plasma of number density N are perturbed by an electrostatic force, they undergo simple harmonic motion due to the restoratory force experienced in order to replace them back to their equilibrium configuration and oscillate at a characteristic frequency known as the *plasma frequency* ω_p defined by:

$$\omega_p = \sqrt{\frac{Ne^2}{\epsilon_0 m}} \text{ rad s}^{-1} \quad (2.4)$$

$$f = \frac{\omega_p}{2\pi} \approx \sqrt{80.5N} \text{ Hz} \quad (2.5)$$

ϵ_0 is of course the permittivity of free space. Since ω_p depends on N , it will vary with altitude in the ionosphere because the electron density profile is non-uniform. Electrons in the plasma of temperature T and density N , perturbed from equilibrium, will oscillate at an amplitude known as the *Debye length*, expressed as

$$\lambda_D = \sqrt{\frac{\epsilon_0 k_B T}{Ne^2}} \quad (2.6)$$

The ionospheric plasma is fully capable of supporting wave modes which give rise to plasma oscillations as well as other plasma motions, and these can be generated by many different mechanisms due to plasma perturbations by external forces. Waves exhibiting positive feedback in amplitude growth are categorised as instabilities. Different conditions dictate what type of instability can occur, and the threshold at which they develop. Two very important instabilities within the discipline of artificial modification experiments are the Parametric Decay Instability (PDI) and Oscillating Two-Stream Instability (OTSI). The effects of these instabilities on the ionospheric plasma have been proven through theoretical work and observed experimentally and will be discussed in greater detail later in this study.

2.2 Refractive Index and the Appleton-Hartree Equation

The concept of a refractive index is very important when considering radio wave propagation through the ionospheric medium. It determines the severity of attenuation in the wave velocity as it encounters a medium denser than a vacuum. Radio waves span the high frequency (HF) band in the range 3-30MHz, and their corresponding wavelengths (100-10m) are short with respect to the distances over which the ionosphere changes with height. In this scenario the ionosphere will appear to an incident radio wave as a slowly-varying dielectric medium, and can be considered as a series of layers of different density and thus refractive index n .

It is mainly the work of Appleton that led to the development of the well-known Appleton-Hartree equation, which forms the theory behind the propagation of radio waves in uniform magnetised plasma, also sometimes referred to as magneto-ionic theory. It defines the complex refractive index n_R of an ionised medium in the presence of a magnetic field:

$$n_R = \sqrt{1 - \frac{X}{1 - iZ - \left(\frac{Y_T^2}{2(1-X-iZ)} \right) \pm \left(\frac{Y_T^4}{4(1-X-iZ)^2} + Y_L^2 \right)^{1/2}}} \quad (2.7)$$

Here, the dimensionless parameters X , Y , Y_T , Y_L and Z are given by:

$$X = \left(\frac{\omega_p}{\omega} \right)^2 \quad Y = \frac{\omega_B}{\omega} \quad Y_T = \frac{\omega_T}{\omega} \quad Y_L = \frac{\omega_L}{\omega} \quad Z = \frac{\nu}{\omega} \quad (2.8)$$

The transverse and longitudinal components of the gyrofrequency, ω_T and ω_L respectively, with respect to the direction of propagation of the radio wave θ (or the direction of propagation with respect to the geomagnetic field) are,

$$\omega_T = \omega_B \sin \theta \quad (2.9)$$

$$\omega_L = \omega_B \cos\theta \quad (2.10)$$

The frequencies $\omega, \omega_B, \omega_p$ and ν are the incident wave frequency, electron gyrofrequency, natural plasma frequency and electron collision frequency respectively. The equation is often simplified by making assumptions under certain propagation conditions. For example, when both absorption and magnetic field effects are negligible, all terms in Y and Z term can be ignored. This leaves a much simplified equation with the solution for the refractive index:

$$n = \sqrt{1 - X} \quad (2.11)$$

For reflection of the radio wave, the condition to be met is:

$$n^2 = 0 = 1 - X \quad \Rightarrow \quad \omega_p = \omega \quad (2.12)$$

Therefore, in the absence of collisions and influence of a magnetic field, the radio wave reflects where its frequency matches the local plasma frequency. This wave mode is termed the ordinary mode ('O' mode). However, where magnetic field effects on the propagation are not negligible, then the equation leads to two solutions. The significance of this result is that the ionosphere acts as a birefringent medium with two characteristic wave modes existing, the O-mode wave and an extraordinary mode ('X' mode) wave. The O-mode simply reflects under condition (2.12) since it is unaffected by the magnetic field, but for quasi-longitudinal radio wave propagation, such as that commonly undergone by radio waves during artificial modification experiments, the X-mode reflects at two levels, given by the upper and lower branches of the solution:

$$n^2 = 1 - \frac{X}{1 \pm Y_L} = 0 \quad \Rightarrow \quad \omega_p = \sqrt{\omega^2 \pm \omega \omega_B \cos\theta} \quad (2.13)$$

For wave incidence parallel to the geomagnetic field, the two reflection levels are

$$\omega^2 = \omega_p^2 \pm \omega\omega_B \quad (2.14)$$

The upper (+) branch of the X-mode is sometimes known as the Z-mode, with a frequency greater than the plasma frequency which reflects above the O-mode reflection height. In contrast, the lower branch X-mode reflects below the O-mode reflection level. Extraordinary mode waves differ from O-mode waves in that they possess opposite polarisation. While all three wave modes are circularly polarised, the electric and magnetic fields of an ordinary mode wave rotate anticlockwise but those of the extraordinary modes rotate clockwise.

2.3 Upper Hybrid Waves

In addition to these wave modes, another particularly important type of wave mode is the upper hybrid wave. They are longitudinal, electrostatic waves and arise from the electron-acoustic dispersion relation in the limit of zero wave number. In the presence of a magnetic field, they travel only parallel to the field. The dispersion function $D(k, \omega)$ for electron-acoustic waves is given by (Robinson, 1989),

$$D(k, \omega) = 1 - \frac{\omega_p^2}{\omega^2 - \omega_B^2} (1 + 3k^2 \lambda_D^2) - \frac{i\nu}{\omega} = 0 \quad (2.15)$$

$$\Rightarrow D(0, \omega) = 1 - \frac{\omega_p^2}{\omega^2 - \omega_B^2} = 0$$

$$\therefore \omega_{UH}^2 = \omega^2 = \omega_p^2 + \omega_B^2 \quad (2.16)$$

Hence, the upper hybrid frequency lies between that of the O- and X-mode waves and are excited at a level between the reflection levels of these waves. However, only waves with O-mode polarisation can excite upper hybrid waves, since X-mode waves will reflect before they reach the upper hybrid height.

2.4 Review of Early Heating Experiments at Platteville

The first artificial modification experiment was carried out in the 1970s using the Platteville heating facility in Colorado. Some of the earlier objectives of these experiments were concentrated on studying the characteristics of the returned radio signal rather than on the 'heating' of the electron gas. Carroll et al. (1974) provide a detailed technical description of the Platteville heater and its capabilities.

However, some rather unexpected and equally surprising outcomes of these experiments were revealed from observations made using digital ionosondes, not predicted by earlier theories. These included the artificial spread-F feature (Utlaut, 1970; Utlaut and Cohen, 1971) which corresponded to the diffuse spread of F region echoes similar to the naturally-occurring phenomena and reduced radio reflectivity (Cohen and Whitehead, 1970), an effect that remained unexplained until further experiments at White Sands using radars in the HF (30MHz) and VHF (54MHz) range yielded observations of the aspect-sensitive nature of the backscatter. This confirmed the earlier speculation (Utlaut, 1970) that the irregularities reflecting the incident waves must somehow be field-aligned.

Based on these fascinating discoveries and the observations made, a physical model of radio wave scattering from field-aligned irregularities (FAI) was developed (Rao and Thome, 1974). Their model described the artificially-modified volume in terms of root-mean-squared (rms) density fluctuations of between 1 to 1.5% parallel to the geomagnetic field and distributed 'diffusely' in a plasma volume of 15km in vertical thickness and 100km in horizontal extent.

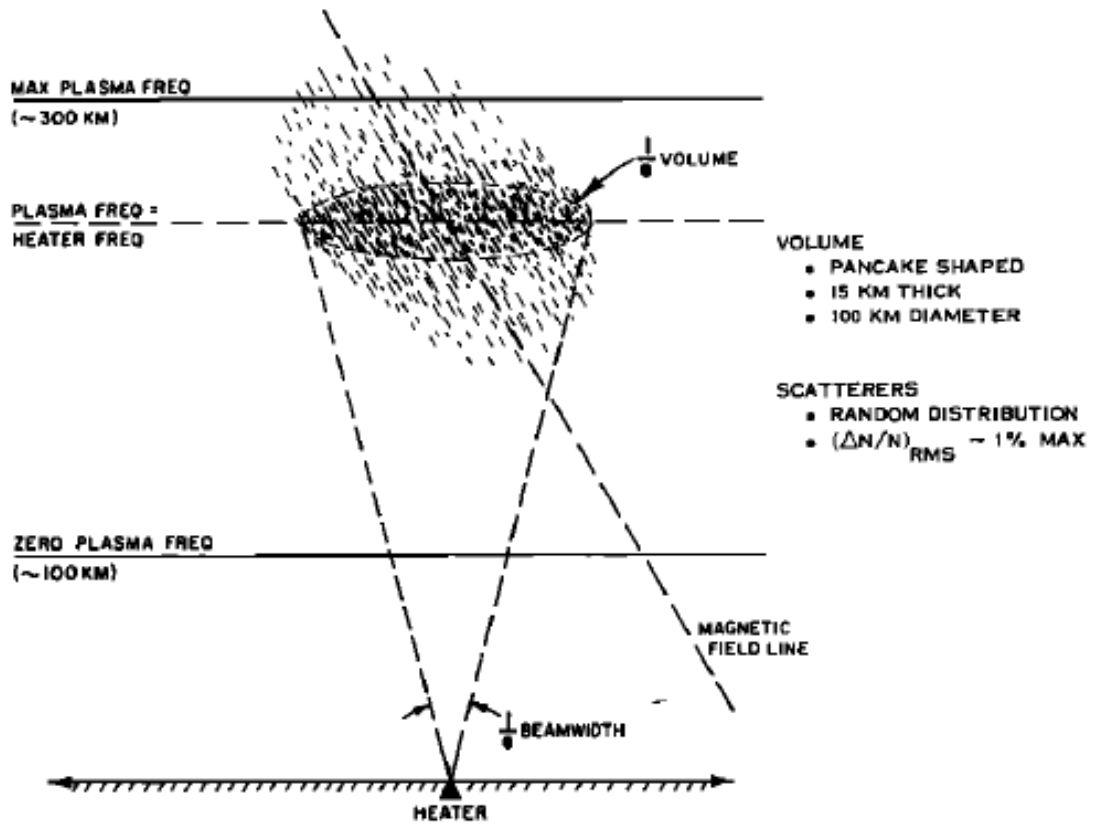


Figure 2.1 Schematic to illustrate the physical model of heater-induced density irregularities responsible for the observed field-aligned radio wave scattering (from Rao and Thome, 1974). The centre of the modified volume is also centred at the O-mode wave reflection height, where the heater and plasma frequency are equal

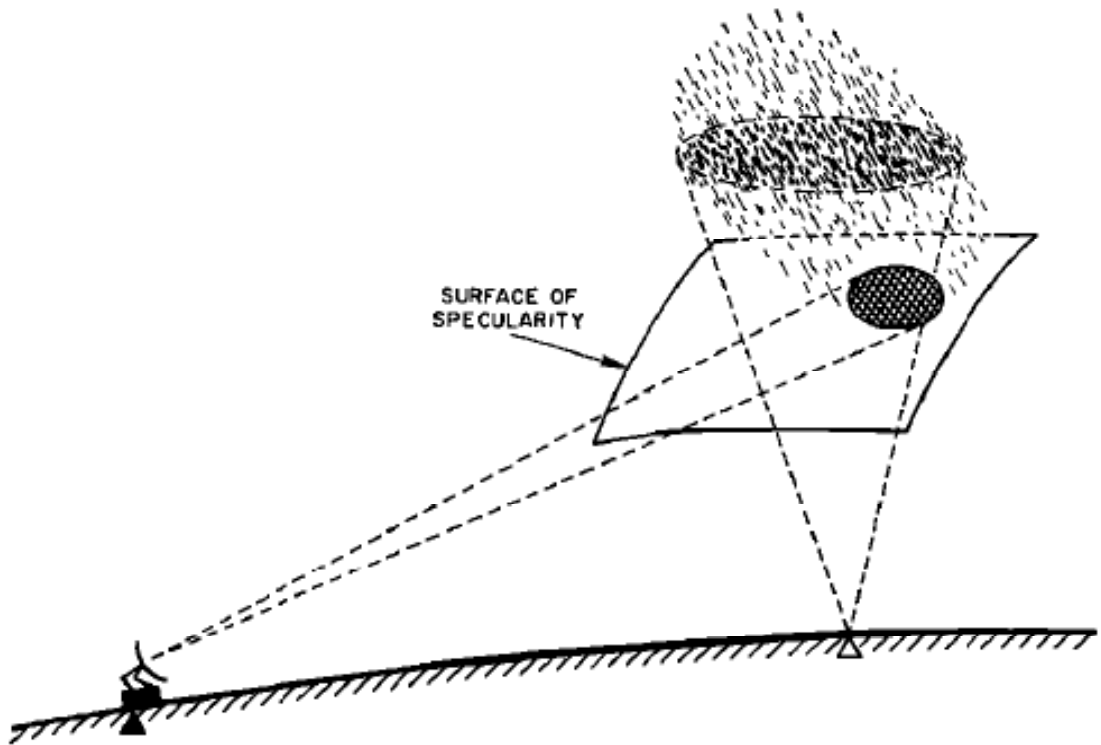


Figure 2.2 The concept of the surface of specularity which relates the geometry of a probing diagnostic radar and scattering irregularities in the artificially heated volume (from Rao and Thome, 1974)

The authors introduced the concept of a surface of specularity (Figure 2.2), which defines the locus of points where an incident diagnostic wave attains orthogonality to the geomagnetic field and thus satisfies the Bragg condition for backscatter. Figure 2.1 is a schematic of this physical model (Fig.1 from Rao and Thome, 1974), showing how the field-aligned density fluctuations were visualized.

Further detailed studies of VHF and UHF backscatter spectra led to the discovery of the centre-line and plasma-line scatter modes (Minkoff et al., 1974a, 1974b). Elevation scanning experiments allowed variation in the viewing geometry of the diagnostic waves with respect to the geomagnetic field, revealing the highly aspect-sensitive characteristics of the centre-line scatter. Centre-line scatter was defined as the spectral component at the transmitted frequency, while plasma line scatter corresponded to two sidebands either side of the centre-line, at the heater frequency. Though both modes exhibited similar bandwidth and temporal behaviour, it was deduced that they originated from two separate and distinct scattering regions. In contrast to centre-line scatter, plasma-line scatter showed very weak (if any) dependence on aspect angle. Subsequent experiments using 15MHz and 30Hz HF radars determined that centre-line scatter could be associated with elongated field-aligned structures (Minkoff et al., 1974b). Later interest in the temporal behaviour of the backscatter enabled timescales over which the disturbed plasma responded to the high power heater waves (Minkoff and Kreppel, 1976) to be determined, and this topic will be reviewed in greater depth in Section 2.9.

This broad range of initial observations and the existence of a physical model providing a morphological description of the modified volume, later facilitated a variety of theories to be proposed to explain the effects. Amongst some of the most important was

the concept of anomalous absorption (Graham and Fejer, 1976) which was shown to provide a satisfactory explanation for the observed reduced reflectivity of O-mode radio waves and the parametric decay instability (e.g. Perkins et al., 1974), introduced to explain spectral effects such as the plasma-line ‘overshoot’ and later amended to consider thermal coupling in order to provide a possible mechanism by which FAI could be generated. These early theories set the foundation for a whole host of other mechanisms for field-aligned irregularity generation to evolve over the course of the following decade.

2.5 Theory of Artificial Modification: F region heating

In the lower ionosphere such as the D region where the collision frequency and plasma density is high, collisional absorption is the dominant heating process. However, in the F region, particle collisions and chemical processes do not play as important a part in heating of the electron gas since the characteristic scale length over which the plasma properties vary is large. Upper hybrid waves play a highly significant role in artificial ionospheric modification experiments, since their collisional damping transfers wave energy to particles in the plasma, thus raising the large-scale plasma temperature. Electromagnetic (EM) waves can perturb the ionospheric plasma to such a degree that instabilities arise and can lead to the generation of further wave types. These will now be examined in further detail in the following two sections, with particular attention being paid to their role in the effective heating of the F region plasma.

2.5.1 Parametric Decay Instability

Various instabilities may be excited in the ionosphere when a high power O-mode radio wave parametrically stimulates electrostatic waves through wave resonances or forces. The parametric decay instability (PDI) is one such example (Perkins et al., 1974), and

involves the coupling of an EM pump wave of high frequency ω_0 to a high frequency plasma (Langmuir) wave ω_1 , and a low frequency ion-acoustic wave ω_2 . The frequency and wave vector matching conditions for the wave coupling are given by

$$\omega_0 = \omega_1 + \omega_2 \quad (2.17)$$

$$\mathbf{k}_0 = \mathbf{k}_1 + \mathbf{k}_2 \quad (2.18)$$

This three-wave interaction is due to the ‘ponderomotive’ or striction force which is electrostatic in nature and proportional to $\nabla|E|^2$. The electric field threshold for the PDI to be excited is given by (Robinson, 1989)

$$E_t = \frac{6.7N_0T_i\nu}{\varepsilon_0\omega_e} \quad (2.19)$$

Here, N_0 , T_i , and ν are respectively the unperturbed electron density, ion temperature and electron collision frequency and ω_e is the electron plasma frequency. For typical F region parameters, this provides an estimate of the threshold field of around 0.1Vm^{-1} (Robinson, 1989). The typical growth time of the instability is of the order of a few milliseconds and its effect has been experimentally observed by incoherent scatter radars, through its consequential enhancements of the ion line and plasma line spectra.

Another type of instability, the oscillating two-stream instability (OTSI) has also been studied by a number of authors (e.g. Kuo et al., 1997, Fejer, 1979) and is also sometimes termed the purely growing mode of the PDI and also due to the ponderomotive force. It is a four-wave interaction where the high frequency EM pump wave couples to two oppositely propagating high frequency Langmuir waves and a non-propagating ion mode. This zero-frequency mode represents a spatially periodic density

irregularity. The OTSI can also give rise to enhancements in the ion line and plasma line spectra, and its significance will be dealt with in greater detail in Chapter 4.

2.5.2 Thermal Parametric Instability

The thermal parametric instability (TPI) is different to the PDI in the fact that the coupling of the waves is thermal rather than electrostatic in nature, which leads to a comparatively longer timescale over which the instability operates. Many theories and models of density irregularity generation by a TPI have been described in literature (e.g. Grach et al., 1977; Das and Fejer, 1979). When an oscillating pump electric field,

$$\mathbf{E}_0 = \mathbf{E}_{00}e^{i\omega_0 t} \quad (2.20)$$

interacts with a spatially periodic density perturbation of zero frequency ($\omega_2 = 0$),

$$n = n_0 e^{ik_2 x} \quad (2.21)$$

a time-varying current density \mathbf{J}_1 is generated, with which is associated a high frequency electrostatic (Langmuir) wave and electric field given by

$$\mathbf{E}_1(\omega_0, \mathbf{k}_2) = \frac{\omega_0}{i\varepsilon_0(\omega_p^2 - \omega_0^2 + i\nu\omega_0)} \mathbf{J}_1(\omega_0, \mathbf{k}_2) \quad (2.22)$$

The three-wave frequency matching condition also holds for the TPI, and can thus be used to deduce the frequency of the Langmuir wave and the wave number of the resulting density perturbation. Since the high frequency pump wave number k_0 is very small in comparison to that of the density perturbation k_2 , then by writing $k_0 = 0$, the following set of conditions are obtained:

$$\omega_0 = \omega_1 \quad (2.23)$$

$$0 = \mathbf{k}_1 + \mathbf{k}_2 \quad (2.24)$$

Hence the Langmuir wave has the same frequency as the EM pump wave and its wave number is equal in magnitude but oppositely directed to that of the density perturbation.

2.6 Theory of Small-Scale Field-Aligned Irregularity Growth

It was initially thought that the PDI could be involved in the production of small-scale irregularities (Perkins et al., 1974). However, the failures of this mechanism included its short growth time in comparison to the timescales of irregularity growth, much more intense low frequency density fluctuations than predicted, and because the observed instabilities were perpendicular to the geomagnetic field rather than close to field-aligned, as was expected for the PDI. Further studies led to the belief that the saturation spectrum of the TPI could lead to strong plasma turbulence over a 10km altitude interval that would produce effective ohmic heating and thus intense density fluctuations (Perkins, 1974). It is now widely accepted that anomalous scattering of a HF pump wave into electrostatic upper hybrid waves by linear mode conversion at pre-existing density irregularities, followed by the coupling of the upper hybrid wave into a secondary upper hybrid wave and density perturbation, is the mechanism by which irregularities grow. The instability that gives rise to this mode conversion is sometimes also known as the resonance instability (Vaskov and Gurevich, 1975, 1977) since it can only be excited when the frequency of an incident O-mode radio wave matches the upper hybrid wave frequency at the upper hybrid level. The scattering leads to strong anomalous absorption of the HF wave (Graham and Fejer, 1976) and wide-band attenuation (WBA). The term ‘anomalous’ arises from the fact that the scattering mechanism is collisionless and does not involve the loss of energy in the process. It is thought to be highly efficient in the presence of pre-existing density irregularities which may consist of an isolated ‘striation’ (Vaskov and Gurevich, 1975, 1977) or a spatially

periodic number density (Das and Fejer, 1979, Inhester et al., 1981), although the threshold amplitude of irregularities required by the different theories for this mechanism vary, as do the nature of their existence. The argument for assuming a spatially periodic number density, rather than an isolated density irregularity was that the direct energy dissipation of mode-converted electrostatic waves should be spread over a broader spectrum of spatial scales, rather than a single field-perpendicular scale size corresponding to that of the isolated irregularity.

The interference of the pump and electrostatic wave electric fields leads to a total field density which gives rise to bulk heating of the plasma (Robinson, 1989) and this takes the form,

$$|\mathbf{E}_0 + \mathbf{E}_1|^2 = |\mathbf{E}_0|^2 + 2|\mathbf{E}_0 \cdot \mathbf{E}_1| + |\mathbf{E}_1|^2 \quad (2.25)$$

$|\mathbf{E}_0|^2$ represents the collisional heating resulting directly from the pump wave; the second term describes the differential heating that arises from beating of the pump and Langmuir wave, which has zero frequency but whose spatial periodicity matches the original density perturbation and thus allows enhancement of their amplitude. The last term is simply the energy density of the Langmuir wave and which determines the degree of anomalous absorption undergone by the EM pump wave. In order to produce enhancement of FAI amplitude, the theory of Das and Fejer (1979) demonstrated that there need not be a threshold irregularity amplitude to give rise to growth, if the interaction of the reflected pump wave field with the incident pump and anomalously-scattered wave fields were included in the mechanism. When the pre-existing density irregularity is an isolated structure (Vaskov and Gurevich, 1975, 1977), its amplitude must exceed a certain threshold before explosive growth and amplification can take place via this resonance instability.

Further development of the theory by Inhester et al (1981) brought the ideas of both Vaskov and Gurevich (1975, 1977) and Das and Fejer (1979) together and suggested that initial spatially periodic irregularities could be seeded in the plasma by the mechanism of Das and Fejer (1979) but could be further amplified by the thermal coupling of multiply-scattered Langmuir waves at the irregularities. They showed that a 'cascade' of scattered Langmuir waves would be intense above a certain threshold, and this would give rise to explosive growth of the initial irregularities. In their mechanism, heating of the irregularity occurs through the scattered Langmuir (electrostatic) waves, and when the ohmic heat input from the scattered wave field exceeds the heat lost from the irregularity by thermal conduction, the instability is excited. A broad spectrum of irregularity scale sizes is expected to result from this process of multiple scattering.

The heating that results from equation (2.25) leads to enhanced electron mobility because of an increase in the thermal pressure. The subsequent acceleration of electrons along the magnetic field due to a pressure gradient force results in plasma expulsion from the heated region and further depletion in the plasma density. The structures are aligned more or less with the geomagnetic field, hence termed 'field-aligned irregularities' which can extend many kilometres in length along the geomagnetic field but few in perpendicular extent. Thus, the geomagnetic field also plays an important role in F region plasma dynamics in the transport of energy and momentum due to the relative infrequency of particle collisions. The perturbations in density and temperature that occur due to artificial modification may be small scale, (a few metres perpendicular to the geomagnetic field) or large scale (with cross-field size of several kilometres). Low-power radio waves close to the pump wave frequency may be used as diagnostics of the amplitude of the density perturbed region containing the irregularities, since they will also experience anomalous scattering as they traverse the heated volume and thus

their path length is modified. This has been shown experimentally as a change in the phase of the reflected signal (Jones et al., 1982). However, their advantage lies primarily in the fact that they will not enhance or modify the amplitude of FAI induced by the pump wave due to their low power.

2.7 Large-Scale Electron Temperature and Density Response

The fundamental equations governing the large-scale density and temperature perturbations are considered. Below 200km, large-scale gradients in the temperature and density have little effect on the transport of heat (energy) and particles (momentum) in the plasma. This leads to energy and momentum balance equations mainly dictated by collisional and chemical processes and expressed as (Robinson, 1989):

$$\frac{3}{2} \frac{\partial T_e}{\partial t} = Q' - \frac{3}{2} R(T_e - T_0) \quad (2.26)$$

$$\frac{\partial N_e}{\partial t} = q_p - q_l \quad (2.27)$$

Q' is the energy input per electron by the pump wave, R is a heat loss term due to collisions between electrons and neutral particles and q_p and q_l are the electron production and loss rates which are mainly due to photoionization and chemical recombination respectively. Heating of the F region below 200km leads to a reduction in the recombination rate of species such as NO^+ and O^+ and hence the loss rate is reduced and the density is enhanced. T_e , T_0 and N_e are simply the electron temperature, undisturbed temperature and density respectively.

Above 200km, the ion gyroradius is smaller than the scale size of the large scale perturbation, and hence, the diffusion of electrons becomes ambipolar in nature. Thermal conduction and diffusion is predominantly along the geomagnetic field so

cross-field terms are neglected. The set of coupled energy and momentum balance equations are given by (Robinson, 1989):

$$\frac{3}{2} \frac{\partial}{\partial t} \left(\frac{T}{T_{e0}} \right) - 4.5 D_{\parallel} \frac{\partial^2}{\partial x_{\parallel}^2} \left(\frac{T}{T_{e0}} \right) = -\frac{3}{2} R \left(\frac{T}{T_{e0}} \right) + \frac{Q}{N_0 T_{e0}} \quad (2.28)$$

$$\frac{\partial}{\partial t} \left(\frac{n}{N_0} \right) - D_a \frac{\partial^2}{\partial x_{\parallel}^2} \left(\frac{n}{N_0} \right) - D_{Ta} \frac{\partial^2}{\partial x_{\parallel}^2} \left(\frac{T}{T_{e0}} \right) = - \left(\frac{\partial q_{\parallel}}{\partial N} \right) \frac{n}{N_0} - \left(\frac{\partial q_{\parallel}}{\partial T} \right) \frac{T}{T_{e0}} \frac{T_{e0}}{N_0} \quad (2.29)$$

In this notation, x_{\parallel} denotes a coordinate in a direction parallel to the geomagnetic field, D_a , D_{Ta} are ambipolar diffusion and thermal diffusion coefficients, Q is the heat input per unit volume from the EM pump wave, R is again a heat loss term due to collisions between electrons and neutral particles, D_{\parallel} is the electron thermal conduction coefficient in the field-parallel direction and $\frac{n}{N_0}$, $\frac{T}{T_{e0}}$ are simply the relative perturbations in the plasma density and temperature respectively, from background values N_0 and T_{e0} . This set of coupled equations can be transformed into stationary perturbation equations and solved under application of the boundary condition that the temperature change must tend to 0 very far from the heat source:

$$\Delta T_e \rightarrow 0 \text{ as } x_{\parallel} \rightarrow \infty,$$

such that the electron density and temperature perturbations are given by (Gurevich, 1978) in the form of Green functions (these need not be replicated here since only special cases are considered). If the heat source is assumed to be represented by a perfect delta function injected at the upper hybrid height, and the characteristic length scale of the temperature inhomogeneity L_T is large, equation 2.28 reduces to

$$\frac{\Delta T_e}{T_{e0}}(x_{\parallel}) = \frac{Q_0}{6N_{e0}T_{e0}^{3/2}} \left(\sqrt{\frac{m_e v}{R}} \right)_0 \exp \left(-\frac{|x_{\parallel} - x_0|}{L_T} \right) \quad (2.30)$$

$$L_T = \sqrt{\frac{3D_{\parallel}}{R}} \quad (2.31)$$

$$D_{\parallel} = \frac{T_{e0}}{m_e \nu_{en}} \quad (2.32)$$

Parameters evaluated at the source height are denoted by subscript 0, which include the heat input per unit volume, the height at which the heat source is injected, x_0 and the product $\sqrt{\frac{m_e \nu_{en}}{R}}$. The electron mass, electron-neutral collision frequency and gyrofrequency are given by m_e , ν_{en} and Ω_e respectively. The temperature T_{e0} is expressed in electron volts (eV).

Equation (2.30) indicates that the temperature change has a sharp peak at the point x_0 and decays away exponentially above and below this point parallel with the geomagnetic field. It should be emphasised that this is a first-order solution to the equations. In practice, the heat input is never injected at a single height but is spread out over a finite range in altitude and thus the assumption of a perfect delta source is not strictly true. Mantas et al. (1981) showed that the width of the region where heating occurs must be increased in order to explain strong asymmetries in the temperature profile described by the theoretical model when the temperature-dependent density solution was accounted for in their numerical computations.

The growth of large-scale density structures may be explained by a thermal self-focusing instability (e.g. Perkins and Goldman, 1981, Gurevich and Karashtin, 1994). This differs from the mechanism by which small-scale FAI develop where it is the differential heating due to thermal coupling of the EM pump wave to a high frequency EM wave and zero frequency density perturbation that enhances the depleted density region. The focusing of the pump wave in regions of depleted density causes direct

heating and thus a feedback mechanism which leads to further growth of the depletion. One of the key results of this instability is that the large scale temperature and density changes should be opposite to each other but experimental observations have shown that this is not always the case (Honary et al., 1993) when chemical processes are more dominant in the lower F region.

2.8 Review of Experimental Work

In this section, a selection of literature describing previous heating experiments and some important scientific results relevant to this thesis will be summarised to provide a background for the work to follow in Chapters 4, 5 and 6. Some of the key topics to be addressed primarily concern the temperature changes associated with artificial ionospheric modification, and the temporal characteristics of FAI as observed by backscatter radar measurements.

Prior to the first experiments using incoherent scatter radar at Tromsø, the temperature changes associated with artificial modification exhibited wide variability, as reported by Mantas et al. (1981) and Djuth et al. (1987) for heating experiments carried out using the facility at Arecibo. Mantas et al. (1981) found relatively modest enhancements, of around 350K in the electron temperature, or 45% above the unperturbed value for night-time conditions, while Djuth et al. (1987) reported observations of very large electron temperature enhancements between 1000K and 2000K during night-time and solar minimum conditions. Depletions in the large-scale electron density of around 10-15% below the unperturbed values were measured. In light of subsequent modelling work undertaken by Newman et al. (1988) for the same experiment, it was concluded that significant enhancements in the electron temperature did not necessarily require strong heat sources, but that the low ambient electron densities due to the quiet ionospheric

conditions was sufficient to reduce the collisional cooling rates associated with electron-ion energy transfer that gave rise to the highly elevated temperatures. Mantas et al. (1981) also determined that collisional cooling played an important role in explaining the asymmetry in their modelled temperature profiles. Here, greater spreading of heat below source than above was attributed to a rapid decrease in density below the source, producing a decrease in energy transfer rates. However the heat lost through collisions with neutral particles was not fast enough to dispense of the energy input and to compensate for this, energy was distributed over a large altitude region.

Effects of artificial modification experiments performed with the heating facility at Tromsø were initially diagnosed using low power diagnostic waves at, or close to the heater frequency. Amplitude and phase measurements proved to be a highly effective tracer of wide-band attenuation (WBA) and hence the degree of anomalous absorption and density changes induced by the action of the heater (Jones et al., 1982). Further experiments involving low-power diagnostic waves confirmed hysteresis effects (e.g. Stubbe et al., 1982; Jones et al., 1983) first predicted through theory in the reflected pump wave signal, whereby stronger anomalous absorption was experienced for any particular pump power after irregularities had already been generated. Later studies (Wright et al., 2006) have also shown hysteresis effects using the CUTLASS backscatter radar facility in conjunction with EISCAT UHF incoherent scatter observations. This provided further evidence in support of a two-stage mechanism for irregularity growth (Inhester et al., 1981) where initial irregularity growth is linear and requires no threshold perturbation amplitude, but may be followed by explosive nonlinear growth if the product of the pump power and irregularity amplitude exceeds a certain limit.

The first observations of large temperature enhancements made using the EISCAT UHF incoherent scatter radar at Tromsø were reported by Jones et al. (1986) and the strong relationship between anomalous absorption and electron temperature enhancements have also been noted (Robinson, 1989). During quiet ionospheric conditions, the heating effect of an O-mode EM pump wave produces a single maximum in the electron temperature height profile (Stocker et al., 1992) and this is borne out in the stationary perturbation (2.30). In their study, temperature increases of 55% above unperturbed values were measured, but density changes were less consistent due to varying influences from transport and chemical processes.

In contrast to daytime observations, when the F-region plasma is dense enough to allow a strong interaction between pump wave and plasma, Rietveld et al. (2003) presented results of heating under solar maximum, geomagnetically quiet night-time conditions. Their findings included electron temperature enhancements up to 300% above the background which exhibited a strong aspect angle preference, as did the location of artificially-induced radio aurora emissions and the intensity of backscatter measured by HF radars in Finland and Iceland; the largest heating effects were produced when the heater beam was tilted along the magnetic zenith. They discussed the possible influence of ionospheric tilts as well as pump wave self-focusing effects (Gurevich et al., 1999) which are highly nonlinear in nature. Similar conclusions were reached by Gustavsson et al. (2001) where an association between substantial temperature enhancements of up to 350% above the background, and artificial airglow emissions was suggested to be due to nonlinear self-focusing of the incident pump waves. However, Rietveld et al. (2003) also suggested that lower electron-neutral collision frequency which would tend to reduce the energy loss rate, could account for the large temperature increases in the night-time conditions. Since the D region also does not exist during night-time, this

would further reduce the absorption at lower altitudes, which could also lead to stronger heating in the F region.

Many other intriguing effects achieved at Tromsø include temporal fluctuations in the density and temperature measurements, which were attributed to chemically-driven changes in the lower F region (Honary et al., 1993), reduced heating, anomalous absorption and irregularity growth for heating at frequencies near to harmonics of the electron gyrofrequency (Robinson et al., 1996; Honary et al., 1999). Robinson et al. (1996) showed peak temperature increases of only 8% above the background when the pump frequency was near to a gyroharmonic, or around half that observed for pumping at non-gyroharmonics.

The well-documented ‘overshoot’ of both the plasma and ion line spectra observed by the EISCAT incoherent scatter radars, was first reported by Showen and Kim (1978). As is now known, both the PDI and OTSI typically have growth times of only a few milliseconds. The coupling of the EM pump wave to an electrostatic Langmuir wave and low-frequency ion-acoustic mode (PDI) or to zero-frequency density perturbations (OTSI) produces a rapid enhancement in the intensity of the plasma lines and ion lines during the first few milliseconds after the heater has been switched on. The intensity of the plasma line enhancements can be 1-2 orders of magnitude above the steady state level (Fejer, 1979) but experience a rapid quenching in the intensity during the subsequent few seconds when anomalous absorption and growth of FAI develop (Showen and Behnke, 1978; Coster et al., 1985). The rapid growth and decay of the enhancements was termed the ‘overshoot’ effect. Das and Fejer (1979) remark that their theory of FAI generation by resonance instability would explain the overshoot effect

due to the eventual attenuation of the pump wave (and thus PDI) which produce the intense plasma and ion lines.

Stubbe et al. (1992) discuss the relative competition between the PDI and OTSI by presenting observations of the zero-frequency 'purely growing' mode (PGM) in ion line spectra observed by the EISCAT VHF and UHF incoherent scatter radars at Tromsø. They concluded that the amplitude of this line with respect to the ion line amplitudes is dependent on ionospheric conditions, radar wave number, pump ERP and proximity to the pump wave reflection altitude where the PDI is thought to dominate. Figure 2.3 illustrates results of experiments carried out in 1970 and 1971 by Stubbe et al. (1992). The upper panel showing UHF data, indicate very distinct OTSI lines at the highest heater power levels and this is shown by the central peak in the spectra. The VHF data are less sensitive to the OTSI, the explanation for which is given in Stubbe et al. (1992).

Recent work has drawn attention to the distortion of the usual Maxwellian-type incoherent scatter spectra by the OTSI or PGM and its effect on the inferred plasma parameters using the usual incoherent scatter analysis software. Honary et al. (1995) and Robinson et al. (1996) note that the PGM usually appears in the range gate containing the O-mode reflection altitude or the upper hybrid resonance level and leads to unreliable temperature estimates during the first few seconds after the heater switch-on. It was also noted by Honary et al. (1993) that the incoherent scatter analysis could not be relied upon to obtain accurate estimates of plasma parameters when heating at a harmonic of the electron gyrofrequency. The invalidity of conventionally analysed data during heating has also been noted (Honary et al., 1999 and Ashrafi et al., 2006).

Gurevich et al. (1998) showed that if an ACF, measured in a scattering volume containing strong temperature inhomogeneities due to striations, was fitted with a

theoretical function based on a homogeneous Maxwellian plasma, the electron temperature could be significantly underestimated. The importance of accurate temperature data during the first few seconds of heating and the information they contain about the nonlinear heating process and energy deposition region of the pump wave has been emphasised (Mantas et al., 1981). The persistence of the PGM in incoherent scatter spectra for entire heating periods for experiments using the SPEAR facility on Svalbard has also been reported (Robinson et al., 2006).

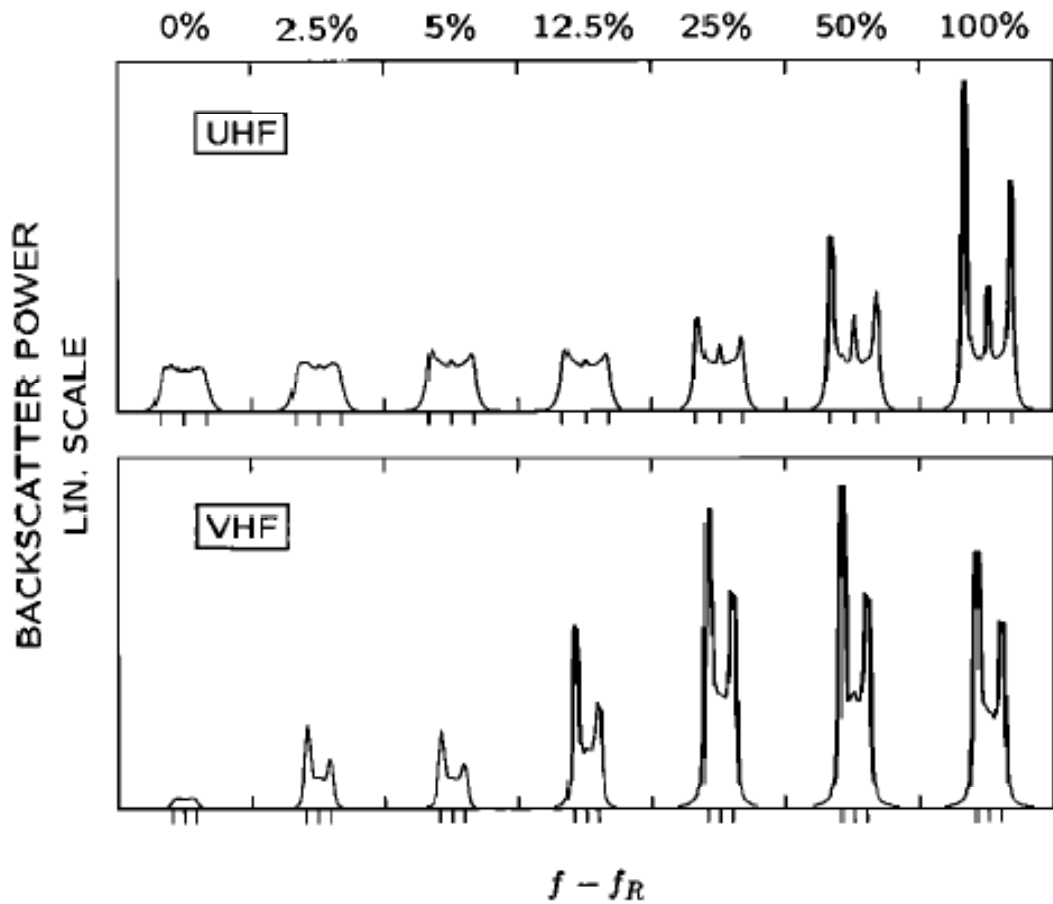


Figure 2.3 Ion line spectra for different heater power levels observed by the EISCAT UHF and VHF radar (from Stubbe et al., 1992) The authors remark that the relative importance of the PDI and OTSI should vary with proximity to reflection altitude, ionospheric conditions, pump power and radar wave number

2.9 Theory and Observations of Irregularity Relaxation

FAI development is highly nonlinear in nature due to the instabilities that produce them and possess characteristic growth and decay rates which have been shown to be strongly dependent on thermal conduction coefficients that are determined by the background electron temperature (Gurevich, 1978, Robinson, 1989). The simplest model of the relaxation behaviour of FAI, after the heater has stopped transmitting, predicts decay rates governed by only cross-field diffusion processes, evaluated at the large-scale background heated plasma temperatures. For small-scale temperature and density perturbations, the energy and momentum balance equations must again be considered. Since the characteristic scale size perpendicular to the geomagnetic field must be accounted for, the energy balance equations is

$$\frac{3}{2} \frac{\partial}{\partial t} \left(\frac{T}{T_{e0}} \right) - 4.5 D_{\parallel} \frac{\partial^2}{\partial x_{\parallel}^2} \left(\frac{T}{T_{e0}} \right) + 2.7 D_{\perp} \frac{\partial^2}{\partial x_{\perp}^2} \left(\frac{T}{T_{e0}} \right) = \frac{Q}{N_0 T_{e0}} \quad (2.33)$$

An approximation can be made in terms of the relative density perturbation:

$$\frac{T}{(T_{e0} + T_{i0})} = - \frac{n}{N_0} \quad (2.34)$$

This yields a differential equation in the density perturbation which can be solved in the absence of a heat source, $Q = 0$, and after making some assumptions (which will not be stated here) and performing analytic integrations, the resulting equation simply reduces to a diffusion equation, which is given by Robinson, 1989:

$$\frac{\partial n(0,t)}{\partial t} + D_2 n(0,t) = 0 \quad (2.35)$$

where the coefficient D_2 is given by

$$D_2 = -1.8 D_{\perp} k^2 \quad (2.36)$$

$$D_{\perp} = \frac{T_{e0} \nu_e}{m_e \Omega_e^2} \quad (2.37)$$

The solution to the equation to a first approximation is simply a falling exponential dependence of the perturbation amplitude with time (Robinson, 1989),

$$n = n_0 e^{-\gamma_0 t} \quad (2.38)$$

The initial value n_0 is the steady state value which is attained after a long period of pumping and the characteristic rate of this fall γ_0 is determined by the field-perpendicular thermal conduction coefficient D_{\perp} and the scale size of the irregularity k (2.36). This allows the characteristic decay time of the irregularities to be deduced:

$$\tau_0 = \frac{1}{\gamma_0} \approx \frac{1}{1.8 D_{\perp} k^2} \quad (2.39)$$

Irregularity decay may be observed experimentally using coherent scatter radars, where the radar beam is directed orthogonal to the scattering structures. In order to receive backscatter from irregularities the wave number of the FAI, k , must be twice the wave number of the probing radio waves. T_{e0} is the averaged electron temperature (expressed in Kelvin, K in equation 2.40) during the interval when the heater is transmitting, after the plasma has reached a steady state. The electron collision rate ν_e (in s^{-1}) is due to collisions between electrons and neutral particles of density N_n (in cm^{-3}) and the temperature-dependent rate is given by (Gurevich, 1978)

$$\nu_e = 5.8 \times 10^{-11} N_n T_{e0}^{5/6} \quad (2.40)$$

In the high-latitude ionosphere, for a radio wave to attain F-region heights perpendicular to the geomagnetic field, coherent scatter radars operating in the HF band must be placed many hundred kilometres away so that the waves undergo appreciable

refraction along their propagation path. The backscattered signal power, P is actually proportional to the square of the density perturbation (irregularity) amplitude,

$$P \propto n^2 \quad (2.41)$$

Hence, the time constant for the decay in the measured backscatter power τ_p is half the magnitude of the true decay time in the density perturbation τ_0 . This may be related by

$$\tau_0 = 2\tau_p \quad (2.42)$$

The earliest studies of irregularity decay (or relaxation) for heating experiments at Platteville were undertaken by Minkoff and Kreppel (1976). They presented observations of the decay in 157.5MHz backscatter cross section using VHF radar. Although not explicitly discussed in the findings, the decay exhibited two stages which took the form of a fast initial decay with a time constant of about 1.4s, followed by a less rapid decay for the majority of the interval that the heater was off. The characteristic decay time associated with this slower stage was 8.3s. Hedberg et al. (1983) performed a series of experiments with the heater at Tromsø facility in 1981 and presented multi-frequency observations of artificial backscatter obtained with the HF radars located at Uppsala, Lycksele and Kiruna (Sweden). By utilising sounding frequencies at 3MHz and 7MHz at Kiruna, not only did they present evidence of the downward and upward extensions of FAI from the narrow height region where upper hybrid waves were excited, but observations of the frequency dependence of the growth and decay times of the backscatter was also shown. On a number of occasions, a two-stage decay process was exhibited (Figure 2.4). This consisted of an initial fast decay, with a characteristic time constant of a few seconds, followed by a much slower, prolonged decay in the backscatter power whose time constant was of the order of tens

of seconds. They did not, as was the case of Minkoff and Kreppel (1976), provide any explanation for this behaviour though.

Coster et al. (1985) presented a more in-depth study of the temporal behaviour of 3-m striations in order to study further the flow of energy between the heater and plasma, for experiments carried out at the Arecibo Ionospheric Observatory. They employed a 50MHz portable radar and fitted the exponential decay model (2.38) to their data using linear regression, and found that this model was satisfactory to describe the backscatter. No evidence of two-stage decay was detected, which was attributed to a lower sensitivity. Hysell et al. (1996) presented evidence of decaying artificial irregularities, where an initial fast decay was explained by cross-scale thermal diffusion processes associated with the decay of small-scale FAI and a later stage of slower decay identified to be the decay of 'parasitic FAI', or large-scale turbulence. Belenov et al. (1977) gave a similar explanation for observations of FAI generated by the heating facility at Gorki, Russia. Attempts have been made previously to address two-stage decay by fitting a sum of two decaying exponentials, each possessing their own characteristic decay time constant given by τ_1 and τ_2 . This function may be expressed by (Bond, 1997)

$$P = Ae^{-\frac{t}{\tau_1}} + Be^{-\frac{t}{\tau_2}} \quad (2.43)$$

Jones et al. (1982) determined growth and decay times that were comparable in magnitude, at around 38s. This was obtained from the timescale over which the phase of a diagnostic wave took to change in response to the density changes. However it should be noted that this method only provided information on the behaviour of the whole wave number spectrum of irregularities, as opposed to a single scale size, which would be obtained from using the former techniques of radar backscatter.

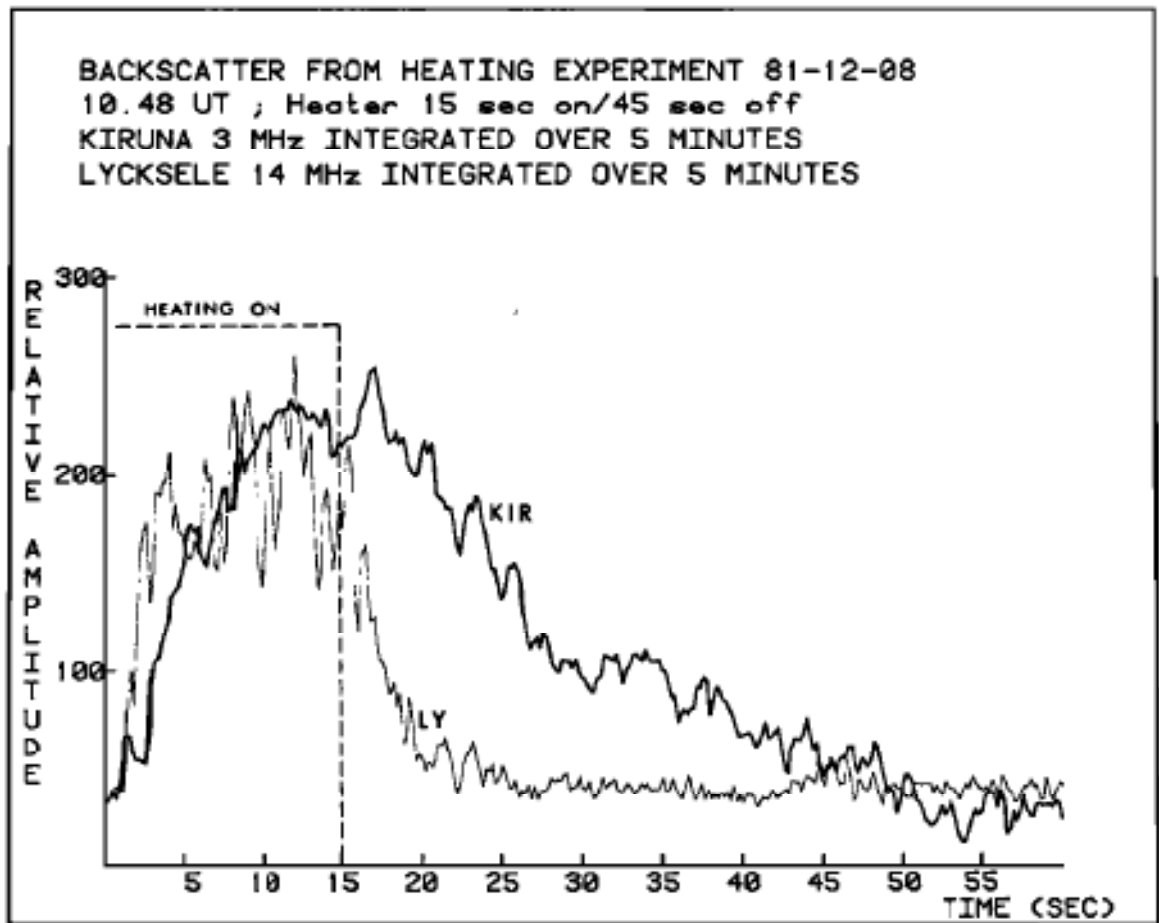


Figure 2.4 Example of backscatter decay profiles measured using the HF radars at Kiruna and Lycksele, from Hedberg et al. (1983). This figure illustrates the two-stage nature of the decay measured at Kiruna ('KIR') which was sounding at a frequency of 3MHz

Chapter 3

Instrumentation

3.1 Artificial Ionospheric Heating Facility

3.1.1 Facility Overview

The high power HF heating facility used for the purpose of ionospheric modification experiments during which observations are reported on in this thesis, is located at Ramfjordmoen (69°N, 19.2°E, L=6.2, magnetic dip angle I=78°) near Tromsø, Norway. It was originally built by the Max-Planck-Institut für Aeronomie in cooperation with the University of Tromsø between 1977-1980 and experiments have been active since 1980. In 1993 ownership of the facility was transferred to the EISCAT (European Incoherent SCATter) Association. The EISCAT heating facility site at Tromsø, together with the four-panel VHF radar and 32m-diameter UHF radar is shown in Figure 3.1. A comprehensive description of the facility and its experimental capabilities is given by Rietveld et al. (1993).

3.1.2 Transmitters

An important measure of the wave power of a radio frequency (RF) source reaching the ionosphere is the effective radiated power (ERP) in kW. This is determined by the linear product of the power supplied to an antenna and the antenna gain. The electric field E , expressed in V m^{-1} , experienced at some distance R (in km) from the source may be defined by (Robinson, 1989)

$$E = \frac{0.25\sqrt{ERP}}{R} \quad (3.1)$$

It is possible to transmit up to 1200MW of continuous wave (CW) power at frequencies between 3.85-8MHz with the Tromsø heater. This is achieved by using 12 amplifiers of 100kW power, each of which is driven by a 1.5kW solid state wideband exciter. This allows tuning and matching at the transmitter output stage.

3.1.3 Antenna Arrays

The RF source for each transmitter is a Hewlett Packard HP 3325A frequency synthesizer/function generator, which is locked to the EISCAT caesium clock. It is possible to programme the frequency, amplitude and phase of the synthesizers via a Commodore PET microcomputer. Transmitter tuning and matching is performed iteratively, whereby the amplitude and phase of the RF source is varied to one transmitter at a time, usually requiring only 4 or 5 steps per transmitter. A pair of transmitters is used to feed a row of crossed dipole antennas (linear full wave dipoles) and each transmitter feeds one of the linear antennas in the crossed dipole.

The heating facility consists of three arrays of crossed dipole antennas, and a bird's eye view of the site layout is presented in Figure 3.2. Array 1 was originally capable of the lowest frequency transmissions but following extensive storm damage in 1985, it was rebuilt and its later capabilities were somewhat different than before. After repair work was finished in 1990, Array 1 comprised 12 rows each with 12 antennas, producing an overall gain 30dB and up to 1200MW of ERP. Its current frequency range is from 5.5-8MHz and has the narrowest beam width of 7°.

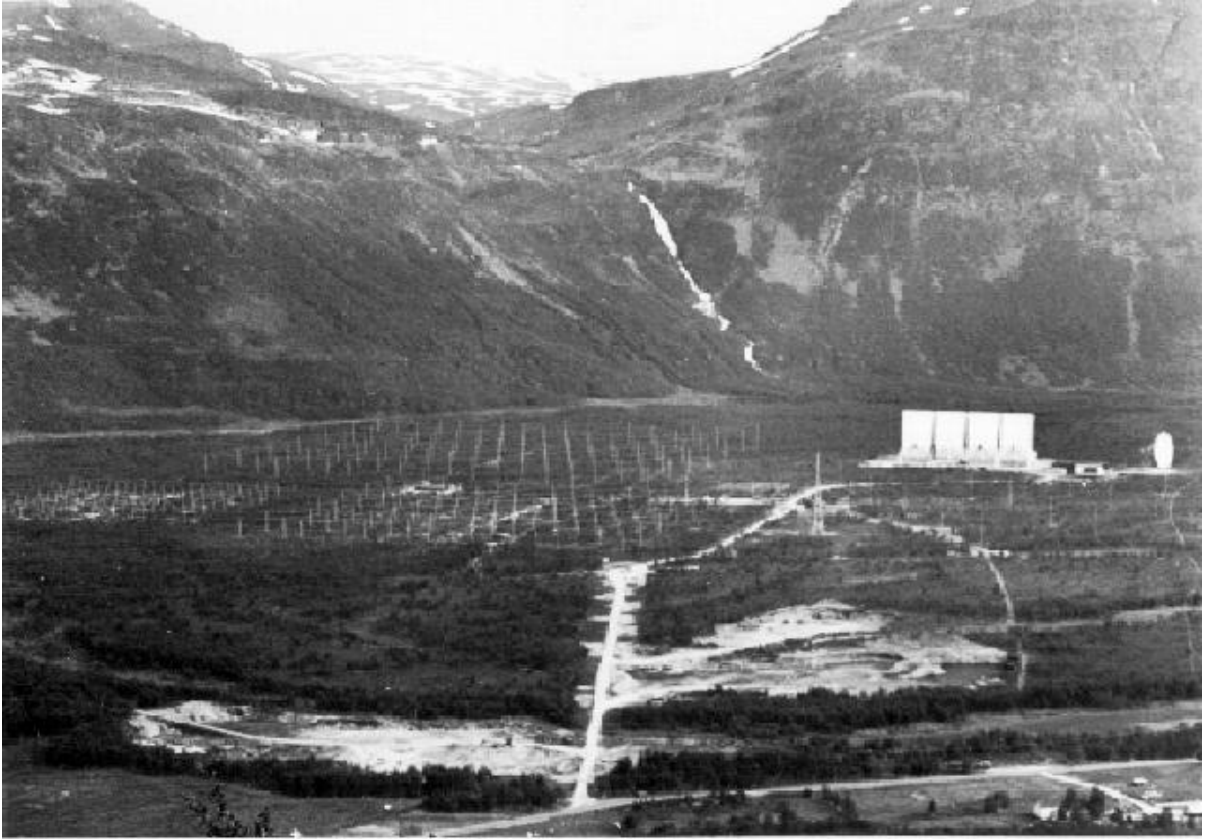


Figure 3.1 The Tromsø high power heating facility in the 1980s (from <http://www.eiscat.com/groups/Documentation/BasicInfo/Heating/heatsite.jpg/view>)

Arrays 2 and 3 consist of 6 rows each containing 6 crossed dipole antennas, with a gain up to 24 ± 1 dBi possible, depending on the frequency. Array 2 can transmit in the range 3.85-5.65MHz whilst Array 3 transmits in the 5.5-8MHz range. Both arrays possess a beam width of 14.5° and up to 300MW of ERP. The antennas rows are oriented in an east-west direction to allow tilting of the beam in a north-south direction. The frequency dependence of the antenna gain is illustrated for each of the arrays in Figure 3.3.

3.1.4 Beam Modulation

During the tuning stage the frequency, polarization, beam direction and power are specified. In order to begin or stop transmitting, the heater is switched ‘on’ or ‘off’ by applying either a +5V or -5V from any RF source to all 12 amplitude modulation inputs of the synthesizers. Generally, the heater is considered ‘off’ when the synthesizer voltage is 37.5dB below the full power. Switching the heater to an ‘on’ state is not instantaneous but takes approximately $5\mu\text{s}$. This also determines the shortest possible pulse length and hence the shortest time the heater can be switched ‘on’ for, and this is $20\mu\text{s}$. However, the heater can remain ‘on’ for several hours or more since there is no limit on the duty cycle although in practice this is rarely performed.

The heater wave amplitude may be modulated at fixed frequencies in the range from 1mHz up to 9.99kHz or swept in frequency between 200Hz to 6.55kHz, but due to power supply resonance frequencies, modulation in amplitude is generally not carried out in the range between 15-200Hz. Modulation of the heater power is performed either by tuning at a different power or by adjusting the amplitude modulation voltage supplied to the RF synthesizers.

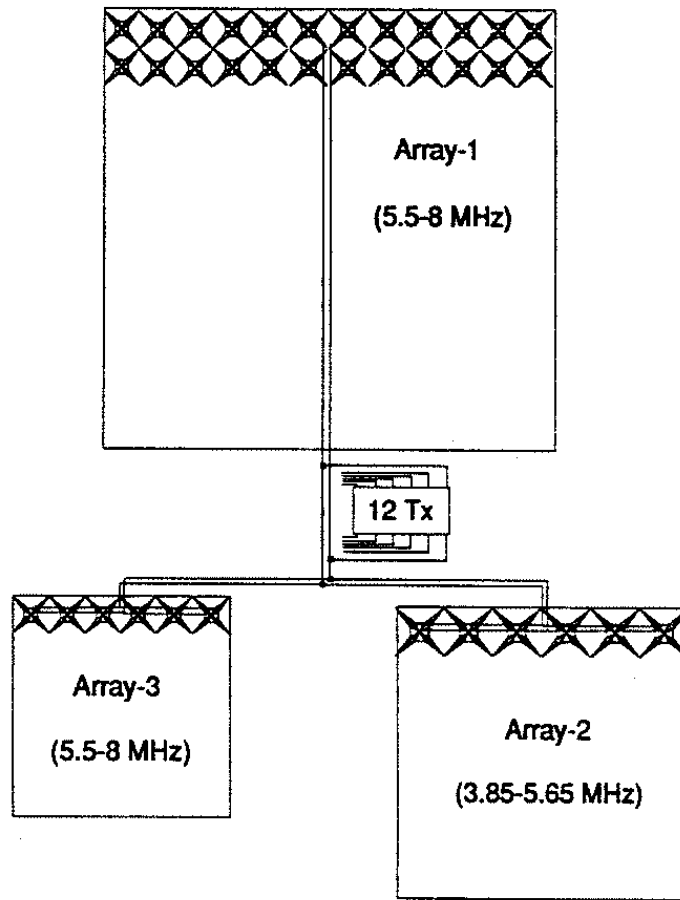


Figure 3.2. A bird's eye view of the heater site and the three antenna array

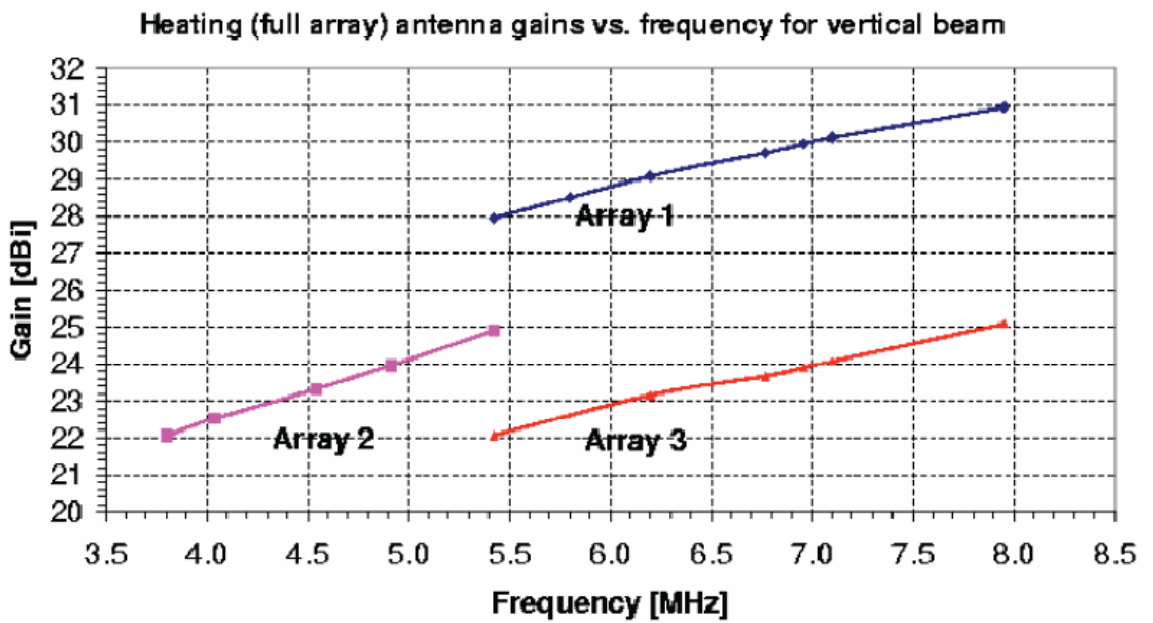


Figure 3.3 A graph illustrating the antenna gain that can be achieved across the frequency ranges possible with the different heater arrays

It is possible to transmit at 40 different power levels, the smallest being 2.5% of the full power which is set at the tuning stage. It is also possible to switch between the circular polarization modes by reversing the phase of the transmitters, for example by applying 1V to the 6 phase modulation inputs of the synthesizers. In addition to this, up to 6 different frequencies can be tuned in 2 transmitter groups in circular polarization, or up to 12 different frequencies in linear polarization. The beam direction and width can also be varied through changing the phase between pairs of transmitters that feed each row of antennas. However, at larger beam angles the beam power has to be lowered due to higher reflected power and the standing wave ratio as the angle increases.

3.2 Incoherent Scatter Radar Measurements

The incoherent scatter technique was first proposed as a diagnostic of the ionospheric plasma by Gordon in 1958 and has grown to be a very powerful tool for making ground-based measurements of the plasma properties over the last several decades. The first theories which treated electrons as independent scatterers (Thomson scattering) and predicted a Gaussian signal spectrum was in fact too simplistic in its approach and was later modified to consider the electrons as being electrostatically coupled to ions. This picture actually allowed a much larger number of plasma properties to be determined than had been originally envisaged. A brief, but relevant description of incoherent scatter theory will be presented in the following sections.

3.3 Incoherent Scatter Technique: Background

The initial belief that the returned radar signal would result from Thomson scattering was partly correct because the backscatter signal power does occur primarily by electrons. However the returned signal spectrum is vastly different from the expected Gaussian due to the role played by ions and hence, the term ‘incoherent scatter’ is not

strictly applicable to the EISCAT radars which will be described here, since it is Bragg scatter which is received, and this is introduced in Section 3.8.

An estimate of the returned signal power and hence electron density, can be made by considering the scattering by individual electrons. The backscattering cross section σ_e of a single electron can be approximated by (Wannberg, 2005):

$$\sigma_e \approx \frac{4\pi(r_e \sin\varphi)^2}{(1+k^2\lambda_D^2)\left(1+\frac{T_e}{T_i}+k^2\lambda_D^2\right)} \quad (3.2)$$

k is the radar wave number, λ_D is the Debye length, T_e and T_i are the electron and ion temperatures. The classical electron radius r_e is,

$$r_e = \frac{e^2}{4\pi\epsilon_0 c^2 m_e} \approx 10^{-15} m \quad (3.3)$$

Thus, the total scattering cross section of volume V of electron number density N is,

$$S = NV\sigma_e \quad (3.4)$$

If the assumption for incoherent scatter and a thermal plasma ($\frac{T_e}{T_i} = 1$) is made, then for a volume of the order $(10\text{km})^3$ illuminated by a radar pulse and a typical number density at F region heights, $N = 10^{11}\text{m}^{-3}$, equation (3.4) gives an estimate of $S \approx 10^{-6}\text{m}^2$ or 1mm^2 . When the same calculations are made for ions, assuming a composition of primarily atomic oxygen, then the total scattering cross section becomes of the order $S \approx 10^{-12}\text{m}^2$, which is negligible in comparison to that of the electrons, since the classical ion radius is around four orders of magnitude smaller than that of an electron. However, the electrons can be thought to form a ‘cloud’ around the ions in order to maintain charge neutrality. Because the radar wavelength is much greater than the electron Debye length which is also a measure of the sphere of influence of an

electron, the backscattered signal represents the collective wave behaviour of the ions and electrons moving together though the backscattered signal power is very much due to the scattering by electrons because of their much larger scattering cross section.

3.4 Radar Equation

The backscattered signal power for a monostatic radar system can be described by the radar equation. This takes into account various factors such as the transmitted signal power P_t and wavelength λ , electron scattering cross section σ_e and antenna gain G . For a scattering volume of size $dV = r^2 d\Omega \Delta r$, the backscattered power may be defined by,

$$\Delta P_r(r) = \frac{n_e(r) \sigma_e P_t \lambda^2}{(4\pi)^3 r^2} \left[\int_{\Omega} G^2(\Omega) d\Omega \right] \Delta r \quad (3.5)$$

The dependence of the theoretical received power on the electron density n_e allows an estimate of the raw electron density to be made by simple inversion of the equation and making the assumption that the electron and ion temperatures are equal and for incoherent scatter conditions ($k^2 \lambda_D^2 \ll 1$):

$$n_e(r) = C \frac{\Delta P_r(r) r^2}{P_t \Delta r} \frac{2}{4\pi r_e^2} \quad (3.6)$$

In this notation, C is sometimes known as the system constant, which is defined in terms of the antenna gain and beam pattern and radar wavelength.

3.5 Ion-Acoustic Waves

Waves transmitted by incoherent scatter radars are reflected from ion-acoustic waves travelling in the same direction (parallel or antiparallel) leading to constructive interference. Ion-acoustic waves in a plasma are somewhat analogous to sound waves that propagate in a non-ionised medium, being longitudinal in nature. Perturbations in the ion density can induce small electric fields in the plasma that accelerate the

electrons and cause them to oscillate. For plasma consisting of one ion species and electrons, the momentum equations are given by

$$m_{i,e}n_{i,e} \left[\frac{\partial v_{i,e}}{\partial t} + (v_{i,e} \cdot \nabla)v_{i,e} \right] = -\nabla p_{i,e} \pm en_{i,e}E \quad (3.7)$$

Here, $m_{i,e}n_{i,e}, v_{i,e}, p_{i,e}$ are the mass, number density, velocity and pressure of the ions and electrons respectively, and E is the electric field which is set up due to the charge separation of the ions and electrons moving at different speeds. For charge neutrality, $n_i = n_e = n$ which is achieved if $v_i = v_e = v$. Also, by considering that $m_e \ll m_i$ then the equation may be rearranged and simplified to the expression

$$E = -\frac{1}{ne} \nabla p_e \quad (3.8)$$

The ideal gas law may also be used in conjunction with the assumption that the compressions are adiabatic,

$$p_{i,e} = nk_B T_{i,e} \quad (3.9a)$$

$$\text{Where, } \frac{\nabla T_{i,e}}{T_{i,e}} = (\gamma - 1) \frac{\nabla n}{n} \quad (3.9b)$$

Then the pressure gradient

$$\nabla p_{i,e} = \gamma k_B T_{i,e} \nabla n \quad (3.10)$$

can be substituted back into the ion momentum equation to give

$$m_i n \left[\frac{\partial v}{\partial t} + (v \cdot \nabla)v \right] = -\gamma k_B (T_i + T_e) \nabla n \quad (3.11)$$

The ion and electron continuity equation is:

$$\frac{\partial n}{\partial t} + \nabla \cdot (nv) = 0 \quad (3.12)$$

The dispersion equation of ion-acoustic waves can be obtained by rewriting the number density n in terms of an unperturbed value n_0 and a small perturbation n' :

$$n = n_0 + n' \quad (3.13)$$

Linearizing the resulting equations and neglecting the higher order terms eventually leads to the equation

$$m_i \omega^2 - \gamma k_B (T_i + T_e) k^2 = 0 \quad (3.14)$$

By making considerations of the electron thermal speed, which is much greater than the phase speed of the ion-acoustic wave, this means the electron compressions are actually isothermal and not adiabatic, so that the term $\gamma k_B (T_i + T_e)$ is replaced by $k_B (\gamma T_i + T_e)$ and the ion-acoustic wave speed is therefore given by:

$$v_{i-a} = \sqrt{\frac{k_B (\gamma T_i + T_e)}{m_i}} \quad (3.15)$$

3.6 Langmuir Waves

Langmuir waves are electrostatic waves, and can be derived from the dispersion relation (2.15) by ignoring effects of the magnetic field, to obtain the electron-acoustic wave speed, which give rise to the plasma lines in incoherent scatter spectra:

$$v_{e-a} = \omega_p \sqrt{\frac{1}{k^2} + 3\lambda_D^2} \quad (3.16)$$

where ω_p is of course the natural plasma frequency, and λ_D is the Debye Length.

3.7 The EISCAT Radars

The European Incoherent SCATter (EISCAT) association was originally set up in 1975, and consisted of research councils from six member countries (Finland, France,

Germany, Norway, Sweden and UK). First operations of the tristatic UHF radar system began in 1981 and subsequent operation of the VHF radar at Tromsø took place later in 1985. The EISCAT site at Ramfjordmoen situates the 930MHz fully-steerable UHF radar, which has a dish diameter of 32m and transmit power of less than 2MW. Ionospheric parameters can be inferred for altitudes from 70 to 700km. Co-located with the UHF radar is the VHF system, comprising four panels, each measuring 40m across by 120m tall, and transmit power of less than 5MW. Both radars have a duty cycle of 12.5%. In 2000, the EISCAT mainland radars underwent extensive renovation which included the installation of new receiver systems. This allowed much better signal processing capabilities and experiments to be developed.

EISCAT radar experiments may be divided into two categories: those that utilise plain pulses and those that use coded pulses that modulate the phase of the pulse. The uncoded pulse type may be short or long pulse transmissions, depending on the spatial resolution requirement. To obtain power profiles, or altitude profiles of the backscattered signal power, short pulses usually of less than $10\mu\text{s}$ are transmitted. Consequently only the zero-lag power of the received sample is calculated which a measure of the raw electron density at relatively high spatial resolution of only a few kilometres. This ‘raw density’ estimate does not however account for the effects of the plasma temperature and Debye length, evident in equation (3.2).

Long pulses typically involve the transmission of 200-400 μs pulses, and as a result have a much greater range ambiguity, since the range resolution is defined by the pulse length. They are typically more useful in probing a slowly-varying ionosphere or that which has a scale height larger than this range ambiguity of the pulse, and the F region typically fulfils these criteria. Lag, (‘crossed’) products are cross-correlations between

signal samples made at different time delays after the radar has started receiving. A correlator combines many of the independent cross-products which are calculated to obtain a mean value for a given time delay, and a series of mean cross-products at different lag times is used to obtain the complex autocorrelation function (ACF). This is the Fourier Transform of the incoherent scatter spectrum. In practice though, the expectation value of each cross-product in the ACF is associated with range and lag ambiguities, because they are not point measurements (Lehtinen and Huuskonen, 1996).

3.8 Bragg Scattering

The elastic scattering of X-ray radiation incident on atoms in a crystal was discovered experimentally by Sir William Bragg in 1912. Since virtually no wave energy is lost in this process, the scattered waves are re-radiated at the same frequency. For a crystal whose structure is composed of regular aligned planes of atoms separated by a distance d , radiation of wavelength λ which is incident at some angle θ will be scattered from consecutive planes, leading to interference between the re-radiated wave fields. The returned wave amplitude is enhanced when the interference is constructive, or when the waves are in phase with each other. This occurs if the phase difference is even integers (j) of π . Bragg's Law defines the condition for constructive interference:

$$j\lambda = 2d\sin\theta \quad (3.17)$$

This principle may be extended to experiments involving the use of High Frequency (HF) and Ultra High Frequency (UHF) waves to probe the periodic plasma structure of the ionosphere during artificial modification experiments. In order for a monostatic system to transmit and receive signals along the same path, the transmitted waves must be incident at an angle perpendicular to the scattering structure. In order to satisfy this criteria, we can express Bragg's Law in terms of the wave vectors of the incident HF

wave, \mathbf{k}_r and the plasma irregularities \mathbf{k}_i that scatter these waves. If $\lambda = \frac{2\pi}{|\mathbf{k}_r|}$ and $d = \frac{2\pi}{|\mathbf{k}_i|}$

then for orthogonal incidence, $\theta = \frac{\pi}{2}$,

$$j \frac{2\pi}{k_r} = 2 \left(\frac{2\pi}{k_i} \right) \quad (3.18)$$

$$\therefore k_i = 2k_r \quad (3.19)$$

3.9 Incoherent Scatter Spectrum Shape

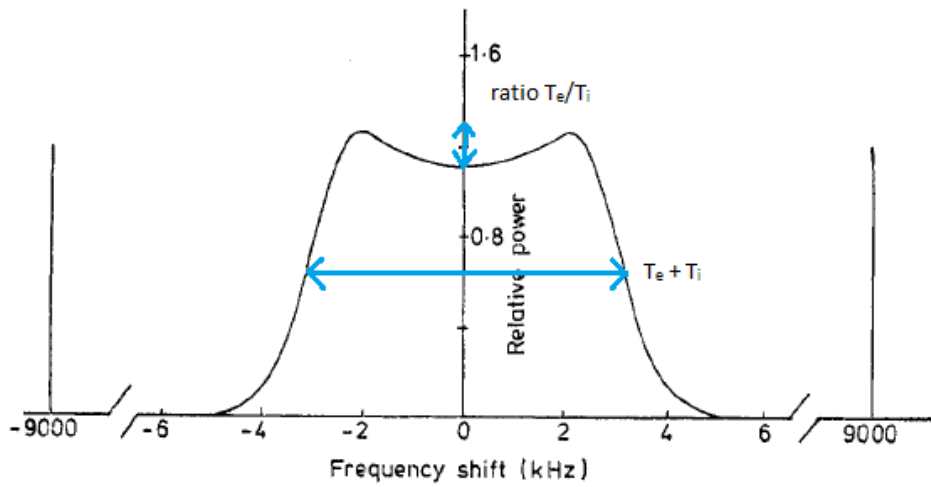
For a Maxwellian plasma, or one in thermal equilibrium, the incoherent scatter spectrum of the backscattered radar signal has a twin-peaked shape (Figure 3.4) corresponding to ion-acoustic waves travelling toward and away from the radar. The centre of the ‘ion line spectrum’ is Doppler-shifted from the transmit frequency due to the bulk motion of the plasma, providing a measure of the ion velocity in the radar line-of-sight direction. Similarly the plasma lines which correspond to electron-acoustic waves, are offset from the transmit frequency in proportion to the plasma density.

The spectrum width may be broadened in proportion to the ion temperature and electron temperature, as the frequency of the ion lines is proportional to the ion-acoustic speed (3.15). Landau damping is the phenomena of wave attenuation in the plasma due to wave-particle interactions and occurs when there is a higher proportion of particles in the plasma travelling slower than the wave. The depth of the ‘valley’ between the ion lines and the centre of the spectrum is controlled by the strength of Landau damping and provides a measure of the electron-to-ion temperature ratio. When this ratio is larger, the mean temperature of the electrons is greater and the ion-acoustic waves are not attenuated as strongly, resulting in weaker damping and ion lines which appear sharper and more well-defined.

3.10 Incoherent Scatter Spectrum Analysis: GUISDAP

In order to infer plasma parameters such as those listed below in Table 1 the spectrum which is measured by the EISCAT radars must be analysed. Fortunately, highly advanced software has been developed since the 1990s to cope with the large-scale data analysis required by the scientific community using the EISCAT facilities. The Grand Unified Incoherent Scatter Design and Analysis Package (GUISDAP) (Lehtinen and Huuskonen, 1996) is essentially an analysis program that uses an iterative process to fit a theoretical spectrum to the measured data in order to estimate these parameters.

Many assumptions are made by the analysis program in order to compute a theoretical spectrum. Known parameters that are used to compute an initial spectrum include system variables such as the transmitted signal and receiver properties, and environment variables such as the raw electron density and ‘a priori’ values of the plasma parameters (which are obtained from an ionospheric model). In addition, a number of crucial assumptions are made, which include background noise, the finite length of the transmitted pulse and receiver filter response and ambiguities in range and lag. Most significantly, GUISDAP assumes that the velocity distribution of particles is Maxwellian. By varying the a priori values at successive iterations, a different theoretical spectrum is generated and a fit residual is calculated, which indicates the quality of the fit of the theoretical spectrum to the measured spectrum.



Ion spectrum and plasma lines. $N = 10^{12} \text{ m}^{-3}$, $T_e = 1000 \text{ K}$, $T_i = 1000 \text{ K}$, $\lambda = 1 \text{ m}$, $M_i = 16$.

Figure 3.4 Illustration of the configuration of a typical incoherent scatter spectrum, showing peaks at the ion-acoustic frequency which correspond to waves travelling away and toward the radar (from Beynon and Williams, 1978). The figure has been annotated to show how the centre ‘valley’ depth depends on the electron-to-ion temperature ratio and how the width of the spectrum depends on the sum of the ion and electron temperatures

Parameters Inferred Directly	Parameters Inferred Indirectly
Electron density, n_e	Neutral density, n_n
Electron temperature, T_e	Neutral temperature, T_n
Ion temperature, T_i	Neutral velocity, V_n
Plasma velocity, V_i	Pedersen conductivity
Collision frequency, ν	Hall conductivity
Ion composition	Electric field
Photoelectron flux	Heat flux

Table 1. The plasma parameters that can be inferred directly and indirectly from the analysis of the incoherent scatter spectrum using the GUISDAP software

3.11 CUTLASS Radars

The Cooperative UK Twin-Located Auroral Sounding System (CUTLASS) is a pair of coherent HF radars at Hankasalmi, Finland [62.3°N, 26.6°E] and Pykkvibaer, Iceland [63.7°N, 19.2°W], shown in Figure 3.5 and Figure 3.6 respectively. The radars were built by the Radio and Space Plasma Physics Group at the University of Leicester and have been operational since 1995 in collaboration with the Swedish Institute of Space Physics (IRF) and the Finnish Meteorological Institute (FMI). Together with twelve other HF radars in the Northern Hemisphere, they form part of the Super Dual Auroral Radar Network (SuperDARN). For a more in-depth description of SuperDARN the reader is referred to Greenwald et al. (1995). The overlapping fields-of-view (Figure 3.7) of the radars allows a highly accurate determination of the plasma convection velocity from merging velocity vectors along different line-of-sight directions.

The radars consist of sixteen 600W solid state transmitters, and these are connected to log-periodic antennas, each of which are separated by a spacing of 15.24m. This allows the radar beam to take up to 16 possible azimuthal directions via a phasing network with an overall coverage of approximately 50° and a beam separation of the order of 3.24°. The beam width is frequency-dependent and the antenna pattern of the main lobe in one beam direction can often overlap the main lobe of an adjacent beam. By incorporating a time delay to the phasing, the beam frequency can be varied from 8MHz to 20MHz, with bandwidth depending on the frequency used. The radar waves undergo sufficient refraction as they propagate through the ionosphere such that they attain orthogonality to the background magnetic field at high-latitudes where the field is near-vertical. The degree of refraction suffered depends on the radar frequency and plasma density.



Figure 3.5 The antennas comprising the CUTLASS Finland radar at Hankasalmi



Figure 3.6 The site of the CUTLASS Iceland radar at Pykkvibaer

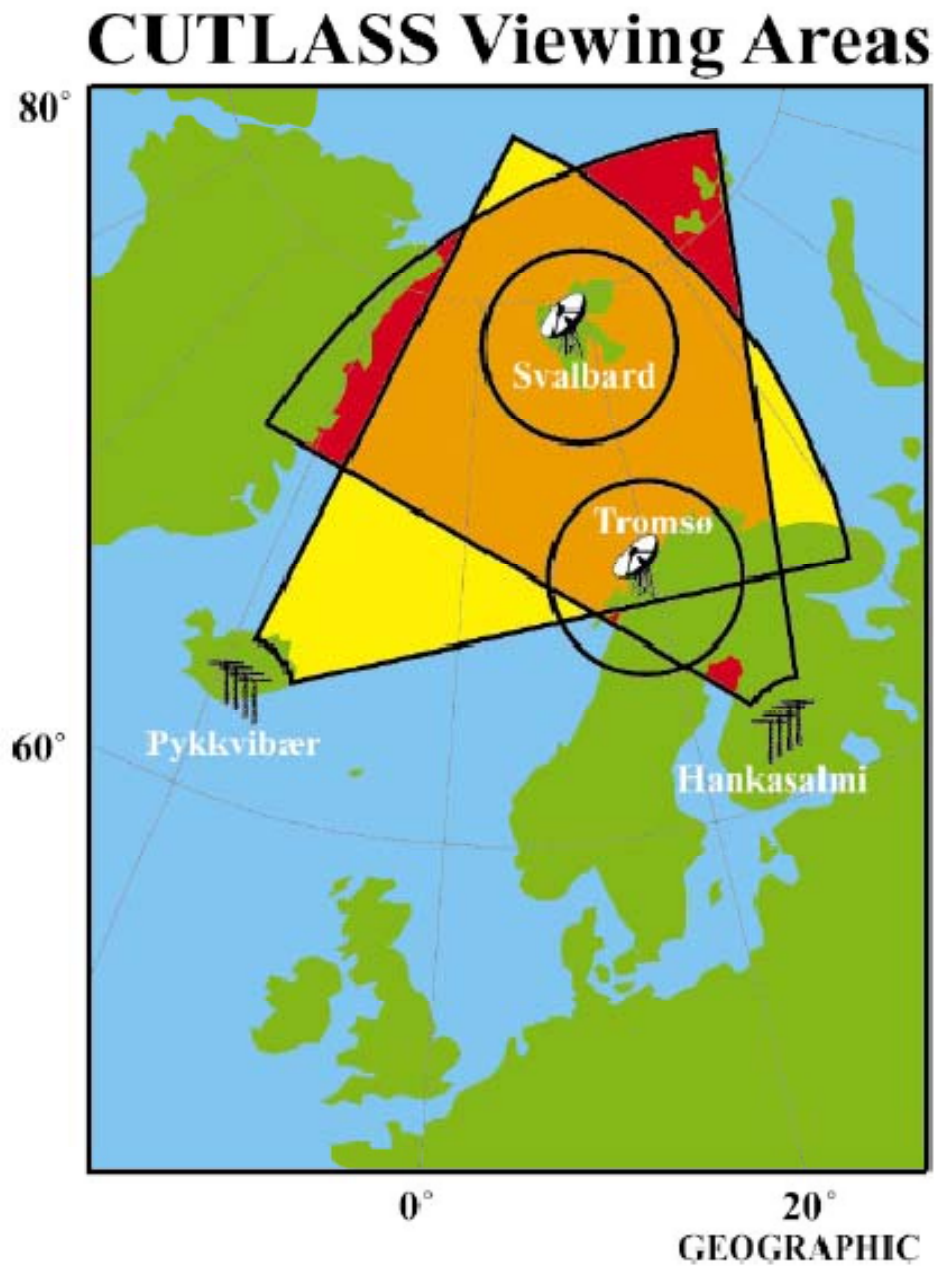


Figure 3.7 The fields-of-view of the CUTLASS radars located at Pykkvibaer, Iceland and Hankasalmi, Finland. Also indicated is the location of the EISCAT heater and UHF/VHF radars at Tromsø and the EISCAT Svalbard radars (from Jones et al., 2001)

The CUTLASS radars are capable of detecting Bragg scatter from a regular arrangement of field-aligned irregularities in the plasma density that have a cross-field wave number that is twice the wave number of the radar wave. Coherence arises because the Bragg-scattered waves are in-phase with each other. A variety of propagation modes are possible which allow different altitude and range regions of the ionosphere (E and F regions) to be accessed by the sounding wave. Due to the finite vertical beam width the backscattered signal originates from a spread in altitudes which is dependent on both the beam properties and the ionospheric conditions, which can modify the expected ray path.

A schematic of some of the modes transmitted by the CUTLASS radars is illustrated in Figure 3.8 (after Milan et al., 1997). In addition to a main array of 16 antennas, there is also a separate array of 4 antennas for a receive-only usage, and these are used for interferometry purposes. The phasing of the received signals allows altitude determination of the scattered wave. For both antenna arrays, the received signals are summed and sent to a receiver channel where they are down-converted to supply a baseband and quadrature output which are sampled by two analogue-to-digital converter channels

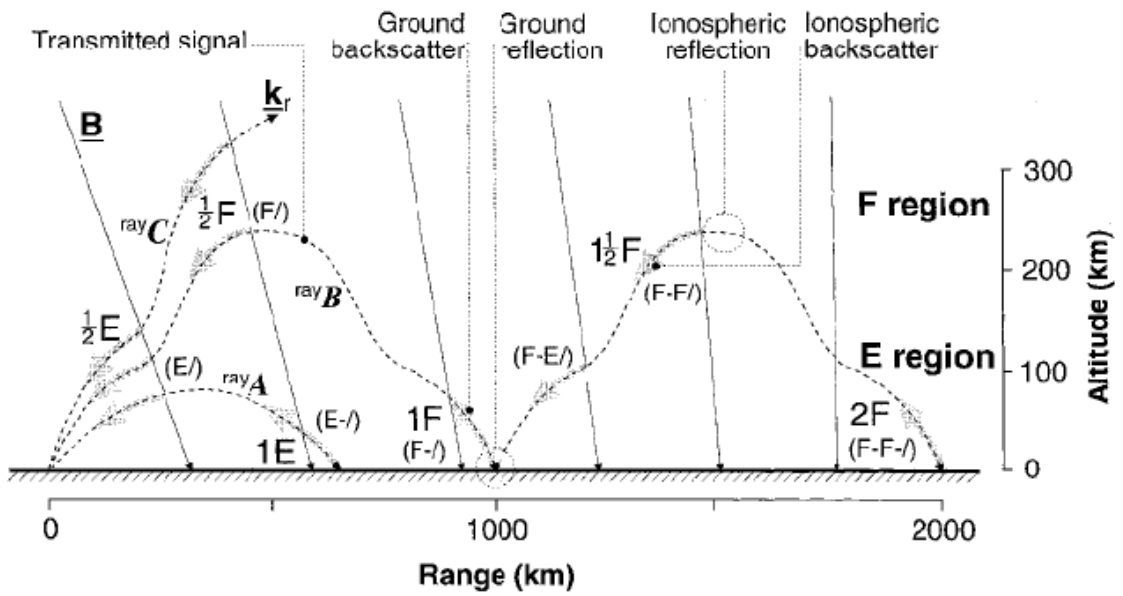


Figure 3.8 Illustration of the wave mode propagation paths that can be transmitted by the CUTLASS HF radars (from Milan et al., 1997)

3.12 CUTLASS Pulse Schemes

The HF waves transmitted by the CUTLASS radars are pulsed, and follow a standard 7-pulse sequence. In a standard operating mode, the length of these pulses are 300 μ s in length which defines the standard range resolution of 45km. During special operating modes, for example in conjunction with an ionospheric heating experiment, this pulse length can be reduced to 100 μ s in order to achieve a higher range resolution of 15km. The basic time unit, τ , in the pulse sequence is 2400 μ s, and this also defines the basic lag separation. The pulses are transmitted at 0τ , 9τ , 12τ , 20τ , 22τ , 26τ and 27τ , as shown in Figure 3.9 (from Barthes et al., 1998). A standard CUTLASS scan involves sounding on each of the 16 beam directions consecutively with a dwell time of 7s in each look-direction, allowing a full scan to be made approximately every 2 minutes. Since each pulse sequence takes 0.1s to transmit, 70 pulse sequences are transmitted on each beam during a standard scan mode.

Figure 3.9 illustrates all possible delays between the cross-correlated received samples. These lag products together make up the ACF which is averaged over the integration (dwell) time for each range gate. Hence, there are 18 lag products that form the ACF, used to derive parameters such as the zero-lag power, line-of-sight drift velocity of the plasma, spectral width and elevation angle-of-arrival. These are derived from standard SuperDARN analysis software known as ‘FITACF’. The decorrelation of the ACF with increasing lag number is modelled either by a Lorentzian or Gaussian function and by least-squares fitting both forms to the integrated ACF, the backscattered signal power may be obtained. The phase is calculated using the real and imaginary values of the ACF:

$$\varphi = \tan\left(\frac{\text{Im}(ACF)}{\text{Re}(ACF)}\right) \quad (3.20)$$

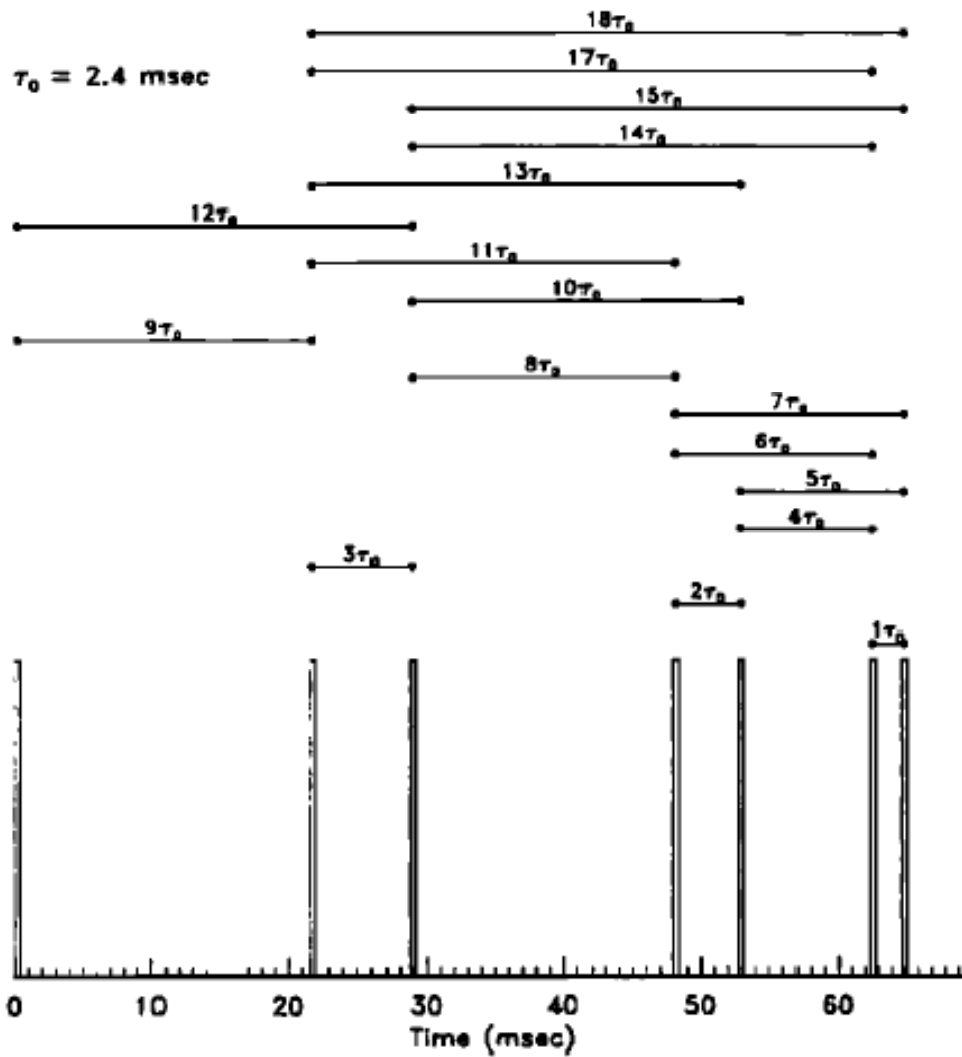


Figure 3.9 An illustration of the typical pulse scheme used by the CUTLASS radars, shown with the range of lag products possible which involves cross-correlating the signal at different time delays to form the autocorrelation function (from Barthes et al., 1998)

A slope $\frac{d\phi}{d\tau}$ is fitted to the phase values and this gives an estimate of the drift velocity along the line-of-sight direction of the radar beam. Special operating modes allow modulation parameters such as the pulse length (and hence range resolution), integration time, lag to the first range, transmission frequency and scan pattern to be specified. During typical heating campaigns when high time and spatial resolution are required, the pulse length is usually set to $100\mu\text{s}$, and the lag to the first range of $3200\mu\text{s}$ or $9800\mu\text{s}$ which corresponds to 480km and 1470km at Hankasalmi and Pykkvibaer respectively.

3.13 Tromsø Dynasonde

Co-located with the Tromsø heater is the Dynasonde facility. This is a digital HF wave sounder, or frequency agile sounder, capable of transmitting radio waves in the 1-30MHz frequency range. The way in which an ionospheric sounder works is outlined in Appendix 1. It can be used in a variety of ways, including fixed frequency soundings in techniques such as Imaging Doppler Interferometry. The Dynasonde typically makes a variety of sounding types. Used as an ionosonde, an ‘I’ sounding is made, which involves sweeping the transmitted radio wave through a frequency range. For more accurate estimates of the Doppler velocity from the echoes, a ‘B’ mode sounding can be made, similar to an ionosonde mode but with additional transmitted pulses at a given frequency during a sounding, so that comparisons of echoes at the same frequency can be made. The ‘K’ and ‘P’ mode are useful for studying certain ionospheric plasma structures that can be probed at a specific frequency.

3.14 Concluding Remarks

The EISCAT heater at Tromsø remains one of the most powerful facilities, in the quantitative sense, worldwide since it began operation in the 1980s and in conjunction

with the broad range of diagnostic instruments that have been built in the subsequent years, substantial and important scientific knowledge has been gained. Higher resolution observational results, combined with a variety of new measurement techniques reveal new and sometimes puzzling phenomena. The CUTLASS Finland and Iceland radars, both ideally placed to observe FAI, and the EISCAT VHF and UHF radars which can derive information about the plasma properties, represent very powerful and complementary tools in the understanding of nonlinear plasma processes induced by the heater. In the forthcoming decade, developments such as EISCAT-3D will become increasingly important in providing simultaneous observations of the heated volume in three-dimensions. This will also hopefully add to the wealth of results and also enable some of the current unknown questions to be answered.

Chapter 4

Evaluation of the electron temperatures recovered by incoherent scatter analysis during artificial ionospheric modification experiments

4.1 Introduction

The purely growing mode (PGM) feature in incoherent scatter spectra during the ‘overshoot’ has a short lifetime of only a few milliseconds, but can strongly distort the incoherent scatter spectrum until it is quenched by the TPI, which can take several seconds to tens of seconds to develop. Since EISCAT UHF data are typically pre-integrated for periods of between 1 and 5 seconds, the PGM feature often only appears in the first one or two data dumps taken after the heater is switched on, and during this period the spectra from the interaction height are very distorted, and exhibiting a triple-humped appearance.

In the standard analysis of EISCAT data using the GUIDAP software, the assumption of Maxwellian distributions in ion thermal velocity clearly cannot apply under conditions of strong plasma turbulence, as evidenced by the ‘overshoot’ spectra. However, the average incoherent scatter spectrum during the remainder of the heating period following the disappearance of the PGM often appears Maxwellian in character, but the possibility of ongoing plasma turbulence cannot be ruled out because of the continuing interaction of the plasma with the strong heater wave. Recent evidence suggests that the overshoot feature may not always be fully quenched, but that some remnant of it can continue to contaminate the measured spectra (Robinson et al., 2006).

4.2 Motivation for the Study

EISCAT UHF data from a number of past heating experiments carried out at Tromsø in which an apparent reduction in the electron temperature occurred after the heater began transmitting, are considered. These depreciations in the electron temperature sometimes lasted for longer than the initial few seconds of heating. Figure 4.1 illustrates plasma parameters derived from conventional GUIDAP analysis of data from a heating experiment on 7th October 1997, when the heater was transmitting in a “power seeding” cycle between 1246UT and 1304UT. This heater cycle consisted of transmissions in 1-minute on, 2-minutes off cycles at increasing power levels of 2.5, 5, 10, 25 and 50% of full power, each followed by a ‘seed pulse’ of 20 seconds duration at 100% power. The reader is referred to Wright et al. (2006) for full details of the experiment. At 1246 UT, 1249 UT, 1252 UT, 1255UT and 1258UT, periods of distinctly lower electron temperatures occurred over the altitude range from approximately 190 to 230km. These can be seen in the third panel of Figure 4.1, and appear to persist for the entire duration of the heating interval during certain intervals, but for only one or two integration periods at other times. At the same time as the electron temperature was apparently reduced, the ion temperature (second panel) was apparently quite appreciably enhanced, while neither the electron densities (upper panel) nor the ion velocities (lower panel) showed any significant change.

The concept of a decrease in the electron temperature under the action of a strong, modifying EM wave field is physically unrealistic. The apparent increase in the ion temperatures might suggest that in these cases when the inferred electron temperature has been observed to decrease, the ion temperatures have been overestimated to compensate for the lower electron-to-ion temperature ratio $\frac{T_e}{T_i}$ fitted by the analysis.

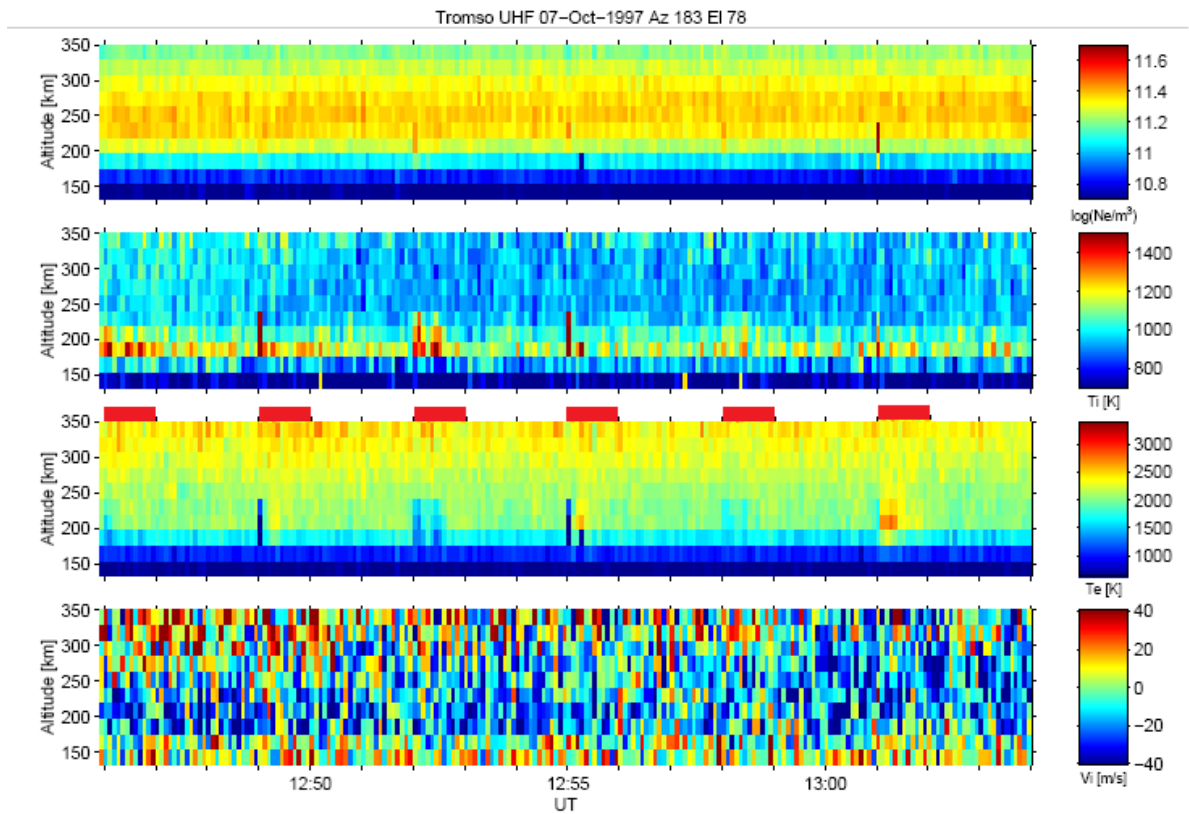


Figure 4.1 Plasma parameters from GUISDAP analysis of EISCAT UHF data, for the heating experiment between 1246-1304UT on 7th October 1997. In the top panel is the electron density (log scale), second panel is the ion temperature, third panel is electron temperature and bottom panel the ion velocity. The red tabs indicate intervals when the heater was transmitting

These facts suggest that, for these events, the apparent temperature reductions are artefacts of the data analysis, occurring because of a reduction in the ratio between the spectral power in the ion-acoustic peaks and the power at the centre of the spectrum. A strong PGM feature would account for such behaviour, and would also explain why the effects are *usually* limited in altitude to a single (22.5 km) range gate, since the plasma turbulence responsible for creating the PGM occurs only within a narrow height region, of the order 10km or less. However, it may be noted from Figure 4.3 that the PGM may contaminate neighbouring range gates as well, under certain conditions.

The objective of this chapter is to present two alternative approaches to obtain an estimate of the temperature at this altitude, particularly in the cases where a decrease in the temperature after the heater has been turned on has been identified, as illustrated in Figure 4.1. This is achieved in the first part of the study by fitting Epstein-type functions to the electron temperature change profile. The justification for this and a more detailed description of the method is given in Section 4.3, along with selection of results of the analysis. In the second approach, a method to remove the PGM feature from the ‘overshoot’ spectra is described, and this technique has been used to correct the spectra in order to produce more realistic temperature estimates. An application of a simple theoretical model of the large scale temperature perturbation is then made to a selection of EISCAT data and compared with the results of the Epstein profile fitting in Section 4.4 to Section 4.5.

As well as removing PGM effects from clearly contaminated spectra, the technique may prove useful for the re-analysis of cases where subtle effects, such as apparent decreases or small enhancements in the electron temperature might suggest that results derived from standard analysis could be questionable. In addition, important parameters related

to characteristics of heater-induced turbulence may be retrieved from the PGM properties. An outline of this spectral correction technique is given in Section 4.6. In Section 4.7 and 4.8, a selection of results from investigations of both overshoot-contaminated spectra and apparently uncontaminated “heater on” spectra are presented and discussed.

4.3 Epstein Function Analysis

4.3.1 Epstein Model Function

Epstein functions are well established functions that have been used extensively to approximate the topside ionospheric electron density profile in the International Reference Ionosphere (IRI) models (Zhang et al., 2002, Depuev et al., 2004). Since electron densities are essentially asymmetrical in nature due to changes in the scale height at different altitudes, these functions might therefore also be well-suited to electron temperature profile approximations during heating experiments which sometimes can exhibit asymmetry around a single peak, with steeper gradients below the peak than above. If this asymmetry were not present, a Gaussian approximation would be appropriate and the theoretical model of a stationary perturbation (equation 2.30) would apply. In order to incorporate some flexibility into the curves and thus fit the measured temperature profiles as closely as possible, an Epstein function of the following form was used as a model profile:

$$f_{eps} = A \frac{e^{\frac{X}{B_2}}}{\left(1 + e^{\frac{X}{B_2}}\right)^2} + G \quad \text{where } X = z - z_m \quad (4.1)$$

Equation 4.1 is a form of the Epstein function used by Zhang et al. (2002) but includes an extra parameter, G , in order to incorporate greater flexibility in the fitting process. A

is a scaling factor, G is a constant, X is the distance between an altitude point z and the altitude of the peak, z_m , and B_2 remains a thickness parameter that essentially controls the rate at which the electron temperature changes with height:

$$B_2(z) = B_0 + kz \quad (4.2)$$

B_0 is a constant and k is also a scaling factor, both of which are allowed to be free parameters in the fitting procedure.

The fitting procedure is outlined in Appendix 2 and was applied to a selection of many heating periods to establish if any statistical trends were present and this was carried out only for the averaged electron temperature profiles. To date, 90 heating cycles have been selected for the purpose of implementing the fitting routines to the corresponding EISCAT electron temperature data. The experiments cover the period between 1996 and 2002 and a large range in transmission frequencies (3.9-7.95MHz) and ERP (90-1100MW). The range of heater beam directions is relatively limited with the majority of experiments in the field-aligned direction (-12°S) and the remainder at vertical incidence (0°S). The Epstein fitting results for a particular heating experiment, using EISCAT UHF electron temperature data for heating from 1410-1412UT on 7th October 1997, are shown in Section 4.3.2 using the averaged temperature change profiles. The results of the wider study for 90 different heating experiments are also presented.

4.3.2 Results of the Temperature Profile Fitting

Between 1410-1412UT on 7th October 1997, the Tromsø heater was transmitting in O-mode polarisation at 4.54MHz and the beam was pointed along the magnetic field. The overshoot power profile for this experiment is shown in Figure 4.2. There is a clear, strong peak in the profile at 216km, and the measured overshoot ion acoustic spectra at

each range gate are shown in Figure 4.3. There is clear evidence of radar cross contamination above and below 209km exhibited by a smaller PGM in the spectrum at the range gates centred on 187km and at 231km. However the greatest enhancement in both the ion lines due to the PDI and the strongest PGM exists in the spectrum at 209km.

Figure 4.4 shows that the averaged temperature change at the interaction height, where the best fit Epstein function value has replaced the original EISCAT measurement, only reaches 30% (0.3) of the background (averaged over heater-off period) even though the Epstein peak lies at twice this measurement at 60% of the background temperature. Though small, the large scale temperature nevertheless indicates that quenching of the PGM from the ion-acoustic spectra should occur within the first one or two data dumps and thus, not cause an underestimation in the temperature during the remainder of the heating period.

As well as examining the differences between the Epstein estimate and the original EISCAT measurement for this individual example, a larger-scale study of this difference for all profiles fitted was made. In Figure 4.5, the difference between the Epstein estimates and the EISCAT measurement, at the interaction height are shown as a function of the original EISCAT measurement, for all 90 of the EISCAT temperature profiles where the Epstein model fitting procedure had been applied to. This temperature difference has been defined in terms of the fractional change measured (EISCAT) and the estimated (Epstein) fractional temperature change:

$$\frac{\Delta T_{e,EISCAT}}{T_e} = \frac{T_{e,av} - T_{off}}{T_{off}} \quad (4.3)$$

$$(Fractional) \text{ difference} = \frac{T_{e,Epstein} - T_{e,av}}{T_{off}} \quad (4.4)$$

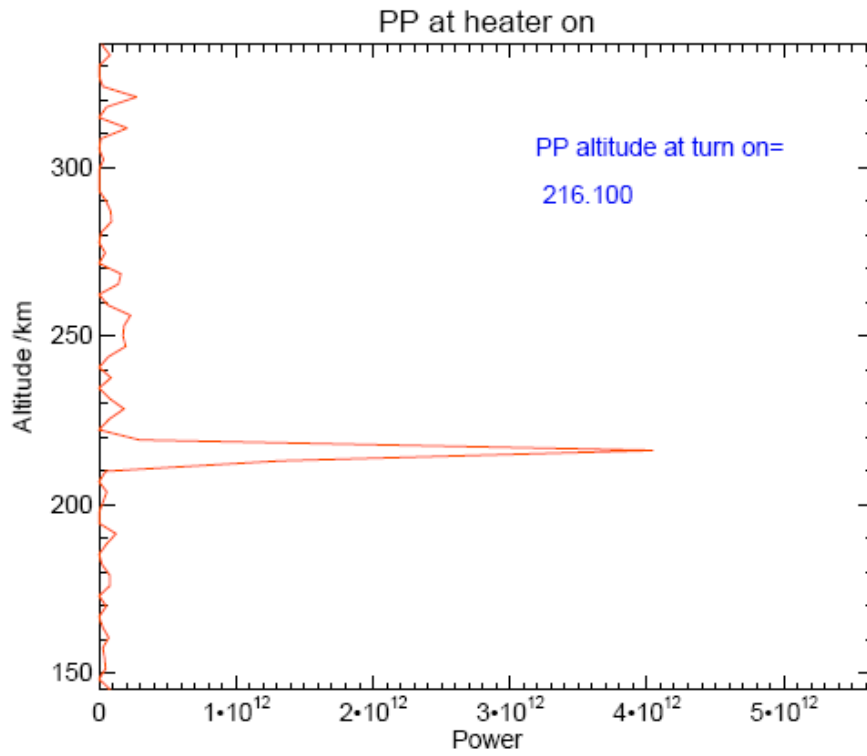


Figure 4.2 EISCAT power profile which indicates an interaction height of 216km with a height resolution of approximately 5km.

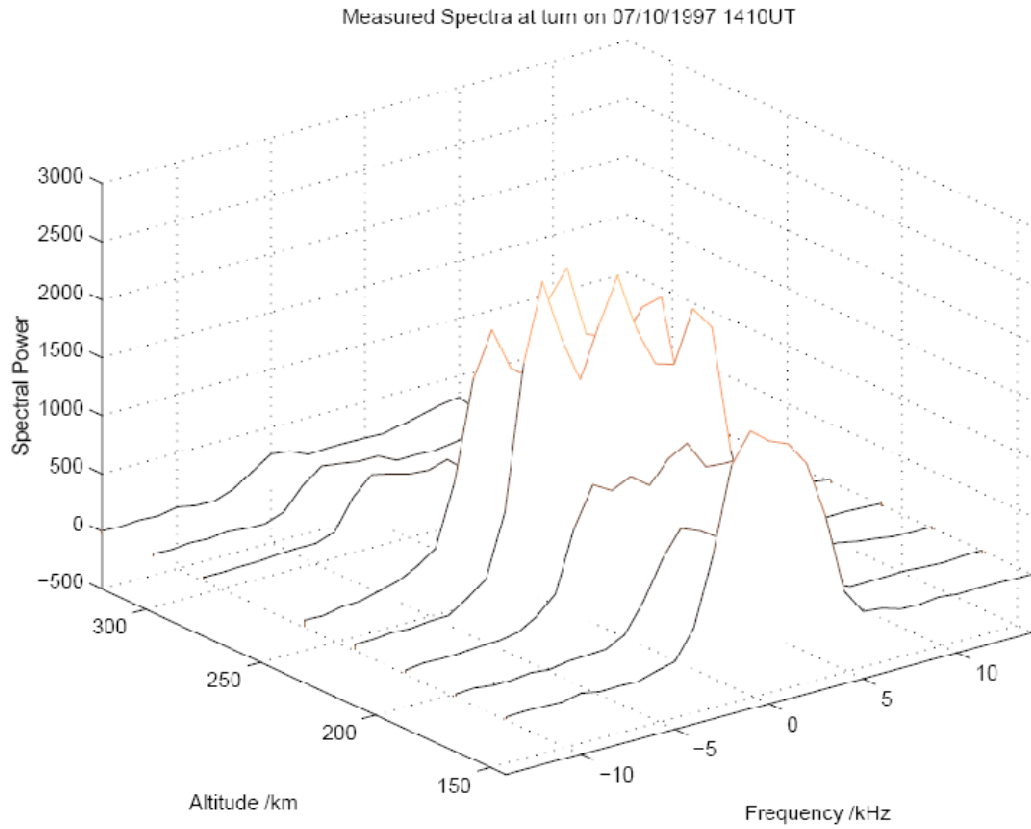


Figure 4.3 Waterfall plot of the overshoot spectra from altitudes of 143km up to 297km at 1410UT on 7/10/1997

There is a strong and negative correlation between the model and measured temperature change estimates, determined by the correlation coefficient of -0.816. The difference in the model estimates is almost always positive, and thus greater than the EISCAT measurements. The general trend appears that as the EISCAT fractional temperature change increases from negative to a larger and positive value, the difference decreases, implying the model estimates converge with the EISCAT measurement as the EISCAT estimates increase. The results suggest that better agreement with the actual EISCAT measurements is obtained when a greater 'heated' temperature exists at the interaction height. This convergence of the model estimates with the EISCAT measurements, occurs when the fractional change is near to unity, or 100% of the unperturbed temperature. A good fit between the averaged temperature change profiles and the Epstein function at these values is most likely obtained because a pronounced peak exists in the profile, which essentially matches the geometry of the Epstein functions. This is especially advantageous as well since it is the averaged temperature change providing information on the thermodynamic response of the plasma high power waves.

From these results, it would appear that the averaged temperature change measured by the EISCAT radars, which are usually inferred from apparently non-distorted spectra, can in the majority of cases be trusted as a true indication of the large-scale temperature changes induced by high power HF waves. However, the method of fitting of Epstein functions suggests a temperature change of appreciable magnitude (of around 100% of the background values) tends to produce the best agreement with the Epstein estimate of the peak temperature change. Nevertheless, this does not imply that the measured temperatures corresponding to smaller observed increases are questionable, but simply that there is a greater discrepancy between the temperatures measured by the radar and what is predicted by the function which is being used to model the temperature profiles.

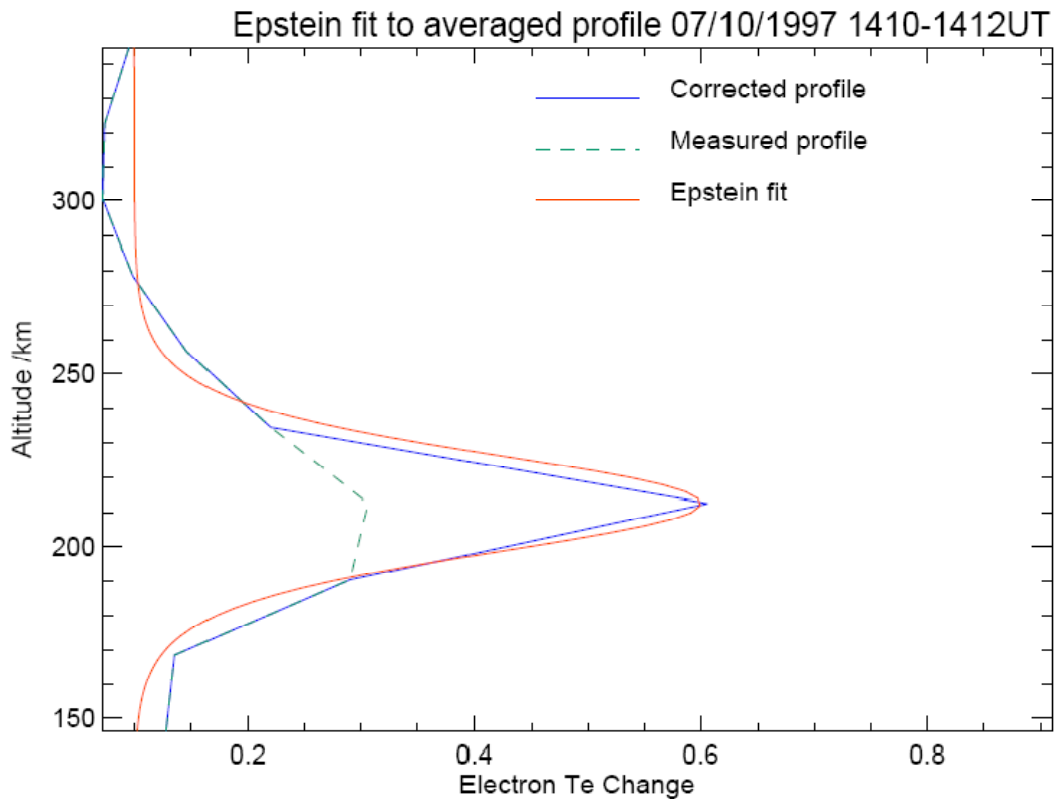


Figure 4.4 Epstein fitted profile for averaged temperature change, averaged 1410:30-1412UT on 7/10/1997. The Epstein function is shown by the red curve, the original temperature profile is the dashed green curve and the corrected temperature profile is illustrated by the blue solid curve. The ‘corrected’ profile is simply the original (measured) profile with the temperature at the interaction height replaced with the Epstein best fit estimate

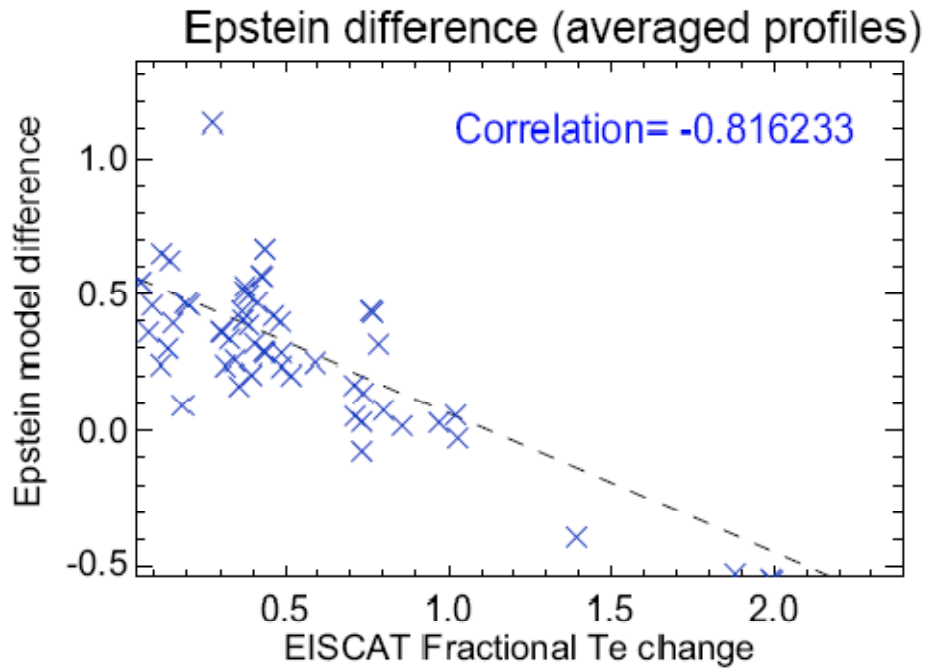


Figure 4.5 Relationship between the measured EISCAT fractional temperature change and the difference in the Epstein model estimate for the averaged temperature change profiles. This is the difference between the fitted Epstein fractional temperature change and the measured temperature change. The correlation of the scatter is given for reference, as is the best fit line shown by the dashed black line

4.4 Theoretical Model of Large Scale Heating

The electron density and temperature response to the action of a strong alternating electric field of an ionospheric heater, based on a system of transport equations and energy balance equations, are described in much detail by Gurevich (1978). By making certain assumptions, the linearized time-dependent electron density (N) and temperature (T_e) perturbations in the field-parallel direction are given by equations (2.28) and (2.29), and the stationary perturbation solution (2.30) is obtained from applying certain boundary conditions. In this section, the stationary solution (2.30) is applied to three EISCAT temperature change profiles corresponding to HF heating experiments, and the results are illustrated in Figure 4.6, 4.7 and 4.8 in the following section. These experiments represent artificial heating where this model solution describes the plasma thermodynamics very well, but in other circumstances, the fit is subject to varying degrees of deterioration.

The scale length of the temperature perturbation, parallel to the geomagnetic field (2.31) is calculated for the heater interaction height. Ionospheric model parameters of the electron-neutral collision frequency ν_{en} , and background electron temperature T_e were obtained from the IRI-2001 model and the electron loss rate R was taken from Table 6.1 of Robinson (1989). The height-integrated heat input, Q was allowed to be a free parameter in fitting the model to the EISCAT profiles until a minimum variance with the measured profiles was produced. This is of course justified because the true heat input that actually reaches the injection height cannot be precisely quantified due to the absorptive nature of the lower ionosphere, which would act to reduce the power that was initially transmitted by the heater. There exist formulas to estimate the wave energy flux at a given distance from the ground (e.g. Robinson, 1989) but these neglect the effects of absorption and refraction. Thus it should be possible to use the ‘best fit’

value of the heat input, Q and compare this with the theoretical flux values at the interaction height to determine just how strongly the heater wave is attenuated before reaching this height.

4.5 Results: Simple Theoretical Model

4.5.1 Example 1: 1308-1312UT, 21st October 1999

In this heating experiment, the EISCAT heater was operating at 4.91MHz, with the beam tilted parallel with the geomagnetic field, and transmitting in cycles of four minutes on followed by four minutes off. Since this was carried out using Array 2, this results in an antenna gain of about 24dB which means the effective radiated power is of the order of 240MW. Figure 4.6 illustrates the EISCAT UHF electron temperature change profile after averaging from 1308:30 until 1312UT, and overlaid on this is the best fit theoretical model profile and Epstein function for the same heating interval. The peak temperature change is reasonably large, and close to 1500K.

There is clearly very good agreement between the measured data, and both the theoretical model and semi-empirical Epstein function. Although there is some evidence of minor underestimation by the two models at heights above the peak, these still fall within the error margins of the EISCAT temperatures. What can also be seen is that the temperature change estimated by both models at the interaction height, which lies at just above 210km, are virtually identical, though this is some 100K greater than the EISCAT measurement.

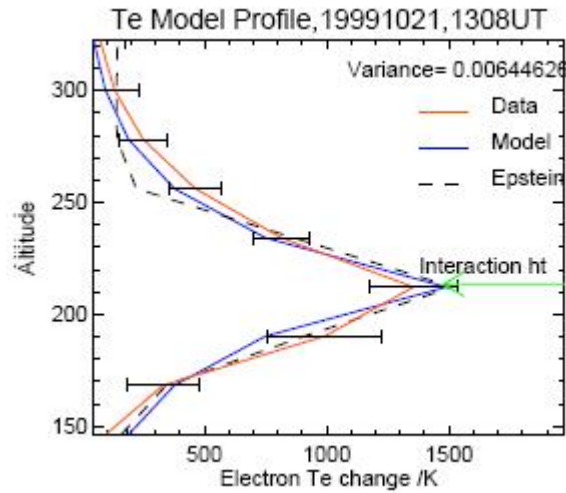


Figure 4.6 The EISCAT averaged electron temperature change profile (red) for heater-on between 1308-1312UT on 21 October 1999, best fitted theoretical model profile (blue) and Epstein function (black dashed curve). Also indicated is the heater interaction height deduced from power profiles, and the averaged error associated with the EISCAT temperatures

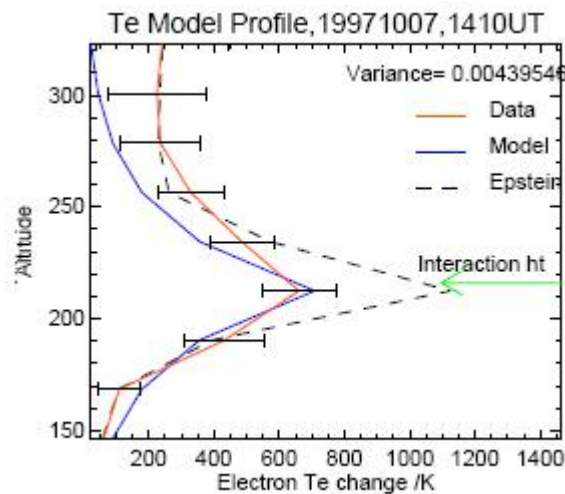


Figure 4.7 The EISCAT averaged electron temperature change profile (red) for heater-on between 1410-1412UT on 7 October 1997, best fitted theoretical model profile (blue) and Epstein function (black dashed curve). Also indicated is the heater interaction height deduced from power profiles, and the averaged error associated with the EISCAT temperatures

4.5.2 Example 2: 1410-1412UT, 7th October 1997

From 1410-1412UT, the heater was operating at a frequency of 4.544MHz on array 2 and again the beam was tilted 12 degrees south, parallel with the geomagnetic field. At this frequency, the antenna gain is approximately 23dB, which results in an ERP of about 190MW. In contrast to the previous example where large change in the electron temperature were measured, in this experiment weaker heating effects were observed as can be deduced from the peak temperature change which is about 650K in Figure 4.7. There is also a more definite underestimation of the temperatures above the peak, by the theoretical model, which appears to worsen at the further ranges, although qualitatively much better agreement with the measured data seems to be achieved beneath and up to the height of the peak temperature change. From an initial glance, an apparently better fit with the data above and below the peak is obtained from fitting the Epstein function, but this seems to have been achieved at the expense of the accuracy of the peak temperature which can be seen to exceed the real data by some 450K which is quite a substantial difference.

Heating of the topside ionosphere is also greater in comparison with Example 1 and the decay in temperature perturbation with altitude is not as rapid despite the interaction height lying at virtually the same level. The Epstein function is therefore favoured by the resulting asymmetry in the heating profile, whereas the theoretical model will undoubtedly produce a symmetrical profile if the length scale L_T , which determines the rate of decay of the temperature, is taken to be a fixed quantity at the interaction height.

4.5.3 Example 3: 1532-1536UT, 19th October 1999

In this final example, the heater was operating at a much higher frequency of 7.1MHz on array 3, with the beam directed along the geomagnetic field. The ERP is not dissimilar to those of the previous two examples and is approximately 240MW. The heater was transmitting at constant power in cycles of four minutes on followed by four minutes off from 1532UT on 19 October 1999. Figure 4.8 shows the expected surge in the level of the interaction height with the high operation frequency at 260km. It is also clear that large increases in the electron temperature of up to 1400K are measured by the EISCAT UHF radar at the height of the peak in heating. Incidentally this lies *below* the actual interaction height of the heater during the overshoot. This might suggest that either a descent in altitude of the interaction height takes place over the course of the heater transmitting due to density changes induced by the artificial modification, or that it is a case of the electron temperatures still being underestimated at the height of the strongest plasma turbulence.

We see from Figure 4.8 that the heated plasma profile is very different in character from those shown in Figure 4.6 and Figure 4.7, with a very broadly peaked region of elevated temperatures which does not decay away rapidly with altitude away from the peak itself. This would seem to imply that thermal transport along the field is less efficient than is predicted by the theoretical model, as there is a clear breakdown of the model profile with the observed data. In this instance the fit of the Epstein function is markedly better than that of the theoretical model. If it were not for the fact that one of the conditions imposed during the Epstein profile fitting was that the peak must be placed at the range gate containing the interaction height, then one might suppose that a profile almost identical to that of the real data could be obtained.

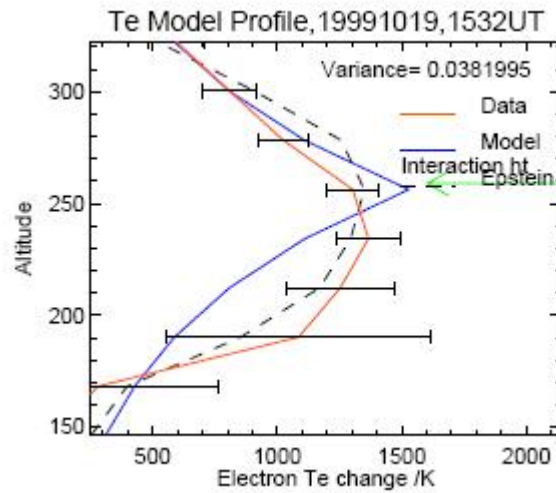


Figure 4.8 The EISCAT averaged electron temperature change profile (red) for heater-on between 1532-1536UT on 19 October 1999, best fitted theoretical model profile (blue) and Epstein function (black dashed curve). Also indicated is the heater interaction height deduced from power profiles, and the averaged error associated with the EISCAT temperatures

This is because it is obvious that the fitted Epstein function follows the geometry of the measured data remarkably well but is shifted up in altitude by a single range gate, due to the altitude uncertainty between the peak temperature change and the interaction height. From a physical perspective the nature of the heating in this example is probably very different to that where the interaction height is lower due to differences in collisional heat loss rates at higher altitude and lower plasma densities which would favour stronger heating. If the heater frequency is also very close to or greater than the F region critical frequency and therefore representative of underdense heating, then the heater wave coupling to electrostatic upper hybrid waves may be weaker which would tend to produce a heat source that is more diffuse as opposed to a narrow in altitude extent. If this is the case then it is not surprising that the theoretical model fails to replicate the real heating profile. In these circumstances the full set of coupled temperature and density equations should be solved numerically, since the assumptions made in obtaining the simplified first order solution given by equation (2.30) does not necessarily hold.

4.6 Ion-Acoustic Spectra: Removal of PGM

In this section, an evaluation of the effect of the PGM on the parameters recovered from incoherent scatter analysis is attempted. To achieve this, a technique to remove the contamination arising from this instability from the incoherent scatter spectrum was developed, so that the analysed parameters could be compared with the PGM effects included and excluded. This section describes the technique that modifies the signal autocorrelation functions (ACFs) measured by the EISCAT radar at the heater wave interaction height in such a way that the PGM feature is removed from the equivalent Fourier Transform spectrum, so that the subsequent analysis of the spectrum using the GUISDAP software produces estimates of the plasma parameters that can be believed with greater certainty to be representative of turbulent plasma at the interaction height.

The ACFs used in this study were obtained from the EISCAT UHF radar when the CP1K experiment was being run, thus producing ACFs at gate separations of 22.5km. The range gate in which the zero lag of the ACF, equivalent to backscattered signal power, reached a maximum value during the ‘overshoot’ was used as a proxy for the heater wave interaction height. The observed overshoot incoherent scatter spectra were recovered from the measured ACF by Fast Fourier Transform. In essence, ‘corrected’ spectra are synthesised by subtracting a Gaussian function from the measured (observed) spectrum, and GUISDAP is allowed to perform its usual multi-parameter fitting to the corrected spectra. That which is associated with the smallest GUISDAP fit residual indicates the Gaussian which PGM to be removed and the plasma parameter estimates from analysis of the ‘best fit’ corrected spectrum are stored. This approach, realised by modifying the standard GUISDAP analysis code, is equivalent to regarding the contaminated spectrum as the superposition of a normal symmetric double-humped incoherent scatter spectrum and a Gaussian function centred at zero frequency, which

occur from different sized scattering volumes. A full description of the technique is given in Appendix 3.

The initial application of the fitting procedure was made to overshoot spectra as these provided very suitable cases on which to apply and test the validity of the technique, since the PGM is most distinguishable here. The importance of obtaining reliable measurements of the temperature changes induced in the initial rise time of the irregularities has also been noted (Mantas et al., 1981) since this provides a wealth of information regarding the energy deposition and anomalous absorption processes.

However, as well as being useful for the analysis of spectra which are clearly contaminated by PGM effects, the technique has equal importance to the average 'heated' spectra measured after the overshoot, in establishing if these plasma temperatures remain underestimated or not. Usually these spectra have been assumed to arise from Maxwellian plasma which should be fitted satisfactorily by conventional analysis technique. Therefore, the fitting technique was applied to average spectra measured during HF heating, allowing an investigation into the possibility that small residual PGM effects, not necessarily be detectable by eye, might continue to contaminate the central region of such spectra after the more obvious PGM contamination has ended.

In the following section, the results produced by the spectrum correction technique are compared with the parameters recovered from standard GUISDAP analysis, in particular the differences in the derived electron temperature. The difference in electron temperature between the standard and modified analyses is investigated as a function of the ratio between the amplitude of the PGM and the amplitude of the (symmetric) ion-acoustic lines. This kind of empirical parameterisation is convenient, since the PGM

contamination in measured spectra can vary greatly due to different instability growth rates or the distance between the interaction height and the range gate centres of the EISCAT data.

4.7 Results: Ion-acoustic spectrum corrections

4.7.1 Example 1: 1358-1400UT, 7th October 1997

During the HF heating experiment from 1358 to 1400UT on 7 October 1997, the EISCAT heater was transmitting at full power at 4.544MHz in O-mode polarisation on Array 2, pointed in a field-aligned direction. The heater was ‘off’ from 1400 to 1402UT. The EISCAT ion-acoustic spectrum is at its most enhanced in the range gate centred on 209km. There is a significant PGM at the centre of the spectrum whose amplitude is greater than the ion lines, but the three spectral lines are still distinguishable from each other. Figure 4.9(a) to Figure 4.9(d) shows a sequence of plots that illustrate the process by which the overshoot spectrum is corrected using the technique outlined previously. In this example, the modified analysis technique was successful in fitting a Gaussian function to the PGM, and removing it from the overshoot spectrum.

This resulted in a difference of 800K between the electron temperatures derived from the standard GUISDAP estimate (1171K) and the corrected spectrum estimate (1971K). It should be emphasised that the estimate of the electron temperature after the initial overshoot has disappeared is the focus of this chapter, in order to study the bulk changes in electron temperature. Hence, the fitting procedure was applied to the averaged ‘heated’ spectra measured during the heating, which excluded the overshoot spectrum, since this was obviously strongly contaminated by PGM effects.

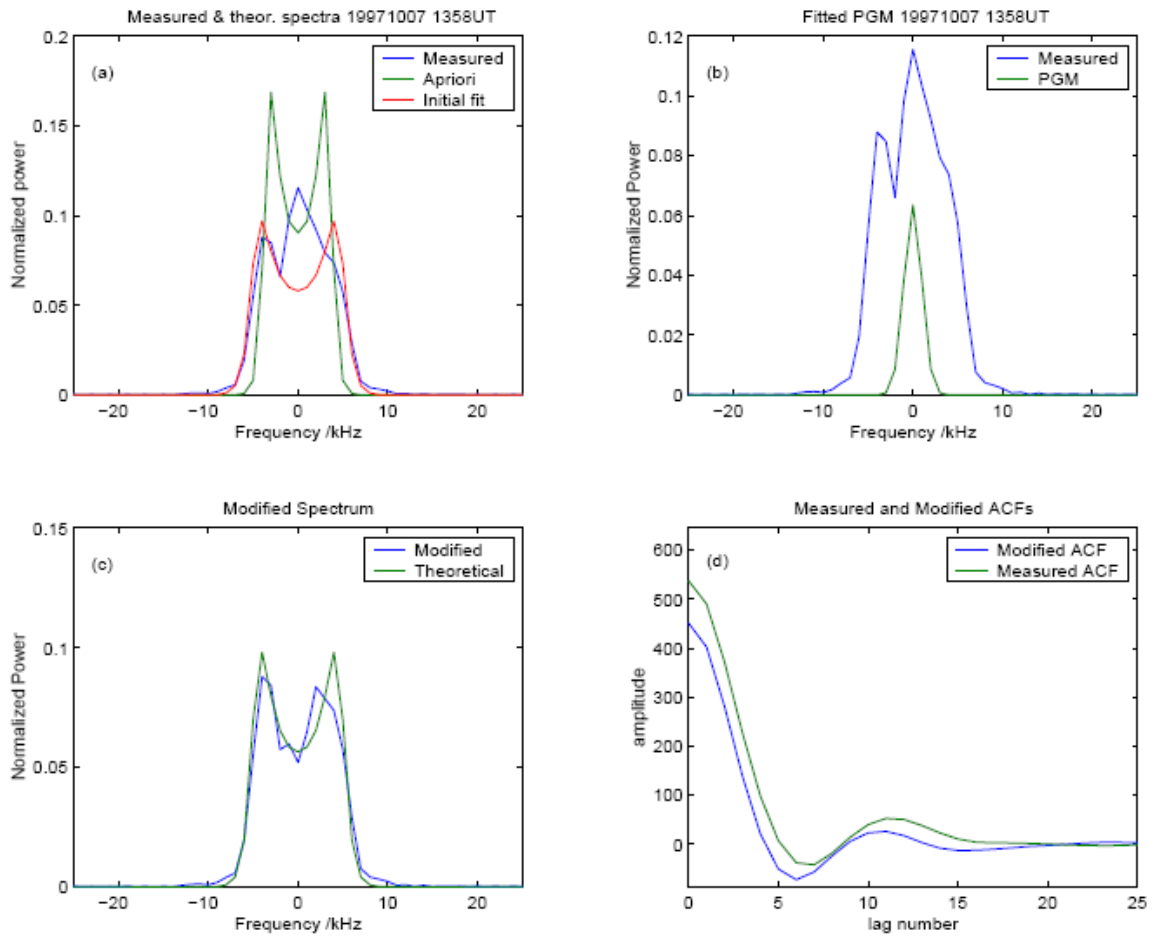


Figure 4.9 (a) The measured overshoot ion-acoustic spectrum at 209km for heating beginning at 1358UT on 7th October 1997 (blue), the apriori theoretical spectrum (green) and the initial fitted theoretical spectrum (red) obtained by varying the electron and ion temperature inputs and minimizing the variance with the measured spectrum, excluding data points within the PGM.

Figure 4.9 (b) The measured spectrum (blue) and best-fitted Gaussian peak producing the minimum variance between a theoretical spectrum and a ‘corrected’ spectrum.

Figure 4.9 (c) The fitted theoretical spectrum (green) and the corrected spectrum (blue).

Figure 4.9 (d) The measured ACF (green) and the ACF that results from the inverse Fourier Transform of the best-fit corrected spectrum (blue)

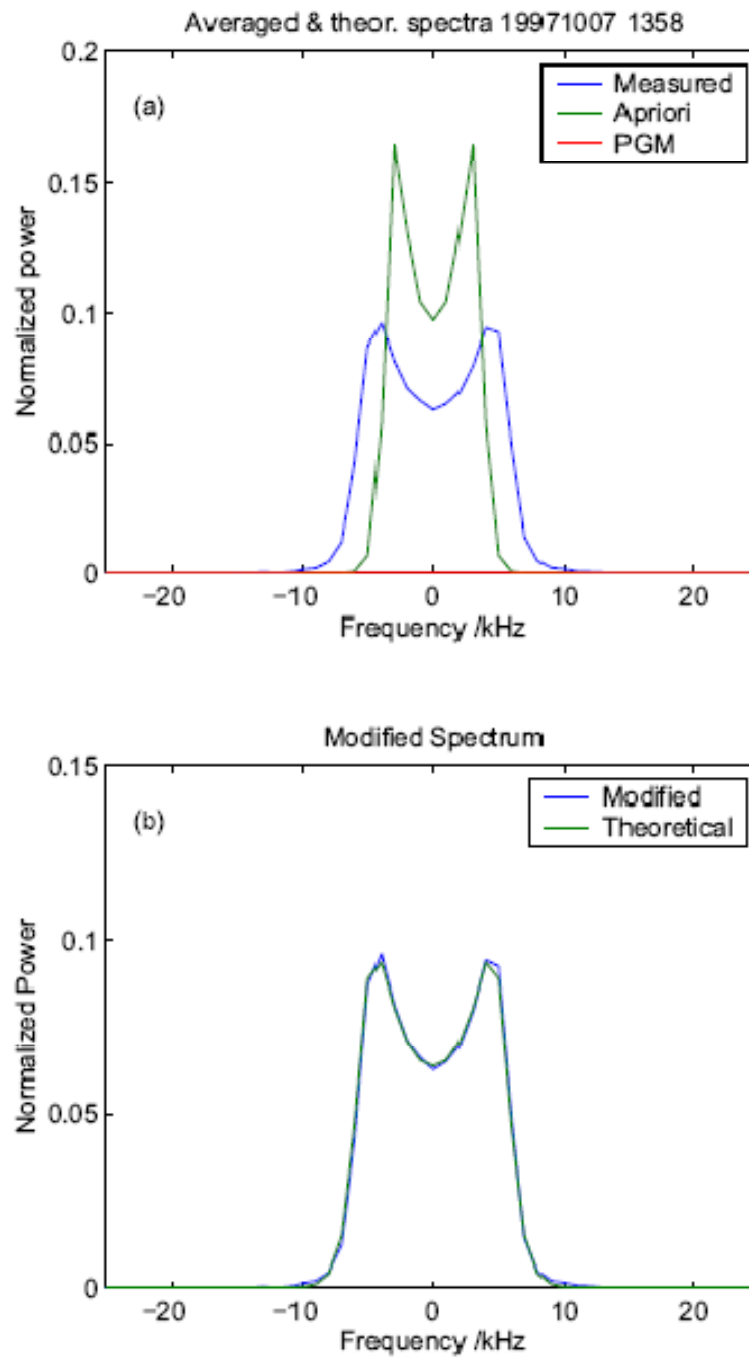


Figure 4.10 (a) The averaged EISCAT ion acoustic spectrum and apriori theoretical spectrum for the heating from 1358-1400UT on 7th October 1997 and (b) best fit theoretical spectrum indicates that no subtraction of a Gaussian peak from the averaged spectrum is required to improve the variance.

In the case of the analysis of the averaged spectrum for the heating from 1358-1400UT on 07/10/1997, no correction was required as shown by the good fit between the best fit theoretical spectrum and the averaged spectrum in Figure 4.10(a) and (b). This implies that the straightforward application of GUISDAP would have given a correct temperature estimate.

4.7.2 Example 2: 1255-1256UT, 7th October 1997

In this example the heater modulation corresponded to the 'LE2' special mode and full details are given in Wright et al. (2006). This comprised pumping at full power for 20 seconds at 1255:00-1255:20UT. The GUISDAP analysis of the data during this period is shown in Figure 4.1, and it is clear that this short interval is associated with an apparent reduction in electron temperature at the range gate centred on 209km, which is where the heater interaction altitude was located within as derived from the raw backscatter power profile measurements. However the apparent reduction is in fact spread over several range gates in altitude between approximately 170km and 230km during the first 5s of heating. Figure 4.11 shows these PGM effects can also be seen in the spectra from these adjacent range gates.

Figure 4.12 displays the same sequence of plots as shown in Figure 4.9, for the overshoot spectrum at 1255UT which is obtained from the most severely contaminated range gate at 209km. Clearly, from the measured spectrum shown in blue on panels (a) and (b), the amplitude of the PGM feature substantially exceeds the amplitude of the ion lines; however the correction routines nonetheless succeeded in removing the central peak. The corresponding ACF of the corrected spectrum is noticeably lower in amplitude when compared with the originally measured ACF (panel (d)), since the subtraction of the PGM contamination led to a considerable reduction in spectral power.

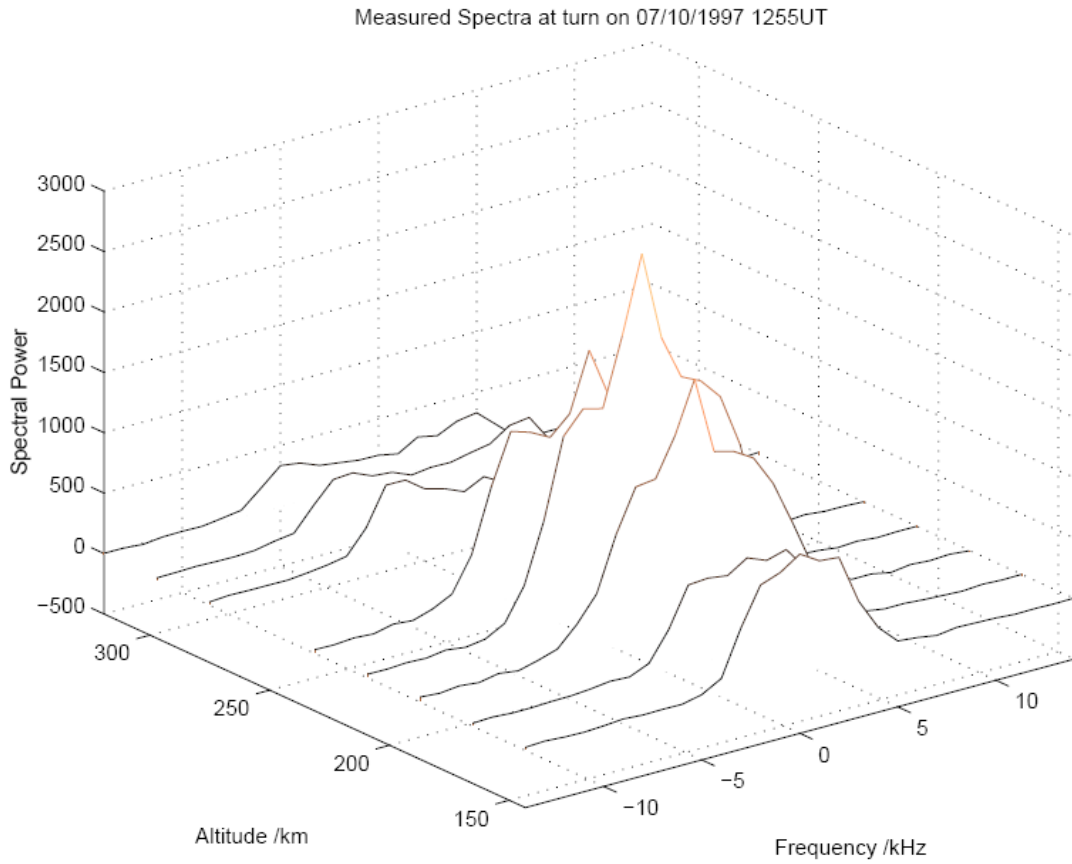


Figure 4.11 Measured EISCAT radar spectra during the initial overshoot for the heating at 1255UT on 7th October 1997

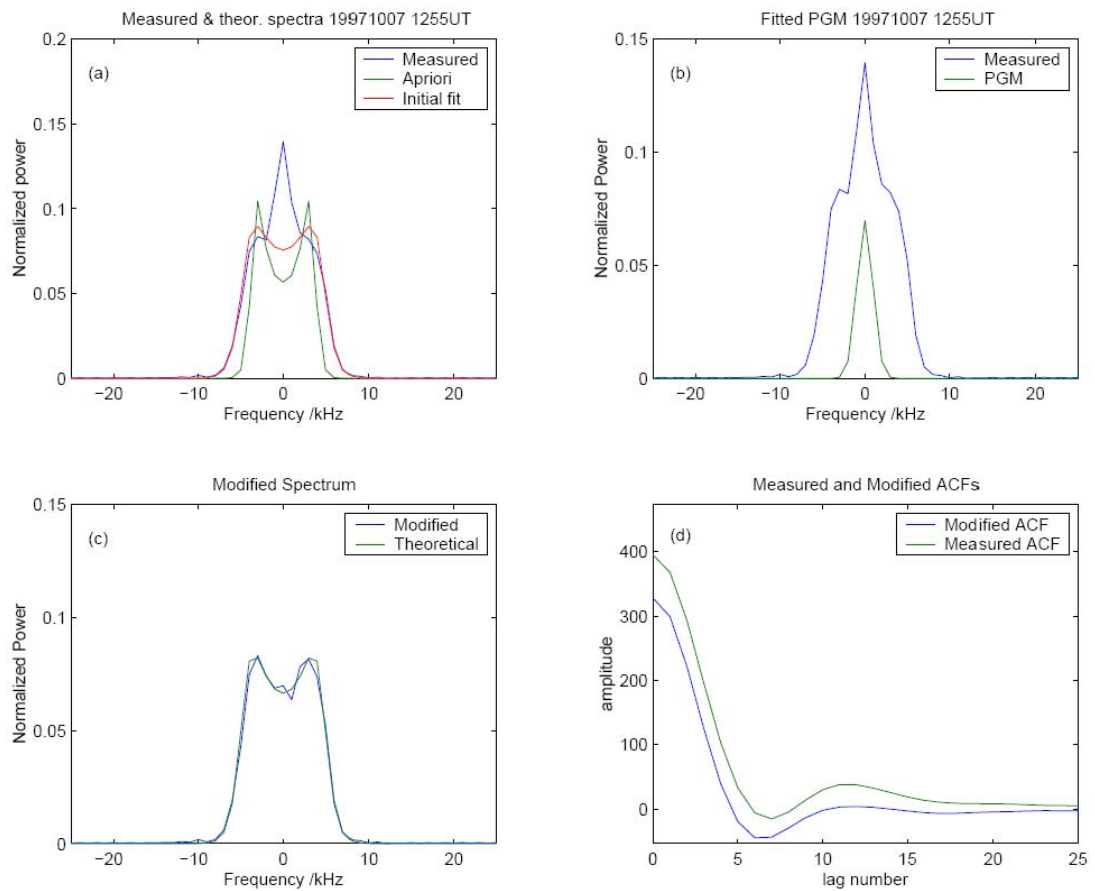


Figure 4.12. Fitting results for the spectrum at 209km, at 1255UT on 7th October 1997.

(a) The measured ion-acoustic spectrum (blue), the apriori theoretical spectrum (green) and initial fitted theoretical spectrum (red).

(b) The measured spectrum (blue) and best-fitted Gaussian peak.

(c) The fitted theoretical spectrum (green) and the corrected spectrum (blue).

(d) The measured ACF (green) and the ACF that results from the Fourier Transform of the best-fit corrected spectrum

The conventional GUISDAP analysis electron temperature from the uncorrected overshoot spectrum at this altitude was 638K, whereas the subsequent analysis estimate based on the ‘corrected’ spectrum was 1652K indicating a difference of over 1000K. It will be noted from Figure 4.1 that temperatures of this order are much more consistent with the majority of the data obtained from this altitude following the overshoot, during the remainder of the heating interval in question.

4.8 Application to a wider study of artificial heating spectra

4.8.1 Overshoot spectra

Based on the results obtained in the examples presented in Section 4.5, a statistical study into the effectiveness of the spectral correction technique was carried out. For this purpose, the set of 90 overshoot spectra corresponding to the data that were used in Section 4.3, which were contaminated by a PGM were re-analysed using the spectrum correction software to obtain the difference between the electron temperature arising from the modified analysis and the original temperature estimate, obtained by using GUISDAP on the uncorrected spectra.

In Figure 4.13 the difference in electron temperature between the two types of analyses is plotted as a function of the ratio of PGM-to-ion acoustic line amplitude. This ratio was taken as the amplitude at zero frequency divided by the mean ion line amplitudes. Figure 4.13 shows a convincing trend relating the difference in temperature estimates to the ratio of the PGM-to-ion line amplitude. In most cases this parameter is positive, implying that the presence of a PGM almost invariably tends to cause an underestimation in the fitted electron temperature by the conventional GUISDAP analysis. The strong correlation and positive gradient of the linear function fitted to the

data points also suggests that the difference is proportional to the PGM amplitude ratio, and the temperature differences from the two types of analysis can be in excess of 1500K when the PGM is particularly strong.

The best linear fit to the data in Figure 4.13 implies that as the PGM amplitude ratio tends to zero, the difference between the two temperature estimates is close to -550K. This suggests that the spectrum correction technique would actually lead to a new temperature estimate which is substantially lower than the 'uncorrected' spectrum measurement. This is, of course an inappropriate conclusion; but without additional results from the correction of small PGM effects, it cannot be determined whether the linear relationship really applies over all PGM amplitudes, or if it begins to break down as the contamination becomes less detectable.

The fit residuals arising from the modified analysis method were also examined, since it is essentially a measure of how well the theoretical spectrum, defined by the final set of analysis parameters fits to the measured spectrum. It is the ratio of the measured error to the error expected for a purely Maxwellian incoherent scatter spectrum. If the removal of the PGM feature really leads to a better fit between the modified spectra and the synthesised theoretical spectra, the fit residual should exhibit consistently smaller values when the spectral correction method is applied to remove the PGM feature. A spectrum which is well described by a theoretical Maxwellian would produce fit residuals with values close to unity.

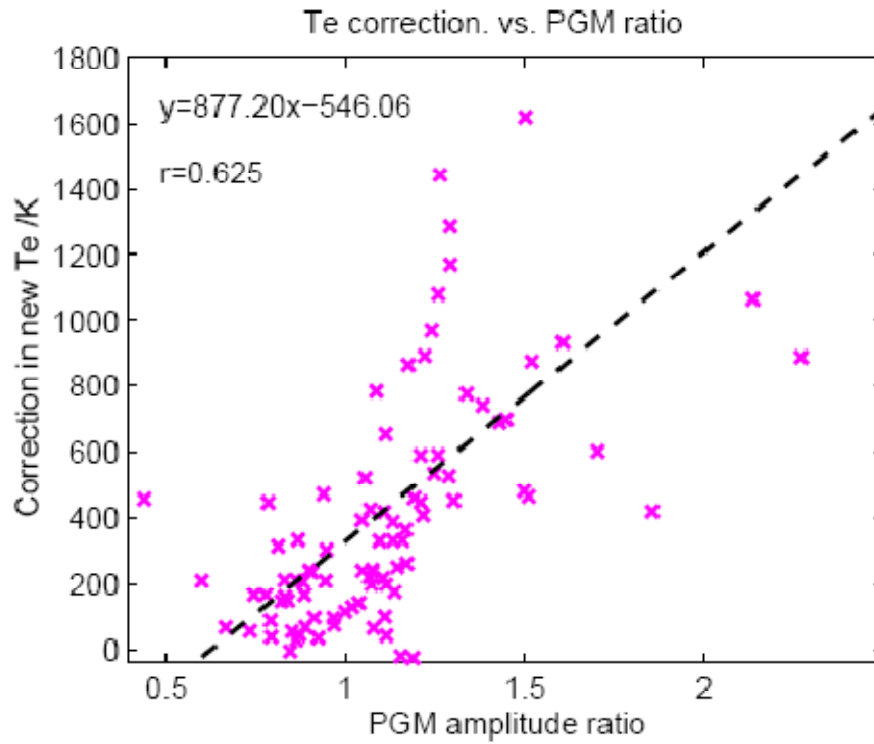


Figure 4.13. Dependence of the difference between electron temperature estimates inferred from the measured and corrected spectra, on the PGM amplitude ratio for all overshoot spectra that were subjected to the modified analyses procedure which was outlined in Section 4.6.

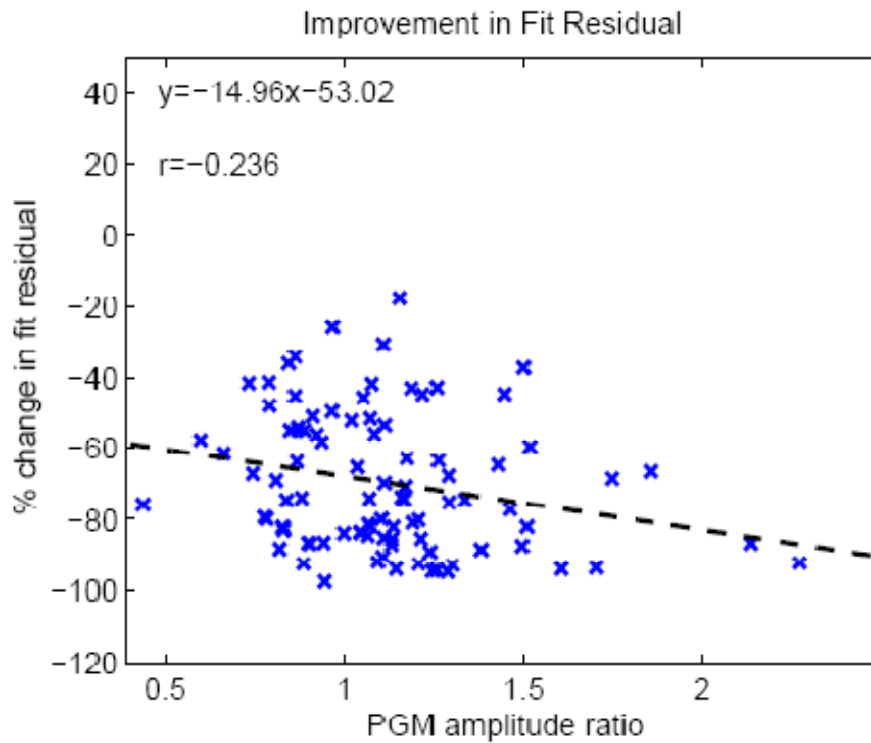


Figure 4.14. The percentage change in the GUISDAP fit residual as a function of the PGM amplitude ratio, obtained from the removal of a Gaussian purely growing mode from the spectrum. The percentage change is calculated as the difference in the fit residual before and after the subtraction of the Gaussian from the spectrum, normalized to the (original) value before the subtraction.

Figure 4.14 shows the percentage change in the fit residual as a function of the amplitude ratio of the PGM to the ion lines and confirms that this is indeed the case. In all instances where the PGM removal has been applied, the change in the fit residual is negative, meaning that the fit residual magnitude has been reduced, as expected from the method by which the PGM was fitted. The reduction may be near to 100% of the standard analysis result, implying a very significant improvement in the fit quality. It is notable that there is no strong trend relating the reduction in the fit residual to the size of the PGM relative to the ion lines as implied by the low correlation coefficient of around -0.236, although Figure 4.14 does suggest that the greatest reductions in the fit residual occur when the largest PGM features are removed.

Figure 4.15 shows the distribution of these changes in fit residual as a histogram, and indicates a high proportion, at around 80% of the total number corrected spectra, where the fit residual is reduced by greater than 50%. These results imply that a significant improvement in the spectrum fit can be made by removing the PGM feature from the overshoot spectra.

This effectiveness of the method cannot be determined from examination of the absolute values of the residuals alone, as indicated by the distribution of the absolute values of the fit residual after the spectrum correction, shown in Figure 4.16. This shows that the corrected spectrum fit residual may still be well in excess of 10, even though they are lower than those of the uncorrected spectrum and the majority of the values lie between 0 and 5. This result may suggest that the overshoot spectrum may still be contaminated by other ‘non-Maxwellian’ effects such as asymmetry in the ion lines, or enhancement of one or both of the lines due to Langmuir turbulence that the technique would not be capable of correcting. Hence the ‘corrected’ spectrum resulting

from this technique may not represent a pure incoherent scatter spectrum, which would be identified by a fit residual close to unity.

4.8.2. Application to a wider study of averaged spectra

The spectra obtained after the overshoot has subsided are expected to reflect the bulk changes in electron temperature caused by the heating, whose determination is important to understand thermal conduction effects in the modified ionosphere. To investigate whether the modified fitting procedure could improve the estimation of plasma temperatures during these intervals, the fitting procedure was applied to the averaged heated spectra for a larger sample of heating intervals. Here, one example is shown when the spectral fitting method was applied to an averaged spectrum obtained during a heating interval from 1506-1509UT on 25th April 1996. The results which were yielded from the analysis are shown in Figure 4.17 and 4.18. As outlined in Section 4.4, the fitting procedure was carried out in such a way that if the variance between the measured spectrum and the best-fit theoretical spectrum at the interaction height was lowest when no Gaussian peak was subtracted, this was taken as an indication that no correction to the spectrum was required.

However for this interval, Figure 4.17 illustrates the averaged spectrum and the initial fit using the GUISDAP apriori parameters with the Gaussian peak which was found to produce the best fit corrected spectrum. In Figure 4.18 the spectrum is shown after removal of a suitable PGM with the best fit theoretical spectrum. It may be seen in Figure 4.18 the subtraction of a very small Gaussian-type PGM is still required to obtain a lower variance with a theoretical spectrum than would have been achieved between the measured spectrum and the apriori theoretical spectrum.

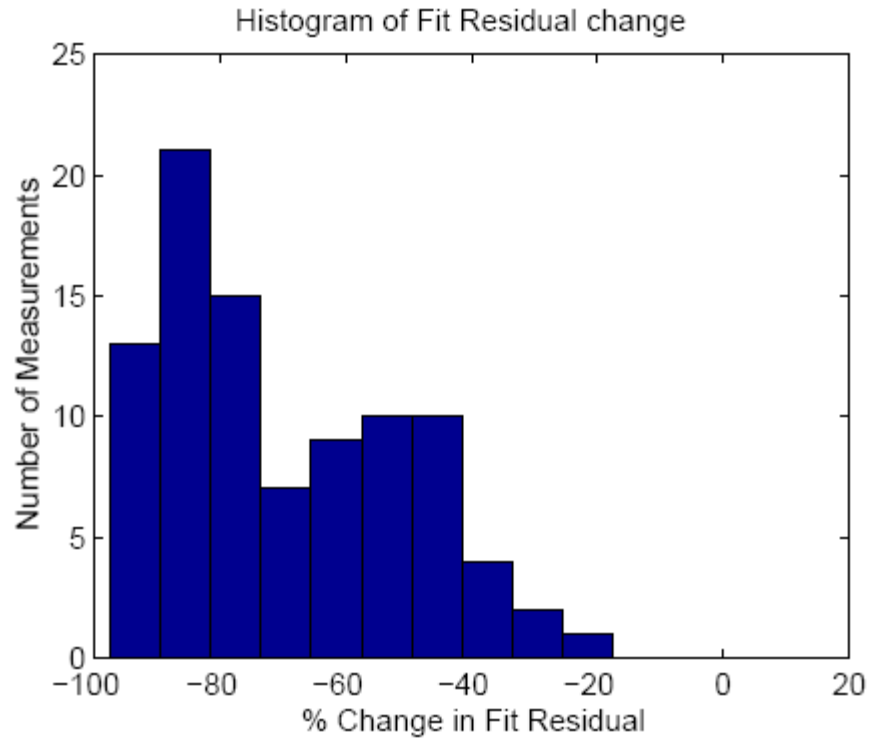


Figure 4.15 Distribution of the percentage change in the GUISDAP fit residual after the subtraction of a fitted Gaussian from all the overshoot spectra subjected to the spectrum correction analysis.

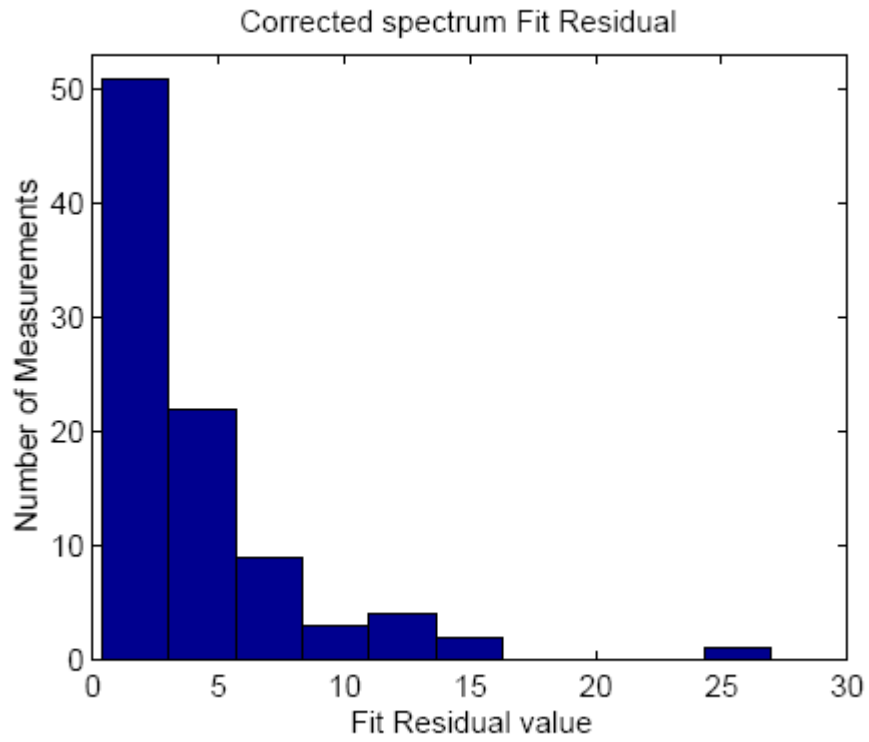


Figure 4.16 Distribution of the absolute values in the corrected spectrum fit residual.

In a statistical study analogous to that reported in Section 4.5, averaged spectra from approximately 50 heating intervals were analysed in this way, omitting the first 30 seconds of the heating interval in each case. The results are displayed in Figure 4.19. The x-axis now shows the ratio between the amplitude of the spectrum at zero frequency and the amplitude of the ion lines. Higher values of this ratio should generally correspond to larger electron temperatures, or at least higher ratios of electron to ion temperature. The y-axis of Figure 4.19 shows the difference between the electron temperatures obtained from the analysis of the corrected spectra (if required) and those obtained from a standard GUISDAP analysis of the uncorrected spectra.

There is a striking dissimilarity between Figure 4.19 and Figure 4.13, where the initial overshoot period is compared with the averaged spectra. It is clear that the electron temperature difference in most cases is zero, implying that the removal of a PGM from the averaged spectra was either unnecessary or had no significant effect. It thus appears that the standard GUISDAP analysis of these averaged spectra would have given a true estimate of the bulk electron temperature change. Nonetheless, a few cases were found where a correction of the spectrum was possible, and some of these had the effect of increasing the electron temperature by up to 90K.

The statistical trend indicated in Figure 4.13 could prove useful in predicting the likely underestimation in cases where the PGM is clearly distinguishable in the averaged ion acoustic spectrum. For example during pumping around an electron gyrofrequency when both the ion line enhancement and sometimes the PGM has been known to persist throughout the heating interval, only modest temperature enhancements could be expected to result from the standard analysis instead of the usual much larger enhancement that evolves through the TPI.

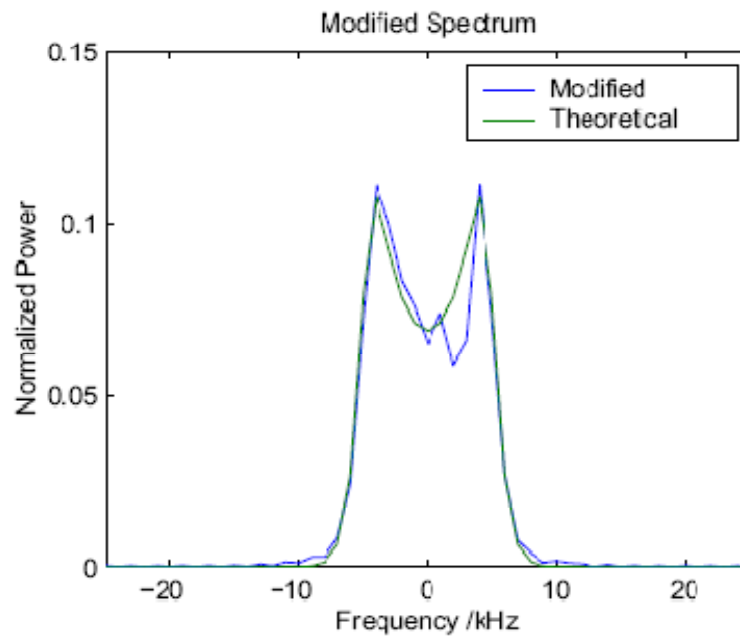
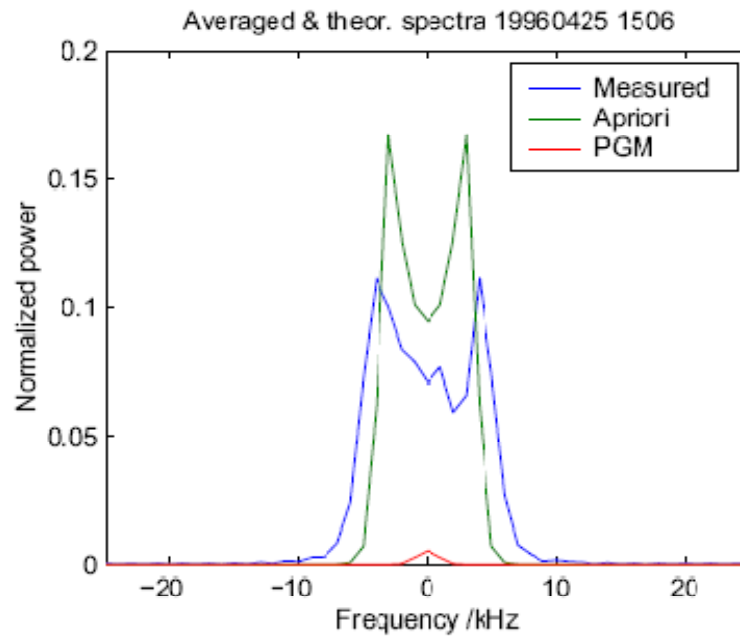


Figure 4.17 (top) Measured spectrum (blue), initial fitted theoretical spectrum and best fit Gaussian peak (green curves)

Figure 4.18 (bottom) The corrected averaged spectrum for 1506UT, 25th April 1996 (averaged 1506:30UT-1509:00UT) after removal of the Gaussian peak at an altitude of 209km

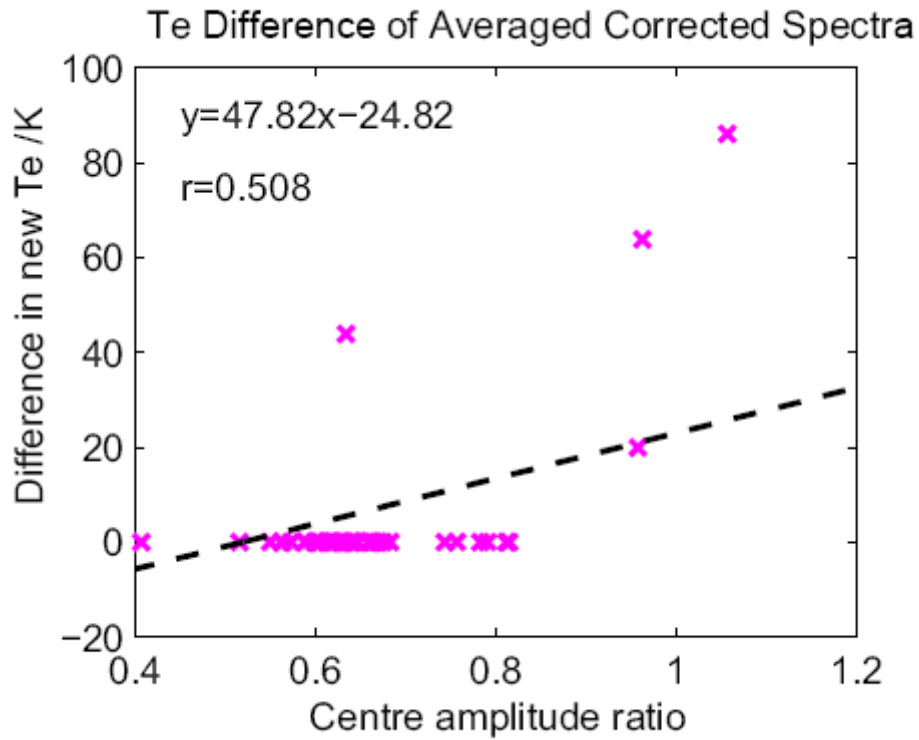


Figure 4.19 Relationship between the amplitude ratio at the centre of *averaged* spectra and error in corrected ACF analysed electron temperature estimates, after the initial overshoot period, for approximately 50 averaged spectra corrected and analysed using the modified analysis routines

In fact the electron temperatures inferred from the standard analysis for an experiment where the heater was pumping close to or at the third gyroharmonic (4.05MHz) between 1222-1240UT on 23rd April 1997 are shown in Figure 4.20 and an apparent decrease occurs during the heating interval in the same manner as the example shown in Figure 4.1.

Simultaneous enhancements in the ion temperature (second panel) and minor increases in the electron density (top panel) take place with these electron temperature reductions, whilst the ion velocity does not exhibit any changes correlated with the heating interval over the altitude range of interest. The averaged spectrum for the heating interval 1238-1240UT was subjected to the method of removing the PGM feature since there is evidence of filling in of the spectrum at its centre (Figure 4.21) and there does indeed to be a successful removal of this in the right hand panel. Clearly from the results presented in this study there is a substantial influence of the power in the PGM on the standard analysis plasma parameters, particularly the electron temperature. In exceptional cases it has been shown that this feature is not always quenched by the TPI and thus the steady state or averaged electron temperatures after tens of seconds of heating cannot be always taken as a reliable estimate using the standard GUISDAP analysis.

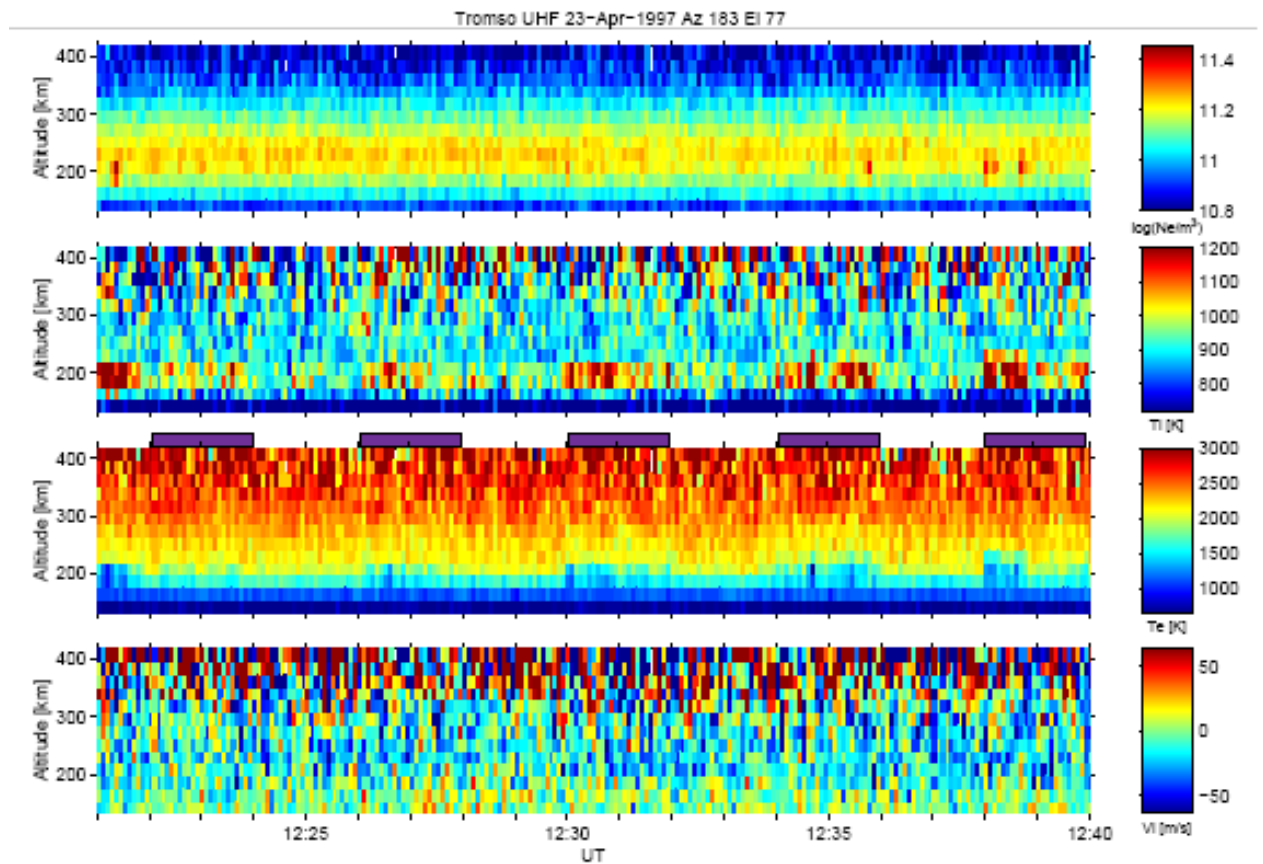


Figure 4.20 Plasma parameters inferred from GUISDAP analysis of EISCAT UHF radar data during the heating experiment at the 3rd electron gyroharmonic, 4.05MHz, from 1222-1240UT on 23rd April 1997. From top to bottom, the panels indicate the electron density, ion temperature, electron temperature and ion velocity. For reference, the purple bars above the electron temperature plot indicate the transmission intervals of the heater. There are clear, apparent decreases in the electron temperatures at times during the heating intervals which occur in the height range from 190-210km

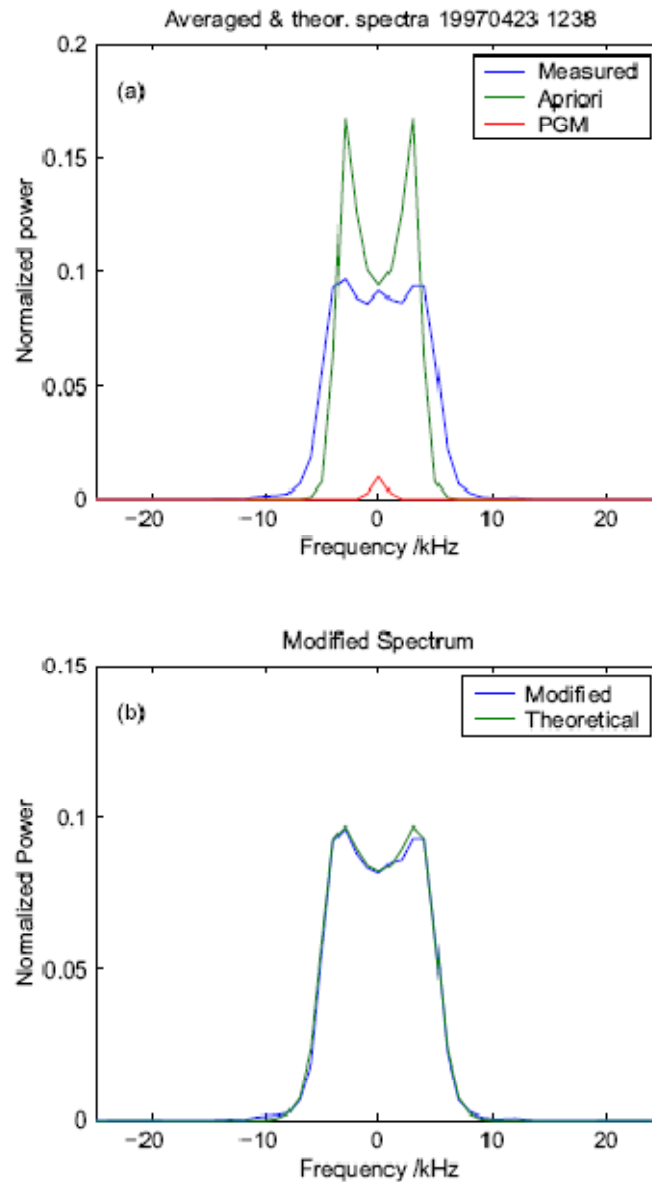


Figure 4.21 (a) The averaged ion-acoustic spectrum at 187km during heating around the third electron gyroharmonic, 1238-1240UT on 23rd April 1997, and panel (b), after a Gaussian peak (shown in green at the centre of the left panel) has been subtracted to obtain a minimum variance with a theoretical spectrum

4.9 Summary

There is strong evidence to support the belief that plasma turbulence excited by the action of high power HF waves can cause large departures of the incoherent scatter spectrum from the Maxwellian case which usually exhibits a double-humped configuration. Specifically the presence of a central peak, otherwise recognised as the purely growing mode (PGM), has been shown to often cause an underestimation in the inferred electron temperatures that are obtained using the EISCAT GUISDAP analysis software. The magnitude of this underestimation has been found to be strongly proportional to the relative amplitudes of the PGM and ion-acoustic lines. There is a large degree of variability in these amplitudes which are most likely caused by prevailing ionospheric conditions and the heater transmission parameters. However, this chapter has addressed the uncertainty regarding whether the PGM continues to contaminate the incoherent scatter spectra after the overshoot and two approaches have been presented in this chapter in order to answer this question.

The Epstein function was shown to be, in some cases, a highly appropriate model for the averaged large-scale temperature change induced by high power radio waves and this proved to be a useful tool in estimating the expected temperature change at the interaction height. However, appreciable discrepancies between the measured and modelled temperature changes at the heater interaction height were found when the measured EISCAT temperature change was marginal. In the second technique where the bulk electron temperatures were investigated, it was found that the average 'heated' incoherent scatter spectrum was well described by a theoretical Maxwellian spectrum, and that the electron temperatures inferred from the standard GUSIDAP analysis of such spectra were indeed reliable.

It should also be noted that the applications of this study are by no means confined to incoherent scatter spectra measured by at the EISCAT Tromsø facilities. For example the SPEAR heating facility on Svalbard has a more dynamic ionosphere to contend with, and as a result, the EISCAT Svalbard radar (ESR) often receives ion-acoustic spectra that contain the central PGM peak which remains present throughout the duration of the heating interval, even at pump frequencies well away from a gyroharmonic. It may well be for this reason why only mild increases, if any are usually observed in the analysed ESR electron temperature data. In addition to this, it should be pointed out that important information regarding the characteristics of heated-induced turbulence such as the amplitude and lifetime of the OTSI could be retrieved from the fitted Gaussians that represent the PGM and a separate investigation dedicated to these details is anticipated.

The principle of correcting spectral distortions by fitting and subtracting Gaussian functions from incoherent scatter spectra may well be appropriate in cases where strong asymmetries or enhancements exist in the ion-acoustic lines, for example due to Langmuir turbulence. It is hoped that this could form the basis for extending the application of this study.

It has also been shown that occasionally the nature of the artificial heating of the plasma does not satisfy the stationary solution to the theoretical model of the electron temperature response to a high power heater wave, and in these cases the full set of coupled equations should be solved in order to reproduce the heater-induced changes in the plasma characteristics. However, while the simple model holds in the majority of heating experiments studied, the solution provides a useful and straightforward tool for checking the physical validity of the alternative temperature estimation techniques

presented in the current work. This study could be extended by applying the full theoretical models using the coupled density and temperature perturbation equations to the data. These theoretical predictions should then be compared with the two approaches presented in this chapter for further validation as to how reliable and justifiable the results in the current investigation really are.

Chapter 5

Characterisation of field-aligned irregularity relaxation and evidence for the existence of isolated striations

5.1 Introduction

The simplest model of FAI relaxation predicts decay rates governed by only cross-field diffusion processes evaluated at the large-scale heated plasma temperatures (eq. 2.39). By studying the temporal evolution of the artificially-generated CUTLASS backscatter power, the theoretical model of irregularity decay can be tested against experimental observations. Kolesnikova et al. (2002) showed how this method may be applied to artificial HF backscatter data, but this was limited to a single heating experiment at low power. The objective of this chapter is to study a variety of heating conditions and irregularity behaviour associated with such conditions. This is significant because the temporal and spatial characteristics of FAI are determined by the degree of anomalous absorption undergone by the heater wave, which is dependent on the state of the ionosphere as well as the heater beam properties and modulation. In Section 5.2 a brief description of how the simple model has been applied to CUTLASS HF radar backscatter data is given. The result of its application and validity for a large number of backscatter profiles is also presented. Where it is necessary to overcome the limitations of the simple model in the cases when it fails, two alternative models of irregularity relaxation are considered and described in further detail in Section 5.3. The results of their application to CUTLASS backscatter are presented in Section 5.4.

5.2 Simple Model of FAI Decay

Density perturbations are set up in the plasma during heating experiments as a result of enhanced electron mobility along the geomagnetic field. The CUTLASS radars are sensitive to the square of these perturbations, so the backscatter signal amplitude falls at a rate dictated by the characteristic decay rates of the small-scale density irregularities.

Figure 5.1 shows a typical range-time-intensity (RTI) plot of the CUTLASS Finland backscatter power measurements in Beam 5, for a heating interval at Tromsø between 1600-1642UT on 25th April 1996. The heater was operated in a three minutes on, three minutes off modulation. Strong backscatter power is produced by the presence of FAI from around range gates 25 to 35 and it is evident that the backscatter power is lower at both the nearest and furthest ranges from the centre of the heated volume. This would be expected since the strength of the heater electric field is also range-dependent and would hence give rise to growth rates that also vary with range. Using equation (2.38), a procedure was developed to fit this function to the CUTLASS backscatter power. Since the CUTLASS powers are usually given in decibel (dB) units, the scale is thus already logarithmic, so a linear function is to be fitted to backscatter power expressed in dB. Thus, by least-squares fitting a function, B,

$$B(t)(dB) = 10\log_{10} \left(\frac{P(t)}{P_0} \right)^2 = -(\gamma_0 \log_{10} e)t \quad \therefore B(t) = -\gamma' t \quad (5.1)$$

to the measured data in dB where γ' was a free parameter, the value of γ_0 could be estimated from the gradient implied by the fitted value of γ' . In equation (5.1), $P(t)$ is the linear backscatter power as a function of time and P_0 is the initial linear power, at the instant the heater has been turned off. The backscattered power, P is proportional to the square of the density perturbation amplitude, n (eq. 2.41) so the rate of decay of the

density perturbation is in fact half the rate of decay of the backscattered power. Fits were made to data points in the heater-off interval which had a magnitude above 3dB to exclude noise-like scatter. An example of one such fit is illustrated in Figure 5.2 where the heater was on between 1506-1509UT. The backscatter profile is taken from the ‘off’ period between 1509-1512UT. Data points are shown by the blue crosses and the fitted decay function is represented by the red curve which yielded an irregularity decay rate of 0.069s^{-1} or a characteristic e-folding time of 14.4 seconds. Previous studies into irregularity relaxation times have reported time scale of around a few seconds to several tens of seconds and longer (eg. Hysell et al., 1996 and Robinson, 1989), hence the characteristic relaxation time found in this example is in agreement with current literature.

The electron temperatures strongly influence the nature and rate of irregularity decay. Therefore it is of interest to test whether the plasma temperatures associated with the modelled decay rates can be reconciled with those measured by the EISCAT UHF radar, in order to determine if the observed CUTLASS backscatter relaxation characteristics comply with the simple exponential decay model of FAI. The temperatures associated with the observed decay rates were obtained by straightforward substitution of equations (2.37) and (2.40) into (2.39) and rearranging the expression to obtain the following:

$$T_{e0} = \left(\frac{m_e \Omega_e^2 \gamma}{10.44 \times 10^{-11} N_n k_B k^2} \right)^{6/11} \quad (5.2a)$$

Here, the units of the neutral particle density N_n is cm^{-3} . The transmission frequencies of the CUTLASS radars are known parameters, and hence from the simple Bragg scatter relation (3.19) the irregularity wave number may be approximated. The Finland radar

transmission frequency was 15MHz, corresponding to an irregularity wave number of 0.63m^{-1} . Typical values of the neutral particle density, N_n were taken as $3 \times 10^9\text{cm}^{-3}$ using the MSIS-90 model parameters at 210km, and the electron cyclotron frequency of $(2\pi)1.35\text{MHz}$. The fitted decay rate of 0.069s^{-1} was then substituted into (5.2), implying a temperature of approximately 3187K. The equivalent EISCAT temperature, when averaged at the interaction height during the heating period was 1788K, some 1400K below the temperature inferred from the relaxation characteristics of the simple decay model. The model overestimation of around 80% is somewhat appreciable but not unacceptable, given that sources of uncertainty lie in parameters such as the neutral density which dictates the electron collision frequency, and the fact that the effects of ions (and hence ambipolar diffusion) have been excluded.

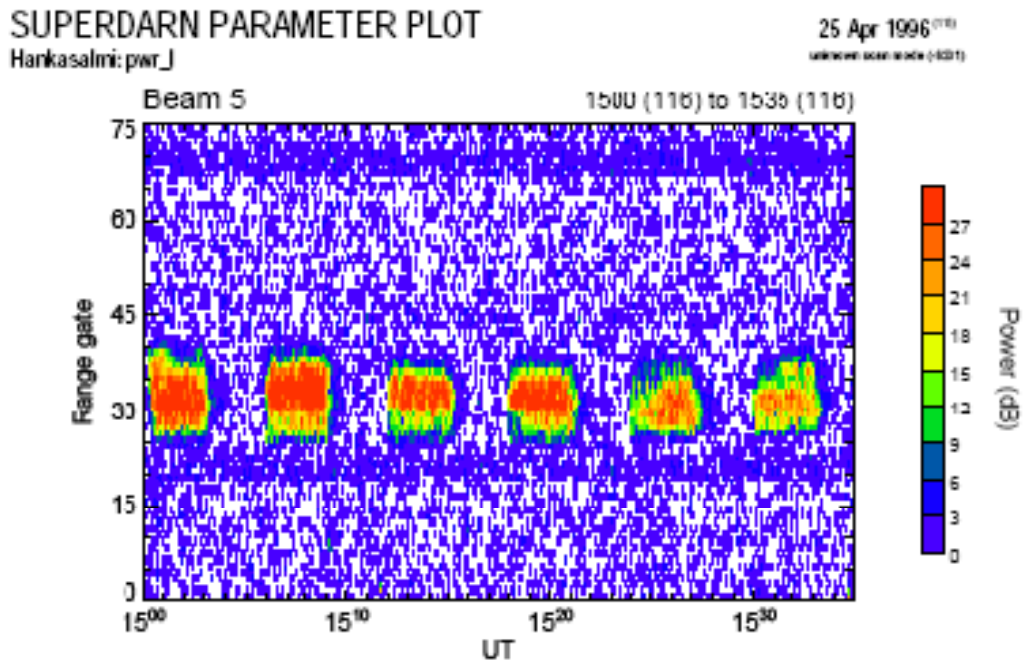


Figure 5.1 A range-time-intensity (RTI) plot of the backscatter power received in Beam 5 of the CUTLASS Hankasalmi radar during heating experiments carried out from 1500-1535UT on 25 April 1996. The power scale is expressed in dB.

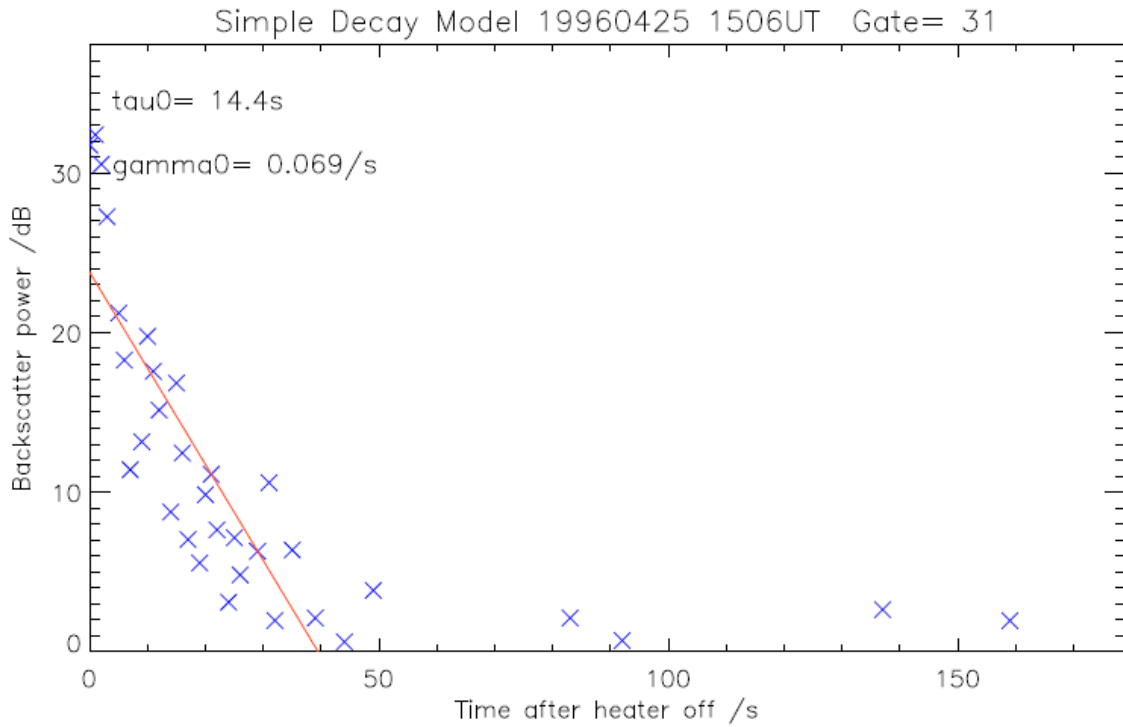


Figure 5.2 The CUTLASS Hankasalmi backscatter power profile from 1509-1512UT at range gate 31 when the heater was off (heater on from 1506-1509UT), shown with the fitted model decay curve (red) and data points which were included (blue) in computing the variance of the model from the data. The values τ_0 and γ_0 are respectively the fitted decay time and decay rate in the number density

It is also not known to what extent the electron-ion collisions influence the overall rate but this result would thus seem to suggest that the decay rate estimated from fitting the model to the data is somewhat reflective of the large-scale background plasma temperature measured by the EISCAT radar just before the heater has been turned off. In light of the relative consistency between this temperature and the EISCAT measurements, it is plausible to determine how recurrent this agreement is. Does it bear any relation to the strength of heating effect which is implied by the measured temperature changes observed in the EISCAT data? An investigation into the relationship between the measured temperature changes made by the EISCAT radars and the temperatures associated with the observed CUTLASS backscatter relaxation rates was carried out, utilising a much larger sample of fitted rates.

In order to carry this out, approximately 200 backscatter decay profiles were selected from the CUTLASS data archive between 1996 to 2006. The simple decay model, outlined earlier was implemented to obtain an estimate of the decay rate for each profile. Backscatter decay profiles corresponded to the range gate which was approximately at the centre of the artificial backscatter. The times at which the heating experiments were performed ranged from 1000UT until 1900UT and at pump frequencies between 3.9MHz and 7.1MHz.

Figure 5.3 illustrates the result of this larger-scale study and shows the CUTLASS simple decay temperature estimates plotted against the corresponding EISCAT ‘heated’ temperatures, averaged over the heating period at the height where the temperature change was strongest. This figure shows that a significant number of CUTLASS decay rate estimates can be much greater than those measured by the EISCAT radar for relatively modest EISCAT temperatures between 1000K and 2000K, as indicated by

those data points lying to the left of the temperature equality line. However there are also a population of data points where the CUTLASS estimates are substantially lower than the EISCAT measurements, when the EISCAT ‘heated’ temperature is much higher, in excess of 3000K. These are also widely scattered about the regression line, which has a very low correlation coefficient with a magnitude of approximately 0.067. Hence, there is no one-to-one correlation between the two estimates. The error, Δ , in the estimate of the temperatures T_γ derived from the fitted CUTLASS decay rates is defined as the difference from the EISCAT estimate, T_{EISCAT} :

$$\Delta = T_\gamma - T_{EISCAT} \quad (5.2b)$$

Figure 5.4 shows the dependence of the error, Δ on the measured EISCAT temperature change (at the height where the change was greatest). It is clear that larger differences of the model from the EISCAT value are associated with greater temperature changes and hence, stronger heating effects. This is plausible if the fitted relaxation rates of FAI are in fact, influenced to a greater extent by the cool ‘background’ temperatures, attained after the heater has been ‘off’ for several tens of seconds, and not the rate that is defined by the initial heated plasma temperature at the instant the heater is turned off.

A second explanation is that in cases of strong heating, the fall in the heated plasma temperature after the heater is turned off is great enough to introduce nonlinear effects, such that the simple model of exponential decay with time is invalid. The strong temperature dependence of the decay rate means that a rapid fall in temperature would modify the decay rate and no single rate of decay can be assigned to the data. One might expect then that at the instant that the heater is turned off, the hot plasma temperatures are associated with a fast decay rate which subsequently decelerates as the plasma cools, so the decay rate will be time-dependent.

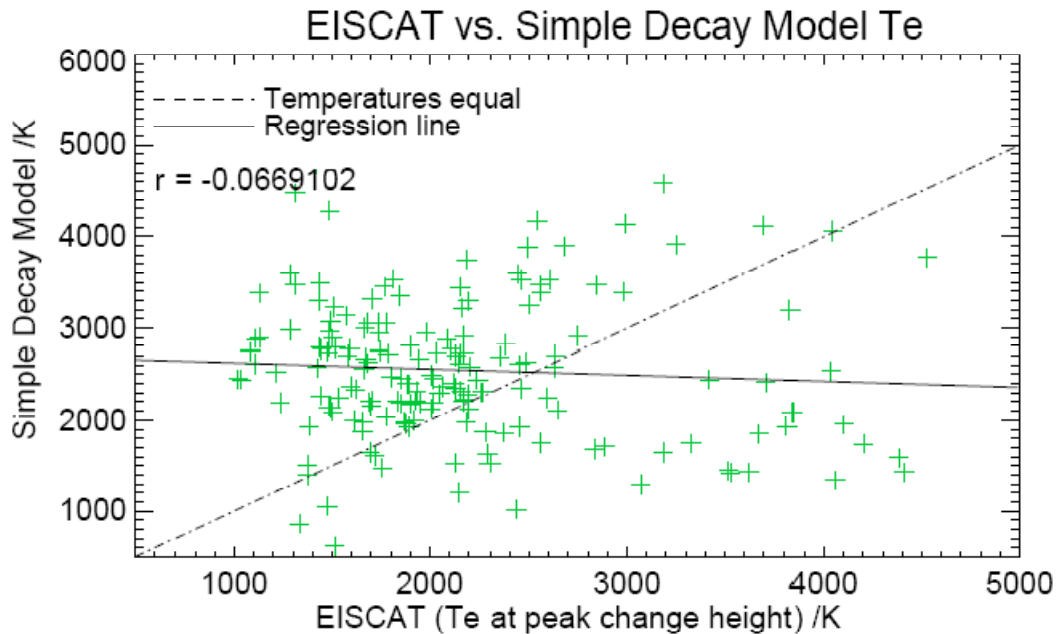


Figure 5.3 Electron temperatures inferred from using the irregularity decay times, derived by least-squares fitting the simple decay model to the data, and shown as a function of the averaged or ‘heated’ electron temperature measured by the EISCAT radar at the height of the peak temperature change. The solid black line shows the best fit line from linear regression, and the dashed black line indicates where the two temperatures would be equal. This shows that the observed scatter about the line may be up to 1000K, which is much greater than the typical error in the EISCAT electron temperatures (of the order of a few hundred Kelvin). Hence, the scatter cannot be solely attributed to uncertainty in the experimental measurements.

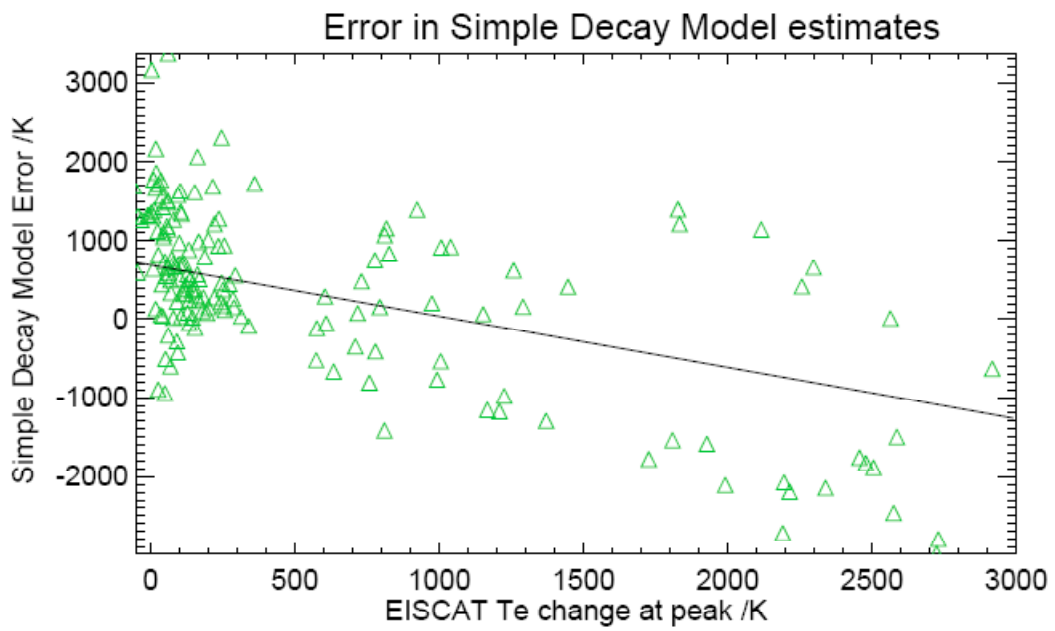


Figure 5.4 The error in the inferred electron temperatures (defined as the difference between the decay model temperatures and the EISCAT heated temperature at the peak) shown as a function of the average measured *temperature change*

In fact, a number of backscatter profiles from a heating campaign in April 1996 were identified to exhibit a two-stage relaxation process, which may provide evidence of this temperature effect where the decay occurs both at the initial ‘heated’ temperature and then slows down after the plasma has cooled. It might also be suspected that in these situations the fitted decay rate may only be a mean value of the fast and slower relaxation rates and Figure 5.5, which shows one such example does seem to suggest this may be the case.

During this particular heating experiment the heater was transmitting O-mode waves at a frequency of 3.9MHz on Array 2 from 1618-1621UT on 25th April 1996. The heater beam was tilted in a direction parallel with the magnetic field, and only 6 of the 12 transmitters were used, with 90kW supplied to each transmitter. The antenna gain at this frequency is around 22dB, which would correspond to an ERP of approximately 90MW. In the application of the simple decay model, all data points above the noise level (3dB) were included in the variance, which produced a time constant for the decay in number density of 103.2 seconds, or 51.6s for the decay time constant in the backscatter power. This is extremely long in comparison to those quoted in literature, which are typically only a few tens of seconds.

On inspection of the fitted model curve (red) in Figure 5.5 it can be seen that the fit is quite likely biased towards the behaviour of the data in the latter 120s of the heater ‘off’ period, rather than the initial decrease exhibited between 0 and 40s after the heater has been turned off. For this reason, the model was subsequently fitted again by constraining data points which were to be included in the variance to only those within the first 60s of the heater-off as well as those above 3dB (Figure 5.6). This resulted in a fitted decay time in the number density of 29.1s, or about 14.6s for the decay time in the

backscattered power, which is less than half the original value and hence implies there were a significant number of data points in the latter half of the interval which were influencing the fitted curve.

These latter data points could well have caused a possible underestimation of the characteristic decay rate and corresponding overestimation in the decay time constant. This slower decay component of smaller amplitude appears to manifest itself at around 30-40s after the heater has been turned off. Two-step decay of artificial HF backscatter has been observed in earlier experiments (e.g. Minkoff and Kreppel, 1976, Hedberg et al., 1983, Hysell et al., 1996). Recently, Blagoveshchenskaya et al. (2007) reported on 'fast' relaxation times of the order 10-20s followed by a second, extremely slow stage of decay on timescales greater than 5 minutes. The observations were attributed to the presence of natural irregularities or the conversion of energy through artificially-induced turbulence which would sustain the irregularities for long times. Though convincing explanations for the physical mechanism producing two-stage decay was provided, the authors did not validate the claims with supporting data analysis.

These special situations provide the motivation to modify the simple model of FAI relaxation to account for possible time-dependent temperature effects, or indeed wave coupling between larger and smaller scales in cases where a significant failure of the simple model occurs. In the next section, a description of two revised decay models are given; the first is based on a falling electron temperature which produces a time-dependent decay rate. In the second model, wave-wave coupling between smaller and larger scale wave forms the basis for a two-stage decay process, and the equations governing the fall in density perturbation due to this mechanism are provided.

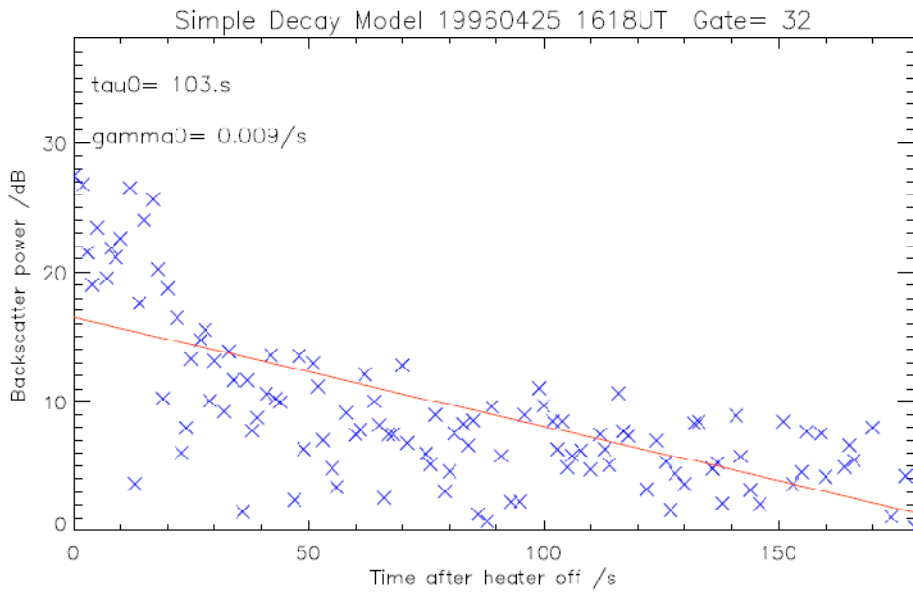


Figure 5.5 The CUTLASS Hankasalmi backscatter power profile from 1621-1624UT at range gate 30 when the heater was off, shown with the fitted model decay curve (red) and data points (blue). This is the fit for all data points above the 3dB noise threshold included in the variance calculation

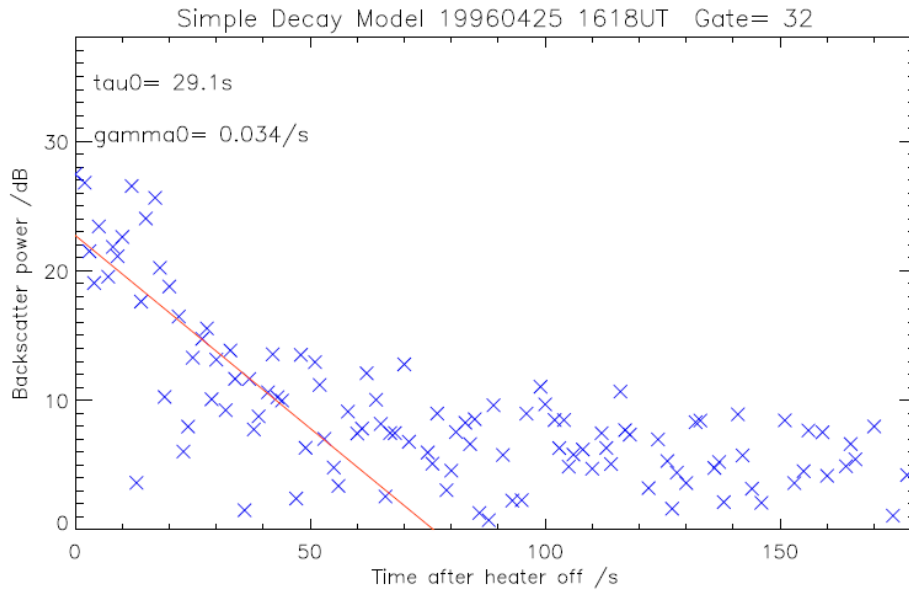


Figure 5.6 The same data set as Figure 5.5 but the fitted model function is computed using only data points above the noise level (3dB) and in the first 60s of the interval since it was suspected that the data in the latter half of the ‘off’ did not contribute to the initial decay, represented by the simple decay model

5.3 Alternative Models of FAI Relaxation

5.3.1. Time-Dependent Temperature Decay Model

As discussed in the preceding section, the simple model of irregularity may fail in circumstances where the plasma is heated significantly above background levels and undergoes rapid cooling after the heater has been turned off. The outstanding question is whether cases exhibiting two-stage relaxation can be explained by the collapse of the plasma temperature in cases of strong heating, or whether the apparent two-stage nature is explained by the decay of a spectrum of irregularities at different scale sizes, as previously suggested (Hysell et al., 1996, Borisov et al. 2005). In the cases where strong heating effects are measured by the EISCAT radar, the assumption of a constant temperature controlling the rate of decay can no longer be assumed. For large-scale changes in the plasma where spatial temperature gradients are insignificant, effects such as thermal conduction may be omitted. This leads to an energy balance equation in the absence of a heat source given by,

$$\frac{dT_e}{dt} = -\delta \nu_e (T_e - T_0) \quad (5.3)$$

Where $\delta = \delta_{el} + \delta_r + \delta_v + \delta_{op} + \delta_i$

Here, δ is the fraction of energy lost by each electron in collisions. This may represent several sources of energy loss, including elastic (δ_{el}) and inelastic collisions involving the excitation of rotational (δ_r), vibrational (δ_v), optical (δ_{op}) and ionization (δ_i) levels. Hence, the parameter δ can become a rather complex function of all these contributory factors. The initial temperature $T_e(t = 0)$, neutral density N_n and δ were allowed to be free parameters, varied to obtain the temperature solution which produced the best fit in calculating the decay rate. The background temperature T_0 was obtained by averaging

the EISCAT temperatures at the interaction height in a heater-off interval prior to a heater ‘on’. In order to solve (5.3) numerically and obtain an approximate solution for $T_e(t)$, a fourth-order Runge-Kutta algorithm was implemented. This is an iterative method, and for a problem defined by the time-derivative $T_e' = f(T_e, t)$ and initial condition $T_e(0) = T_{e0}$, the Runge-Kutta set of equations can be defined by equations 5.4 to 5.9.

$$T_{e,n+1} = T_{e,n} + \frac{1}{6}h(k_1 + 2k_2 + 2k_3 + k_4) \quad (5.4)$$

$$t_{n+1} = t_n + h \quad (5.5)$$

$$k_1 = f(T_{e,n}, t_n) \quad (5.6)$$

$$k_2 = f(T_{e,n} + \frac{1}{2}hk_1, t_n + \frac{1}{2}h) \quad (5.7)$$

$$k_3 = f(T_{e,n} + \frac{1}{2}hk_2, t_n + \frac{1}{2}h) \quad (5.8)$$

$$k_4 = f(T_{e,n} + hk_3, t_n + h) \quad (5.9)$$

where h is the time step, and $k_{1,2,3,4}$ are slopes in the function at the beginning, mid-points and end of the time interval h . The solution for T_e , evaluated at each time step from the numerical integration was substituted into equations 2.37 and 2.40 to derive a time-dependent thermal conduction coefficient and collision frequency and hence the decay rate as a function of time (2.39). By applying this temperature modification to the decay model, it is possible to test if the apparent two-stage nature exhibited in certain cases of CUTLASS backscatter data can be attributed to a substantial fall in the electron temperature, or if previous suggestions of Hysell et al. (1996) relating to the different scale sizes of irregularities is more appropriate.

5.3.2 ‘Wave-Wave’ Model of FAI Decay

Building on the ideas of previous authors that a two-stage decay may be explained by energy conversion over a range of spatial scales of artificially-induced turbulence (e.g. Blagoveshchenskaya et al., 2007), a second alternative model of FAI decay was developed and implemented, based on wave-wave coupling. This describes the decay of a primary wave of time-varying amplitude $n(t)$ and associated with an initial number density n_0 (time $t = 0$) at some rate γ_1 , which is coupled to a secondary wave of different wavelength and therefore scale size with amplitude $m(t)$ and initial number density m_0 , which itself decays at its own rate γ_2 . Given the presence of this secondary source $m(t)$, The set of coupled equations governing this proposed decay mechanism can be given by (Robinson, private communication)

$$\frac{dn}{dt} = -\gamma_1 n + \alpha m(t) \quad (5.10)$$

$$\frac{dm}{dt} = -\gamma_2 m(t) \quad (5.11)$$

$$m = m_0 e^{-\gamma_2 t} \quad (5.12)$$

Here, α is simply a coefficient that represents the additional number density supplied by the decaying secondary source $m(t)$. Thus, by substituting solution (5.12) into equation (5.10) then after some manipulation and simplifications, the equation to be solved may be expressed as

$$\frac{dne^{\gamma_1 t}}{dt} = \alpha m_0 e^{(\gamma_1 - \gamma_2)t} \quad (5.13)$$

The analytic solution can be obtained through integration methods and the resulting expression describes the time-dependent amplitude of the primary wave in the presence of a larger-scale secondary wave source after the heater has been turned off:

$$n(t) = (n_0 - \sigma_0)e^{-\gamma_1 t} + \sigma_0 e^{-\gamma_2 t} \quad (5.14)$$

$$\sigma_0 = \frac{\alpha m_0}{\gamma_1 - \gamma_2} \quad (5.15)$$

The decay rates of both waves, γ_1 and γ_2 and the initial primary and secondary wave amplitude n_0 and σ_0 were allowed to be free parameters such that a unique curve $n(t)$ for the heater-off period was generated for each set of guess values. The model curve whose variance was minimized with the measured data provided the best estimates of the trial parameters. This indicated how strong the secondary wave component was, relative to the primary wave, and also the equivalent plasma temperature (eq. 5.2a) associated with the estimates of the primary decay rates due to their dependence on T_e .

The functions describing the revised decay of FAI using the time-dependent temperature model and the ‘wave-wave’ decay model were computed and fitted to approximately 30 CUTLASS Finland radar backscatter profiles at range gates across the artificial backscatter region for heater-off periods in a number of heating intervals during a 1996 campaign where a two-stage decay was identified. In the temperature-dependent model, varying the neutral particle density and value of δ was a viable procedure, given that the height from which maximum backscatter originated is somewhat ambiguous and covers an interval of several kilometres to several tens of kilometres, over which both these parameters may vary greatly.

5.4 Alternative Decay Model Fit Results

In this section, four examples of backscatter profiles to which the new models were fitted are presented, shown in Figure 5.7 to 5.10. These periods correspond to (heater-on) heater-offs starting at (1539) 1542UT on 22nd April 1996, (1534) 1537UT on 24th April 1996, (1606) 1609UT and (1618) 1621UT on 25th April 1996.

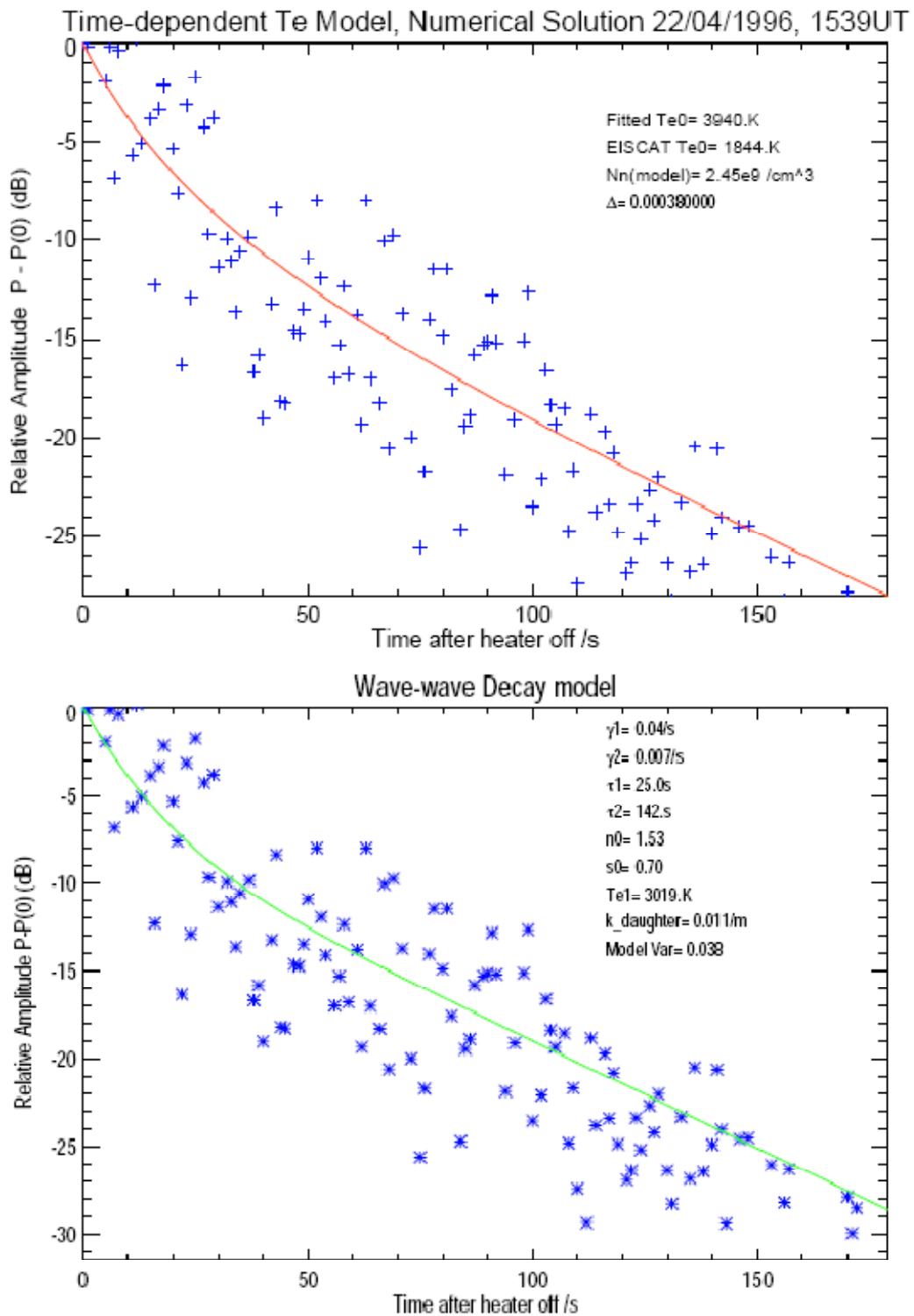


Figure 5.7 Time dependent model (upper panel) and equivalent wave-wave model (lower panel) fits made to the backscatter profile for the heater ‘OFF’ beginning at 1542UT on 22nd April 1996

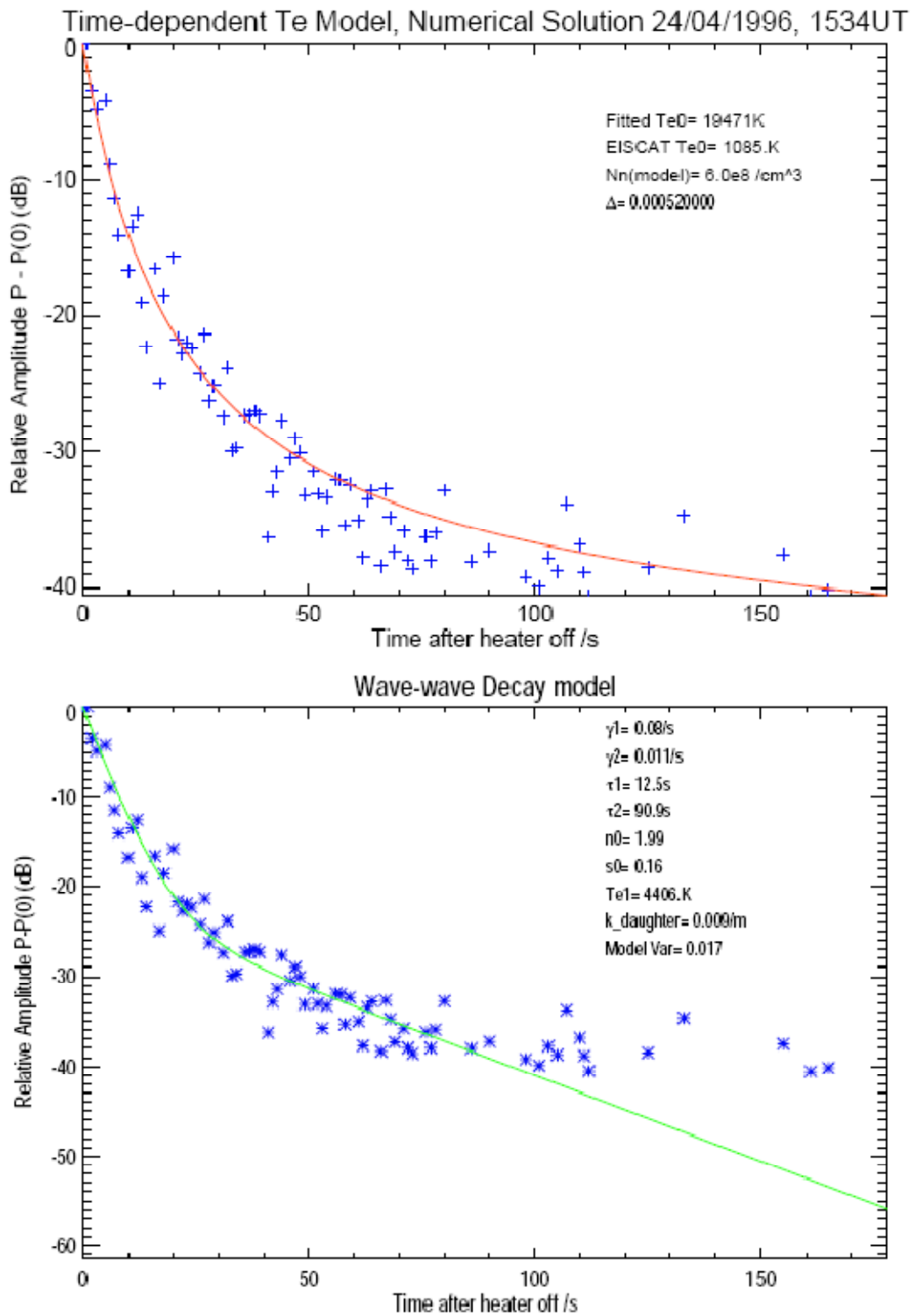


Figure 5.8 Time dependent model (upper panel) and equivalent wave-wave model (lower panel) fits made to the backscatter profile for the heater ‘OFF’ beginning at 1537UT on 24th April 1996

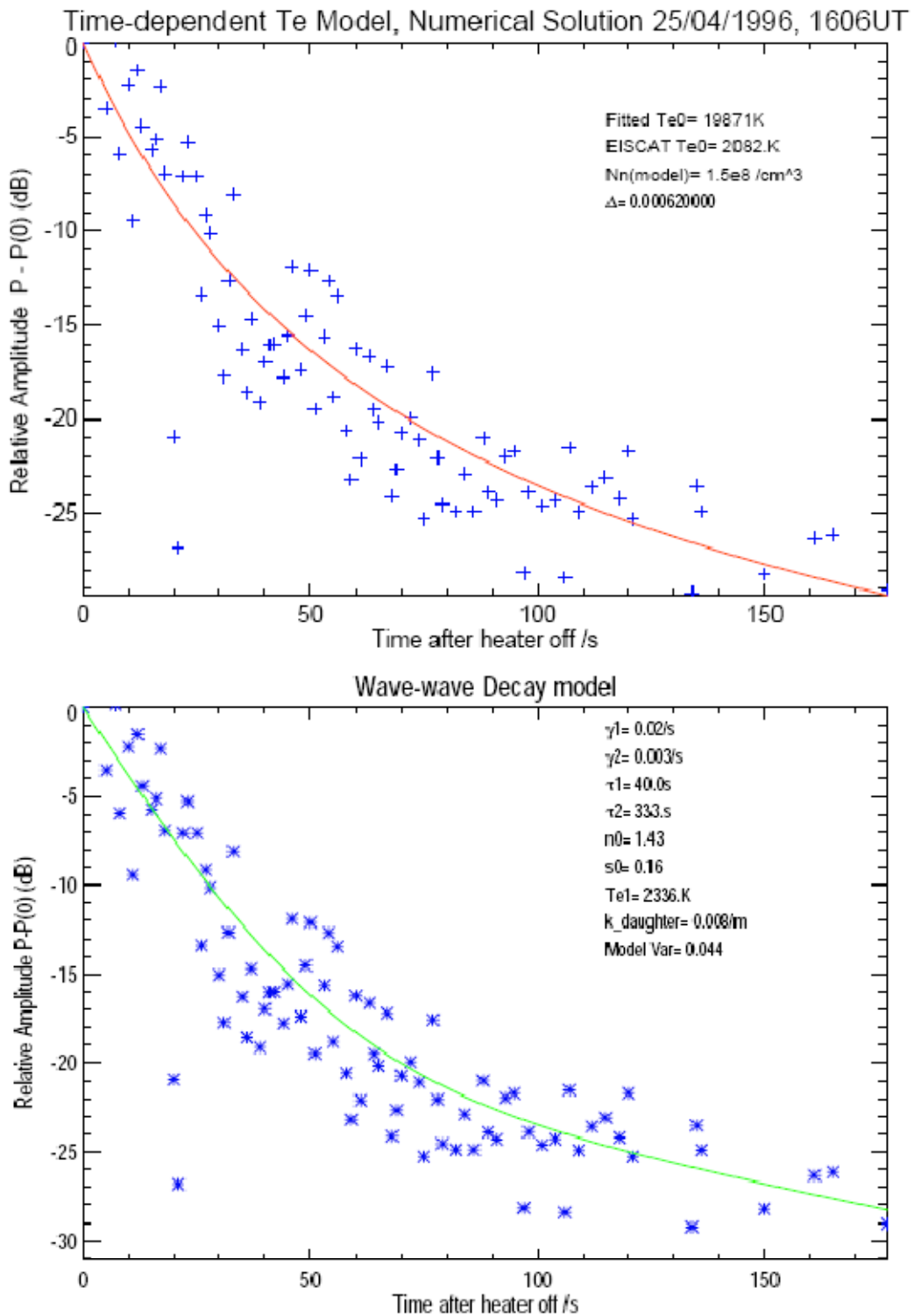


Figure 5.9 Time dependent model (upper panel) and equivalent wave-wave model (lower panel) fits made to the backscatter profile for the heater ‘OFF’ beginning at 1609UT on 25th April 1996

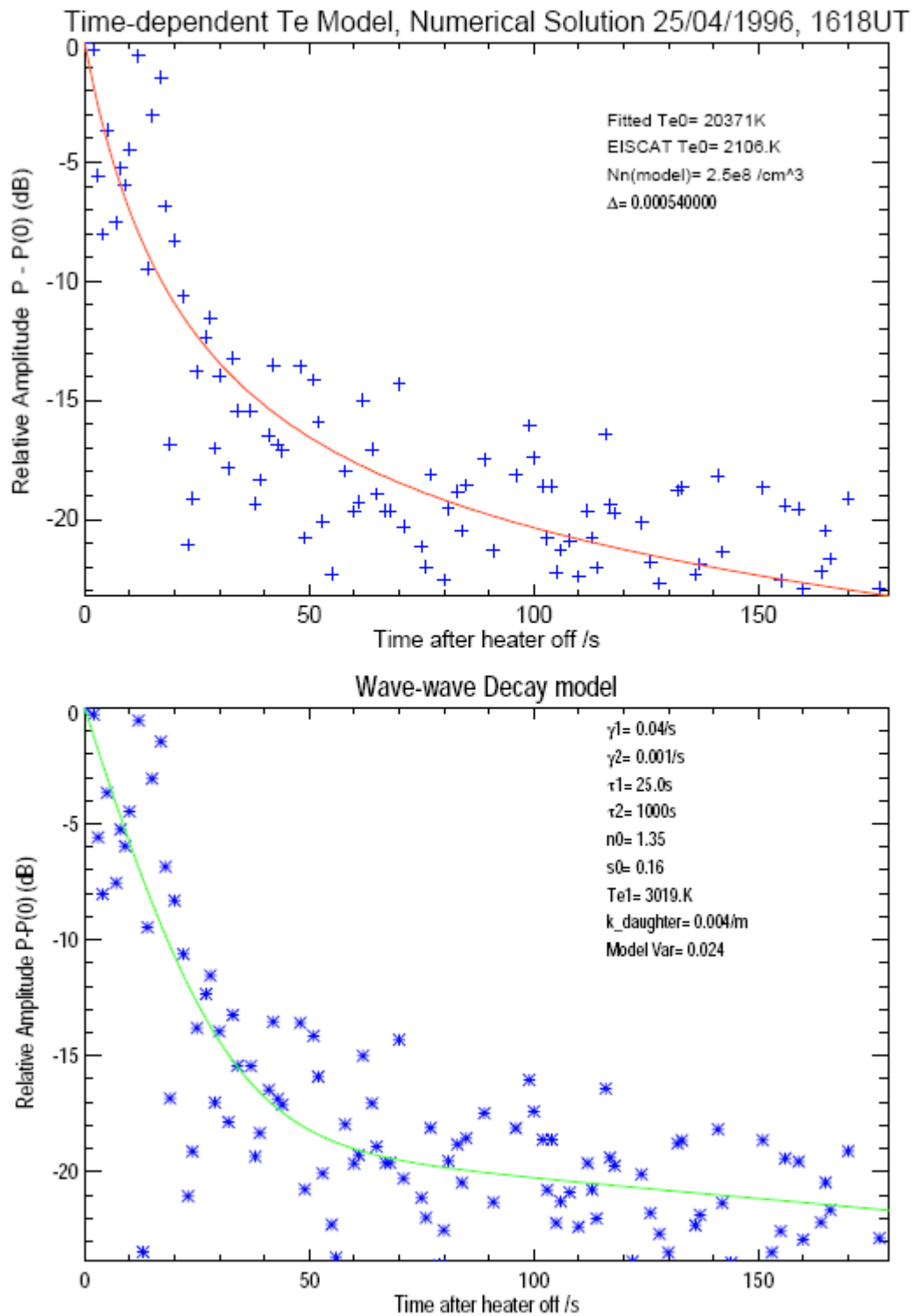


Figure 5.10 Time dependent model (upper panel) and equivalent wave-wave model (lower panel) fits made to the backscatter profile for the heater ‘OFF’ beginning at 1621UT on 25th April 1996

Figure 5.7 suggests qualitatively good fits between the time-dependent temperature model and data has been obtained with an initial plasma temperature of 3940K, neutral density N_n , $2.45 \times 10^9 \text{cm}^{-3}$ and δ value of 0.00038 for the backscatter profiles starting at 1542UT on 22nd April 1996. Similarly, the wave-wave model also produced a reasonable fit with a primary wave decay rate of 0.04s^{-1} and secondary wave decay rate of 0.007s^{-1} . The equivalent temperature that would result in perpendicular diffusion at the fitted primary wave decay rate of 0.04s^{-1} is 3019K, derived from equation 5.2 and assuming N_n was $3 \times 10^9 \text{cm}^{-3}$ (also used in the application of the simple FAI decay model). This temperature is not dissimilar to the initial temperature fitted by the time-dependent temperature model, which may arise because the value of the neutral density which produced the best temperature model fit to the data is almost identical to that which was assumed for the equivalent primary wave temperature. In comparison, the mean EISCAT temperature at a heater interaction height of 214km, averaged over the heating period was 1533K. This would suggest that both models require appreciably higher temperatures than what is experimentally measured by incoherent scatter technique, in order to explain the rapid initial decay rate. The modest peak temperature change of around 150K at this interaction height is only 10% above the background, as indicated in Figure 5.11.

However, there are consistently large discrepancies between the best fit temperature model initial temperatures and the mean EISCAT temperatures for the examples shown in Figure 5.8, 5.9 and 5.10. For the heating between 1534-1537UT on 24th April 1996, the backscatter profile for the corresponding heater ‘OFF’ interval is shown in Figure 5.8. Here, the temperature model predicts that the initial ‘heated’ temperature should be as high as 19471K, but the mean EISCAT temperature at 217.5km is only 1737K. The temperature change profile, shown in Figure 5.12 for this interval shows that the

electron temperature actually decreased by around 10K with respect to the unperturbed ‘background’ value at this height while the most notable increase in temperature took place at about 150km which was only 20K. This might suggest that only a very weak interaction took place between the heater wave and the plasma, leading to a less well-defined interaction height. In comparison, the wave-wave interaction model shown in the lower panel of Figure 5.8 produced a relatively good fit to the data for the first part of the backscatter profile with a primary wave decay rate of 0.08s^{-1} until about 40s after the heater was turned off. After this period it can be seen that the fitted model profile does not match the data as well as the temperature model. The temperature inferred from the fitted primary wave decay rate for this profile was 4406K, again, substantially higher than the mean EISCAT temperature. It may also be argued though, this estimate is somewhat unreliable because of the poorer fit to the data than the temperature model.

In Figure 5.9, there is a much better fit and correspondingly lower variance to the backscatter profile for the heater ‘OFF’ beginning at 1606UT on 25th April 1996 produced by the wave-wave interaction model. The fitted primary and secondary wave decay rates were 0.02s^{-1} and 0.003s^{-1} respectively, which corresponds to a primary wave temperature of 2336K. Again this assumes that the decay rate is dominated by perpendicular diffusion and electron-neutral collisions only. This temperature is much closer to the mean EISCAT heated temperature of 2066K at the interaction height of 214km, while the initial temperature estimated by the time-dependent temperature model is still far greater at 19871K. However, although it is not very poor, the fit of this model was not as good as the wave-wave interaction model from around 100s after the heater is turned off and can be seen to overestimate both the change in backscatter power and the rate of decay in the power between 100 and 180s after the heater is turned off.

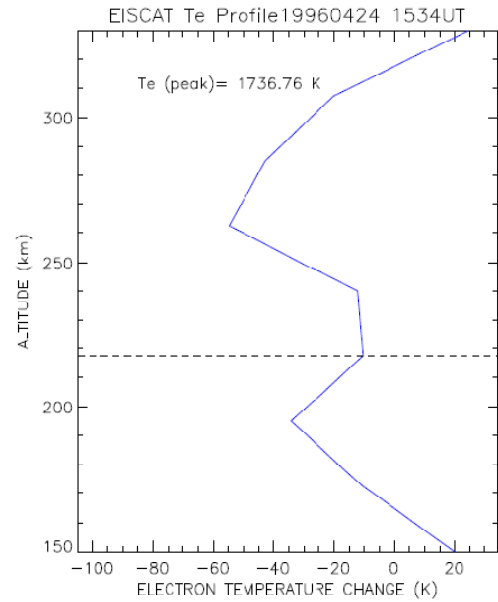
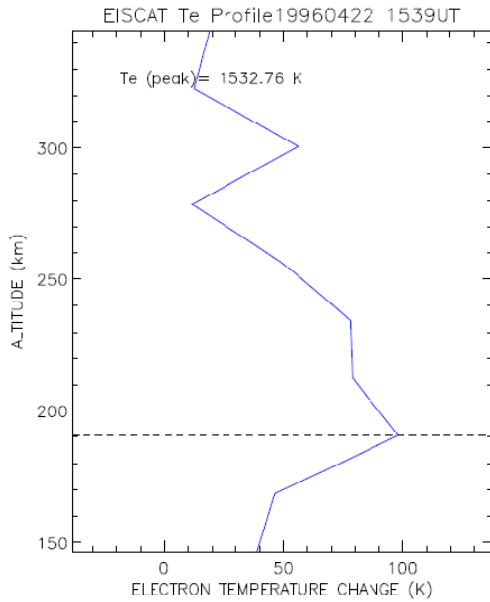


Figure 5.11 (left) Profile of the electron temperature change induced by the Tromsø heater, averaged between 1539-1542UT on 22nd April 1996. The dashed black lines indicate the range gate containing the peak temperature change

Figure 5.12 (right) Temperature change averaged for the heating 1534-1537UT on 24th April 1996

A similar situation is also borne out in the results shown for the fitted temperature and wave-wave model profiles for the backscatter data beginning at 1621UT on 25th April 1996 as shown in Figure 5.10. It would appear both qualitatively and quantitatively that the wave-wave model provides a slightly more suitable description of the temporal behaviour in the backscatter power than the temperature model with a fitted primary and secondary wave decay rate of 0.04s^{-1} and 0.001s^{-1} respectively, which corresponds to an equivalent primary wave temperature of 3019K. Although this estimate is 50% greater than the EISCAT measurement of 2048K, it is not unreasonable when the assumptions which were made in calculating the equivalent primary wave temperature are accounted for, such as the fact that the effect of ions and electron-ion collisions are not included. In contrast, the time-dependent temperature model which is shown in the upper panel of Figure 5.10 predicts an initial temperature of 20371K although the backscatter profile associated with this temperature is not too different from that of the wave-wave decay model.

However, even when the temperature model does appear to fit the data better than the wave-wave decay model, the electron temperatures associated with the rapid initial decay of the backscatter are vastly higher than the average heated temperatures measured by the EISCAT UHF radar by an order of magnitude in many cases. This was seen to be the case in particular for the profiles beginning at 1542UT on 22nd April 1996 and 1537UT on 24th April 1996, shown in Figure 5.7 and Figure 5.8. One cause of the significant temperature difference could be attributed to the crude assumption that the decay occurs only by perpendicular diffusion. If the effects of the ion temperature, for ambipolar diffusion, were to be included this would certainly affect the initial starting temperature which is required to produce a good fit of the model with the data. The role of ions and the associated electron-ion collisions are not investigated in this chapter, but

an examination of their contribution, as well as chemical processes to the decay rates is made in Appendix 4.

Secondly, it may be that the temperature model had been fitted with a lower neutral particle density than the true value, and hence lower electron-neutral collision frequency. However, because the decay rate is proportional to both the collision frequency and the electron temperatures, any reduction in the collision frequency must be compensated by an increase in the electron temperature and the fitted neutral density may not necessarily be as high as what would be obtained from a neutral atmosphere model such as the MSIS-2000 model.

An additional source of error may lie in the estimate of δ , the collisional energy loss term. It was highlighted earlier that this parameter represents the fraction of energy lost in several types of collisional processes, depending on the collision frequency and the electron temperature. The timescale over which the energy is lost is inversely proportional to the collision frequency. Hence there is potential for over- or under-estimates of δ to be made when it is estimated indirectly by fitting a model to temporal behaviour in number density.

The temperatures implied by the decay rates estimated from the two decay models are based on physically different principles. The time-dependent temperature model initial temperatures are those expected at the instant the heater is turned off and would not remain at this level for more than a few seconds before a rapid quenching in the temperature and the corresponding rate of decay occurs. Conversely, the temperatures equivalent to the initial rate of decay associated with the fitted primary wave decay rate would represent the average temporal behaviour in the backscatter power over time scales of a few tens of seconds or more and not the instantaneous rate at the time the

heater is turned off. If the electron temperatures, derived from the fitted temperature profile were averaged over the typical characteristic time scale of the primary wave, a significant reduction could be expected when compared to the initial temperature estimated by the temperature model.

The mean decay rates of the primary and secondary waves obtained from fitting the model to the sample of backscatter profiles were $(0.144 \pm 0.101) \text{ s}^{-1}$ and $(0.0138 \pm 0.0154) \text{ s}^{-1}$ respectively. Therefore the secondary wave decay rates are on average, ten times smaller than those of the primary wave although there is clearly a large degree of variability in both these rates, as is obvious from the statistical uncertainties associated with these mean values. However, if this ten-fold reduction in the decay rate were associated with a fall in the heated temperature, it could be expected that this temperature must decrease by around a factor of 3.5 because the rate of decay is almost proportional to the square of the electron temperature.

Certain authors have speculated that electron temperatures could be as high as 10000K within the striations (Rietveld et al., 2003) as opposed to the bulk electron temperature on much larger scales which is typically measured by incoherent scatter radars. It was shown theoretically, by Gurevich et al., (1995) that trapping of upper hybrid wave modes could lead to enhancements within these density cavities of 2 to 4 times the bulk (or large-scale) temperature, whose cross-field scale size and depletion strength is in proportion to its field-parallel or longitudinal scale. Consequently, the localised nature of these very hot temperature would be unlikely to be detected by remote sensing facilities such as incoherent scatter radars since the backscattered signal is essentially an average of a much larger scattering volume (Gurevich et al., 1998a), and thus not reflective of small-scale striations embedded within it.

If the enhancements within the striations are between 2 and 4 times the bulk plasma temperature, which can itself be around 2 to 3 times the unperturbed or ‘unheated’ electron temperature, then this would imply a potential for the temperature within the striations to be between 4 to 12 times the unperturbed temperatures. For an unperturbed temperature of around 1500K, this would correspond to a possible striation temperature of anywhere between 6000K and 18000K. This large range of temperatures is not dissimilar to those fitted to the backscatter profiles which were presented earlier in this chapter. However, the mean ‘heated’ EISCAT temperatures for these heating experiments were typically 1.5 times the background level at most, so the range of potential temperatures within the striations, based on the work of Gurevich et al. (1995) would be more like 4500K to 9000K.

One candidate scenario would be that the very hot model temperatures are those of the striations and these dictate the initial stage of relaxation of the irregularities, with both the temperature and decay rate falling rapidly within the first few seconds after the heater has been turned off. These very hot striations could be present in the scattering volume of the EISCAT radar but not seen in the incoherent scatter radar data if the volume concentration is such that their overall contribution in raising the large-scale plasma temperature is relatively small. Large density cavities, associated with high plasma temperatures would be a likely source of strong backscatter measured by the CUTLASS radars, since the backscatter power is in proportion to the square of the perturbation amplitude.

There has also been convincing experimental evidence to support the theory (Gurevich et al., 1995) of hot filamentary-type irregularities. Kelley et al. (1995) presented data collected by instruments on board a rocket flown through the heated volume above the ionospheric heater at Arecibo which showed fluctuations above the background density that were on average 6%, over cross-field scale sizes which were of 7m and some depletion depths extended to more than double this mean value. This view of the heated volume would provide an explanation which could perhaps consolidate the conflicting measurements made by the coherent and incoherent scatter radars. Ideally, further in-situ measurements made by rocket-borne instrument would be able to probe the temperature structures of such small scales. It is unfortunate that high spatial and temporal resolution rocket observations of the heated volume over Tromsø do not exist.

5.5 Drift Velocity Dependence

The fast initial rates of irregularity decay exhibited in certain intervals of CUTLASS radar data have been shown to be sometimes incompatible with those expected from only cross-field diffusion processes at the large-scale heated electron temperatures typically measured using the EISCAT UHF radar. Additional mechanisms such as parallel diffusion, collisions and chemical recombination may contribute to raising the rates of decay at a given electron temperature have been considered but are included in Appendix 4. However, these processes are stationary, giving rise to a ‘local’ rate of decay and are independent of the nature of the background F-region flow. Artificial irregularities typically drift at the background plasma speed (Eglitis et al., 1998), but it has not been established whether sufficiently strong flows in the plasma could control the decay of the irregularities seen by the radar. A further consideration addressed in this study is whether the discrepancy in the fitted rates of decay could be attributed to a

combination of these local decay processes and a dependence on dynamic influences such as the background plasma drift velocity.

To account for advective processes occurring in the plasma, a total rate of decay in the backscattered power measured by the radar in a given volume of the artificially heated plasma must be considered. This is the sum of the local decay rate of the irregularities and an advection term which represents plasma transported out of a volume at some drift velocity V . The following set of equations describes this total rate (Robinson, private communication), whereby P is the backscattered power, A is the area of the irregularities in the plane of the flow and n^2 is simply the perturbation amplitude of the irregularities.

$$P = \alpha n^2 A \quad (5.16)$$

$$\frac{dP}{dt} = \alpha \left(A \frac{dn^2}{dt} + n^2 \frac{dA}{dt} \right) = \alpha \left(\gamma n^2 A + n^2 A \frac{V}{L} \right) \quad (5.17)$$

$$\frac{dP}{dt} = \alpha n^2 A \left(\gamma + \frac{V}{L} \right) \quad (5.18)$$

Here, α is a constant of proportionality, γ is the local rate of decay due to mechanisms such as diffusion, collisions, chemistry and L is a characteristic scale size of the region exiting the volume at flow speed V , at some distance probed by the radar. The overall enhancement in the rate $\frac{dP}{dt}$ in the presence of a flow V is the effect measured by the radar, irrespective of the location of the strongest scattering region and its subsequent positions resulting from advection. The fitted decay rates obtained from the wave-wave decay model are used to represent the *total observed* rates of decay in backscatter power, γ' due to the superposition of local and advective processes occurring simultaneously, so that the slope of the best fit line between the CUTLASS Doppler

velocity and the difference between the fitted and local decay rates, $\Delta\gamma$ should be indicative of the quantity $1/L$. This can be simplified to:

$$\frac{1}{P} \frac{dP}{dt} = \gamma' = \left(\gamma + \frac{V}{L} \right) \quad (5.19)$$

$$\Delta\gamma = (\gamma' - \gamma) = \frac{V}{L} \quad (5.20)$$

The difference $\Delta\gamma$ of the observed decay rate γ' from the local decay rate γ may therefore be attributed to flows in the plasma which are acting on structures of the scale size L . In order to implement this full model of backscatter decay, the fitted primary wave decay rates (Section 5.4) and the mean CUTLASS Doppler velocity measured when the heater was ‘on’ were combined as defined by (5.20). To maximise the sample size the mean Doppler velocities and decay rates have been determined over several range cells exhibiting artificial backscatter during the individual heating cycles. These were obtained by simply fitting the wave-wave decay model to the backscatter profiles at each of the range cells in question.

In Figure 5.13 the fitted primary wave decay rates (γ' , blue) and the difference $\Delta\gamma$ between the observed and local rates (green) are plotted as a function of on the drift velocity measured along Beam 5, by the Hankasalmi radar. The local rate here has been assumed to be the sum of all the stationary components calculated using model parameters (diffusion, collision and chemical recombination rates) which are shown as additional material in Appendix 4.

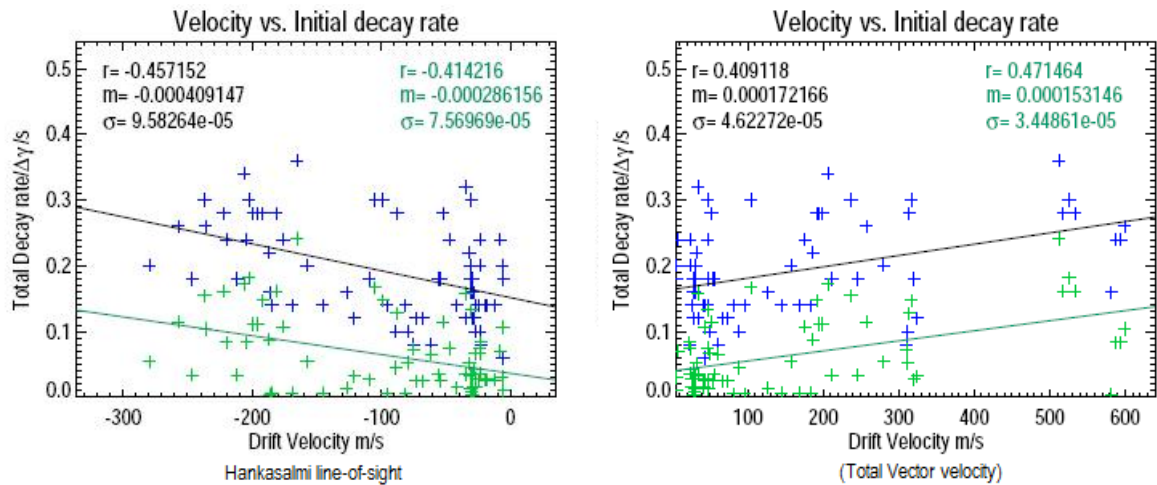


Figure 5.13 (left) A scatter plot of the fitted initial decay rates (blue data points) and the average ‘heated’ background plasma velocity, measured along the line-of-sight of beam 5 of the Finland Hankasalmi radar. The green data points correspond to the *difference* between observed and theoretical (local) decay rates (equation 5.20) and its dependence on the measured flow velocities.

Figure 5.14 (right) The same parameters plotted as in Figure 5.13 but for the total vector velocity, calculated using the Iceland Pykkvibaer velocities measured along the line-of-sight of Beam 15, which overlies the Tromsø site. r , m and σ given in each plot are the correlation coefficients, slope and standard deviation of the regression lines which have been fitted to the two sets of data points and plotted in black and green respectively. Both Figure 5.13 and Figure 5.14 indicate that there is a finite difference between the observed and computed local decay rate which increases in magnitude with stronger flow velocity.

In Figure 5.14, γ' and $\Delta\gamma$ are shown as a function of the total vector velocity which has been obtained by combining the mean velocities measured during a heater ‘on’ by the Hankasalmi and Pykkvibaer radars, where sufficient backscatter was available although, due to the longer propagation distance from the heated volume to the Iceland radar, the strength of the backscattered signal was often too weak to make any reliable spectral fits, which results in no estimate of the drift velocity being made.

Figure 5.13 shows that there is a weak correlation between the total rate and the drift velocity, represented by the linear relationship with slope of magnitude 0.0004 m^{-1} , implying a spatial inhomogeneity in the flow with a field-perpendicular scale of 2.5km. This characteristic scale size is a proportion of the heated ‘patch’ contributing to the change in backscatter power as the irregularities are carried out of the source volume, due to the flow measured by the radar. This is also only a fraction of the true vector velocity. By way of theoretical considerations, it has been shown that ‘bunching’ of striations can develop due to self-focusing effects of the strong pump wave on the striations (Gurevich et al., 1998*b*) which can produce irregularities of this scale.

Moreover, there is a very similar correlation between the difference of the total and local decay rates and the drift velocity. The slope of the regression line that best fits these data points to the velocities (0.0003 m^{-1}) is associated with spatial inhomogeneities of characteristic scale 3.3km, or using the total vector velocity, around twice this magnitude at $\sim 6.5\text{km}$. It is notable from Figure 5.13 and Figure 5.14 that for negligible or absence of flow, at $V = 0 \text{ m s}^{-1}$, the difference between the observed and theoretical local rates of decay is also very close to zero. Therefore the data does on average, agree very well with the new model, and provides an alternative explanation for the discrepancies between the large scale electron temperature measured by the

EISCAT radar and the higher plasma temperatures required to produce the fast initial rates of decay that are sometimes observed. The observed scatter about the best fit line in Figure 15 and Figure 16 may be explained by the fact that in regions of strongest flow the measured rates of decay may not be the fastest if the irregularity amplitudes are being maintained via an advection process. In addition to this, the weak correlation may arise because the velocities measured are those along the line of sight of the radar beam, but may not necessarily be the true flow direction.

This section has addressed the possible effects that the background plasma flow may have on the rate at which the backscattered power received by the CUTLASS radars, from FAI, is observed to decay at. It was noted from Figure 5.13 and Figure 5.14 that an apparent increase in the rate of decay of the backscattered power measured by HF radar due to the transport of the irregularities out of the heated volume existed, as well as a larger departure of the expected local rate of decay from the observed rate of decay, as the flow magnitude increased. In the following section, a heating experiment is identified in order to test if the ‘flow’ model predicts correctly the observed behaviour of the CUTLASS backscatter, given that applicable conditions with regards to the background flow were present.

5.6 Flow Effects on the Decay of CUTLASS Backscatter

In Figure 5.15, the CUTLASS Iceland backscatter power, drift velocities and widths measured in beam 15 during a heating experiment on 30th October 2000 are presented. From 1800UT to 1830UT the heater was transmitting O-mode radio waves at a frequency of 4.04MHz on Array 2 in a 4 minutes ‘on’, 4 minutes ‘off’ modulation with the beam tilted in a direction 0°S. The centre panel indicates there are strong flows of approximately 400 m s⁻¹ associated with the FAI, directed towards the radar.

SUPERDARN PARAMETER PLOT

30 Oct 2000⁽³⁰⁴⁾

PYK BEAM 15: PWR_L, VEL AND WIDTH_L

unknown scan mode (-8318)

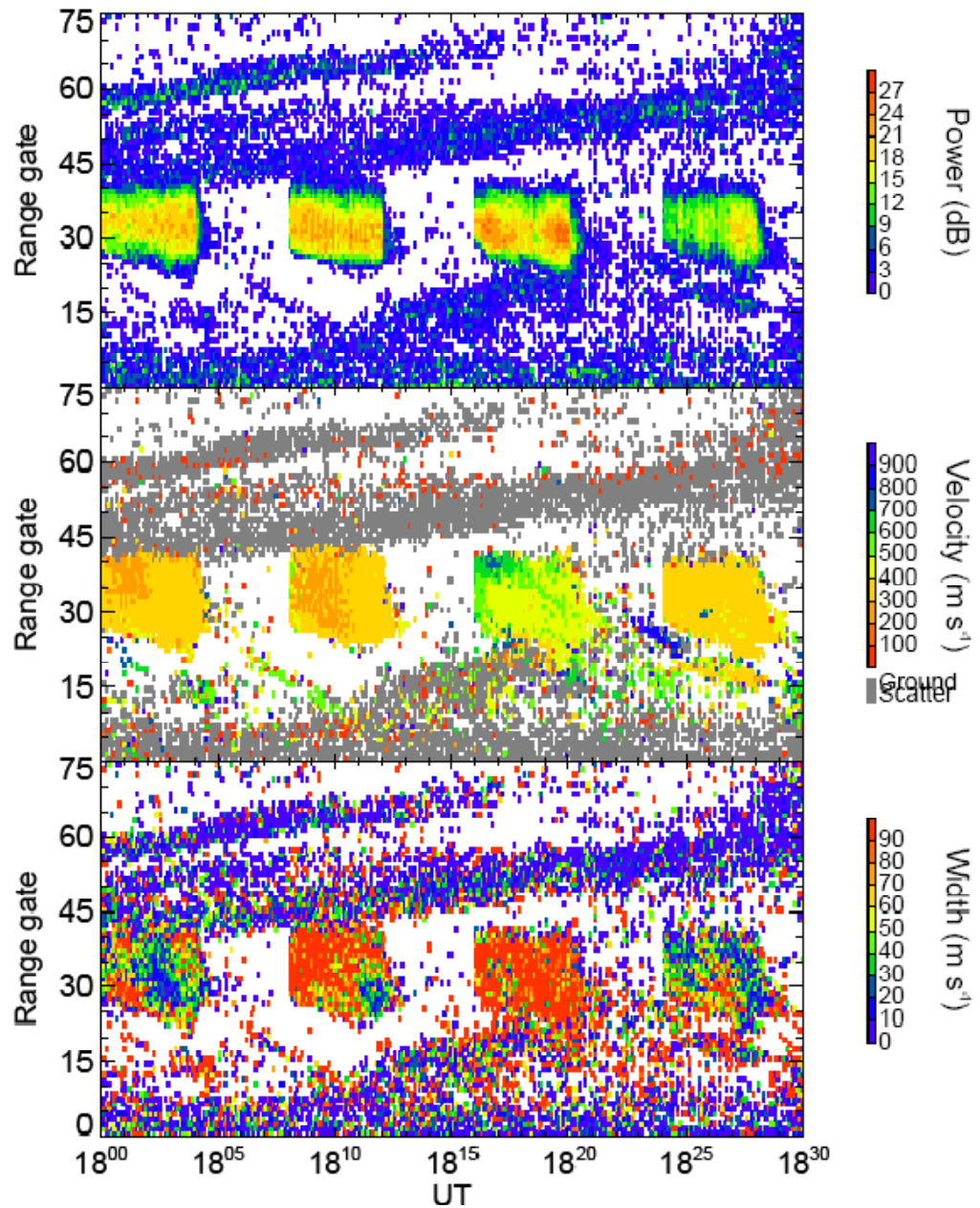


Figure 5.15 The backscatter power, velocity and widths measured along Beam 15 of the CUTLASS Pykkvibaer radar in Iceland between 1800-1830UT on 30th October 2000, shown in order from the upper to lower left hand panels. The colour scale indicates the values of these parameters.

Since the irregularities are drifting toward the radar with the background flow after the heater is turned off, backscatter at the furthest range gates will be shifted into nearer ranges, thus raising the number density of decaying irregularities. Hence, at the furthest gates, there should be an apparent increase in the rate of decay of the backscatter power due to the advection of irregularities from their source region and subsequent lack of replenishment because the heater is no longer transmitting. At the nearest range cells the irregularity decay due to local processes (diffusion, collisions, chemical recombination) is compensated by additional backscatter contributed from irregularities transported from neighbouring range cells, so the decay rate in backscatter power could be expected to be reduced at nearer ranges.

Figure 5.16 illustrates this effect more clearly in range-time plots for each of the heater-on intervals between 1800-1830UT, where the final minute of heating, and the first two minutes after the heater was turned off is shown. There are clear indications of an extended ‘tail’ in the backscatter at the closest range gates between approximately gate 25 and gate 28, after the heater has been turned off, particularly for the ‘off’ intervals beginning at 1812UT and 1828UT. In order to determine whether range variations in the decay of backscatter power measured by the radar existed, due to this expected ‘flow’ effect, decay curves were fitted to the backscatter power at consecutive range gates across the heated volume and this was carried out using the procedure described in Section 5.2. Figure 5.17 shows the fitted decay curves for the heater-off period beginning at 1824UT, for backscatter across range gates 28 to 32. The decay time of the backscatter power, stated in each plot, is the sum of the local and advective processes acting on the irregularities. Clearly there is an appreciable reduction in the observed decay time (increase in the decay rate) of the backscatter power with range, changing from 19.6 seconds at range gate 28, to 13.5 seconds at range gate 32.

SUPERDARN PARAMETER PLOT
 PYK/BEAM 15/PWR_L

30 Oct 2000 ⁽³⁰⁴⁾
 unknown scan mode (-8318)

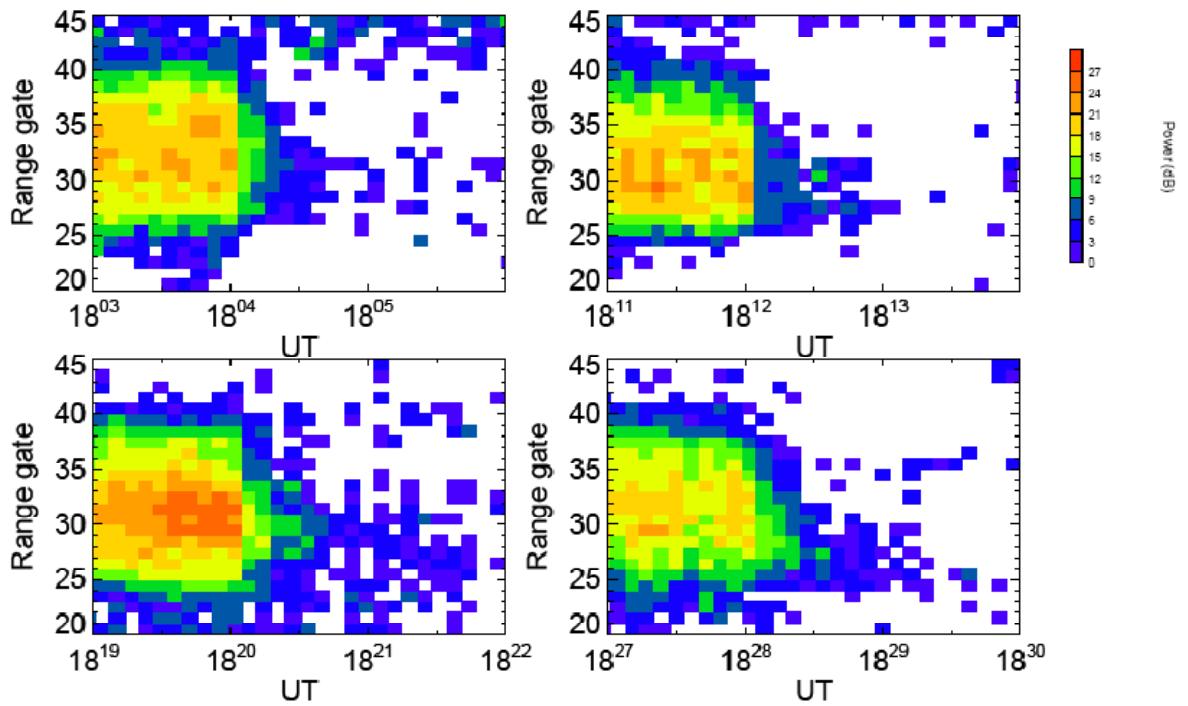


Figure 5.16 Range-Time plots for the four heating intervals between 1800-1830UT on 30th October 2000. The time range has been limited to show the last minute of the four minutes heating for each interval, with the first two minutes of the heater-off interval. It can be seen that there is an extended ‘tail’ of backscatter at the nearer range gates for each backscatter ‘patch’, which indicates a prolonged decay time with respect to the further ranges

Pykkvibaer Backscatter Decay 30/10/2000 1824–1828UT

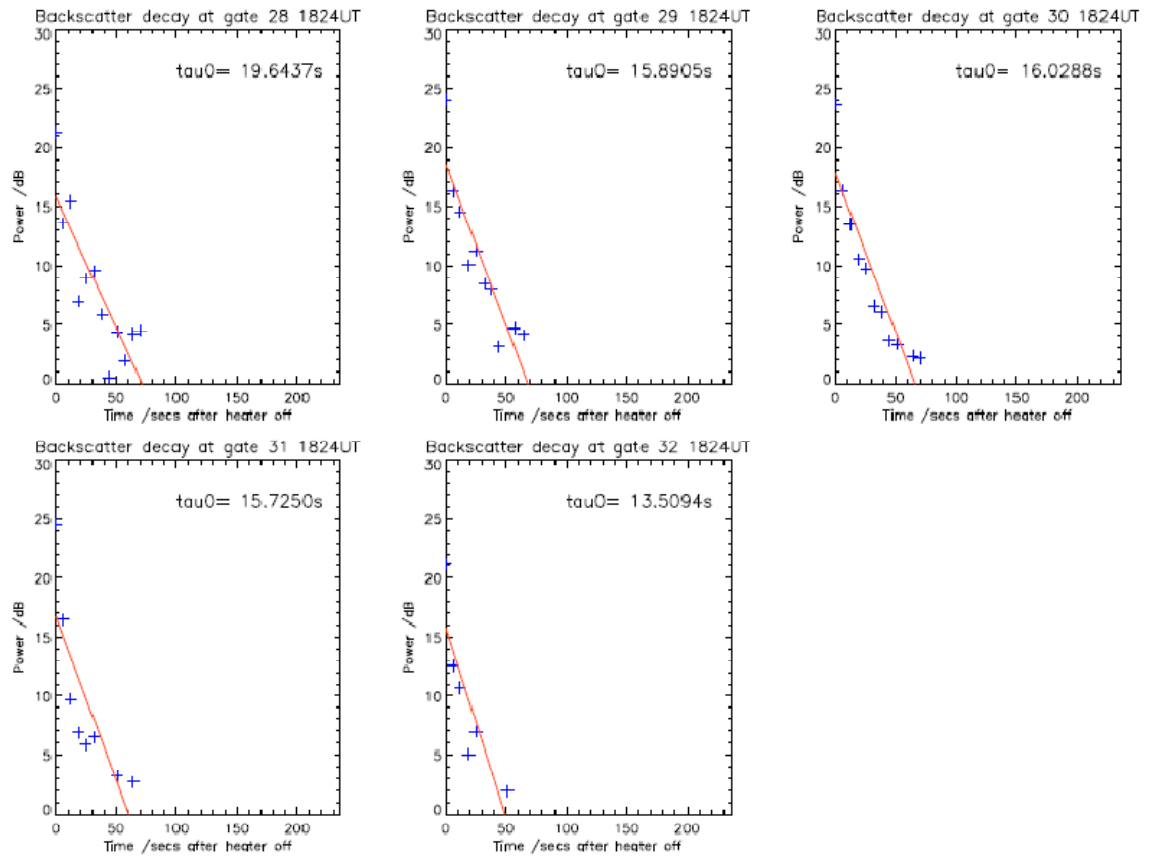


Figure 5.17 The decay in the CUTLASS Pykkvibaer backscatter power for the heater-off period between 1824-1828UT on 30th October 2000. It is shown for range gates 28 to 32 and demonstrates the decrease in the decay time (faster decay rate) toward the further range gates

This implies a reduction in the decay time of nearly 1 second per 12.5km in horizontal distance in the direction toward the radar, which confirms the effect of flow on the apparent rate of decay of the backscatter. This was expected due to the combined effect of the ‘advective’ decay in the backscatter power and local rate of decay of the FAI. However, it is pointed out that the increased backscatter power decay rate at the furthest ranges is only a relative effect, because the reduced rate at the nearest range cells due to accumulation of artificial backscatter may not actually represent the decay rate of the FAI. That is to say, the apparent lifetime of the backscatter power may be greater than the true lifetime of the FAI at the near-ranges if it is artificially prolonged by additional backscatter advected from further ranges.

5.7 Summary and Concluding Remarks

It has been shown that the relaxation of field-aligned irregularities obey the simple theoretical model in the majority of cases and typically decay over e-folding time scales of a few seconds to tens of seconds, in agreement with current and previous literature. The effective plasma temperature corresponding to the rate of decay by diffusion only is generally in reasonable agreement with the large scale, background temperature measured by the EISCAT UHF radar. However, the model has been found to fail in a small number of experiments where the decay is of a multi-stage nature, and two alternative models have been developed in order to reproduce and describe the nature of the irregularity decay under these circumstances.

Small-scale irregularities at the 10m-scale have been found to exhibit relaxation behaviour that can be modelled well by both a time-dependent temperature decay model, and a wave-wave interaction model. The majority of backscatter profiles studied usually showed preference over one of these models. Those profiles where the wave-

wave model fitted better to the data imply that the irregularities initially decay rapidly at the primary wave decay rate and the amplitudes are maintained for a longer time than would be predicted from only cross-field diffusion. The larger-scale secondary wave was found to decay at a rate which is on average, ten times smaller. The fast primary wave decay rates are associated with plasma temperatures that are generally much higher than the bulk plasma temperatures measured by the EISCAT radar. However the initial temperatures predicted by the time-dependent temperature model tended to be well in excess of 10000K. If these temperatures really exist, the result would suggest that the irregularities are not spatially-periodic perturbations in the background plasma but intense, isolated ‘filaments’ of plasma depletion. In the cases where only the temperature model was found to suit the data, the multiple-stage nature of the decay was probably due only to the large temperature changes, modifying the decay rate of the ‘filaments’ by cross-field diffusion. Cases where the simple decay model provided a satisfactory description of the data serve as evidence that the heated volume is probably structured by FAI taking the form of periodic small perturbations which decay at the rates expected from the mean EISCAT temperatures measured during the heating.

Finally, a dependence of the observed rate of decay of artificial backscatter on the ionospheric drift velocity, through advection of larger-scale structuring within the heated volume has been shown. The characteristic size of over which the flow affects the observed backscatter is typically of the kilometre-scale, and the effect has been proposed to be a possible mechanism to explain variation in the decay rate of artificial backscatter at different range gates. Emphasis is placed on the distinction between the apparent rate at which the backscattered signal in HF radar data decays at, when there is a non-zero flow present in the heated volume, and the true ‘local’ rate at which the FAI are decaying.

Chapter 6

Observations of artificial HF backscatter in the presence of strong flows and natural irregularities

6.1 Introduction

FAI produced using the EISCAT heating facility usually exhibit low spectral width when measured using the CUTLASS HF backscatter radars (Eglitis et al., 1998; Dhillon et al., 2002). In this chapter however, observations of artificial backscatter are presented, where the spectral width as deduced using the SuperDARN ‘FITACF’ analysis software appear unusually broadened. An investigation into the possible origins of these observations is made and to achieve this, the Burg maximum entropy analysis method is applied to CUTLASS HF radar backscatter ACFs, combined with standard ‘FITACF’ results. The characteristics of the broadened artificial backscatter spectra will be discussed in detail, and compared with previously reported enhanced artificial backscatter widths. The results of the analysis are examined in terms of the possibility of mixed artificial and naturally-occurring echoes and for evidence that the heater may influence naturally occurring irregularities lying well outside the usual heated volume.

6.2 Background

Modest enhancements in the spectral width of HF radar backscatter from FAI, when they do occur, have been attributed to ULF waves (Wright et al., 2004), associated with the heated region being in daylight while its conjugate point was in darkness

(Blagoveshchenskaya et al., 2007) and pumping at a heater frequency just above the third and fourth harmonics of the electron gyrofrequency (Ponomarenko et al., 1999). Bi-static scatter measurements of HF diagnostic waves made during an experiment at Tromsø revealed variations in the drift velocity of artificial irregularities (FAI) across the heated volume (Blagoveshchenskaya et al., 2006), which were interpreted as being due either to two different modes of propagation generating irregularities that were horizontally separated, or to a temperature gradient-drift instability leading to grouping of irregularities at different altitudes. Both would produce splitting in the Doppler HF spectrum. Other observations of two-component Doppler spectra from artificial FAI have been associated with slow radial drift of the FAI from the centre of the heated volume (Koloskov et al., 2002), producing a broadening of 0.5-1Hz in HF signals.

Naturally-occurring double-peaked Doppler spectra may arise from plasma waves superposed on a background flow towards and away from the radar line-of-sight direction due to gradient drift instabilities (Huber and Sofko, 2000) and Schiffler et al. (1997) related the origin of their double-peaked spectra to soft electron precipitation and enhanced ion fluxes observed by DMSP satellite. A strong correspondence between the spatial occurrence of multi-component spectra, high spectral widths and large fit errors inferred using standard SuperDARN analysis techniques has also been established (Andre et al., 2002) and a number of attempts have been made to address these problems (see for example, Barthes et al., 1998; Ponomarenko and Waters, 2006; Ponomarenko et al., 2008) although these need not be discussed here.

In this chapter the HF spectral characteristics of artificial FAI, produced during a HF heating experiment when the ionosphere was particularly disturbed, are studied. The CUTLASS Finland and Iceland radars were operated to diagnose the naturally-

occurring and heater-induced phenomena. The focus of the chapter will be on the asymmetry in spectral width observations of the FAI backscatter, when the Iceland radar exhibited much broader values than those which were measured at Finland, a result not previously reported on which makes the observations particularly unique. In the following section, details of the heating experiment and the CUTLASS diagnostics are described.

6.3 Heating experiment details

During the interval from 1632UT until 1820UT on 30th October 2000, the EISCAT Tromsø heater transmitted O-mode polarisation waves at 4.04 MHz in a four minutes on, four minutes off cycle on Array 2 with the beam pointed vertically (0°S). At 1824UT the beam was changed to the field-aligned position (-12°S) and remained in this direction until 2004UT. Two transmitters received 60 kW, while the remaining eight transmitters used received 80 kW. This resulted in a total linear power of 760 kW and antenna gain of 23 dB, so the heater ERP was therefore around 150 MW.

The results of this chapter are focused on a small interval of the experiment between 1800 and 1830UT. Measurements made by the Tromsø Dynasonde indicated that the critical frequency, f_oF_2 was just above 4MHz at 1800UT, but this diminished to a less than 4MHz by 1820UT, implying that for the majority of the interval the HF pump frequency was only slightly greater than or very near to the f_oF_2 so the heating was marginally overdense.

In conjunction with the heating experiment, the CUTLASS Iceland radar at Pykkvibaer operated in the 12.1-12.2.MHz band, making 7s scans across beams 13, 14 and 15, thus dwelling for approximately 2s in each of the three beam directions. The operation mode employed therefore allowed high temporal and spatial resolution (15km) measurements,

with the distance to the first range gate being 1470km in one-and-a-half hop propagation mode. The CUTLASS Finland radar at Hankasalmi was operated simultaneously in the 8.9-9.1MHz band and made 7s scans across beams 3, 4, 5, 6 and 7, yielding a dwell time of approximately 1s in each pointing direction. The distance to the first range gate was set to 480km, associated with a half-hop propagation mode.

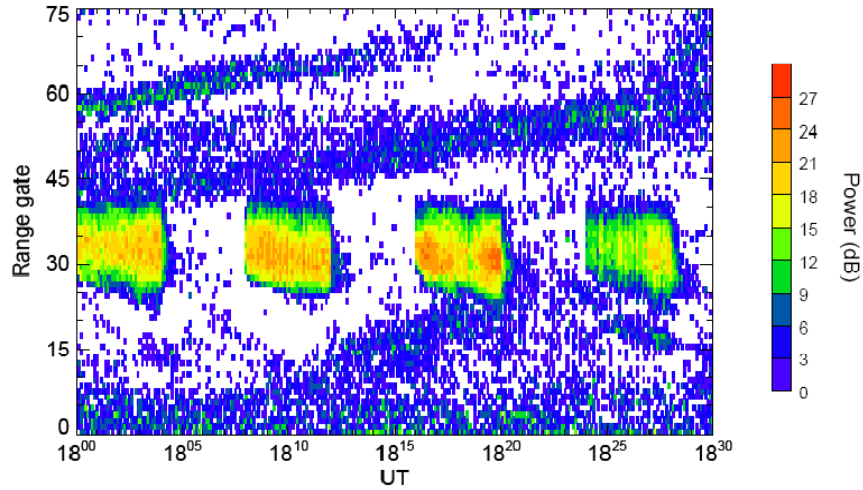
6.4 CUTLASS Observations

Range-time plots of the standard SuperDARN fit parameters (power, background drift velocity and spectral widths) derived for beam 15 of the Iceland radar are shown in the upper panels of Figure 6.1(a), (b) and (c). The corresponding parameters measured in beam 5 at Finland are shown in the lower panels of Figure 6.1(a), (b) and (c). Figure 6.1(a) shows strong artificial scatter patches are produced in both the Iceland and Finland observations after the heater is turned on at 1800, 1808, 1816 and 1824UT. There is also an apparent drift of the FAI towards the Iceland radar, as soon as the heater is turned on, indicated by the change in range with time of the near-edge of the artificial backscatter. This rate of change in range is also consistent with the Doppler velocity of the artificial irregularities of approximately 400 m s^{-1} , measured at Iceland in beam 15 (Figure 6.1(b)). The effect might also suggest that the artificial irregularities are being transported out of their source region by the background convection, since the drift effect only occurs at one edge of the backscatter.

The strong artificial backscatter in the Finland beam 5 observations during the intervals of heater ‘on’ appear to move in range with time, in a direction away from the radar as seen in the lower panel Figure 6.1(a). The motion is consistent with the negative line-of-sight velocities indicating flow away from the radar, indicated in the lower panel in Figure 6.1(b). There is also a region of naturally-occurring irregularities at ranges further from the heated region (more northerly latitudes) in the Finland observations. This region of natural backscatter is present at weaker intensities at the range gates of the artificial backscatter when the heater is ‘off’. Hence it may be presumed that there are underlying natural irregularities, co-located with the heated region as well, with typical backscatter power of a few dB at gates 35 to 37 (heater ‘off’).

SUPERDARN PARAMETER PLOT
PWR_L: PYK Beam 15

30 Oct 2000 ⁽³⁰⁴⁾
unknown scan mode (-6318)



SUPERDARN PARAMETER PLOT
PWR_L: HAN Beam 5

30 Oct 2000 ⁽³⁰⁴⁾
unknown scan mode (-6318)

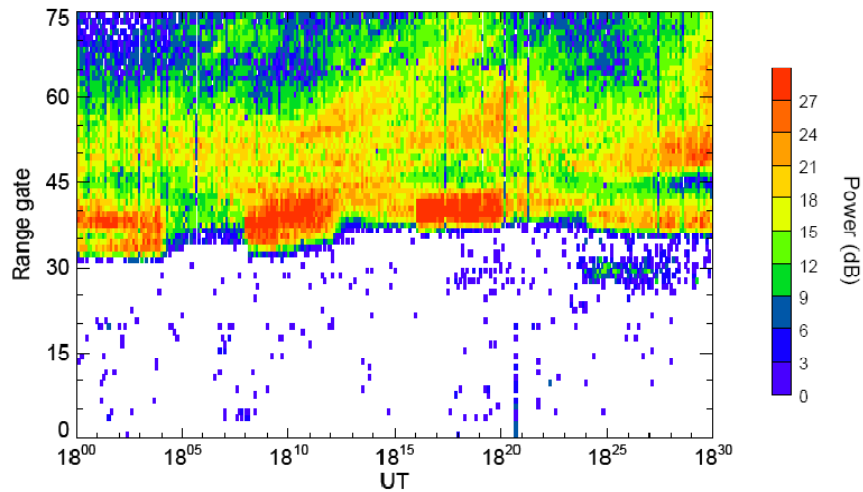


Figure 6.1(a) The range-time plots of the SuperDARN ‘FITACF’ analysis backscatter power for the CUTLASS Iceland radar in beam 15 (upper panel) and Finland radar in beam 5 (lower panel), for artificial heating between 1800-1830UT on 30th October 2000.

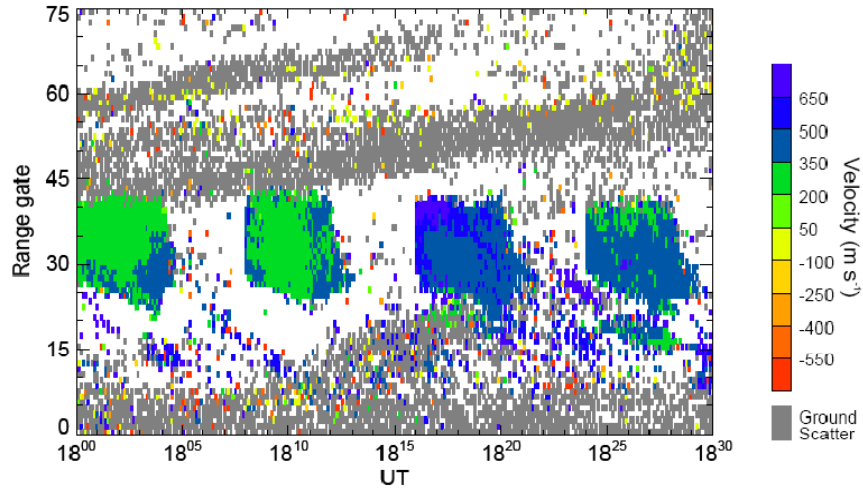
The natural backscatter arises from irregularities which are above the noise threshold of the radar and are observed when the heater is ‘off’, while artificial backscatter is that which arises from the excitation of naturally-occurring instabilities by the action of the heater, previously too weak to exceed the noise threshold to be observed by the radar.

There is large variability in the fitted spectral widths of the artificial backscatter observed in the Iceland data (upper panel, Figure 6.1(c)). During the initial part of the first ‘on’ from 1800-1804UT, it can be seen that relatively high ($>100 \text{ m s}^{-1}$) spectral widths are fitted but this width subsequently diminishes to only 10-20 m s^{-1} or less, which are more typical values for artificial HF backscatter. However, the spectral widths during the second and third ‘on’ intervals exceed 100 m s^{-1} and remain high across all the range gates where artificial backscatter was produced. The corresponding spectral widths observed in Finland beam 5 (lower panel, Figure 6.1(c)) are consistently low at around 10 m s^{-1} and no broadening of the artificial backscatter appears even though there is underlying natural backscatter present. This leads to the unusual circumstances of high artificial backscatter spectral width being measured in one direction but low width in a direction almost orthogonal to it.

The backscatter power, velocity and spectral widths measured in the Iceland beams 13, 14 and 15 are compared in Figure 6.2(a), (b) and (c) respectively over the time interval from 1720 to 1830UT (no CUTLASS Iceland observations were available until 1720UT). FAI appear clearly in the Iceland beam 14 and 15 observations throughout the interval but appear substantially weaker in beam 13 until the heater ‘on’ beginning at 1808UT.

SUPERDARN PARAMETER PLOT
VEL: PYK Beam 15

30 Oct 2000 ⁽³⁰⁴⁾
unknown scan mode (-6318)



SUPERDARN PARAMETER PLOT
VEL: HAN Beam 5

30 Oct 2000 ⁽³⁰⁴⁾
unknown scan mode (-6318)

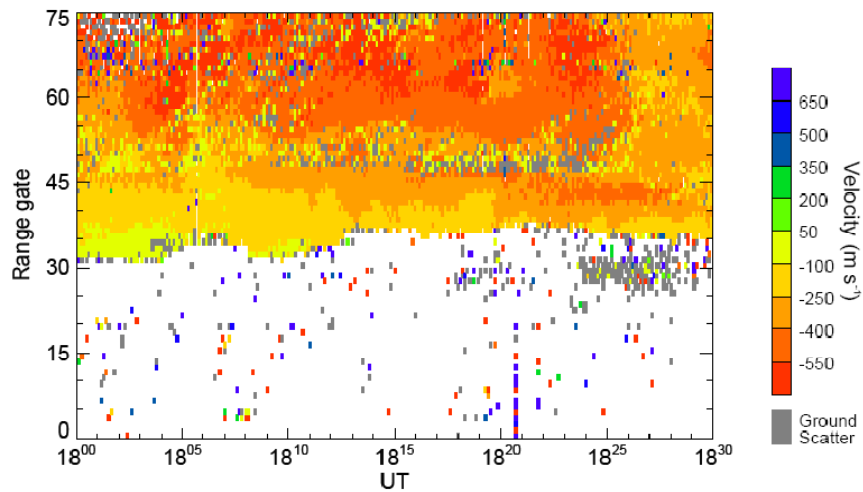
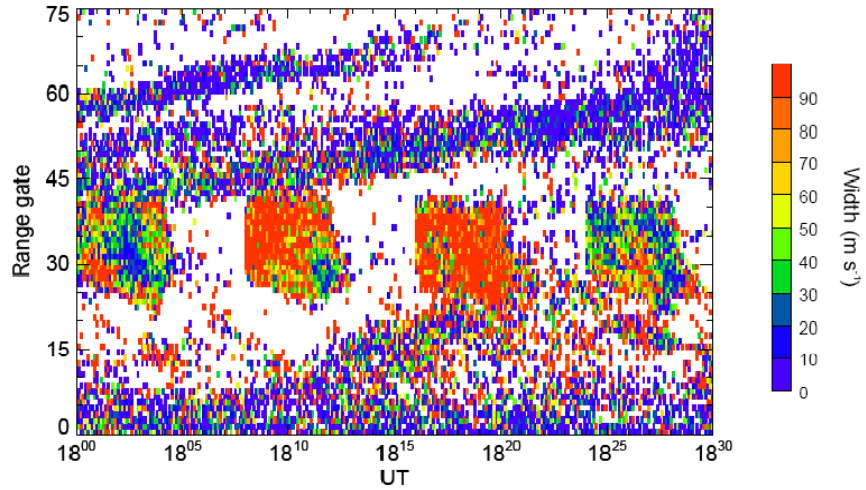


Figure 6.1(b) The range-time plots of the SuperDARN ‘FITACF’ analysis Doppler velocity for the CUTLASS Iceland radar in beam 15 (upper panel) and Finland radar in beam 5 (lower panel), for artificial heating between 1800-1830UT on 30th October 2000.

SUPERDARN PARAMETER PLOT
WIDTH_L: PYK Beam 15

30 Oct 2000 ⁽³⁰⁴⁾
unknown scan mode (-6318)



SUPERDARN PARAMETER PLOT
WIDTH_L: HAN Beam 5

30 Oct 2000 ⁽³⁰⁴⁾
unknown scan mode (-6318)

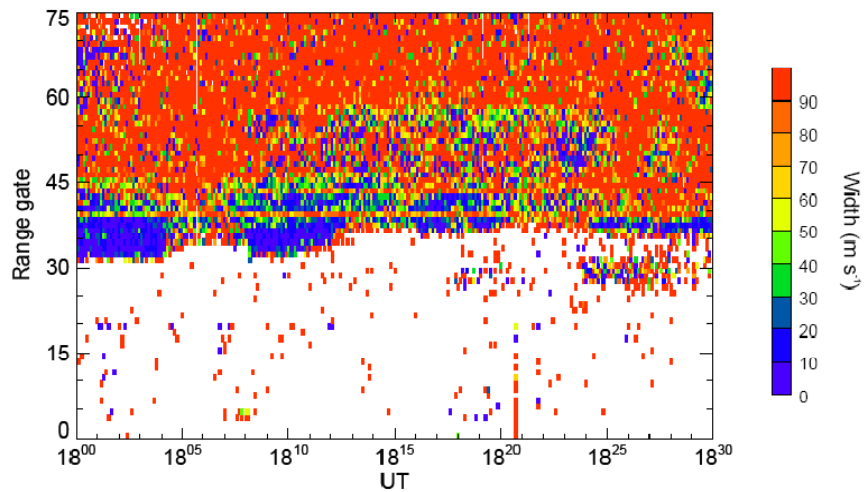


Figure 6.1(c) The range-time plots of the SuperDARN ‘FITACF’ analysis spectral width for the CUTLASS Iceland radar in beam 15 (upper panel) and Finland radar in beam 5 (lower panel), for artificial heating between 1800-1830UT on 30th October 2000.

It is also clear that beam 13 and 14, which are situated northwards of beam 15, measure spatially extensive regions of naturally-occurring irregularities, located closer to the radar than the artificial irregularities, and whose backscattered power is typically an order of magnitude (~ 10 dB) higher in beam 13 than in beam 14. This natural backscatter did not appear in beam 14 until after 1800UT.

The mean measured flow velocities are compared in Table 2 for each of the Iceland beams for the natural scatter (heater ‘off’) and the FAI (heater ‘on’). It is clear that the flow speed of FAI measured in beam 13 is consistently higher than in beam 14 and 15, which at first seems puzzling, since FAI known to move with the background plasma. The apparent discrepancy is likely to be due to the superposition of natural scatter and artificial scatter from differing latitudes but identical ranges, within the same broad radar beams. Hence, the backscattered signal at the range gate where FAI are observed may be increasingly dominated by underlying natural irregularities flowing at a higher speed which may explain why the FITACF estimate is biased toward a higher flow speed due to the stronger presence of natural irregularities observed in beam 13 and 14.

The spectral widths, illustrated for each Iceland beam in Figure 6.2(c) show that the artificial backscatter spectra were broad in beam 13 for most of the period between 1720 to 1830UT, the exception being that there were a few narrow widths measured for the FAI produced in the heating from 1752 to 1756UT. For beam 14, prior to 1800UT there was little natural backscatter present and the measured widths were quite typical of artificial irregularities. However, after 1800UT, the beam 14 spectral widths increased to 100 m s^{-1} or more, typical of naturally-occurring irregularities. The arrival of natural irregularities after 1800UT thus happened to coincide with the distinct and persistent increase in the measured artificial irregularity widths in beam 14.

Beam Number	Mean Flow Velocity (Heater off)	Mean Flow Velocity (Heater on)	Difference between 'on' and 'off'
13	$899 \pm 39 \text{ m s}^{-1}$	$570 \pm 126 \text{ m s}^{-1}$	$\sim 330 \text{ m s}^{-1}$
14	$682 \pm 23 \text{ m s}^{-1}$	$473 \pm 101 \text{ m s}^{-1}$	$\sim 210 \text{ m s}^{-1}$
15	N/A (no backscatter)	$370 \pm 70 \text{ m s}^{-1}$	

Table 2. Comparison of the mean Doppler velocity measured in Iceland beams 13, 14 and 15 at range gate 31, averaged over all heater 'off' and heater 'on' intervals between 1800-1830UT. The exception to this is for beam 13, where the averaging during heater 'on' was only performed using the intervals from 1808-1812UT and 1816-1820UT when FAI were strong enough to be detected in the backscatter power measurements. Insufficient backscatter was available during the heater 'off' intervals observed in beam 15, and hence no mean velocity was deduced here

SUPERDARN PARAMETER PLOT

30 Oct 2000 ⁽³⁰⁴⁾

PWR_L: PYK Beam 13,14,15

unknown scan mode (-8318)

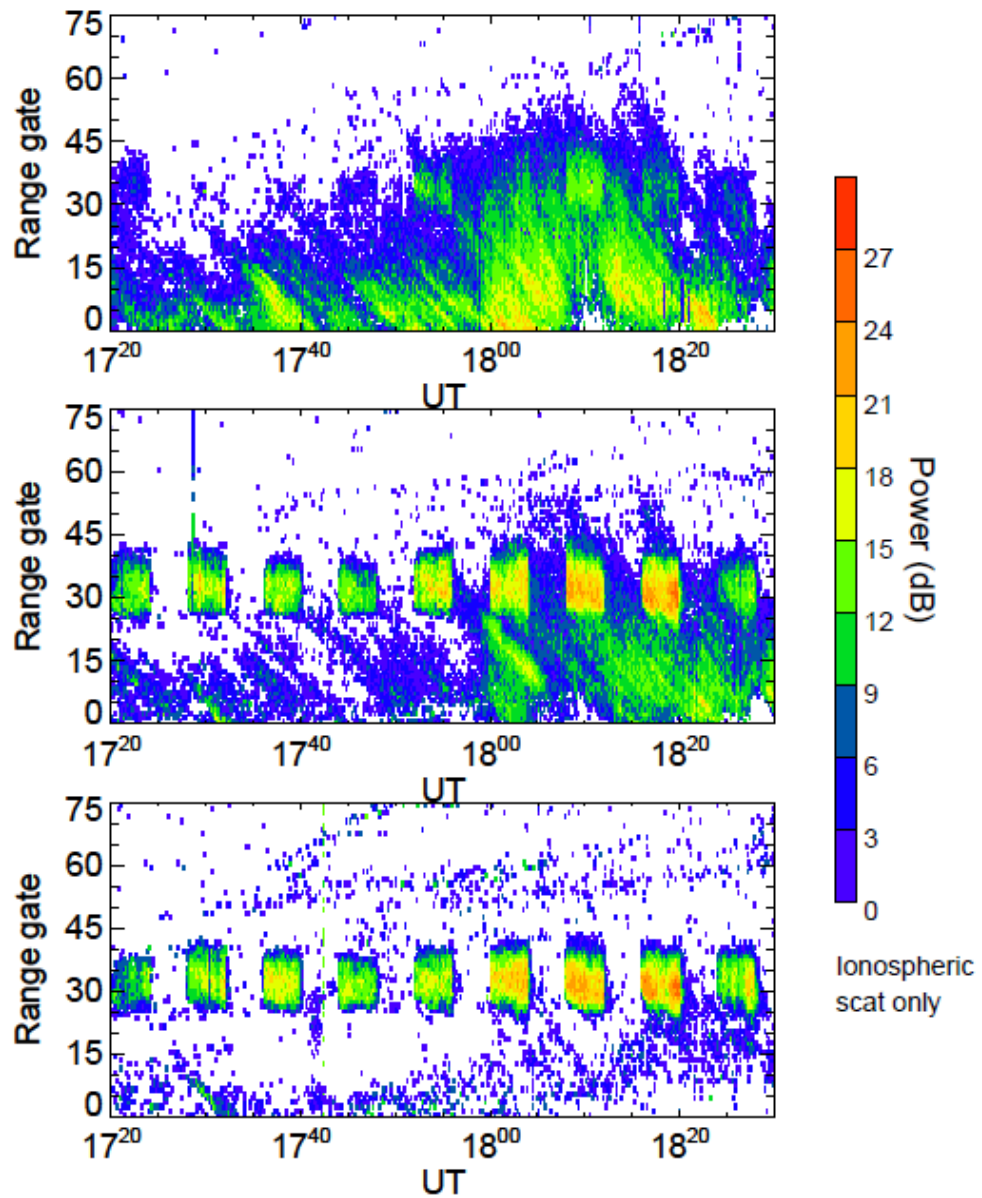


Figure 6.2(a). The upper to lower panels show a comparison of the FITACF backscatter power derived from beams 13 (upper), 14 (centre) and 15 (bottom) of the Iceland radar respectively plotted from 1720UT, before the interval of interest to 1830UT. Here, one may note the stronger presence of natural scatter in beams 13 and 14 as compared to beam 15 which is centred over the Tromsø heater.

SUPERDARN PARAMETER PLOT

30 Oct 2000 ⁽³⁰⁴⁾

VEL: PYK Beam 13,14,15

unknown scan mode (-8318)

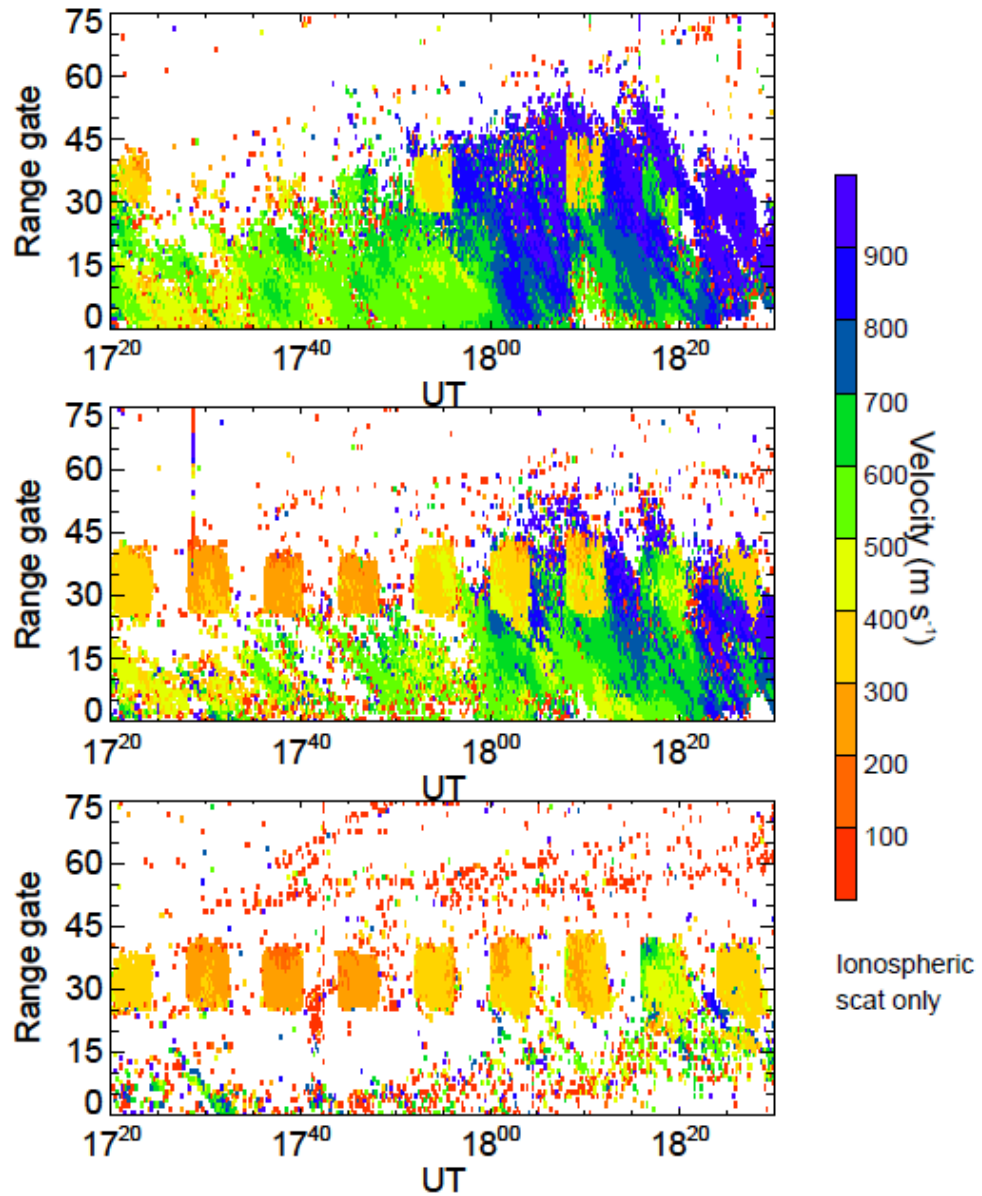


Figure 6.2(b) The corresponding FITACF Doppler velocities for the same interval as shown in Figure 6.2(a) for beams 13, 14 and 15 of the CUTLASS Iceland radar. Only ionospheric scatter echoes have been plotted in these panels.

SUPERDARN PARAMETER PLOT

30 Oct 2000 ⁽³⁰⁴⁾

WIDTH_L: PYK Beam 13,14,15

unknown scan mode (-8318)

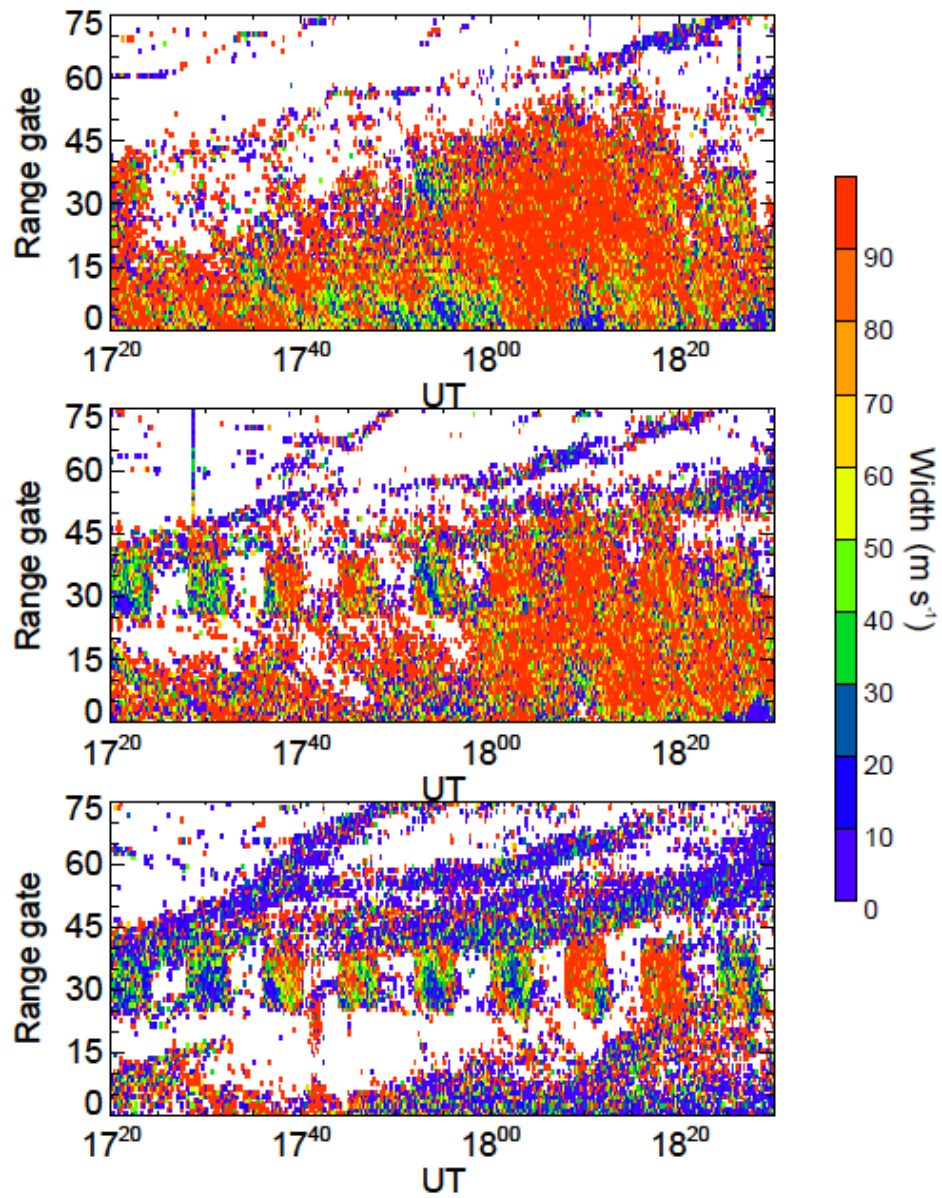


Figure 6.2(c) The FITACF spectral widths for the interval as shown in Figure 6.2(a) and (b) for beams 13, 14 and 15 of the CUTLASS Iceland radar

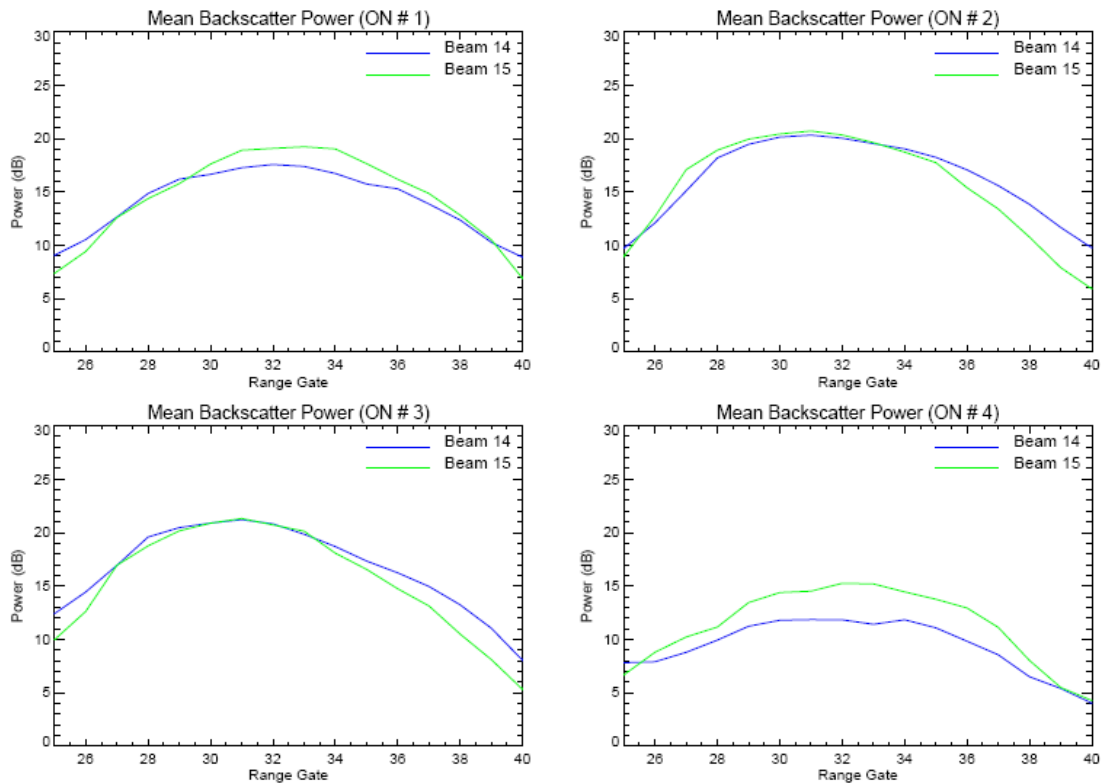


Figure 6.3 Mean backscatter power at all range gates where artificial backscatter appeared, for beams 14 and 15, averaged over each heater ‘on’ interval between 1800 and 1830UT (beginning at 1800, 1808, 1816 and 1824UT). The maximum averaged power measured in beam 15 were 19.2 ± 2.0 dB, 20.7 ± 1.8 dB, 21.3 ± 2.9 dB and 15.2 ± 3.1 dB for each heating, typically at range gate 31 or 32. The corresponding maximum averaged powers measured in beam 14 were 17.6 ± 1.6 dB, 20.3 ± 1.7 dB, 21.2 ± 2.8 dB, and 11.8 ± 2.2 dB respectively, implying the beam 15:beam 14 power ratio was near unity for the first three heater ‘on’ periods, so the heated volume was almost equidistant from the modelled centres of beam 15 and beam 14. The exception to this is for the heater ‘on’ beginning at 1824UT, when the heater beam direction changed from 0 to -12° S, resulting in a beam 15 to beam 14 power ratio of about 1.3, consistent with a heated region shifted further south and therefore closer to the centre of beam 15.

Similarly, this change in the spectral width also occurred at about 1800UT in the beam 15 observations. Some low spectral widths were observed during part of the heater ‘on’ periods between 1800-1804UT and 1824-1828UT in beam 15 but remained broad for the majority of the 1800-1830UT interval. However, the difference between the beam 14 and beam 15 observations is that there is no evidence of underlying natural irregularities which would be expected to be present when the heater was ‘off’.

It is the increased spectral widths in beam 15 in the absence of any obvious natural backscatter and the asymmetry in the spectral width measured at Iceland and Finland which are studied in this chapter. The objective is to investigate how naturally-occurring flows and irregularities in the plasma may influence the CUTLASS HF backscatter characteristics from FAI through studying the radar spectra properties. The Burg spectral analysis technique is chosen to deduce whether the increase in the spectral widths with respect to typical artificial irregularity spectral widths can be explained by multiple component HF backscatter spectra, as previously studied for natural backscatter (Schiffler et al., 1997; Huber and Sofko, 2000). The Burg method which was applied is described in Appendix 5.

6.5 Results of the Burg Spectrum Analysis

In Figure 6.4 examples of the CUTLASS Iceland spectra where the Burg analysis resulted in a double-peaked spectrum meeting the imposed criteria are illustrated. The time interval of these examples is between 1808-1810UT (18.133-18.158UT expressed in decimal hours in the figure) at range gates 32, 33 and 34, therefore corresponding to the first two minutes of the second heater ‘on’ period which began at 1808UT. Figure 6.4 shows that the relative amplitude of the Burg peaks can be highly variable, and unrelated to the velocity separation of the peaks or the absolute magnitude of the velocity component. In the majority of the cases, the conventional Fourier Transform spectrum (black dashed curves) did not resolve the peaks detected by the Burg method, as indicated where two Burg components appear to originate from within a broad, single peak in the Fourier spectrum. Hence, where certain spectral components might be masked through conventional methods of obtaining spectra from ACFs, these can be resolved using the Burg analysis.

The Burg analysis was also performed on beam 13 and beam 14 ACFs of the Iceland radar, and beam 5 ACFs of the Finland radar. The Iceland beam 14 results are shown in Figure 6.6(a) to Figure 6.6(f) and the Finland beam 5 results in Figure 6.7(a) to (f) but it is the results from Iceland beam 15 which are concentrated on in this chapter since it is these observations where increased spectral width in the absence of natural backscatter was observed, as well as asymmetry with respect to the Finland observations.

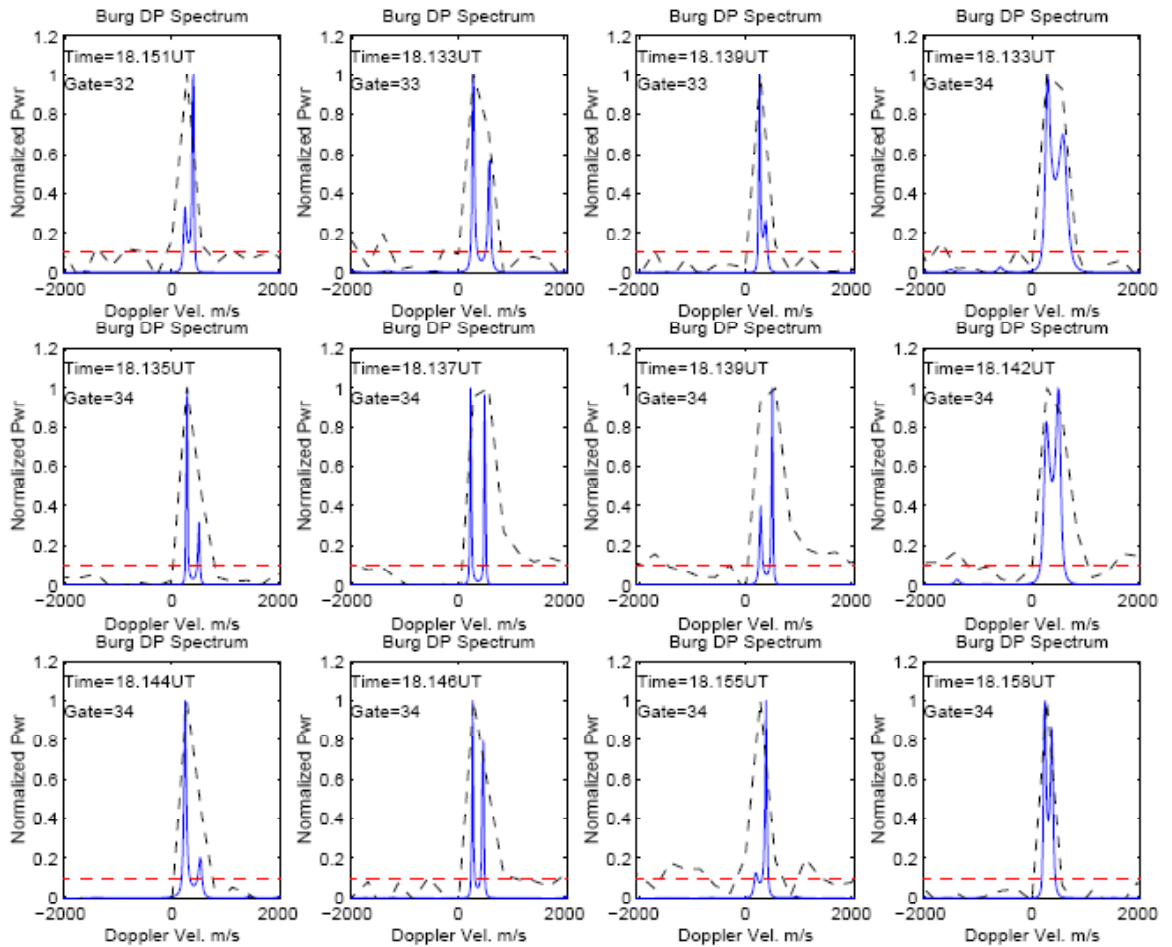


Figure 6.4 Examples of the Burg spectrum and the equivalent Fourier Transform spectrum where a double-peaked Burg spectrum was identified, in the interval from 1808-1810UT occurring in the range gates 32 to 34. The solid blue curve shown is the Burg spectrum computed from the CUTLASS Pykkvibaer ACF, and the dashed black curve is the Fourier Transform spectrum. The threshold amplitude of the second peak is indicated by the dashed red line, and the time given as decimal UT and the range gate of the spectrum is printed in the top left hand corner of each plot

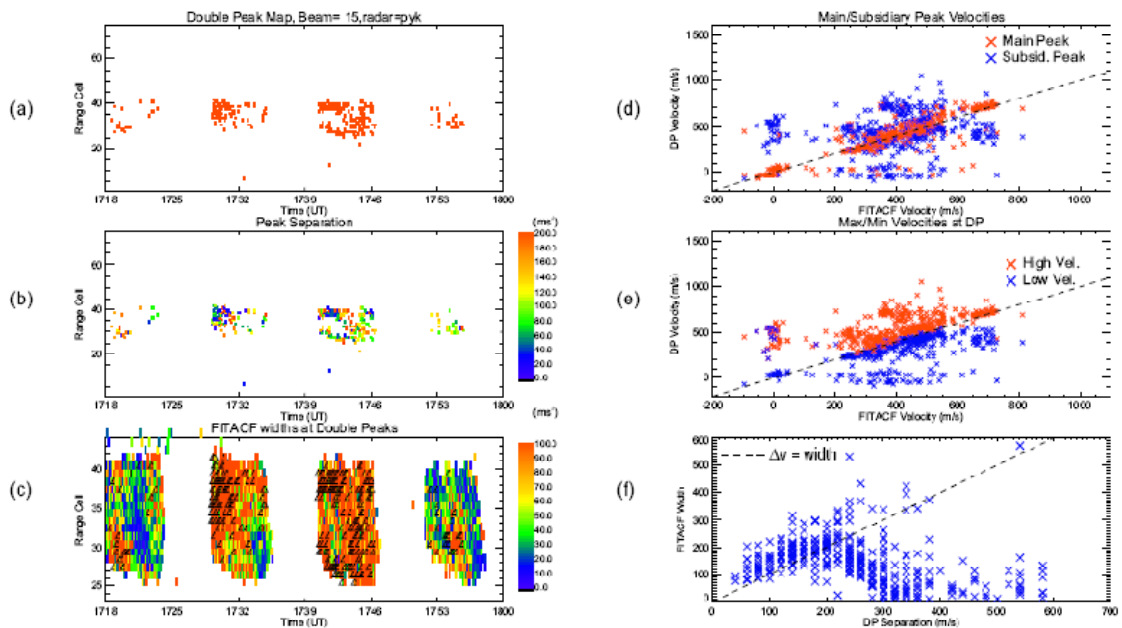


Figure 6.5. Results of the Burg double-peak spectrum analysis shown in (a) as a range-time ‘map’ of the occurrences in the beam 15 data of the Pykkvibaer radar, where the power was also above 7dB, since previous authors have noted that observations of increased width at low backscatter power could be considered as an effect of a decrease in signal to noise ratio (Huber and Sofko, 2000) (b) the occurrences colour-coded according to the velocity difference of the two Burg peaks (c) range-time-width plot of the FITACF spectral widths with black triangles overlaid at the positions where double-peaked spectra were identified, (d) the velocity of the main (red) and subsidiary (blue) peaks plotted against the FITACF velocity, (e) the high (red) and low (blue) velocities of the two peaks plotted against the FITACF velocity and (f) the FITACF width shown as a function of the velocity separation of the two peaks. Plots (a) and (c) essentially display the same information, but in plot (c) the double-peak spectrum occurrences have been overlaid as black triangles on the FITACF range-time-width results and the limits of the y-axis have been restricted to only the range gates where artificial backscatter was detected

Figure 6.5(c) indicates there are similarities between the times and range cells where the spectral widths appear to be broadened and the occurrence of double-peaked spectra. However, there are also a few occurrences of double-peaked spectra where low spectral width is measured. For example, at the beginning of the heating at 1824UT at around range gate 38, there is a relatively low fitted spectral width but this also coincides with the identification of double-peaked spectra, as marked by the black triangular symbols. The Burg analysis also revealed (but not shown here) that prior to 1800UT when the spectral widths observed in Beam 14 and 15 had been predominantly narrow with some short periods of broadening appearing in the artificial backscatter, substantially fewer – if any, double-peaked spectra were identified. Those which were detected tended to occur when the spectral widths were more enhanced. The appearance of natural backscatter in beam 14 after 1800UT, taken with the simultaneous and persistent broadening of the radar spectra and appearance of double-peaked spectra may imply some connection between the features, as will be discussed in the following section.

Figure 6.5(e) shows the Burg peak velocities plotted against the FITACF velocity, with the red crosses corresponding to the highest velocity (Burg) component and the blue crosses corresponding to the lower velocity peak. There is much scatter, almost symmetrically about the line indicating where the Burg and FITACF estimates would be equal. The discrepancy between the FITACF velocity and the two peak velocities can be several hundred metres per second, with largest ambiguity in components that are close to 0 m s^{-1} . Those data points where the FITACF velocity is around 0 m s^{-1} match the lower velocity peak of the double-peaked Burg spectrum most closely while the higher velocity peak can be in excess of 500 m s^{-1} , so there can be a significant difference between the two types of estimate.

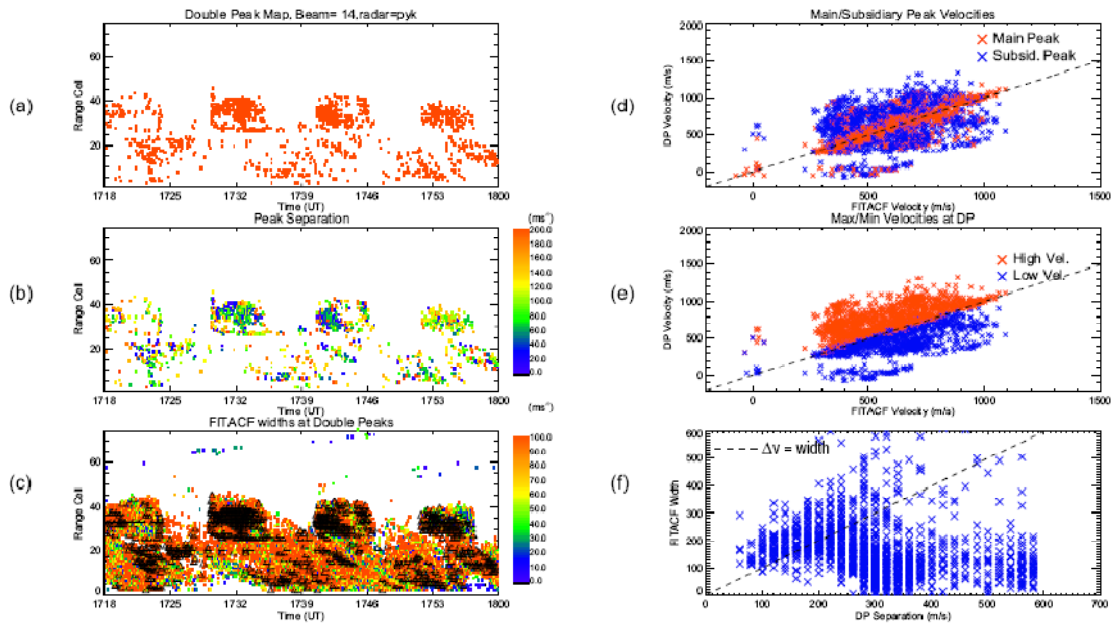


Figure 6.6. Results of the Burg double-peak spectrum analysis are shown in (a) as a range-time ‘map’ of the occurrences in the beam 14 data of the Pykkvibaer radar, where the power was also above 7dB, (b) the occurrences colour-coded according to the velocity difference of the two Burg peaks (c) range-time-width plot of the FITACF spectral widths with black triangles overlaid at the positions where double-peaked spectra were identified, (d) the velocity of the main (red) and subsidiary (blue) peaks plotted against the FITACF velocity, (e) the high (red) and low (blue) velocities of the two peaks plotted against the FITACF velocity and (f) the FITACF width shown as a function of the velocity separation of the two peaks. Plots (a) and (c) essentially display the same information, but in plot (c) the double-peak spectrum occurrences have been overlaid on the FITACF range-time-width results

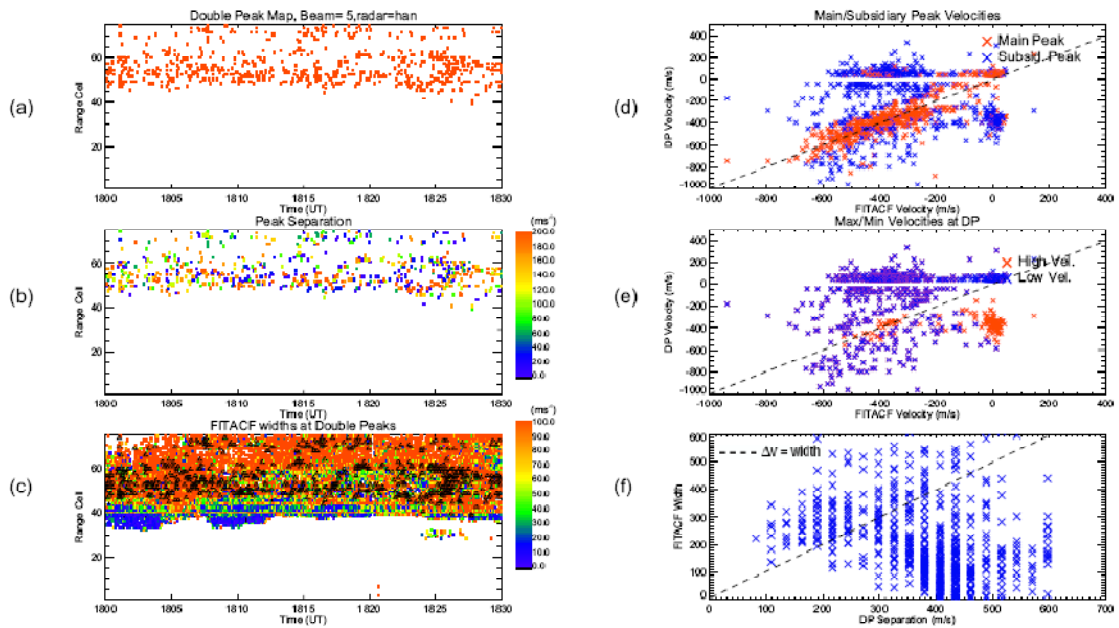


Figure 6.7 Burg double-peak spectrum analysis results for the Beam 5 spectra of the Hankasalmi radar. The panels are displayed in the arrangement as for (a) to (f) as shown in Figure 6.5 and Figure 6.6. It is apparent here that the double-peaked nature of the Pykkvibaer spectra are aspect-dependent, such that the look-direction of the Hankasalmi radar is not sensitive to the same flow components affecting the Pykkvibaer data

Similarly, when the lower velocity Burg peak is close to 0 m s^{-1} , the FITACF estimates are scattered between 0 m s^{-1} to 700 m s^{-1} . Figure 6.5(d) shows the FITACF velocity plotted against the velocity of the Burg peaks which are colour-coded by the Burg spectral amplitude (as opposed to the velocity magnitude). The data points lying closest to the equality line are those where the FITACF velocity is in agreement with that of the strongest peak in the Burg spectrum and the subsidiary peak velocities are represented by the data points that deviate far from this line.

In Figure 6.5(f) it can be seen that the FITACF width increases more or less linearly with the Burg peak separation for velocity difference of up to 200 m s^{-1} , also consistent with the results of Danskin et al. (2004). Beyond this value the large majority of data points show a decreasing FITACF width at larger peak separations, or for two spectral components which have a small difference in their ACF decorrelation times. This trend would suggest that for two-component ACFs which are decorrelating at similar rates, the FITACF method estimates a spectral width which is representative of an average of the two components rather than being biased toward one or the other, if there was a large difference between their rates of decorrelation. Coincidentally, the typical resolution of the Fourier transform spectrum is also of the order of 200 m s^{-1} (depending on the radar frequency) which may add support to this interpretation. Additionally, if this is the case then it would explain the presence of double-peaked Burg spectra with low FITACF widths when the separation of the peaks is sufficiently large.

Histograms of the peak separation of the two Burg spectral components were also examined for beams 13, 14 and 15 of the Iceland data and are illustrated in Figure 6.8. It is clear that the beam 13 and beam 14 spectra are most numerous for peak separations in the $280\text{-}330 \text{ m s}^{-1}$ range, with a small proportion of double-peaked echoes whose

peaks are separated by more than 400 m s^{-1} . In contrast, the beam 15 distribution consists of a broad peak across the range from approximately $100\text{-}200 \text{ m s}^{-1}$, and separations of over 400 m s^{-1} are almost non-existent.

However, in order to assess whether there were any differences between the distributions of the Burg peak separation from the double-peaked echoes inside and outside of the usual heated volume, the measurements were spatially separated into those occurring between range gates 0 to 25 and 26 to 45. Gates 0 to 25 represent the region in beams 14 and 15 where predominantly natural backscatter is observed and the latter (26 to 45) where artificial irregularities were observed. In beam 13, these regions lie at approximately gates 0 to 30 and 31 to 50, as can be deduced from the stark contrast in flow velocities of the two range regions in Figure 6.2. A further temporal filtering was applied to those occurrences in the range gates 26 to 45 (31 to 50) so that only double-peaked echoes present during each heater ‘on’ interval were counted as those from FAI inside the heated volume. The range-separated histograms for each beam are illustrated in Figure 6.9.

For the beam 13 echoes, the ‘natural’ double-peaked echoes (red) and also those from FAI (blue) peak in the range $280\text{-}330 \text{ m s}^{-1}$. However, the distribution of the artificial echoes also possesses a greater proportion of double-peaked spectra with larger peak separations. The relative proportion of echoes below 250 m s^{-1} is much less than that of the ‘natural’ double-peaked echoes. For beam 14, the peak separation distributions of both the natural-only and artificial echoes are virtually identical with comparable numbers of double-peaked echoes in each bin, and the peak of both distributions lie in the $280\text{-}330 \text{ m s}^{-1}$ range. However, there are also more echoes with separations below 250 m s^{-1} , when compared to those in beam 13. In the beam 15 distributions there are

very few ‘natural’ double-peaked echoes due to the absence of naturally-occurring backscatter detected across range gates 0 to 25. The distribution of double-peaked echoes from FAI peaks at a smaller velocity difference of around 150 m s^{-1} when compared with the FAI distributions for beams 13 and 14.

Figure 6.9 suggests that double-peaked Burg spectra detected within the usual heated volume exhibit an apparent latitudinal dependence in the Iceland radar observations. This is deduced from the higher proportion of double-peaked spectra with smaller peak separations in beam 15 than in beam 13, whose main lobe is centred northwards of beam 15 and the greater number of FAI-related echoes at larger peak separations in beams 13 and 14. The apparent difference in the mean FITACF velocity of the natural and artificial backscatter observed by the CUTLASS Iceland radar of around 330 m s^{-1} in beam 13 and 210 m s^{-1} in beam 14 is not dissimilar to the dominant Burg peak separations in beam 13 and 14 that were identified here. The relation between this latitudinal dependence of the Burg peak separation and the FITACF velocity difference between the two types of backscatter is explored in the next section.

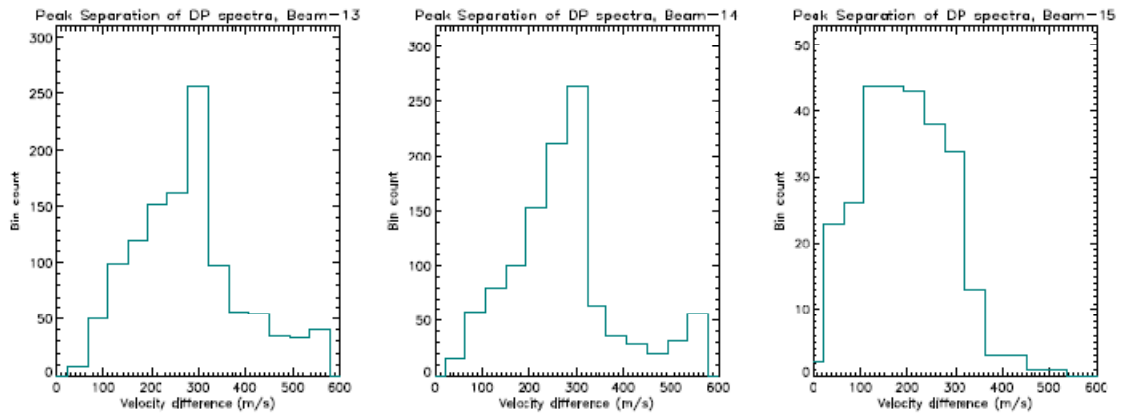


Figure 6.8. Histograms illustrating the distribution of the velocity difference between the two peaks of double-peaked Burg spectra, restricted to the range $0\text{--}600\text{ m s}^{-1}$ and shown from left to right for beams 13, 14 and 15 respectively

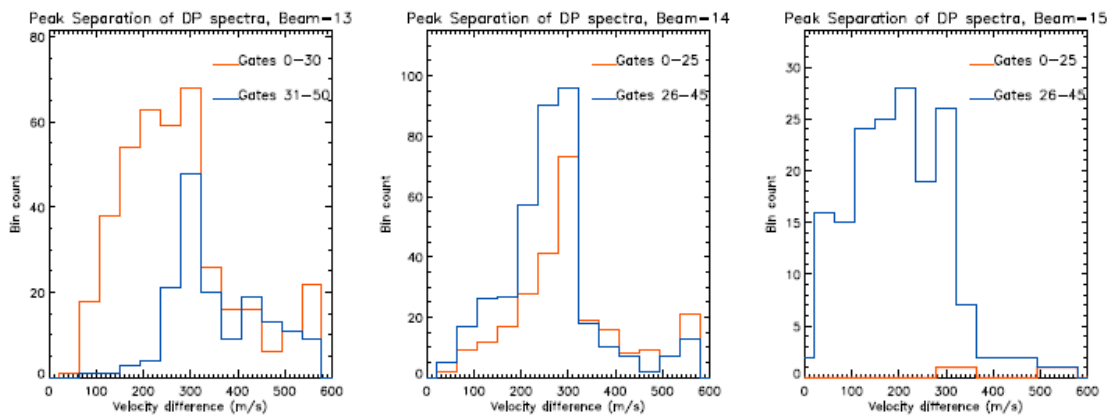


Figure 6.9. Histograms illustrating the distribution of the velocity difference between the two peaks of double-peaked Burg spectra, separated into the two spatial regions corresponding to artificial scatter and natural scatter, which for beam 13 was range gates 0 to 30 and 31 to 50 respectively, and for beams 14 and 15, gates 0 to 25 and 26 to 45 respectively. Double-peaked echoes included in the distributions have been confined to those in the range $0\text{--}600\text{ m s}^{-1}$ and shown from the left to the right hand panels for beams 13, 14 and 15.

6.6. Discussion

6.6.1 Comparison with Previous Work

It has been reported in previous literature that the occurrence of double-peaked spectra can arise due to the radar simultaneously accessing two spatially separated regions of the ionosphere at the same group range, which thus produce two spectral components (Huber and Sofko, 2000). These authors considered the possibility that the spatial separation may be an altitude difference due to the finite vertical beam width of the radar or a horizontal difference, and also the possibility of two backscatter sources separated in azimuth arising from signals detected by the side antenna lobe as well as the main beam. It was suggested that this effect would produce double-peaked spectra which were relatively long-lived features, since the radar propagation mode should not change rapidly. The observations of double-peaked spectra in this study also appear to persist over several integration periods at all ranges where they were observed.

Danskin et al. (2004) noted in their study of naturally-occurring E-region double-peaked echoes, that if the additional flow component was detected by the side antenna lobe, then a decrease in the separation of the two spectral peaks would be expected with the beam directions, because of a change in the line-of-sight component of the background flow vector. However, their observations were made using the CUTLASS Finland radar, whose beam directions point roughly polewards. Hence, individual Finland beams integrate longitudinally and would therefore not superpose different flows, which tend to arise latitudinally. Therefore it would not be possible to apply the same argument to the results presented here because the different beam directions of the CUTLASS Iceland radar are equivalent to a latitudinal variation in the flow velocity rather than a variation in the magnitude of the line-of-sight flow component.

Nevertheless, the peak separation distribution of the double-peaked spectra from the artificial backscatter in this study did indeed vary between beams 13, 14 and 15.

Blagoveshchenskaya et al. (2006), proposed that drift waves may give rise to two modes of pump wave propagation and thus produce FAI spatially separated in altitude and azimuth and travelling at different flow speeds. This was suggested to explain the observed splitting of the Doppler spectra, where the typical shift of the peaks from a median value was between 0.2-0.8Hz. Hence, the maximum separation of the peaks here could not be more than about 2Hz. This contrasts with the typical peak separation found in this study of around 300 m s^{-1} in the Iceland beam 13 and 150 m s^{-1} in beam 15, equivalent to a frequency difference of 12Hz and 6Hz respectively. Therefore it is unlikely that their mechanism could explain the present observations.

In another study already mentioned, the splitting of the HF Doppler spectra from artificial backscatter was attributed to radial drift of the irregularities (Koloskov et al., 2002). However, the double-peaked spectra occurred in a restricted spatial region in the centre of the heated volume whereas those which were observed in this study were identified at times to exist only at the edges and at other times across the whole of the heated volume. The same authors also noted a three-stage temporal development in the properties of their double-peaked spectra, where peak separation maximized during the 'stationary' period after the initial growth of the irregularities. No such temporal development was found in the peak separation distribution of the present observations. Also, this mechanism should produce double-peaked spectra in all directions which is not the case here. Therefore, because both the spatial and temporal characteristics of the double-peaked spectra shown in this analysis differ from those presented by Koloskov et al. (2002), the radial drift model is unlikely to explain the occurrence of double-

peaked HF artificial backscatter spectra found here. Furthermore, the splitting observed in the aforementioned study produced spectral widths which ranged from 0.5 to 1Hz, which is significantly less than those observed in this study by an order of magnitude.

Double-peaked spectra have also been attributed to vortical structures associated with particle precipitation (Huber and Sofko, 2000; Schiffler et al., 1997), but as with the radial drift model, they would be expected to enhance the spectral widths in any direction of observation, and the observed asymmetry identified in this study suggests that the broadening cannot be attributed to this mechanism.

A final consideration must be given to the observation of Ponomarenko et al. (1999), that heating just above harmonics of the electron gyrofrequency can increase spectral width of scatter from FAI to values typically around 5Hz . In the experiment reported in this chapter, the heater operated at 4.04 MHz which is close to the third electron gyroharmonic and spectral widths were comparable to those reported by Ponomarenko et al. (1999). However, pumping at gyroharmonics is also known to suppress upper hybrid turbulence and hence FAI growth which would lead to reduced HF backscatter (Honary et al., 1999). In contrast, both the Finland and Iceland radars observed strong artificial backscatter throughout the heating interval here, suggesting the heater frequency was not at the gyroresonance itself. Unfortunately it cannot be determined if the heater frequency was just above or below the resonance since the exact value of the gyrofrequency is not known and can generally vary between 1.3-1.4MHz. But, there is no reason to suppose that the results of Ponomarenko et al. (1999) would be aspect-sensitive and hence an explanation for the anisotropic broadening results remains to be found. In the following section, other possible explanations are considered.

6.6.2 Other possible factors

There are major features in the results presented in this chapter which cannot be explained by the mechanisms offered previously, the most significant being that the high artificial backscatter spectral widths were only observed by one of the CUTLASS radars. One feature of the data certainly worth considering is the large difference between the flow velocities in the artificial and natural backscatter, measured in beam 13 and beam 14 of Iceland. The flow speed of the artificial irregularities appeared several hundred m s^{-1} lower when the heater was 'on' than that of the natural irregularities when the heater was 'off' as shown in Figure 6.2. This reduction in speed cannot be a real effect but most probably due to the detection of artificial backscatter at the edge of beam 13 which was not only located at a lower latitude but also moving at a lower speed. This interpretation is illustrated schematically in Figure 6.10, showing the geometry of the naturally-occurring and artificial irregularities produced by the Tromsø heater and how the two types of backscatter may be spread across beams 13, 14 and 15.

The 'simultaneous' detection of two types of backscatter could occur if the product of the beam gain with the artificial irregularity amplitude was either comparable to, or exceeded that of the natural irregularities which were present in the centre of beam 13 where the beam gain was actually strongest and this idea is illustrated with the aid of Figure 6.11. The distance from the bore sight of the Iceland radar to the heated volume (around range gate 31) is of the order of 1900km.

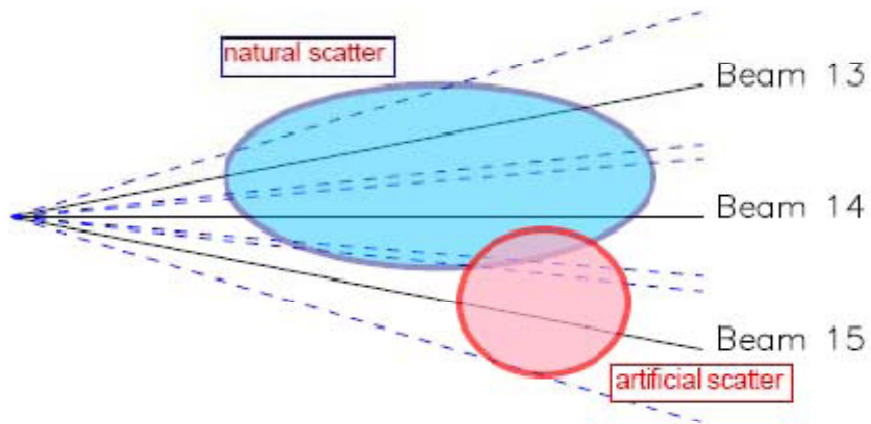


Figure 6.10 Schematic to show how natural scatter detected in beams 13 and 14 is located in relation to the artificial scatter measured in beam 15. In this scenario it is anticipated that the natural scatter is much weaker than the artificial scatter that lies at the edge of the main lobe or even in the side lobe of beam 13 and 14, but at the range of the artificial scatter, beams 13 and 14 measure an ACF (spectrum) that corresponds to the characteristics of the artificial irregularities.

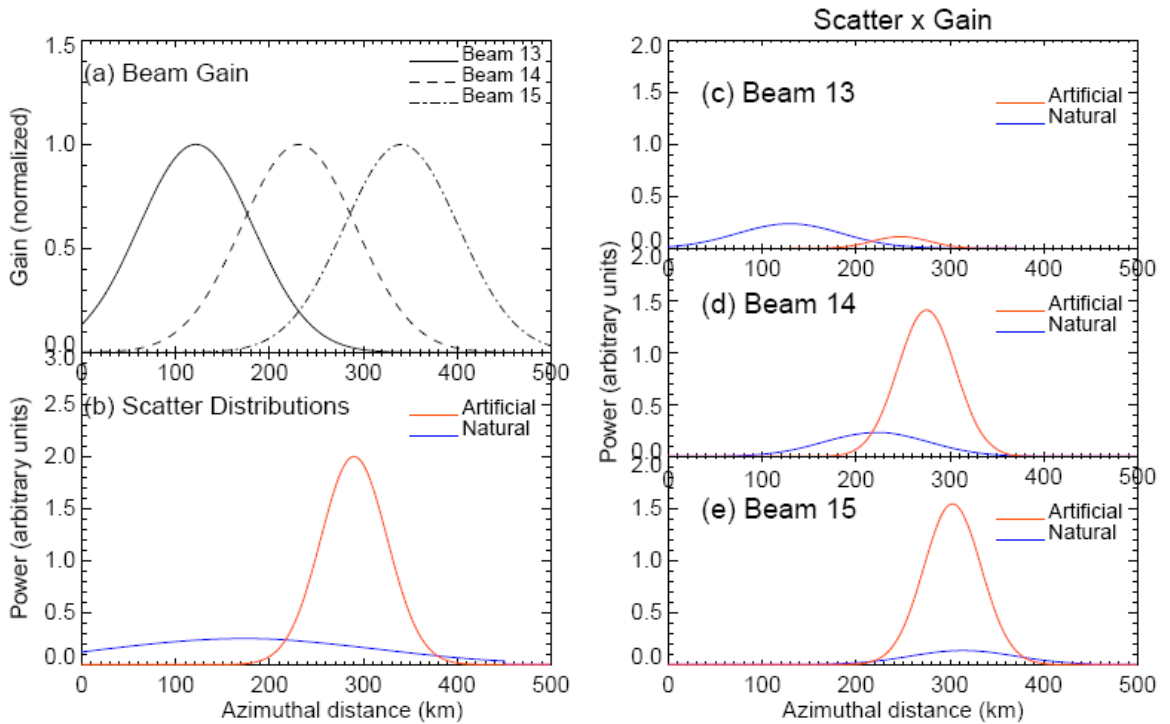


Figure 6.11 An illustration to show how artificial scatter may be detected at the edge of beam 13 of the Iceland radar where the antenna gain is comparatively weak; (a) shows how the main beam gain may overlap for beams 13, 14 and 15 due to the finite spread of the beam at a distance of around 1900km from the radar bore site (\sim range gate 31); (b) is a simple Gaussian illustration of the natural and artificial scatter distributions; (c), (d) and (e) are respectively the product of the main beam gain and the artificial and natural scatter power distributions for beams 13, 14 and 15.

The spatial spread may be approximated using this distance and the beam width of 3.6° . Panel (a) shows the azimuthal (latitudinal) distribution of the gain of beams 13, 14 and 15; (b) illustrates the region of natural irregularities (blue), which are a relatively weak, but spatially broad background in comparison to a much stronger localized region of artificial scatter (red).

The power variations of the artificial and natural backscatter are considered as Gaussian in character. The product of the gain for each of the main beams, with the scatter distributions of the artificial and natural irregularities is shown in panels (c), (d) and (e) for beam 13, 14 and 15 respectively. In this scenario, the artificial irregularities detected by beam 13 are of comparable amplitude to the natural irregularities across the range gates where artificial irregularities are actually generated. If the contribution to the signal recorded in each beam is the integral of the irregularity amplitude times antenna gain, then it is clear that the spectra in beams 13 and 14 will have significant velocity contributions from the lower latitude artificial irregularities as well as the higher latitude natural scatter which are non co-located populations.

A similar explanation involving non co-located population superposition could be invoked for the double peaks obtained from the Burg analysis of the artificial scatter in beam 15. That is to say, the double peaked spectra may arise through the contamination of the artificial backscatter spectra of beam 15 by the natural irregularity flow component which is of measurable amplitude in beam 13 and 14. In this case the natural backscatter source would be detected either by the edges of the main beam or by the side antenna lobes because the natural irregularities lie to the north of the artificial irregularities in beam 15. However, an obvious weakness of this interpretation is the absence of natural backscatter in the vicinity of the artificial backscatter in the

CUTLASS Iceland beam 15 observations when the heater is both ‘on’ and ‘off’. This suggests that the natural irregularities cannot be strong enough to contribute to the artificial irregularity spectrum at that range gate. This view is confirmed by the model results in panel (e) of Figure 6.11. Therefore one may ask how it should be possible for the natural irregularities to contaminate the artificial backscatter spectra if they are too weak to be visible in the backscatter power measurements?

The action of the heater may lead to enhancement of natural backscatter which is already detectable by backscatter radar (without the heater) and lying well outside the usual heated volume defined by the main lobe of the heater beam (Jones et al., 2001). This is distinguished from the usual case of artificial backscatter which arises from the amplification of natural instabilities which are below the noise threshold of the radar. It is possible that during these experiments, natural irregularities of detectable amplitude in beam 14, but otherwise insufficient amplitude to be detected in beam 15 because they were located too far north, were amplified sufficiently during heater ‘on’ periods, allowing a backscatter power contribution to beam 15 of the Iceland radar.

The backscatter power data measured from Finland was assessed for possible heater-induced amplifications at those range gates where natural scatter was observed to determine whether this was a plausible explanation. The main region of natural scatter lies approximately at range gates 45 to 55 in the Finland beam 5 observations (Figure 6.1(a)) while scatter from FAI occupies mainly range gates 36 to 44. The change in mean backscatter power between each heater ‘on’ and ‘off’ measured at Finland across range gates 36 through to 55 was calculated and is shown in Figure 6.12(a), for each of the heating cycles. The mean ‘off’ power levels were determined using the measurements in the four minutes before each cycle.

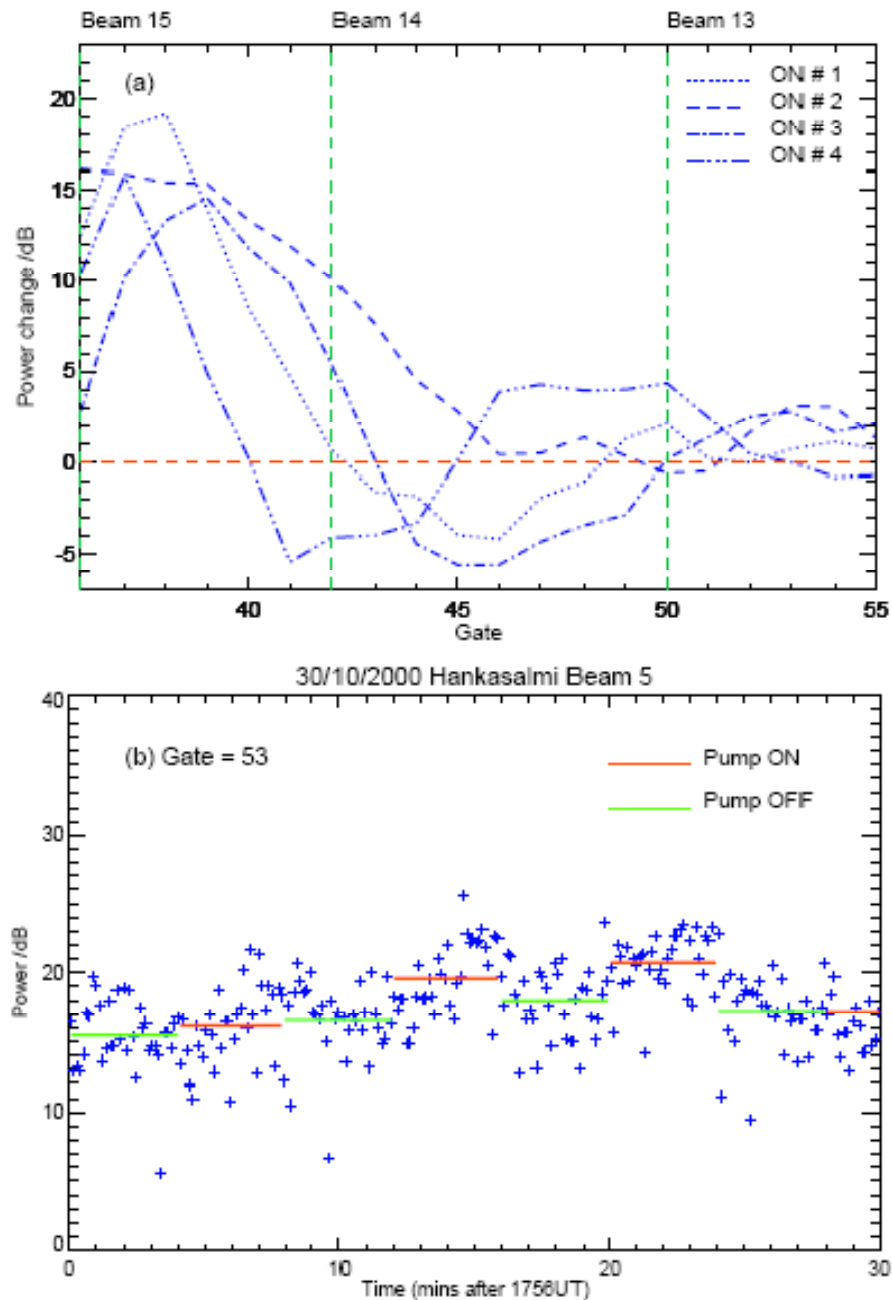


Figure 6.12 (a) The change in backscatter power between heater ‘off’ and ‘on’, measured at range gates 36 to 55 in beam 5 of the Finland radar for the four heating periods beginning at 1800, 1808, 1816 and 1824UT respectively. The green dashed lines correspond to the approximate Finland beam 5 range gates where beam 13, 14 and 15 of the Iceland radar would intersect with beam 5; (b) the change in backscatter power at range gate 53 with the mean power level for each heater ‘on’ (red) and ‘off’ (green)

The region of artificial irregularities is clear from the substantial enhancements of greater than 10dB, occupying range gates 37 to 40. Also evident is a secondary region of smaller enhancements due to the heater being 'on', occurring at gates 52 to 54 for the first three 'on' periods that begin at 1800, 1808 and 1816UT respectively and at closer range gates for the 'on' at 1824UT. This may be traced to a change in the heater beam direction from 0°S to -12°S (field-aligned), leading to a heated region moving closer to the Finland radar and hence the enhancements are shifted to nearer ranges as well.

The spatial separation between the two regions of enhancements of around 14-15 range gates is thus consistent with the expected horizontal spatial separation (~200km) between scatter located in the centres of beam 13 and 15 of the Iceland radar which are separated by around 6.5°. Also indicated are the Finland range gates where beam 13, 14 and 15 of the Iceland radar would intersect with beam 5 of the Finland radar, showing that the strongest artificial irregularities due to the heater actually lie slightly further to the north of the centre of beam 15 (range gate 36), and similarly the region of smaller enhancements of natural irregularities is slightly further north of the centre of beam 13 (range gate 50), which may be around 3dB in magnitude.

Though the enhancements are not significant, the results are indicative of heater-induced amplification of naturally-occurring irregularities lying in faster flow separated from the main region of artificial irregularities by around 14 to 15 range gates. The enhancements also occur during the heating intervals where the most double-peaked spectra were detected in beam 15, beginning at 1808 and 1816UT (Figure 6.5(a)). It is possible that a 3dB enhancement in the backscatter power of these natural irregularities would be sufficient to allow their detection by the edge of the beam 15 of the Iceland radar when the heater is 'on'.

Hence, there is some evidence supporting the interpretation that the double-peaked Burg spectra from FAI produced by the EISCAT heater are a special case of mixed artificial and natural echoes. Additionally, because beam 13 and beam 14 observe not only higher natural irregularity backscatter power but also a greater number of double-peaked spectra and persistently high spectral widths at the range gates where artificial backscatter is produced also supports the argument that greater backscatter power from the natural irregularities would produce more frequent contamination, and thus give rise to the double-peaked spectra. It is emphasised though that this is at present, very much a tentative explanation and the process by which the observations presented here arise, remains an open question since it is clear that a 3dB amplification of irregularities at the latitude of beam 13 would correspond to a marginal difference if detected in beam 15.

6.7 Summary

In this chapter, multi-beam observations of HF backscatter characteristics from the CUTLASS radars during an ionospheric modification experiment carried out at Tromsø, during active geomagnetic conditions have been presented. For the first time, unusual spectral characteristics during these experiments were identified, where spectral widths obtained from the standard SuperDARN FITACF analysis in one radar (Iceland), were considerably broadened by a factor of around ten times compared with corresponding widths seen from the other (Finland) radar. It is significant that the radar beams of the two radars are roughly orthogonal in azimuth, and also that both natural radar aurora, as well as artificial scatter was present simultaneously in all but one of the beams (Iceland beam 15). The Burg maximum entropy technique was applied to all of the observed spectra and found that those that were broadened generally produced double peaks in their corresponding Burg spectra.

In the two approximately eastward pointing Iceland beams where both natural backscatter as well as artificial backscatter was detected (beams 13 and 14), it was possible to account at least semi-quantitatively for the broadening and the Burg double peaks in terms of the superposition of scatter from a slower moving artificial irregularity population located equatorwards of a faster moving population of natural scatterers, within the azimuthally broad beams which were thus sensitive to scatterers from a wide latitudinal range.

A puzzling result was the observation of similarly broadened and corresponding double-peaked Burg spectra in the southernmost beam (beam 15) of the Iceland radar because here, unlike in the two more northerly Iceland beams there was no sign of natural scatter when the heater was off. It was thus hard to conclude that the broadening effect was due to the superposition of scatter from two spatially separated regions, one artificial, one natural, despite the fact that the double peaks in the corresponding Burg spectra were characteristic of the flow speeds seen in the lower latitude artificial patch and the higher latitude natural patch. However evidence was found for heater-induced amplitude enhancements of the natural scatter well outside the usual heated volume. Although this effect could in principle explain why the contributions of the natural irregularities were only seen in Iceland beam 15 when the heater was on, was rather marginal in terms of amplitude. Hence the evidence for the superposition of slow artificial and faster natural populations of scatters is somewhat circumstantial at present, and definitive confirmation of what is at the moment speculation, may have to await further experimentation in the future.

Chapter 7

Summary of Major Results

7.1 Introduction

The key scientific results of this thesis have been demonstrated through the use of both experimental observations and application of theoretical and numerical models. Experimental observations made during a large number of heating experiments carried out using the EISCAT heating facility since 1996 have contributed to the work of this thesis. Specifically, it has long been known that incoherent scatter spectra measured by the EISCAT UHF radar are strongly affected by plasma instabilities excited by high power radio waves but no attempts to date had been made to parameterise the effects or quantify their influence on the inferred plasma parameters. The EISCAT UHF radar played a very large part in the earlier investigations presented in this thesis. The CUTLASS radars were used as the primary diagnostic in the latter two chapters. These studies focused on the temporal and spatial characteristics of the irregularities and an experimental heating campaign carried out in April 1996 was found to give rise to more complicated temporal behaviour in the irregularities, and justified the need to account for nonlinear effects in alternative models of relaxation.

Finally the last part of this work was dedicated to CUTLASS observations of a heating experiment in October 2000, when natural irregularities and strong background plasma flow were present simultaneously with the artificial irregularities. The CUTLASS backscatter measurements exhibited unusual spectral width characteristics and an autoregressive model was employed to determine the origin of the spectral components.

7.2 Principal Scientific Findings

The major results of this thesis are summarised as follows:

- The computationally-straightforward Epstein function was applied to a broad range of electron temperature perturbation profiles measured using the EISCAT UHF radar and compared with the stationary solution to a theoretical model of the electron temperature response to a high power heater wave. It was found that the parameters incorporated into this function allowed a wider degree of flexibility in the profile description compared to the simple theoretical model, and this enabled a better estimate of the peak electron temperature to be made under heating conditions when the heating did not obey the stationary perturbation solution.
- The purely growing mode (PGM) which is known to appear in the ‘overshoot’ incoherent scatter spectra measured by the EISCAT UHF radar during the first few milliseconds of heating leads to underestimation of the electron temperatures obtained using the standard GUIDAP analysis software. It was shown that the underestimation is strongly proportional to the relative amplitudes of the PGM and ion-acoustic lines, which varied widely due in part to prevailing ionospheric conditions and the heater beam parameters. However, the electron temperatures, inferred from the average ‘heated’ spectrum after several tens of seconds of heating, were found to be sufficiently reliable that the possibility of the PGM remaining in averaged spectra was discarded.
- The relaxation characteristics of field-aligned irregularities have been found to obey the simple theoretical model in many cases studied and typically possess e-folding time scales of a few seconds to tens of seconds, consistent with current and older literature. The effective plasma temperature corresponding to the rate

of decay by diffusion only was compared with complementary measurements of the bulk plasma temperature as measured by the EISCAT UHF radar and found to agree in most cases. The model is suspected to fail in experiments where the decay is of a multi-stage nature, and two alternative models were employed to describe the nature of the irregularity decay under these circumstances. It was shown that the behaviour can be modelled well by both a time-dependent temperature decay model and a wave-wave interaction model. The majority of backscatter profiles studied usually showed preference over one of the models. The instantaneous decay rates predicted by the time-dependent temperature model were often associated with very hot plasma temperatures which are suggestive of intense, isolated ‘filaments’ of plasma depletion, but without in-situ measurements to compare the model predictions with, the result is rather speculative at present.

- CUTLASS Iceland radar observations of FAI in the presence of strong background flows have been presented and the temporal characteristics of backscatter power were consistent with the apparent effects predicted by a flow-dependent decay model. Emphasis was placed on distinguishing between the apparent rate at which HF backscatter power decays at and the true ‘local’ rate at which the FAI decay at when there is significant or non-zero plasma flow.
- Under the same conditions, the spectral width of artificial backscatter was not only enhanced by around one order of magnitude above typical values when measured using the CUTLASS Iceland radar but also exhibited asymmetry, where the enhanced widths were not measured by the Finland radar in a direction almost orthogonal to the Iceland beam. The Burg maximum entropy method was applied to the CUTLASS ACFs and indicated a close relation

between the occurrence of double-peaked spectra and where the Iceland beam 15 spectral widths appeared broadened.

- Previous reports and explanations for the enhanced artificial backscatter widths were found to be incompatible with the results found in this study. An alternative but tentative explanation for the origin of these multi-component echoes was proposed, in terms of simultaneous detection of natural and artificial scattering sources spatially separated in latitudinal direction by around 200km, by the edges and centre of the main lobe. This could only be possible if the naturally-occurring irregularities were amplified by the action of the heater.

7.3 Outstanding Questions and Further Work

The applications of the results concerned with the effect of the PGM on the inferred electron temperatures measured by incoherent scatter spectra are not confined to the EISCAT Tromsø facilities. It is known that the SPEAR heating facility on Svalbard suffers a more dynamic ionosphere and has been found to produce more persistent spectral distortions in the spectra measured by the EISCAT Svalbard radar (ESR), often lasting for entire heating intervals instead of only a few data dumps. This presents a problem for interpreting the heating effects induced by the facility when using the standard analysis electron temperature data. It may well be for this reason why only mild increases, if any are observed in the ESR electron temperatures. Thus, it would prove a worthwhile cause to develop the technique of correcting the ion-acoustic spectra by removing the PGM to those averaged spectra measured by the ESR. It is anticipated that an extension to the study would also include developing the software to correct spectra at higher spatial resolution, and to investigate the turbulence characteristics associated with the PGM, as modelled by the Gaussian functions.

Reports of a two-stage decay nature of artificial irregularities have been relatively infrequent since the first backscatter measurements were made and thus it is not really known what particular conditions are required for this behaviour. This work has raised an important issue regarding the morphology of the modified volume when this temporal behaviour is observed and would seem to suggest that an existence of very hot filamentary-type structures could produce a two-step decay. Future developments of incoherent scatter facilities at high-latitudes, namely the 'EISCAT-3D' project is likely to be one of the most important diagnostics available to test these ideas. Thorough coverage of the modified volume above the heater and high temporal and spatial resolution observations would be obtained through employing the interferometry-type technique. With an absence of in-situ measurements available at present and apparently infrequent nature of this two-stage relaxation of HF backscatter, it will be perhaps some time before these ideas can be confirmed.

Furthermore an in-depth search of the CUTLASS data archive is needed to identify more heating experiments where strong background flows introduce a drift effect into the spatial extent of the artificial irregularities. One might expect that these physical processes may occur at other heater locations, for example at HAARP in Alaska or with SPEAR on Svalbard. However the generation of artificial irregularities often requires a stable, quiet ionosphere and it is likely that on most occasions when natural irregularities are present during artificial heating, naturally-occurring waves prevent the strong interaction of the pump wave with the plasma and consequently, artificial backscatter is often very weak or absent. In the example interval studied in Chapter 6 it was perhaps a fortunate coincidence that the ideal combination of conditions was present which allowed the rather unique CUTLASS observations to be made. It should also be added that such strong backscatter generated by the Tromsø is very rarely

obtained using the Iceland radar because of the longer distance traversed by the sounding waves, so this event was quite special. It is unfortunate that no complementary measurements of the plasma parameters were made by the EISCAT radars in conjunction with the heating experiment. Lastly, optical instruments may also prove a useful source of information on how the artificially-induced plasma turbulence may be modifying the properties and behaviour of natural phenomena such as particle precipitation, which is believed to be located close to the artificially heated volume during this event. There are certainly still a lot of interesting questions surrounding the nature of artificial modification during geophysical events, and the flexibility to carry out heating experiments as and when suitable conditions occur would be needed.

Appendix 1. Ionospheric Sounding and the Tromsø Dynasonde

The basis of ionospheric sounding is the vertical transmission of a radio frequency pulse and the subsequent measurement of the time it takes for the reflected signal, or echo, to return. In the absence of collisions, reflection of the wave occurs where the radio wave frequency matches the local plasma frequency, and this is proportional to the plasma density (2.4). The height from which the echo occurs, also known as the virtual height, is calculated from half the return time of the reflected wave signal, and assumes that it travels at the speed of light. This of course neglects attenuation of the wave speed due to refraction as the wave passes through increasing plasma density along its flight path, hence the term virtual height, which is usually an overestimate of the true value.

The speed of the wave is given by the group speed u , and this is itself given by the group refractive index n_g

$$u = \frac{c}{n_g}, \quad n_g = \frac{1}{n} \quad (\text{A1.1})$$

The slowing of the wave with increasing group refractive index is sometimes referred to as group retardation, and where this effect is strong gives rise to elongated echoes or ‘cusp-like’ echoes with almost no change in frequency.

This occurs as the wave approaches a local maximum in the plasma density, where the density gradient is changing fastest. However, it is possible to account for group retardation effects and hence generate a real height profile of echoes. By making a sweep in frequency of the transmitted wave, the plasma density can be determined as a function of virtual height, since the waves of different frequencies will be reflected over a range of altitudes and thus take different lengths of time to be received at the ground.

An ionogram illustrates the altitude profile of the echoes as a function of frequency, and an example of an ionogram from the Tromsø Dynasonde is shown in Figure A1. The green traces correspond to 'X' mode echoes, and the blue traces are 'O' mode wave echoes.

The critical frequency of the different ionospheric regions is simply the maximum frequency of the layer, and the highest frequency of the complete ionosphere defines the penetration frequency. This parameter determines the maximum frequency a radio wave from the ground may be transmitted at and still be reflected so above this value, waves simply propagate out to space and no echoes are received. The F region critical frequency is often termed the ' f_0f_2 '. It is of interest to use ionograms during artificial modification experiments because the critical F region frequency will determine whether underdense or overdense heating will take place, given a particular pump frequency. We may recall that for reasonable heating effects to take place, a strong interaction between the plasma and the pump wave is required, and this is usually achieved when the pump frequency is below the critical F region frequency.

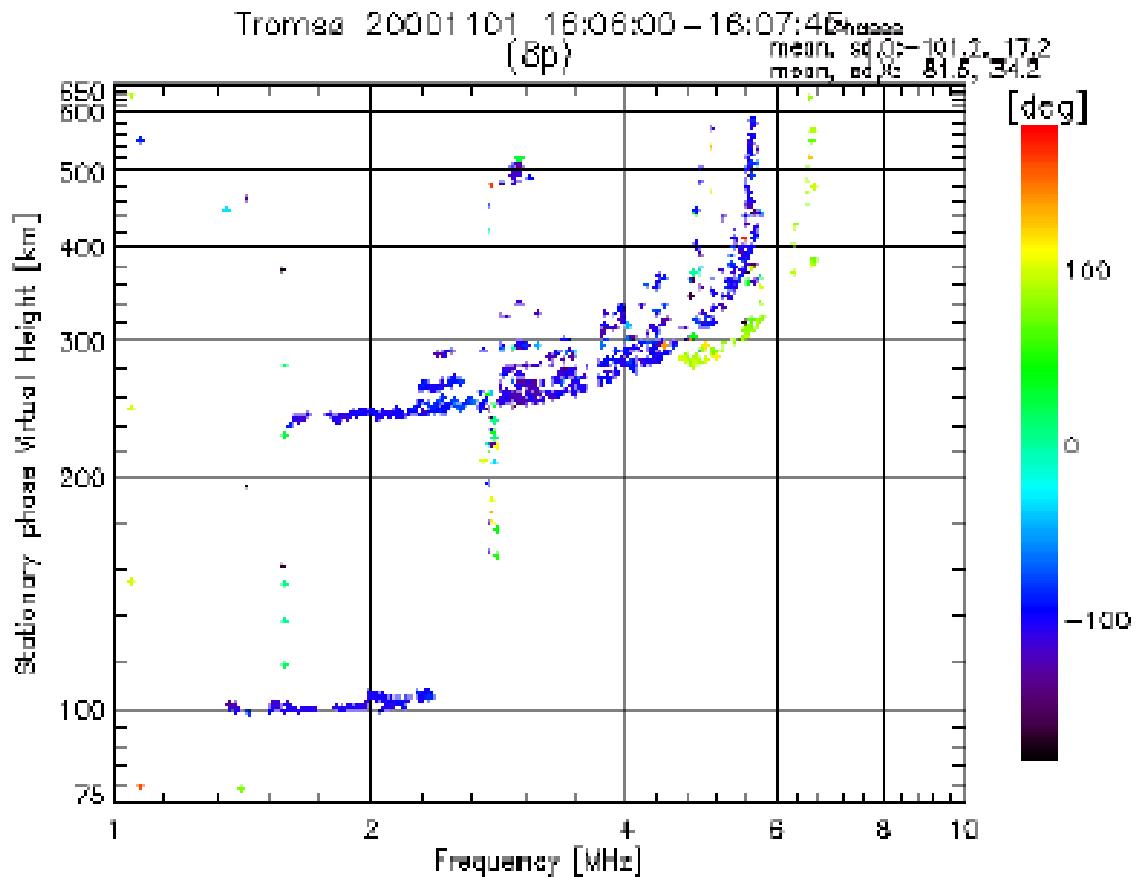


Figure A1. Example of an ionogram which exhibits E and F-region echoes at 100km and around 240-400km respectively. The blue traces correspond to O-mode echoes and the green trace represents X-mode echoes. The ‘spread-F’ effect can be easily identified by the cusp-like trace that extends over a large height range but with little change in frequency which demonstrates where the transmitted wave is approaching a local maximum in the plasma density. Ionogram obtained online at http://dynamite.eiscat.uit.no/idlwebgifs/ana_iono/2000a/200011/20001101/T229036B.GIF

Appendix 2. Epstein Function Fitting Procedure

EISCAT UHF electron temperature data for heating experiments at Tromsø were chosen where the heater had been transmitting for at least one minute and the power was constant throughout the heating interval. This was necessary since the bulk plasma temperature changes evolve on time scales of tens of seconds or more through the TPI until a steady state is achieved, resulting in a large scale temperature change by the end of the heating period with a single peak in the electron temperature profile around the interaction height. In all the heating experiments chosen, the EISCAT UHF radar was run in the CP1K mode. This is an uncoded long pulse experiment where the radar points in a fixed direction to make measurements of the backscattered signal. The Grand Unified Incoherent Scatter Design and Analysis Package (GUISDAP) analysis of the long pulse data provided a time resolution of 5s, although the altitude separation of consecutive range gates in the analysed data was approximately 22.5km.

Epstein functions were fitted to the time-averaged electron temperature change profile using linear regression by varying the free parameters. The average ‘heated’ temperature profiles were computed from a period of 30s after the heater had begun transmitting until the end of the heating, and the average unperturbed temperature was subtracted to calculate the large-scale temperature change. Overshoot profiles were excluded from the averaging since they correspond to turbulent plasma and would not represent physical parameters expected from plasma which is in a steady state. The Epstein function peak was matched to the range gate containing the heater interaction height, since the altitude separation of the upper hybrid level and the interaction altitude is much smaller than the range gate separation of the electron temperature data.

The heater interaction height, where the ion line spectra were ‘distorted’ was determined from the altitude where EISCAT power profiles maximised. Power profiles were generated from raw electron density measurements taken from electron plasma lines that become sufficiently enhanced as a result of the PDI at the heater wave reflection height within the first few milliseconds of heating. These backscatter power measurements are made at a height resolution of 5km. However, because the ion line spectra were gated at the same altitude separation as the electron temperatures in the analysis, the nearest range gate to the height of the power profile maxima was used as the altitude at which the spectra were distorted by the PGM feature. Thus, the altitude of the nearest range gate to the power profile measurement potentially incurred an error of up to 11.25km (half the temperature altitude resolution) from its true altitude.

The temperature profiles covered the altitudes in the range from approximately 150km up to 340km. To account for a possible discrepancy between the altitude of the maximum temperature change, and the real interaction altitude indicated by the power profiles, the electron temperature at the interaction altitude was allowed to be a free parameter so that a ‘modified’ electron temperature change profile was obtained by replacing the real measurement with a trial value. Epstein functions (equation 4.1) were computed for all possible combinations from 100 trial values of B_0 , and k . The model profiles producing a minimum variance with the ‘modified’ EISCAT temperature change profiles indicated the best fit values for B_0 and k . A subsequent fitting routine where trial values of the parameters A and G were used to compute model functions was then carried out. In this case the scale height and thickness parameter B_2 varied only with altitude, using the pre-determined ideal values of B_0 and k . The model function was again calculated and the minimum variance of the model function from the experimental data determined the best fit values of A and G . The set of best fit

values were used to obtain the model estimate of the electron temperature change at the range gate containing the interaction altitude. An example of an Epstein curve is shown in Figure A2 to illustrate the geometry of the function, which is given by (4.1),

$$f_{eps} = A \frac{e^{\frac{X}{B_0}}}{\left(1 + e^{\frac{X}{B_0}}\right)^2} + G \quad \text{where } X = z - z_m$$

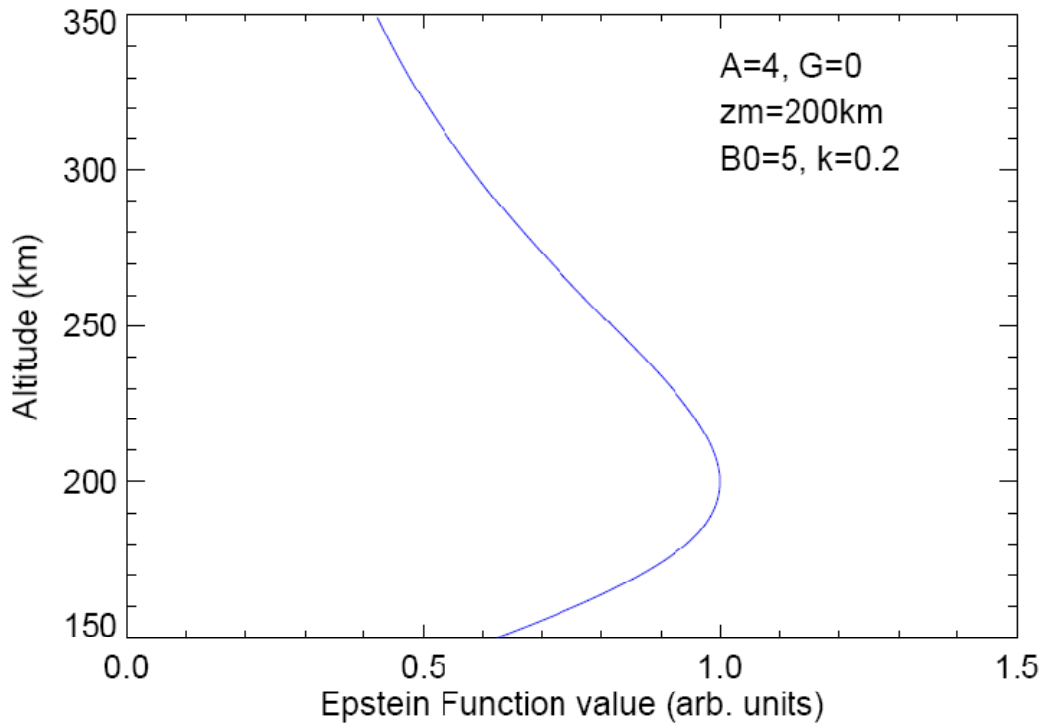


Figure A2. Example of an Epstein function, defined with a peak height at 200km, and values of A , G , B_0 and k (equation 4.1) given by 4, 0, 5 and 0.2 respectively.

Appendix 3. Incoherent Scatter Spectrum Correction

In the standard analysis, the GUISDAP fitting routines are initiated by taking apriori plasma parameter estimates of the ion temperature, line-of-sight drift velocity, neutral particle concentration, electron temperature and electron density, which are supplied from an ionospheric model. These are used as a starting point from which to compute an ensemble of theoretical spectra, based on Maxwellian assumptions using GUISDAP. The plasma parameters are varied iteratively over a number of steps until an acceptable convergence between the measured and theoretical spectra is achieved, and a fit residual, R_1 of the fitted theoretical spectrum with the unmodified spectrum is calculated. This parameter is a measure of how well the theoretical spectrum, defined by the final set of analysis parameters, fits to the measured spectrum. It is the ratio of the measured error to the error expected for a Maxwellian incoherent scatter spectrum.

In our modified algorithm, an additional procedure follows this usual GUISDAP fitting. This involves subtracting Gaussian functions defined by different amplitude and width from the measured spectrum to produce a “corrected” spectrum. A theoretical spectrum is fitted to each corrected spectrum using the GUISDAP routines, corresponding to a different set of plasma parameters and fit residual. The corrected spectrum associated with the smallest fit residual, R_2 , was taken as the best result which could be achieved by modifying the spectrum. In order to determine the significance of the Gaussian peak (PGM) in the incoherent scatter spectra, the fit residuals of the measured and corrected spectra were compared against each other. That is to say, if R_2 was less than R_1 , then the plasma parameters estimated from the fitted corrected spectrum were stored as the best result. Where R_1 was not improved by modifying the spectrum, this was taken as an indication that a correction to the spectrum was not necessary.

Appendix 4. Rates of Decay from Transport and Chemical Processes

In order to assess what physical mechanisms may play significant roles in the decay of irregularities, model values of the rates contributed by parallel and perpendicular diffusion, electrons-neutral collisions, electron-ion collisions and chemical recombination are computed for a range of electron temperatures from 1000K up to 6000K. In this context, model values refer to those which would be expected using typical values of background ionosphere and neutral atmosphere parameters. The total rate, computed from the sum of each component may be defined as

$$\gamma_{total} = 1.8(D_{\perp}k_{\perp}^2 + D_{\parallel}k_{\parallel}^2) + \delta\nu_e + \beta \quad (\text{A4.1})$$

where equations (2.32) and (2.37) define the field-parallel and field-perpendicular thermal conduction coefficients and the coefficient δ is approximately 10^{-4} (Gurevich, 1978). Equation (2.40) was also used in order to calculate the electron-neutral collision frequency at the range of temperatures. Values of the background parameters at an altitude of 200km were obtained from Gurevich (1978) and the MSIS-2000 neutral atmosphere model and the background electron and ion temperatures were taken to be $T_{e0} = 1600K$ and $T_i = 1100K$ respectively, electron-neutral and electron-ion collision frequencies of $\nu_{e0} = 150s^{-1}$ and $\nu_{ei0} = 440s^{-1}$ respectively and neutral particle density $N_n = 3 \times 10^9 cm^{-3}$. The irregularity scale size k_{\perp} perpendicular to the geomagnetic field was assumed to be that probed by a HF radar frequency of 15MHz, corresponding to a wave number of $0.63m^{-1}$ and wave number of the irregularities in the field-parallel direction, $k_{\parallel} = 1 \times 10^{-5}m^{-1}$, based on a typical scale length parallel to the field of 100km. The chemical contribution given by the rate β , is defined through the ionization balance equation,

$$\frac{dN}{dt} = q_{i0} - \beta N \quad (\text{A4.2})$$

$$\beta = \beta_1 N_{N_2} + \beta_2 N_{O_2} \quad (\text{A4.3})$$

Typical values of β_1 and β_2 were taken to be $1 \times 10^{-12} \text{cm}^3 \text{s}^{-1}$ and $2 \times 10^{-11} \text{cm}^3 \text{s}^{-1}$ respectively, whilst typical N_2 and O_2 densities at an altitude of 200km were taken from Gurevich (1978). Typically, $\beta \approx 0.017 \text{s}^{-1}$. Figure A2 illustrates the dependence on electron temperature of each individual rate component. For the cases when ion contributions were included in the temperature and collision frequency, the rates were defined by

$$D_{\perp} = \frac{k_B(T_{e0} + T_i)(v_{en} + v_{ei})}{m_e \Omega_e^2} \quad (\text{A4.4})$$

$$D_{\parallel} = \frac{k_B(T_{e0} + T_i)}{0.51 m_e (v_{en} + v_{ei})} \quad (\text{A4.5})$$

$$v_{ei} = v_{ei0} \left(\frac{T_i}{T_e} \right)^{3/2} \quad (\text{A4.6})$$

Decay rates due to perpendicular diffusion are illustrated by the solid black curve, parallel diffusion by the solid blue curves and collisions in the solid green curve. Each of the solid curves correspond to the expressions defined in (2.32) and (2.37), whilst the equivalent perpendicular, parallel and collisional rates with ion effects included are shown by the dashed curves. Figure A3 would suggest that the mean fast decay rate of the primary wave (deduced in Section 5.4) can be explained by perpendicular diffusion at relatively high electron temperatures of 4700K, if only electrons and electron-neutral collisions are considered in the rate calculations. When the effect of ions are also included, the electron temperature required by perpendicular diffusion processes to produce this high rate is lowered significantly to about 3100K.

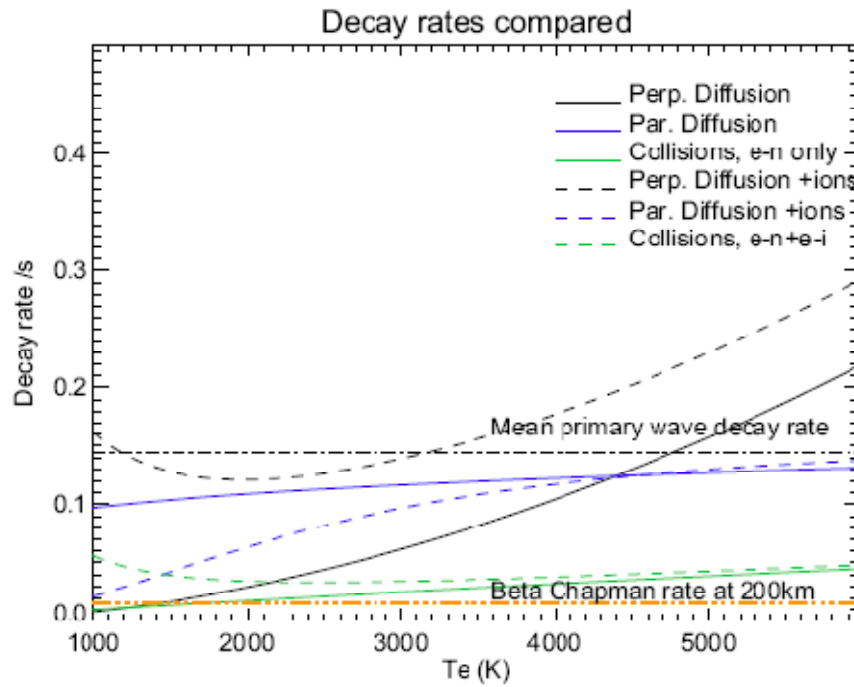


Figure A3. Model decay rates at different temperatures for processes of perpendicular and parallel diffusion, electron collisions and chemical recombination

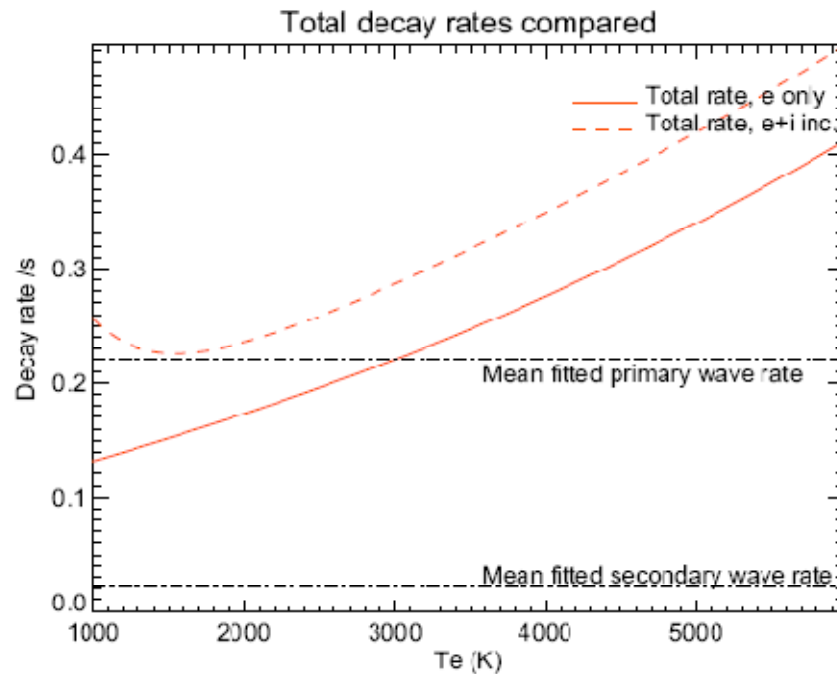


Figure A4. The sum of all contributions by each process with respect to the mean fitted primary and secondary wave decay rates derived from our wave-wave model simulations

However, even in these instances this is usually still greater than those temperature measured by the EISCAT radar in this particular heating campaign, as was shown by the temperature change profiles in Figure 5.11 and Figure 5.12. The mean fitted secondary decay rate of 0.0138s^{-1} lies close to those of perpendicular diffusion, electron-neutral collisions and also chemical recombination at the background temperature. This would indicate that the secondary wave could be decaying at a rate which is governed by the background electron temperature, after the temperature has fallen from its initial enhanced value. However, given that all three mechanisms give rise to such similar rates of decay it would be very difficult to distinguish which is playing the dominant role at this temperature. Figure A4 shows the sum of all four contributions, again with the mean decay fitted decay rates of the primary and secondary rates indicated by the dash-dot lines.

The figure suggests that the decay rate of the primary wave is comparable to the total rate from all four processes when ion effects on the plasma temperature and total collision frequency are neglected. The total rate by all four processes is around the mean fitted primary wave decay rate at electron temperatures of 3000K and 1500K for only electron diffusion and electron and ion diffusion respectively. The value of 1500K is typical of the large-scale temperatures measured by the EISCAT radar during the April 1996 heating campaign when two-stage decay profiles were exhibited in the backscatter data, but typically low when compared with those temperatures from other campaigns. However since the decay rate of the secondary wave is too slow to be explained by this total rate for electron diffusion at even the lowest temperatures considered here then this suggests that a switch from a decay phase that is being controlled by all these processes (in the total rate) to a single regime which is dominated by either perpendicular diffusion, electron-neutral collisions or chemical

recombination because it was discussed earlier that any of these processes took place at comparable rates to the mean secondary wave decay rate.

It was also found that the electron temperature implied by the fast decay rate of the fitted primary wave could also be reduced to those measured by the EISCAT radar if the neutral density was raised by an order of magnitude above the MSIS model value. But it is unlikely that the level of uncertainty in the neutral density would be as high as an order or magnitude so this result was discarded. It could be perhaps that the scale size of the irregularities may become important. The decay rate curves computed in Figure A3 and Figure A4 correspond to a probing HF wave at 15MHz, which is a typical operating frequency of the CUTLASS HF radars used in ionospheric heating experiments. It also dictates the cross-field scale sizes of the irregularities that can be ‘seen’ by the radar. Therefore at different probing frequencies, one might expect the decay rate dependence on electron temperature to vary accordingly. Hence, for a range of frequencies from 0 to 40MHz in 0.1MHz steps, the decay rates due to perpendicular diffusion only are shown in Figure A5 for a selection of scale sizes. The scale size indicated on the figure has been defined by $L = \frac{2\pi}{k_{\perp}}$ and given in metres.

Evidently, the primary and secondary decay rates derived from the wave-wave interaction model are compatible with a field-perpendicular diffusive regime at the scale size of just under 10m which is the typical irregularity size probed by the CUTLASS radars. This may be deduced from the fact that both rates intersect with the curve for $L=9.37\text{m}$ in the temperature range considered, the mean primary wave decay rate at around 4500K and the mean fitted secondary wave rate at around 1000K. The value of 4500K is still between 1.5 to 2 times the typical electron temperatures measured by the EISCAT radar during heating experiments though, and around 3 times

the large-scale temperatures that were measured during April 1996 when the two-stage decay in the CUTLASS backscatter was observed. At a scale size of $L=5\text{m}$, only the primary wave decay rate intersects with the curve at approximately 2900K, but the secondary wave decay rate is too slow to explain perpendicular diffusion at this scale size; one may see that the equivalent plasma temperature for perpendicular diffusion at the scale $L=5\text{m}$ would have to be much lower than even 1000K, which is lower than the background or 'unheated' electron temperatures suggested by ionospheric models at typical heater interaction heights of 200km. It should also be pointed out that in order to observe irregularities at this scale size, a probing frequency of around 30MHz would have to be used by the HF radar, and the CUTLASS facility does not currently transmit at such high frequencies. On the other hand, the mean decay rate of the secondary waves fitted are equivalent to perpendicular diffusion rates at around 2500K for irregularities that are of the scale size $L=18.75\text{m}$. To make observations of irregularities at this scale size, a frequency of 8MHz, which lies at the lowest limit of the CUTLASS operation range, would be required.

It was discussed earlier that the temperature-type model was, in some cases, able to replicate well the character of the backscatter decay but some disregard was given to the validity of this model due to the large discrepancies between the initial temperatures required, and EISCAT measurements. However, based on the latter evidence in Figure A3 to Figure A5 which has been presented in order to explain the observed rates fitted by the wave-wave interaction model, there would appear to be some justification for considering elevated electron temperatures in playing a significant role in the wave-wave model, and that aspects of both models may be needed to provide an accurate description of irregularity relaxation in the cases where multiple stages are exhibited in CUTLASS backscatter data.

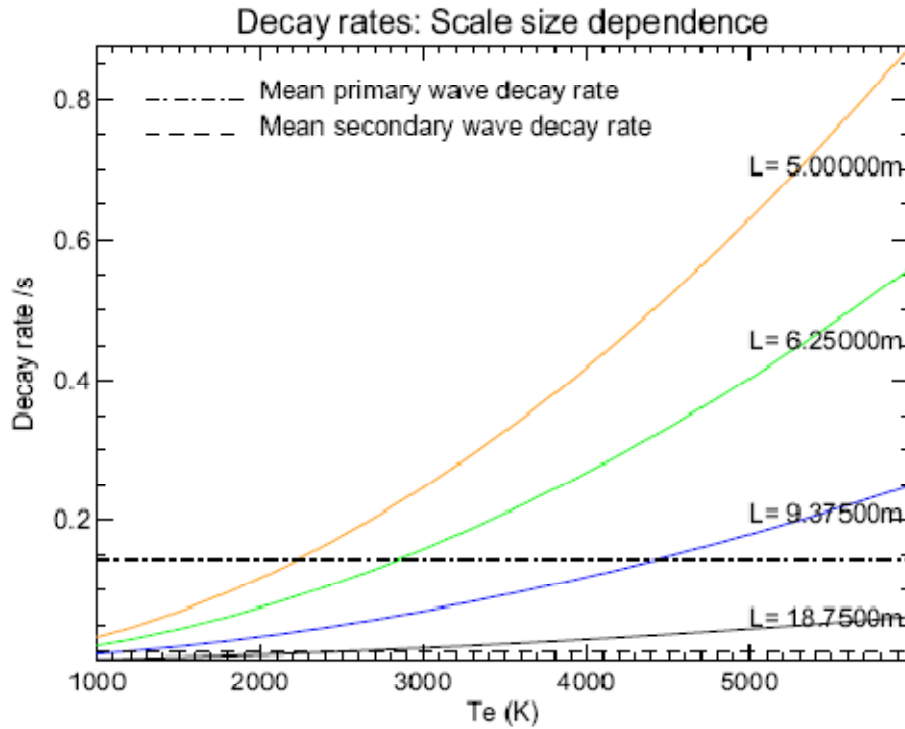


Figure A5 Irregularity scale size dependence of the decay rates (perpendicular diffusion) in the absence of ion effects. The mean fitted primary and secondary wave decay rates have again been plotted to indicate the scale sizes required to explain these values if decay was by perpendicular thermal diffusion only

Appendix 5. Burg Spectrum Analysis

The Burg maximum entropy method selects a spectrum corresponding to the most random time series model which is consistent with its ACF. The method is particularly advantageous because it is known to result in a spectrum of higher resolution than the usual Fourier Transform method and can thus resolve close spectral components that might not otherwise be revealed (Burg, 1975), and has been implemented in previous work involving studies of broad naturally-occurring HF backscatter (Schiffler et al., 1997; Huber and Sofko, 2000). The occurrence and characteristics of double-peaked spectra were studied in great depth using this method. Therefore this technique should prove equally beneficial to investigate in further detail the nature of the artificial backscatter spectra whose spectral widths appeared enhanced above typical artificial backscatter values.

During the experiment, the CUTLASS radars transmitted HF radio waves in multi-pulse sequences, with pulse lengths of 100 μ s, corresponding to range resolution of 15km for each range gate. The transmission of a complete sequence of 7 pulses, takes 0.1s and hence, approximately 20 soundings are made over the dwell time of around 2s in each beam direction. The 2s-integrated ACFs corresponding to each sounding, which were measured by the Iceland radar were used to obtain their corresponding Burg spectra. The procedure employed is very similar to that described by Schiffler et al. (1997) and Huber and Sofko (2000). Here, a two-sided Burg spectrum of order eight was computed from the complex ACF. The order was required to be less than half the number of lags in the ACF (Schiffler et al., 1997). By choosing a relatively low order with respect to the length of the ACF, spurious peaks in the Burg spectrum may be avoided.

The first step in the procedure involved locating the main peak, after which the Burg spectrum was inspected for an additional peak by considering the gradients and turning points in the spectrum. In order to be classified as a 'peak', and thus distinguish double-peaked spectra, the constraints of Schiffler et al. (1997) were applied, and are outlined below:

1. The peak amplitude of the second peak was at least 10% of the main peak
2. The Doppler velocity of any peak was confined to values, $< -25 \text{ m s}^{-1}$ or $> 25 \text{ m s}^{-1}$
3. The velocity separation of the two peaks was $< 600 \text{ m s}^{-1}$

Criterion 2 was imposed to exclude ground scatter and criterion 3 was simply based on their statistical argument that very few spectra above this separation occurred. Each double peaked spectrum which was 'flagged' satisfied the conditions described above and the corresponding time and range cell from which the ACF was obtained were recorded.

Bibliography

- André, R., Pinnock, R.M., Villain, J.P. and Hanuise, C.: Influence of magnetospheric processes on winter HF radar spectra characteristics, *Ann. Geophys.*, **20**, 1783-1793, 2002
- Ashrafi, M., Kosch, M.J. and Honary, F.: Heater-induced altitude descent of the EISCAT UHF ion line enhancements: Observations and modelling, *Adv. Space Res.*, **38**, 2645-2652, 2006
- Baker, K.B., Dudeney, J.R., Greenwald, R.A., Pinnock, M., Newell, P.T., Rodger, A.S., Mattin, N., and Meng, C.-I.: HF radar signatures of the cusp and low-latitude boundary layer, *J. Geophys. Res.*, **100**, 7671–7695, 1995
- Barthes, L., André, R., Cerisier, J.-C., and Villain, J.-P.: Separation of multiple echoes using a high resolution spectral analysis in SuperDARN HF radars, *Radio Science*, **33(4)**, 1005–1017, 1998
- Belenov, A.F., Bubnov, V.A., Erukhimov, L.M., Kiselev, Yu. V., Komrakov, G.P., Mityakova, E.E., Rubtsov, L.N., Uryadov, V.P., Frolov, V.L., Chugunov, Yu. V. and Yukhmatov, B.V.: Parameters of artificial small-scale ionospheric irregularities, *Radiophys. Quant. Electron.*, Engl. Transl., **20**, 1805-1813, 1977
- Beynon, W.J.G. and Williams, P.J.S.: Incoherent scatter of radio waves from the ionosphere, *Rep. Prog. Phys.*, **41**, 1978
- Blagoveshchenskaya, N.F., Borisova, T.D., Kornienko, V.A., Leyser, T.B., Rietveld, M.T. and Thidé, B.: Artificial field-aligned irregularities in the nightside auroral ionosphere, *Adv. Space Res.*, **38**, 2503-2510, 2006
- Blagoveshchenskaya, N.F., Borisova, T.D., Kornienko, V.A., Frolov, V.L., Rietveld, M.T. and Brekke, A.: Some distinctive features in the behaviour of small-scale artificial ionospheric irregularities at mid- and high latitudes, *Radiophys. Quant. Electron.*, **50**, 2007
- Bond, G.E.: The interaction of radio waves with the auroral ionosphere, University of Leicester, Ph.D Thesis, 1997
- Borisov, N., Senior, A. and Honary, F.: Stationary state and relaxation of artificial irregularities excited in ionospheric heating experiments, *J. Plasma Physics*, **71**, 315-334, 2005
- Brekke, A.: Physics of the Upper Polar Atmosphere, John Wiley & Sons Ltd., Chichester, 1997
- Burg, J.P.: Maximum Entropy Spectral Analysis, Stanford University, PhD Thesis, 1975
- Carroll, J.C., Violette, E.J., Utlaut, W.F.: The Platteville high power facility, *Radio Science*, **9(11)**, 889-894, 1974
- Cohen, R. and Whitehead, J.D.: Radio-reflectivity detection of artificial modification of the ionospheric F layer, *J. Geophys. Res.*, **75**, 6439–6445, 1970

- Coster, A.J., Djuth, F.T., Jost, R.J. and Gordon, W.E.: The Temporal Evolution of 3-m Striations in the Modified Ionosphere, *J. Geophys. Res.*, **90(A3)**, 2807-2818, 1985
- Danskin, D.W., Koustov, A.V., Makarevich, R.A. and Lester, M: Observations of double-peaked E region coherent spectra with the CUTLASS Finland HF radar, *Radio Science*, **39**, doi:10.1029/2003RS002932, 2004
- Das, A.C. and Fejer, J.A.: Resonance instability of small-scale field-aligned irregularities, *J. Geophys. Res.*, **84**, 6701–6704, 1979
- Depuev, V.H. and Pulinets, S.A.: A global empirical model of the ionospheric topside electron density, *Adv. Space Res.*, **34**, 2016-2020, 2004
- Dhillon, R.S., Robinson, T.R. and Wright, D.M.: Radar ACFs and turbulence characteristics from artificially generated field-aligned irregularities, *Geophys. Res. Lett.*, **29(17)**, 1830, doi:10.1029/2002GL015364, 2002
- Djuth, F.T., Thidé, B., Lerkic, H.M. and Sulzer, M.P.: Large F-Region Electron-Temperature Enhancements Generated By High-Power HF Radio Waves, *Geophys. Res. Lett.*, **14(9)**, 953-956, 1987
- Fejer, J.A.: Ionospheric Modification and Parametric Instabilities, *Rev. Geophys. Space Phys.*, **17(1)**, 135-153, 1979
- Eglitis, P., Robinson, T.R., Rietveld, M.T., Wright, D.M. and Bond, G.E.: The phase speed of artificial field-aligned irregularities observed by CUTLASS during HF modification of the auroral ionosphere, *J. Geophys. Res.*, **103**, 2253-2259, 1998
- Gordon, W.E.: Incoherent scattering of radio waves by free electrons with applications to space exploration by radar, *Proc. IRE* 46, 1824–1829, 1958
- Grach, S., Karashtin, A., Mityakov, N., Rapoport, V. and Trakhtengerts, V.: Parametric interaction between electromagnetic radiation and ionospheric plasma, *Radiophys. Quant. Electron. Engl. Transl.*, **20**, 1254, 1977
- Graham, K.N. and Fejer, J.A.: Anomalous radio wave absorption due to ionospheric heating effects, *Radio Science*, **11**, 1057–1063, 1976
- Greenwald, R.A., Baker, K.B., Dudeney, J.R., Pinnock, M., Jones, T.B., Thomas, E.C., Villain, J.P., Cerisier, J.C., Senior, C., Haniuse, C., Hunsucker, R.D., Sofko, G., Koehler, J., Nielsen, E., Pellinen, R., Walker, A.D.M., Sato, N., and Yamagishi, H.: DARN/SuperDARN: A global view of the dynamics of high latitude convection, *Space Sci. Rev.*, **71**, 761–795, 1995
- Gurevich, A.V.: *Nonlinear Phenomena in the Ionosphere*, Springer, New York, 1978
- Gurevich, A.V. and Karashtin, A.N: Self-focusing instability of plasma waves excited by powerful HF radiation, *Phys. Lett. A.*, **195**, 362-368, 1994
- Gurevich, A.V., Zybin, K.P. and Lukyanov, A.V.: Stationary Striations developed in the Ionospheric Modification, *Phys. Rev. Lett.*, **75 (13)**, 2622-2625, 1995

- Gurevich, A.V., Hagfors, T., Carlson, H., Lukyanov, A.V. and Zybin, K.P.: Electron temperature measurements by incoherent scattering in the presence of strong small temperature irregularities, *Phys. Lett. A*, **246**, 335-340, 1998a
- Gurevich, A.V., Hagfors, T., Carlson, H., Karashtin, A. and Zybin, K.: Self-oscillations and bunching of striations in ionospheric modifications, *Phys. Lett. A*, **239**, 385-392, 1998b
- Gurevich, A.V., Carlson, H., Kelley, M., Hagfors, T., Karashtin, A. and Zybin, K.P.: Nonlinear structuring of the ionosphere modified by powerful radio waves at low latitudes, *Phys. Lett. A*, **251**, 311-321, 1999
- Gustavsson, B., Sergienko, T., Rietveld, M.T., Honary, F., Steen, A., Brändström, B.U.E., Leyser, T.B., Aruliyah, A.L., Aso, T., Ejiri, M. and Marple, S.: First Tomographic estimate of volume distribution of HF-pump enhanced airglow emission, *J. Geophys. Res.*, **106(A12)**, 29105–29123, 2001
- Hargreaves, J.K.: The solar-terrestrial environment, Cambridge University Press, Cambridge, 1995
- Hedberg, Å., Derblom, H. and Thidé, B.: Observations of HF backscatter associated with the heating experiment at Tromsø, *Radio Science*, **18(6)**, 840-850, 1983
- Honary, F., Stocker, A.J., Robinson, T.R., Jones, T.B., Wade, N.M., Stubbe, P. and Kopka, H.: EISCAT observations of electron temperature oscillations due to the action of high power HF radio waves, *J. Atmos. Terr. Phys.*, **55**, 1433–1448, 1993
- Honary, F., Stocker, A.J., Robinson, T.R., Jones, T.B. and Stubbe, P.: Ionospheric plasma response to HF radio waves operating at frequencies close to the third harmonic of the electron gyrofrequency, *J. Geophys. Res.*, **100**, 21489-21501, 1995
- Honary, F., Robinson, T.R., Wright, D.M., Stocker, A.J., Rietveld, M.T. and McCrea, I.: First direct observations of the reduced striations at pump frequencies close to the electron gyroharmonics, *Ann. Geophys.*, **17**, 1235-1238, 1999
- Huber, M. and Sofko, G.: Small-scale vortices in the high-latitude F region, *J. Geophys. Res.*, **105**, 20,885–20,897, 2000
- Hysell, D.L., Kelley, M.C., Yampolski, Y.M., Beley, V.S., Koloskov, A.V., Ponomarenko, P.V. and Tyrnov, O.F.: HF radar observations of decaying artificial field-aligned irregularities, *J. Geophys. Res.*, **101**, 26981-26993, 1996
- Inhester, B., Das, A.C. and Fejer, J.A.: Generation of small-scale field-aligned irregularities in ionospheric heating experiments, *J. Geophys. Res.*, **86**, 9101–9106, 1981
- Jones, T.B., Robinson, T.R., Stubbe, P. and Kopka, H.: Phase changes induced in a diagnostic radio wave passing through a heated region of the auroral ionosphere, *J. Geophys. Res.*, **87**, 1557–1564, 1982
- Jones T.B., Robinson T.R., Stubbe P. and Kopka H.: A hysteresis effect in the generation of field-aligned irregularities by a high power radio wave, *Radio Science*, **18**, 835 -839, 1983

- Jones, T.B., Robinson, T.R., Stubbe, P. and Kopka, H.: EISCAT observations of the heated ionosphere. *J. Atmos. Terr. Phys.*, **48**, 1027–1035, 1986
- Jones, T.B., Lester, M., Milan, S.E., Robinson, T.R., Wright, D.M. and Dhillon, R.S.: Radio wave propagation aspects of the CUTLASS radar, *J. Atmos. Sol. Terr. Phys.*, **63**, 99-105, 2001
- Kelley, M.C., Arce, T.L., Salowey, J., Sulzer, M., Armstrong, W.T., Carter, M., and Duncan, L.: Density Depletions at the 10m Scale Induced by the Arecibo Heater, *J. Geophys. Res.*, **100**, 17 367–17 376, 1995
- Kolesnikova, E., Robinson, T.R., and Davies, J.A.: Predicted and observed characteristics of small-scale field-aligned irregularities generated in the F region by low power HF heating, *Ann. Geophys.*, **20**, 647-653, 2002
- Koloskov, A.V., Leyser, T.B., Yampolski, Yu. M. and Beley, V.S.: HF pump-induced large scale radial drift of small scale magnetic field-aligned density striations, *J. Geophys. Res.*, **107(A7)**, 10.1029/2001JA000154, 2002
- Kuo, S.P., Lee, M.C. and Kossey, P.: Excitation of oscillating two stream instability by upper hybrid pump waves in ionospheric heating experiments at Tromsø, *Geophys. Res. Lett.*, **24(A10)**, 2969–2972, 1997
- Lehtinen, M.S. and Huuskonen, A.: General incoherent scatter analysis and GUIDAP, *J. Atmos. Terr. Phys.*, **58**, 435-452, 1996
- Mantas, G.P., Carlson Jr., H.C. and LaHoz, C.: Thermal Response of the F Region Ionosphere in Artificial Modification Experiments by HF Radio Waves, *J. Geophys. Res.*, **86(A2)**, 561-574, 1981
- Milan, S.E., Yeoman, T.K., Lester, M., Thomas, E.C., and Jones, T.B.: Initial backscatter statistics for the CUTLASS HF radar, *Ann. Geophys.*, **15**, 703-718, 1997
- Minkoff, J., Kugelman, P. and Weissman, I.: Radio frequency scattering from a heated ionospheric volume, 1, VHF/UHF field-aligned and plasma-line backscatter measurements, *Radio Science*, **9(11)**, 941-955, 1974a
- Minkoff, J., Laviola, M., Abrams, S. And Porter, D.: Radio frequency scattering from a heated ionospheric volume, 2, Bistatic Measurements, *Radio Science*, **9(11)**, 957-963, 1974b
- Minkoff, J. And Kreppel, R.: Spectral Analysis and Step Response of Radio Frequency Scattering From a Heated Ionospheric Volume, *J. Geophys. Res.*, **81(16)**, 1976
- Newman, A.L., Carlson Jr., H.C., Mantas, G.P. and Djuth, F.T.: Thermal Response of the F-Region Ionosphere For Conditions of Large HF-Induced Electron-Temperature Enhancements, *Geophys. Res. Lett.*, **15(4)**, 311-314, 1988
- Paschmann, G., Haalund, S. And Treumann, R.: Auroral Plasma Physics, Kluwer Academic Publishers, Dordrecht, 2003
- Perkins, F.W.: A theoretical model for short-scale field-aligned plasma density striations, *Radio Science*, **9(11)**, 1065-1070, 1974

- Perkins, F.W., Obermann, C. and Valco, E.J.: Parametric instabilities and ionospheric modification, *J. Geophys. Res.*, **79**, 1478-1496, 1974
- Perkins, F.W. and Goldman, M.V.: Self-Focusing of Radio Waves in an Underdense Ionosphere, *J. Geophys. Res.*, **86(A2)**, 600-608, 1981
- Ponomarenko, P.V., Leyser, T.B. and Thide, B.: New electron gyroharmonic effects in HF scatter from pump-excited magnetic field-aligned ionospheric irregularities, *J. Geophys. Res.*, **104**, 10081-10087, 1999
- Ponomarenko, P.V. and Waters, C.L.: Spectral width of SuperDARN echoes: measurement, use and physical interpretation, *Ann. Geophys.*, **24**, 115-128, 2006
- Ponomarenko, P.V., Waters, C.L. and Menk, F.W.: Effects of mixed scatter on SuperDARN convection maps, *Ann. Geophys.*, **26**, 1517-1523, 2008
- Rao, P.B. and Thorne, G.D.: A model for RF scattering from field-aligned heater-induced irregularities, *Radio Science*, **9(11)**, 987-996, 1974
- Rietveld, M.T., Kohl, H., Kopka, H. and Stubbe, P.: Introduction to ionospheric heating at Tromsø - I. Experimental overview, *J. Atmos. Terr. Phys.*, **55(4)**, 577-599, 1993
- Rietveld, M.T., Kosch, M.J., Blagoveshchenskaya, N.F., Kornienko, V.A. Leyser, T.B. and Yeoman, T.K.: Ionospheric electron heating, optical emissions, and striations induced by powerful HF waves at high latitudes: Aspect angle dependence, *J. Geophys. Res.*, **108(A4)**, doi:10.1029/2002JA009543, 1141, 2003
- Robinson, T.R.: The heating of the high latitude ionosphere by high power radio waves, *Phys. Rep.*, **179**, 79-209, 1989
- Robinson, T.R., Honary, F., Stocker, A.J., Jones, T.B. and Stubbe, P.: First EISCAT observations of the modification of F region electron temperatures during RF heating at harmonics of the electron gyrofrequency, *J. Atmos. Terr. Phys.*, **58**, 385-395, 1996
- Robinson, T.R., Stocker, A.J., Bond, G.E., Eglitis, P., Wright, D.M., Jones, T.B. and Rietveld, M.T.: First CUTLASS-EISCAT heating results, *Adv. Space Res.*, **21(5)**, 663-666, 1998
- Robinson, T.R., Yeoman, T.K., Dhillon, R.S., Lester, M., Thomas, E.C., Thornhill, J.D., Wright, D.M., van Eyken, A.P. and McCrea, I.W.: First observations of SPEAR-induced artificial backscatter from CUTLASS and the EISCAT Svalbard radars, *Ann. Geophys.*, **24**, 291-309, 2006
- Schiffler, A., Sofko, G., Newell, P.T. and Greenwald, R.: Mapping the outer LLBL with SuperDARN double-peaked spectra, *Geophys. Res. Lett.*, **24**, 3149-3152, 1997
- Showen, R.L., and Behnke, R.A.: The effect of HF-induced plasma instabilities on ionospheric electron temperatures, *J. Geophys. Res.*, **83**, 207-209, 1978.
- Showen, R.L., and Kim, D.M: Time variations of HF-induced plasma waves, *J. Geophys. Res.*, **83**, 623-628, 1978

- Stocker, A.J., Honary, F., Robinson, T.R., Jones, T.B., Stubbe, P. and Kopka, H.: EISCAT observations of large scale electron temperature and electron density perturbations caused by high power HF radio waves, *J. Atmos. Terr. Phys.*, **54**, 1555-1572, 1992
- Stubbe, P., Kopka, H., Lauche, H., Rietveld, M.T., Brekke, A., Holt, O., Jones, T.B., Robinson, T.R., Hedberg, A., Thide, B., Crochet, M. and Lotz, H.I.: Ionospheric modification experiments in northern Scandinavia, *J. Atmos. Terr. Phys.*, **44**, 1025-1041, 1982
- Stubbe, P. and Hagfors, T.: The Earth's Ionosphere: A Wall-less Plasma Laboratory, *Surv. Geophys.*, **18**, 57-127, 1997
- Utlaut, W.F.: An ionospheric modification experiment using very high power, high frequency transmission, *J. Geophys. Res.*, **73** (31), 6402-6405, 1970
- Utlaut, W.F., and Cohen, R.: Modifying the ionosphere with intense radio waves, *Science*, **174**, 245-254, 1971
- Vaskov, V. and Gurevich, A.: Nonlinear resonant instability of a plasma in the field of an ordinary electromagnetic wave, *Sov. Phys. JETP Engl. Transl.*, **42**, 91-97, 1975
- Vaskov, V.V., and Gurevich, A.V.: Resonance instability of small scale plasma perturbations, *Sov. Phys. JETP, Engl. Transl.*, **46**, 487, 1977
- Villain, J.P., André, R., Hanuise, C. And Grésillon, D.: Observation of the high latitude ionosphere by HF radars: Interpretation in terms of collective wave scattering and characterization of turbulence, *J. Atmos. Terr. Phys.*, **58**, 943, 1996
- Wannberg, G.: Incoherent Scatter Radar Techniques – An Overview, EISCAT Radar School presentation, Kiruna, 2005
- Wright, D.M., Yeoman, T.K., Baddeley, L.J., Davies, J.A., Dhillon, R.S., Lester, M., Milan, S.E. and Woodfield, E.E.: High resolution observations of spectral width features associated with ULF wave signatures in artificial HF radar backscatter, *Ann. Geophys.*, **22**, 169-182, 2004
- Wright, D.M., Davies, J.A., Yeoman, T.K., Robinson, T.R. and Shergill, H.: Saturation and hysteresis effects in ionospheric modification experiments observed by the CUTLASS and EISCAT radars, *Ann. Geophys.*, **24**, 543-553, 2006
- Yeoman, T.K., Wright, D.M., Robinson, T.R., Davies, J.A., Rietveld, M.: High spatial and temporal resolution observations of an impulse-driven field line resonance in radar backscatter artificially generated with the Tromsø heater, *Ann. Geophys.*, **15**, 634-644, 1997
- Zhang, M.L., Radicella, S.M., Kersley, L. and Pulinets, S.A.: Results of the modelling of the topside electron density profile using the Chapman and Epstein functions, *Adv. Space Res.*, **29**, 871-876, 2002